1884 1984
A CENTURY OF ELECTRICAL PROGRESS

IEEE TRANSACTIONS ON
INSTRUMENTATION AND MEASUREMENT

DECEMBER 1984 VOLUME IM-33 NUMBER 4 (ISSN 0018-9456)

A PUBLICATION OF THE IEEE INSTRUMENTATION AND MEASUREMENT SOCIETY

EDITORIAL

PAPERS

SHORT PAPERS

1884 1984
A CENTURY OF ELECTRICAL PROGRESS

IEEE INSTRUMENTATION AND MEASUREMENT SOCIETY

The Instrumentation and Measurement Society is an organization, within the framework of the IEEE, of members with principal professional interest in instrumentation and measurement. All members of the IEEE are eligible for membership in the Society and will receive this TRANSACTIONS upon payment of the annual Society membership of $8.00. For information on joining write to the IEEE at the address below.

ADMINISTRATIVE COMMITTEE

BERNARD P. GOLLOMP, *Society President*
Test Systems Div.
The Bendix Corp.
Teterboro, NJ 07608
(201) 393-2505

FRED LIGUORI, *Society Vice President*
38 Clubhouse Rd.
Browns Mills, NJ 08015
(201) 323-2842

HAROLD S. GOLDBERG, *Society Secretary-Treasurer*
Analogic Corporation
Audubon Road
Wakefield, MA 01880
(617) 246-0300 Ext. 2202

Term Expires 1984	*Term Expires 1985*	*Term Expires 1986*	*Term Expires 1987*
HARRY M. CRONSON	DAVID W. BRAUDAWAY	CHARLES C. EVANS	OLIVER T. CARVER
HENRIECUS KOEMAN	FRANK J. DOUCET	BERNARD P. GOLLOMP	MARY CWIKLEWSKI CHIU
FRED LIGUORI	HAROLD S. GOLDBERG	ROBERT A. LAWTON	LAWRENCE D. FREEMAN
NORRIS S. NAHMAN	ROBERT A. KAMPER	LOUIS A. LUCERI	FRANK K. KOIDE

Ex Officio
Society Jr. Past President
REUVEN KITAI
Society Sr. Past President
A. RAY HOWLAND, P.E.
Transactions Editor
FRED LIGUORI

Newsletter Editor
ALEX F. MELONI
Prospective Computer
Analysts, Inc.
1791 Route 37 West
Toms River, NJ 08757
(201) 240-7007

Division II Director
IRVIN N. HOWELL, JR.
South Central Bell Telephone Co.
P.O. Box 771
Birmingham, AL 35201
(205) 321-2094

Standing Committee Chairmen

Awards and Membership Recognition: S. F. ADAM (415) 968-4900
W. D. George Award: J. A. BARNES (303) 499-1000, Ext. 3294
A. R. Chi Award: R. D. CUTKOSKY (301) 921-3806
Chapter Activities and Development: FRANK J. DOUCET (819) 997-3571
Conferences and Meetings: OLIVER T. CARVER (617) 229-3241
Finance: FRED LIGUORI (201) 323-2842
HAROLD S. GOLDBERG, co-chairman (617) 927-8885
Constitution and By-laws: A. RAY HOWLAND (404) 292-0782
Historian: ROBERT A. SODERMAN (408) 727-4400
Student Activities: LOUIS A. LUCERI (516) 391-5592
Long-Range Planning: A. RAY HOWLAND (404) 292-0782
Membership Development and Services: FRANK K. KOIDE (714) 632-3923
Chapter Activities & Development: FRANK J. DOUCET (819) 997-3571
Development & Education: FRANK K. KOIDE (714) 632-3923
Student Activities: LOUIS A. LUCERI (516) 391-5592
Organization/Nominations: REUVEN KITAI (416) 525-9140, Ext. 4966
Publications: HENRIECUS KOEMAN (206) 543-4491
L. D. FREEMAN, co-chairman (617) 863-2266
Technical and Standards Activities: DAVID W. BRAUDAWAY (505) 844-6556
R. A. KAMPER, co-chairman (303) 497-3535

Technical Committee Chairmen

Electromagnetic Measurements, State of the Art:
ARTHUR J. ESTIN (303) 443-0817
DC–LF Standards, Instrumentation and Measurements:
BARRY A. BELL (301) 921-2727
Frequency and Time: HELMUT W. HELLWIG (617) 927-8220
ATLAS Coordinating Committee: JOHN LEWIS (714) 736-5451
S. M. SCHLOSSER, co-chairman (703) 683-8422
HF Instrumentation and Measurements: GUNTHER U. SORGER
(415) 854-6965
Instrumentation Safety: CHARLES G. GORSS, JR. (617) 369-4400, Ext. 2336
Automated Instrumentation: FRED LIGUORI (201) 323-2842
Automotive Sensors and Diagnostics: WILLIAM G. WOLBER (812) 378-7166
Waveform Measurement and Analysis: ROBERT A. LAWTON (303) 497-3339

Representatives on Other IEEE Bodies

Oceanic Engineering: T. M. DAUPHINEE (613) 993-2313
Autotestcon: O. T. CARVER (617) 229-3241; C. SCATORO (201) 393-2519
CPEM: R. A. KAMPER (303) 497-3535
Liaison Standards Board: D. W. BRAUDAWAY (505) 844-6556
PACE Coordinator: H. M. CRONSON (617) 271-7579
Editorial Board of IEEE Micro: H. KOEMAN (206) 543-4491
Editorial Board to Proceedings: H. KOEMAN (206) 543-4491
Editorial Board to Computer Design and Test: P. JACKSON (201) 729-5888
Research and Development: O. PETERSONS (301) 921-2328
Div. II Rep. IEEE Pub. Board: D. H. SHEINGOLD (617) 329-4700, Ext. 294
Committee on Man and Radiation: S. DHURJATY
Steering Committee of the IEEE J. Lightwave Technol.:
L. A. LUCERI (516) 391-5592
B. P. GOLLOMP (201) 393-2505
Society on Social Implications of Technology: OLIVER T. CARVER (617) 272-400

THE INSTITUTE OF ELECTRICAL AND ELECTRONICS ENGINEERS, INC.

Officers

RICHARD J. GOWEN, *President*
CHARLES A. ELDON, *President-Elect*
HENRY L. BACHMAN, *Executive Vice President*
V. PRASAD KODALI, *Secretary*
CYRIL J. TUNIS, *Treasurer*
J. BARRY OAKS, *Vice President, Educational Activities*
RUSSELL C. DREW, *Vice President, Professional Activities*
JOSE B. CRUZ, JR., *Vice President, Publication Activities*
MERRILL W. BUCKLEY, JR., *Vice President, Regional Activities*
STEPHEN KAHNE, *Vice President, Technical Activities*
IRVIN N. HOWELL, JR., *Division II Director*

Headquarters Staff

ERIC HERZ, *Executive Director and General Manager*
ELWOOD K. GANNETT, *Deputy General Manager*

THOMAS W. BARTLETT, *Controller*
DONALD CHRISTIANSEN, *Editor of Spectrum*
IRVING ENGELSON, *Staff Director, Technical Activities*
LEO FANNING, *Staff Director, Professional Activities*
SAVA I. SHERR, *Staff Director, Standards*
DAVID L. STAIGER, *Staff Director, Publishing Services*
CHARLES F. STEWART, JR., *Staff Director, Administration Services*
DONALD L. SUPPERS, *Staff Director, Field Services*
THOMAS C. WHITE, *Staff Director, Public Information*
JOHN F. WILHELM, *Staff Director, Educational Services*

Publications Department

Production Managers: ANN H. BURGMEYER, CAROLYNE TAMNEY, GAIL S. FERENC
Associate Editors: MARY E. GRANGEIA, MONA MITTRA, NELA RYBOWICZ, BARBARA SOMOGYI

IEEE TRANSACTIONS ON INSTRUMENTATION AND MEASUREMENT is published quarterly by The Institute of Electrical and Electronics Engineers, Inc. **Headquarters:** 345 East 47 Street, New York, NY 10017. Responsibility for the contents rests upon the authors and not upon the IEEE, The Society, or its members. **IEEE Service Center** (for orders, subscriptions, address changes, Region/Section/Student Services): 445 Hoes Lane, Piscataway, NJ 08854. **Telephones:** Headquarters 212-705 + extension: Information -7900, General Manager -7910, Controller -7748, Educational Services -7860, Publishing Services -7560, Standards -7960, Technical Services -7890. IEEE Service Center 201-981-0060. Professional Services: Washington Office 202-785-0017. NY Telecopier No. 212-752-4929. Telex No. 236-411 (International messages only). Individual copies: IEEE members $6.00 (first copy only), nonmembers $12.00 per copy. Annual subscription price: IEEE members, dues plus Society fee. Price for nonmembers on request. Available in microfiche and microfilm. **Copyright and Reprint Permissions:** Abstracting is permitted with credit to the source. Libraries are permitted to photocopy beyond the limits of U.S. Copyright law for private use of patrons: (1) those post-1977 articles that carry a code at the bottom of the first page, provided the per-copy fee indicated in the code is paid through the Copyright Clearance Center, 29 Congress Street, Salem, MA 01970; (2) pre-1978 articles without fee. Instructors are permitted to photocopy isolated articles for noncommercial classroom use without fee. For other copying reprint or republication permission, write to Director, Publishing Services at IEEE Headquarters. All rights reserved. Copyright © 1984 by The Institute of Electrical and Electronics Engineers, Inc. Second-class postage paid at New York, NY and at additional mailing offices. **Postmaster:** Send address changes to IEEE, 445 Hoes Lane, Piscataway, NJ 08854.

Editorial
Another "Changing of the Guard"

IN OUR June issue, I had the pleasure of introducing our new European Associate Editor, Dr. Peter Kartaschoff, while at the same time offering our thanks to Dr. Claude Audoin who served us so faithfully for three years prior. Now it is time to bid farewell to our Region 10 Associate Editor, Dr. Osamu Nishino. He also has served us faithfully for three years and was kind enough to recruit his own replacement. With our sincere thanks, Dr. Nishino can now add "service as the first Japanese Associate Editor of the IEEE TRANSACTIONS ON INSTRUMENTATION AND MEASUREMENT" to his long list of accomplishments and honors. As I pointed out in our June editorial, Japan topped our honor role in 1983 for having more authors with publications in our TRANSACTIONS than any other nation. This achievement is due, in large measure, to the fine work of Dr. Nishino as Associate Editor. Honored as Professor Emeritus by the University of Tokyo, he has contributed substantially to our profession as an outstanding educator. He was honored as an IEEE Fellow in 1973. We all wish him continued success and a long, healthy life ahead.

Taking over as the new Associate Editor for Region 10 is another distinguished Fellow of the IEEE, Dr. Makoto Kanno. He was so honored this year for contributions and leadership in the development of precise capacitance standards and for his research work in precision electrical measurements.

We are indeed fortunate to have such a capable volunteer to serve us. I shall look forward to the pleasure of a long, enjoyable relationship with him while you, our members and readers, may continue to enjoy a bounty of quality published papers from our fellow professionals in Region 10.

FRED LIGUORI
Editor

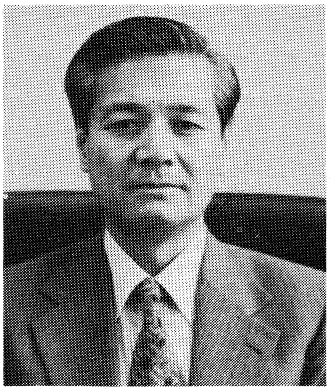

Dr. Makoto Kanno (SM'66-F'84) was born in Sendai, Japan on April 1, 1925. He received the B.E. degree in communications engineering and the Ph.D. degree in engineering from Tohoku University, Sendai, Japan.

From 1947 to 1952, he worked in medical electronics at Tohoku University. In 1952, he joined the research staff of the Electrotechnical Laboratory, Ministry of International Trade and Industry, Tokyo, Japan, where he worked on national standards of fundamental electric quantities. From 1961 to 1963, he was with the National Research Council, Ottawa, Ont., Canada, as a Postdoctorate Fellow. Since 1974, he has been a Professor and Dean of the Faculty of Engineering, Tamagaw Univerity, Tokyo, Japan.

A "Call to Arms"

AS YOU MAY SEE from the increasing number of paper reviewers on our Editorial Review Committee listed on the inside back cover, we are constantly adding to our ranks I am pleased to note that we now have a member from Mexico, Dr. Carlos Urbana Pacheco, among our new additions. Yet, with all this help, we are still in need of more reviewers. Because of our policy of assigning three reviewers per paper and a volume of over a hundred new papers to review per year, a minimum of 300 "work units" of manuscript reviews are required annually. Even with 30 reviewers, this would generate a workload of ten or more manuscripts per reviewer if all work could be spread evenly. Of course, not all reviewers are willing to do that much reviewing. Furthermore, the limitations dictated by reviewers' areas of expertise also forces uneven distribution of work. As a consequence, we have a few dedicated reviewers who handle 15 or more papers per year. This is really asking too much. As editor, I am therefore calling on our distinguished and capable readers to join this fine group of unselfish professionals who give of their personal time so that we can continue to enjoy our TRANSACTIONS. If you are able and willing to serve, please contact the Associate Editor closest to your region or myself. Our addresses are found on the inside back cover of every TRANSACTIONS. We are in particular need of reviewers qualified in computerized and microcomputer-embedded instrumentation, circuit theory, high-frequency instrumentation, waveform synthesis and analysis, and space or astronomical instrumentation. The range of electrical and electronic instrumentation covered by the TRANSACTIONS is very broad indeed, so we can probably use you no matter what your specialty. So pick up your pen and heed the call, for indeed, it is mightier than the sword.

FRED LIGUORI
Editor

A Switched-Capacitor Digital Capacitance Bridge

KENZO WATANABE, MEMBER, IEEE, AND GABOR C. TEMES, FELLOW, IEEE

***Abstract*—A switched-capacitor bridge has been developed for capacitance measurements. It consists of four arms connected between the low-impedance output and virtual ground nodes of an op-amp, and hence is insensitive to parasitic capacitances. The capacitance to be measured is first given a proportional charge. This charge is then compared successively with charges quantized by means of a programmable binary-weighted capacitor array, until a balance is reached. This digital balance operation makes it possible to accomodate an automatic calibration scheme, which affords, in conjunction with the parasitic-insensitive configuration, an accurate measurement. Error analysis has shown that a 10-bit quantization accuracy and a relative error as small as 0.1 percent are attainable when the bridge is fabricated in LSI circuit form using present MOS technologies. A prototype bridge built using discrete components has confirmed the principles of operation. Examples of measurement are also given.**

I. INTRODUCTION

Balancing a bridge by nulling a meter is a fundamental procedure for measuring a capacitance using the transformer-ratio-arm or Schering bridge [1]. A measurement accuracy of 1 part/10^6 is attainable by this method, but the procedure is cumbersome and time consuming because of the manual balance operation involved. The four-terminal-pair method [2] has eliminated the manual operation by detecting the voltage across and the current through the impedance to be measured. The price paid for the automated measurement is the complicated signal processing necessary for calculating the impedance. In addition, this method requires a special sample holder because it is susceptible to parasitic capacitances [3]. This makes it difficult to apply this method to the characterization of integrated MOS capacitors in which parasitic capacitances are inevitable.

McCreary and Sealer have proposed a novel technique to characterize binary-weighted MOS capacitor arrays [4]. Based on the voltage-divider principle, their method has facilitated the capacitor ratio measurement, but it cannot measure the absolute value of each capacitor.

In a recent publication [5], a switched-capacitor circuit has been proposed for digital multiplication. This circuit has been modified to form a capacitance bridge which allows quick measurement of the absolute value as well as the ratio of capacitors. This paper describes the bridge configuration, the principles of measurement, and calculates the expected accuracy. A prototype bridge implemented using discrete components and some examples of measurement are also presented.

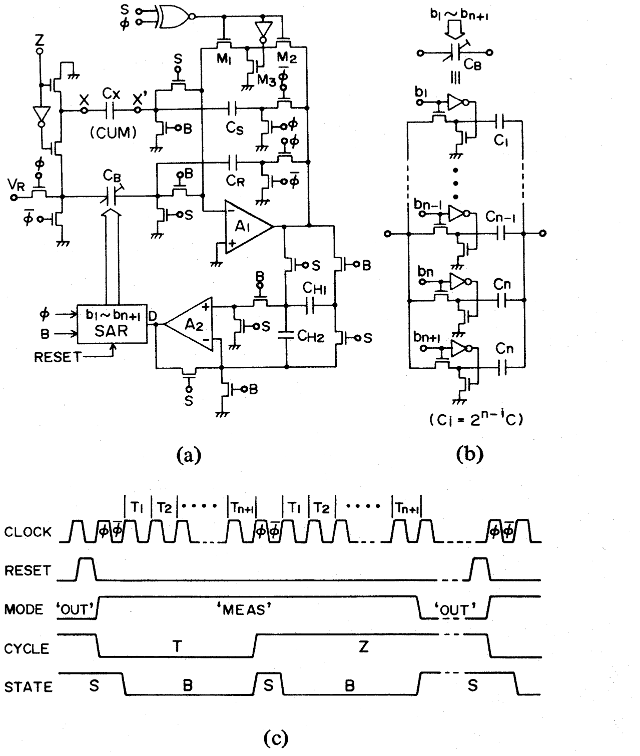

Fig. 1. (a) The schematic diagram of the capacitance bridge. CUM denotes the "Capacitor Under Measurement" and SAR the "Successive-Approximation Register." (b) The configuration of the programmable binary-weighted capacitor array C_B. (c) The timing sequence of the digital signals controlling the bridge operation.

II. THE CAPACITANCE BRIDGE

Fig. 1(a) shows the schematic diagram of the capacitance bridge. The capacitor C_X under measurement (CUM) is connected between the terminals X-X'. Its value is to be measured with reference to C_S. Therefore, C_S must be a standard capacitor of known value when an absolute value measurement is desired. C_B is a programmable binary-weighted capacitor array whose configuration is shown in Fig. 1(b). C_B is related to the reference capacitor C_R. These four capacitors C_X, C_S, C_B, and C_R form the four arms of the bridge. Since each arm is connected between a voltage source and the virtual ground of op-amp A_1, the parasitic capacitances to ground have no effect upon the bridge balance if op-amp A_1 is ideal. The holding capacitor C_{H_2} corresponds to the detector arm of a conventional bridge. Controlled by the signal from op-amp A_2, the successive-approximation registers SAR programs C_B so that the charge on C_{H_2} becomes zero, thereby bringing the bridge into a balance.

The transistors M_1, M_2, and M_3 form a reset switch. When M_1 and M_2 are "on" and M_3 is "off," the switch is closed and

Manuscript received November 28, 1983; revised March 8, 1984. This work was supported in part by the National Science Foundation under Grant ECS-8105166.

K. Watanabe is with the Research Institute of Electronics, Shizuoka University, Hamamatsu 432, Japan.

G. C. Temes is with the Department of Electrical Engineering, University of California, Los Angeles, CA 90024.

0018-9456/84/0900-0247$01.00 © 1984 IEEE

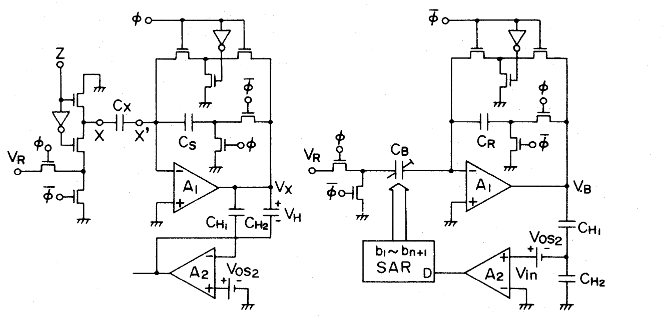

(a) (b)

Fig. 2. The circuit configurations in the S and B states: (a) The offset-free amplifier (S state). (b) The successive-approximation A/D converter (B state).

it short circuits C_S and C_R. When M_1 and M_2 are "off," on the other hand, the switch is open. The transistor M_3 is "on" to prevent the source-to-drain feedthrough capacitors of M_1 and M_2 from contributing to the feedback path of op-amp A_1 when M_1 and M_2 are "off."

The bridge operation is controlled by digital signals, whose timing sequence is shown in Fig. 1(c). A "Reset" signal sent from an external device initiates the measurement. Upon receiving this signal, the bridge clears the SAR and turns the operation into the "Measurement" mode. This mode consists of the "Test" (T) and "Zero" (Z) cycles. In the T cycle, the bridge measures the capacitance C_X in conjunction with the residual capacitance C_{res}. In the Z cycle, it measures only C_{res} which is then subtracted from the value measured in the T cycle. Each cycle is divided into the "Sample" (S) state in which the capacitor being measured is given a proportional charge, and the "Balance" (B) state during which the charge is approximately balanced with a charge quantized by means of a successive-approximation A/D conversion. When the B state in the Z cycle is completed, the operation changes into the "Out" mode. The capacitance value C_X is then available in the SAR in binary form. This mode continues until the next reset signal starts a new cycle of measurement. The operation in the T cycle will be next described in detail.

A. Operation in the S State of the T Cycle

In this state, $S = 1$ and $B = 0$. Thus the capacitors C_X and C_S are connected to the inverting input terminal of op-amp A_1 to form an offset-free noninverting amplifier [6]. Since $Z = 0$, the input of this circuit is the reference voltage V_R in the $\bar{\phi} = 1$ phase, as shown in Fig. 2(a). The output voltage is therefore

$$V_X = (C_X/C_S)\, V_R. \tag{1}$$

The op-amp A_2 forms a voltage follower with a grounded input. Its output is thus its own input-referred offset voltage V_{os_2}. The two holding capacitors C_{H_1} and C_{H_2} are connected in parallel in this state. Their top and bottom plates are driven by op-amps A_1 and A_2, respectively. Therefore, the voltages V_H across C_{H_2} is $V_X - V_{\text{os}_2}$. This voltage represents the initial voltage of C_{H_2} during the subsequent B state if the circuit condition is ideal. The operation under nonideal conditions will be described in Section III.

B. Operation in the B State of the T Cycle

Since now $B = 1$ and $S = 0$, the bridge contains C_B and C_R in place of C_X and C_S, respectively. The op-amp A_1 then forms an offset-free D/A converter. C_{H_1} and C_{H_2} are now connected in series, holding the voltage V_H stored in the previous S state. The op-amp A_2 now operates as a comparator. The whole circuit, including the SAR, is shown in Fig. 2(b). It forms a successive-approximation A/D converter [8]; the voltage to be converted is $V_H + V_{\text{os}_2} = V_X$.

The A/D conversion is performed as follows. In time slot $T_i (i = 1, 2, \cdots, n+1)$, the ith bit of the SAR (b_i) is temporarily set to 1, while the previously tested $i-1$ values of b are stored. The capacitance of the array C_B is then

$$C_B^{(i)} = \sum_{j=1}^{i-1} b_j \cdot 2^{n-j} C + 2^{n-i} C. \tag{2}$$

Charging this capacitor to the reference voltage V_R in the $\phi = 1$ phase, the D/A converter produces an output

$$V_B = -(C_B^{(i)}/C_R)\, V_R. \tag{3}$$

This tentative output value is divided by capacitors C_{H_1} and C_{H_2}. The input voltage V_{in} of the comparator is then

$$V_{\text{in}} = V_H + V_{\text{os}_2} + \frac{C_{H_1}}{C_{H_1} + C_{H_2}} V_B$$

$$= \left[\frac{C_X}{C_S} - \frac{C_{H_1}}{C_{H_1} + C_{H_2}} \cdot \frac{C_B^{(i)}}{C_R}\right] V_R. \tag{4}$$

Depending on the polarity of V_{in}, the SAR keeps b_i as 1 (if V_{in} is positive) or resets it to 0 (if V_{in} is negative). Repeating this process $n+1$ times makes V_{in} approximately zero, so that

$$\frac{C_X}{C_S} \simeq \frac{C_{H_1}}{C_{H_1} + C_{H_2}} \cdot \frac{C_B}{C_R} \tag{5}$$

holds, where

$$C_B = \sum_{i=1}^{n} b_i \cdot 2^{n-i} C + b_{n+1} C. \tag{6}$$

When $C_{H_1} = C_{H_2}$ and $C_R = 2^{n-1} C$, the SAR stores the ratio C_X/C_S (i.e., the capacitance C_X scaled by C_S) in binary form

$$C_X/C_S = b_1 \cdot 2^{-1} + b_2 \cdot 2^{-2} + \cdots + b_n \cdot 2^{-n} + b_{n+1} \cdot 2^{-n}. \tag{7}$$

It is worth noting here that the above operation is not affected by op-amp offset voltages if the open-loop gains of op-amps A_1 and A_2 are sufficiently high. Therefore, the bridge can be fabricated in a fully integrated form by MOS IC technologies.

III. ACCURACY ESTIMATE

The operation of the practical bridge circuit is affected by many error sources, such as mismatches in the capacitance ratio between C_B and C_R, the offset voltages and finite gains of op-amps A_1 and A_2, parasitic capacitances, and the feedthrough of the clock signals. These nonideal circuit conditions disturb the ideal balance condition, imposing a limit on the measure-

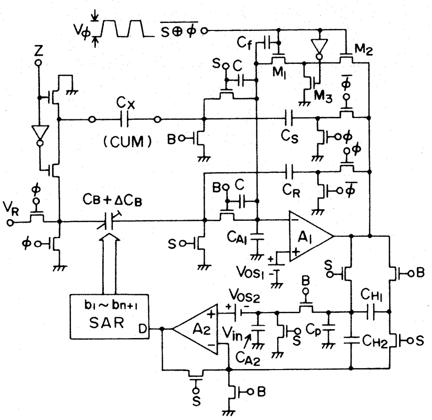

Fig. 3. The practical bridge circuit, including parasitic elements.

ment accuracy. In this section, we calculate the estimated accuracy when all of the bridge circuit (except C_X and C_S) is implemented by MOS IC process.

The bridge in Fig. 1(a) contains, in fact, many parasitic capacitances including the gate-source and gate-drain feedthrough capacitances of the MOS switches. Those residual capacitances, however, which are connected to the low-impedance nodes (except to virtual grounds) have no effect on the bridge balance. Furthermore, some of the feedthrough capacitances have matched couterparts driven by a complementary clock signal, such as C_ϵ and C_δ in Fig. 3. The feedthrough charges due to these paired capacitances can be neglected in a first-order approximation because they tend to cancel each other. Extending the above considerations into the overall circuit and including the other nonideal effects, we find the practical circuit model of the bridge shown in Fig. 3. In this figure, C_f is the feedthrough capacitance of M_1, C_p is the combined top-plate stray capacitance of C_{H_1} and C_{H_2}, and C_{A_1} and C_{A_2} are the input capacitances of op-amps A_1 and A_2, respectively. The mismatch between C_B and C_R is represented by ΔC_B.

The output voltage of op-amp A_1 in the $\overline{\phi} = 1$ phase of the S state is now, assuming $Z = 0$

$$V_X' = \frac{C_X V_R + C_f V_\phi + C_{\text{TS}} V_{\text{os}_1}/(1 + A_1)}{C_S(1 + C_{\text{TS}}/C_S A_1)} \tag{8}$$

where V_ϕ is the amplitude of the clock signal applied to the reset transistor M_1, and

$$C_{\text{TS}} = C_X + C_S + C_f + C_\epsilon + C_\delta + C_{A_1} \tag{9}$$

is the sum of the capacitances connected to the inverting input terminal of A_1 in the S state. The voltage follower A_2 produces the output voltage

$$V_A' = \frac{A_2}{1 + A_2} V_{\text{os}_2}. \tag{10}$$

The voltage across the holding capacitors C_{H_1} and C_{H_2} is thus $V_X' - V_A'$, while that across C_p is V_X'.

When the successive-approximation A/D conversion is completed, op-amp A_1 produces the output voltage

$$V_B' = \frac{-(C_B + \Delta C_B) V_R + C_f V_\phi + C_{\text{TB}} V_{\text{os}_1}/(1 + A_1)}{C_R(1 + C_{\text{TB}}/C_R A_1)}. \tag{11}$$

Here

$$C_{\text{TB}} = C_{\text{BT}} + C_R + C_f + C_\epsilon + C_\delta + C_{A_1} \tag{12}$$

is the sum of the capacitances connected to the inverting input terminal of A_1 in the B state, and $C_{\text{BT}} = 2^n C$ is the total capacitance of the array C_B.

The op-amp A_2 and the SAR balance the bridge so that

$$V_{\text{in}} = \frac{2C_H(V_H' - V_A') + C_p V_X' + C_H V_B'}{2C_H + C_p + C_{A_2}} + V_{\text{os}_2} = 0 \tag{13}$$

holds. In deriving (13), the mismatch between C_{H_1} and C_{H_2} is lumped into C_p and thus $C_{H_1} = C_{H_2} = C_H$ is assumed without loss of generality. Substituting (8), (10), and (11) into (13), we have

$$C_{\text{meas}} = \frac{C_S(C_B + \Delta C_B)}{2C_R} + \epsilon C_X + C_{\text{res}} \tag{14}$$

where

$$\epsilon = \left[1 + \frac{C_p}{2C_H}\right] \left[1 + \frac{1}{A_1} \cdot \frac{C_{\text{TB}}}{C_R}\right] \bigg/ \left[1 + \frac{1}{A_1} \cdot \frac{C_{\text{TS}}}{C_S}\right] - 1 \tag{15}$$

$$C_{\text{res}} = \left[1 + \epsilon + \frac{C_S}{2C_R}\right] \frac{C_f V_\phi}{V_R} + \left[1 + \frac{(1 + \epsilon) C_{\text{TS}}}{C_S}\right] \cdot \frac{C_S V_{\text{os}_1}}{(1 + A_1) V_R} + \left[\frac{1}{1 + A_2} + \frac{C_p + C_{A_2}}{2C_H}\right] \frac{C_S V_{\text{os}_2}}{V_R}. \tag{16}$$

$C_B + \Delta C_B$ represents the measured capacitance including the digital error caused by the mismatch between C_B and C_R, while $\epsilon C_X + C_{\text{res}}$ represents the analog error due to parasitic capacitances, clock feedthrough, and the nonideal performances of op-amps A_1 and A_2. They will be discussed separately in the following.

A. Digital Error

Each capacitor in the array C_B is assumed to be fabricated by connecting an appropriate number of MOS unit capacitors of magnitude C in parallel. The error in each capacitor is assumed to be random, normally distributed, and uncorrelated. The error charge ΔQ_B in the array C_B due to the capacitance error is then given by

$$\Delta Q_B = \sqrt{\sum_{i=1}^{n+1} (b_i \cdot \Delta C_i)^2}\; V_R \tag{17}$$

where ΔC_i is the standard deviation of each capacitor. If this error charge is smaller than half of that held in the LSB capacitor, then the A/D conversion process is monotonic and the digital output is accurate down to its LSB. Formulating this in terms of the capacitance mismatch, we have the condition

$$\sqrt{\sum_{i=1}^{n+1} (\Delta C_i / C_{\text{BT}})^2} \leqslant 2^{-(n+1)}. \tag{18}$$

Each term under the square root can be estimated by using the data presented by McCreary [7]: $\Delta C_1 / C_{\text{BT}} = 0.03$ percent, $\Delta C_2 / C_{\text{BT}} = 0.02$ percent, $\Delta C_3 / C_{\text{BT}} = 0.015$ percent, and so on. Substituting these values into (18), we find that the quantization accuracy obtainable with present MOS technologies is 10 bits [8].

B. Analog Error

The analog error can be described in terms of the relative error ϵ and the residual (or offset) error C_{res}. Noting that $C_{\text{TB}}/C_R = 2$, we have from (15)

$$\epsilon \simeq C_p/2C_H. \tag{19}$$

The top-plate stray capacitance C_p ranges from 0.1 to 1 percent of C_H, depending on the capacitor size and technology [9]. Therefore, the relative error can be reduced to a value as small as 0.1 percent.

To obtain a rough estimate of the residual capacitance C_{res}, suppose that we are measuring a small capacitance using a 1-pF standard capacitor for C_S. Assume also the following pessimistic values for the op-amp and circuit parameters: $A_1 = A_2 = 60$ dB, $V_{\text{os}_1} = V_{\text{os}_2} = 30$ mV, $C_{A_1} = C_{A_2} = 1$ pF, $C_f = C_\epsilon = C_\delta = 10$ fF, $(C_p + C_{A_2})/2C_H = 10^{-3}$, $V_R = 3$ V, $V_\phi/V_R = 4$, and $C_S \ll 2C_R$. Then, the residual capacitance due to the clock feedthrough is 40 fF, while that due to the offset voltages of the op-amps is about 5×10^{-5} C_S, although its precise value depends on C_X. This result indicates that the feedthrough component dominates C_{res}, and thus C_{res} is positive irrespective of the offset voltage polarity.

Consider now the bridge operation in the Z cycle. Since now $Z = 1$, C_X is disconnected from the reference source and is grounded. Therefore, the first term in the numerator of (8) vanishes and thus C_{meas} in (14) equals C_{res}; that is, the bridge in the Z cycle measures the residual capacitance which should be subtracted from the value measured in the T cycle. This self-calibrating ability allows the precise measurement of small capacitances.

Summarizing this section, we can conclude that a 10-bit quantization accuracy and a relative error as small as 0.1 percent is attainable with the integrated version of the bridge.

IV. MEASUREMENT EXAMPLES

A prototype bridge has been built using one half of an LM347 quad JFET op-amp chip, MC14066 CMOS analog switches, and discrete capacitors. The capacitor array was controlled by 10 bits. To reduce the capacitance spread in the array, a split reference source was incorporated into the bridge. The source supplied 3.2 V and 0.1 (= $3.2/2^5$) V to two 5-bit arrays, each consisting of 4-, 2-, 1-, 0.5-, and 0.25-nF capacitors. These two arrays were combined so that the array driven by 3.2-V source formed the upper half, and that driven by 0.1-V source the lower half, of the 10-bit array. Another 0.25-nF capacitor was incorporated into the lower half of the array, to form another LSB. Capacitors C_R, C_{H_1}, and C_{H_2} were chosen to be 4 nF.

Fig. 4 shows the voltage waveforms observable at the noninverting input terminal of op-amp A_2 during the B state when a ceramic capacitor (nominal value 2 pF) was measured with reference to a $C_S = 11.71$ pF capacitor. In the figure, the $\phi = 1$ phase in time slot T_i ($i = 1, 2, \cdots, 11$) is indicated by b_i so that each bit can be identified by the voltage level. Also shown (indicated by V_X) is the voltage stored in C_{H_2} in the previous S state. The upper trace shows the waveform in the T cycle. Inspecting the voltage levels[1] in the b_i phases, one obtains the ratio $(C_X + C_{\text{res}})/C_S = (00\,111\,001\,100)_B = 115/512$. The lower trace shows the waveform in the Z cycle. Now one obtains the ratio $C_{\text{res}}/C_S = (00\,001\,110\,000)_B = 7/128$. Thus $C_X = 1.99$ pF and $C_{\text{res}} = 0.64$ pF. The measured capacitance of C_X agrees exactly with that measured by a commercially available four-terminal-pair bridge. This bridge displays the result in a four-digit BCD form and its measurement error is 0.1 percent + 3 LSB. The measured residual capacitance, which is ten times larger than that estimated in the previous section, was found experimentally to be mostly due to the large clock feedthrough of the CMOS analog switch used for the reset transistor M_1 which is connected to the virtual ground created by op-amp A_1.

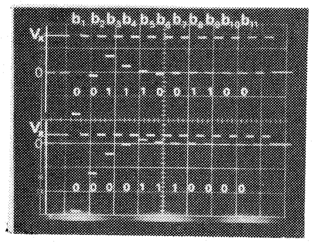

Fig. 4. Waveforms appearing at the noninverting input terminal of op-amp A_2 during the B state, when a $C_X \simeq 2$ pf ceramic capacitor was measured with reference to a $C_S = 11.71$ pF capacitor. Upper trace: waveform in the T cycle. Lower trace: waveform in the Z cycle. Vertical scale: 0.5 V/div. Horizontal scale: 0.2 ms/div.

A large number of capacitors were measured, and the results were compared with those obtained by the abovementioned commercial bridge. Capacitors ranging from 10 pF to 1 μF in decade steps were used for C_S, so that C_X/C_S was less than 1. Table I lists some of the results. It can be seen that the discrepancies between the measured results are mostly within 1 percent, although they tend to increase with decreasing capacitance. This probably can be attributed to the large clock feedthrough of the MOS switches, which violates the assumption that the charges due to paired feedthrough capacitances are negligible. In an LSI realization, these error sources will be greatly reduced.

V. CONCLUSIONS

An automatic switched-capacitor bridge, which allows the precise measurements of discrete and MOS IC capacitors, has been described. Error analysis has shown that a 10-bit quantization accuracy and a relative error as small as 0.1 percent are attainable by fabricating the bridge using presently available MOS technologies. A prototype bridge, implemented using discrete components, has confirmed the principles of opera-

---

[1] For b_7–b_{11}, the values are too small to show the sign of the signal. However, they are sufficient to drive the comparator op-amp A_2 unambiguously.

TABLE I

COMPARISON BETWEEN THE CAPACITANCES C_{SCB} MEASURED BY THE PRESENT SWITCHED-CAPACITOR BRIDGE AND THOSE C_{FTB} BY THE COMMERCIAL FOUR-TERMINAL-PAIR BRIDGE

(C_{nom} denotes the nominal capacitance and ϵ_r is the deviation between C_{SCB} and C_{FTB})

C_{nom} (pF)	C_{SCB} (pF)	C_{FTB} (pF)	ε_r (%)
1	1.062	1.044	1.72
2	1.960	1.992	1.61
4	4.324	4.227	1.10
10	10.42	10.39	0.29
22	21.74	21.95	0.96
47	45.48	45.42	0.13
100	103.5	102.8	0.68
220	206.1	205.4	0.34
470	455.8	453.3	0.55
1000	960.5	952.4	0.85
2200	2450	2448	0.08
4700	4528	4518	0.22
10000	10616	10530	0.82
22000	23016	23170	0.65
40000	38695	38350	0.90

tion. Incorporating a split reference source, a standard capacitor bank, and an automatic range-selecting circuit will provide the bridge with a wide measurement range. The extension to the measurement of grounded capacitors is another future problem.

The bridge described here features a circuit configuration suitable for LSI realization and high accuracy made possible by the digital balance operation and the parasitic-insensitive configuration. Therefore, it is also useful for the interface for "smart" capacitive transducers.

ACKNOWLEDGMENT

The authors are grateful to K. Kondo of the Research Institute of Electronics, Shizuoka University, for his help in the construction and the measurement of the bridge.

REFERENCES

[1] B. M. Oliver and J. M. Cage, *Electronic Measurements and Instrumentation.* New York: McGraw-Hill, 1971, ch. 9.

[2] A. C. Corney, "A universal four-pair impedance bridge," *IEEE Trans. Instrum. Meas.*, vol. IM-28, pp. 211-215, Sept. 1979.

[3] Hewlett Packard Operating Manual: Model 4275A Multi-frequency LCR Meter, Mar. 1982.

[4] J. L. McCreary and D. A. Sealer, "Precision capacitor ratio measurement technique for integrated circuit capacitor arrays," *IEEE Trans. Instrum. Meas.*, vol. IM-28, pp. 11-17, Mar. 1979.

[5] K. Watanabe and G. C. Temes, "Switched-capacitor digital multiplier," *Electron. Lett.*, vol. 19, pp. 33-34, Jan. 20, 1983.

[6] R. Gregorian and S. Fan, "Offset-free high resolution D/A converter," in *Proc. 14th Asilomar Conf. on Circuits, Systems, and Computers*, Nov. 1980, pp. 316-319.

[7] J. L. McCreary, "Matching properties, and voltage and temperature dependence of MOS capacitors," *IEEE J. Solid-State Circuits*, vol. SC-16, pp. 608-616, Dec. 1981.

[8] J. L. McCreary and P. R. Gray, "All-MOS charge redistribution analog-to-digital conversion techniques-Part I," *IEEE J. Solid-State Circuits*, vol. SC-10, pp. 371-379, Dec. 1975.

[9] R. W. Brodersen, P. R. Gray, and D. A. Hodges, "MOS switched-capacitor filters," *Proc. IEEE*, vol. 67, pp. 61-75, Jan. 1979.

A TRA Bridge Technique for In-Circuit Impedance Measurement

MAHFOOZUR RAHMAN, MUSLIM T. AHMED, MEMBER, IEEE, AND
VEMPATI G. K. MURTI, SENIOR MEMBER, IEEE

Abstract—A bridge technique is given for the measurement of impedances of two-terminal passive components in an arbitrary network without opening the circuit connections. It is ideally suited to the in-circuit measurements of passive elements in hybrid integrated circuits (HIC's) and printed circuit boards (PCB's). The method employs a new type of bridge, basically improvised from a transformer ratio-arm (TRA), a quadrature amplifier (QA), and two standard capacitors. All the measurements are in terms of the capacitors and the turns ratios of the TRA, and provide results with good accuracy. The range of measurement, together with the sources of error and their minimization, are discussed. Experimental results are found to be in good agreement with the theory.

I. INTRODUCTION

THE PROBLEM of in-circuit measurement of impedances/admittances is of contemporary importance. Such measurements are of particular significance in the component measurement of hybrid integrated circuits (HIC's), where they are required in the determination of initial tolerances of film resistors and capacitors to within 0.1 and 1.0 percent, respectively [1], [2]. Recently, methods for manual operation have been proposed for the in-circuit measurements [3], [4]. These are, however, limited to resistance measurement in all-resistor loops.

Some versatile automatic circuit test systems are also available in the market, such as an HP3060A Board Test System [5], which is microprocessor based and permits fault coverage for in-circuit testing, as well as analog and digital function testing. The automatic test systems are, however, expensive, costing in the range of \$86 000.

In this paper, a technique is given for the in-circuit measurement of impedances (admittances), which obviates the mentioned drawbacks of the methods given in [3], [4]. In addition, it is suitable for conventional as well as in-circuit measurements of *RLC* components with high-grade accuracy. A very attractive feature of the instrument is in its low cost, which comes to about \$1000 for a system fabricated in laboratory with high-grade components. Low cost and a high degree of accuracy constitute a very significant advantage of the instrument over the automatic test systems, particularly for the Third World countries.

The technique employs a transformer-ratio-arm (TRA) bridge, which provides results in terms of two variable, standard capacitors and turn-ratios of the TRA. The scheme requires a simple shielding arrangement for minimizing the effects of earth admittances and capacitive couplings. The sources of errors and the minimization are considered in detail. The measurements cover a wide range of component values. Experimental results are included in support of the theory.

II. THE MEASUREMENT TECHNIQUE

For demonstrating the basic technique on which the bridge scheme is based, an arbitrary passive network N (without mutual coupling) of Fig. 1(a) is considered. Let it be desired to measure the admittance Y_x connected[1] between nodes x and y, without breaking the circuit connections. The procedure is to ground all the nodes (or terminals), except node y, whose branches are connected to node x. In the figure, the step implies the connection of 1, 2, and 4 to 0, and is depicted by dotted lines. It can easily be verified that the resulting network is equivalent to a pi-section, shown in Fig. 1(b). Note that the admittance Y_x remains unaffected in the indicated operation.

The pi-representation is utilized in the measurement of in-circuit impedance/admittance by the scheme shown in Fig. 2. The bridge setup employs a TRA of low leakage impedance, a quadrature amplifier (QA) realized with active-*RC* circuit, two standard capacitors C_1 and C_2, and a low impedance detector D. The operational amplifier-*RC* realization of the QA is given in Fig. 3. The bridge scheme uses a simple shielding arrangement, as shown in the figure. In the in-circuit measurement of Y_x, between nodes x and y, the grounded nodes of the circuit, viz., 0, 1, 2, 4, are connected to the common ground 0 of the bridge. The nodes x and y are, respectively, connected to terminals x and y. At balance, the equivalent shunt admittances Y_{p1} and Y_{p2} of the pi-network are ineffective, as Y_{p1} is directly across the TRA and Y_{p2} appears across the detector. Thus, effectively the technique converts the network N to a single admittance (Y_x) for the purpose of measurement. In a similar way, the method may be repeated in the determination of the other network admittances.

The bridge is balanced by adjusting the capacitors C_1 and C_2 and the turns-ratios of the TRA. Balance is obtained when the current through the detector is zero, i.e.,

$$i_x + i_{C_1} + i_{C_2} = 0. \tag{1}$$

Manuscript received July 7, 1983; revised March 2, 1984.

M. Rahman and M. T. Ahmed are with the Department of Electrical Engineering, Z. H. College of Engineering and Technology, Aligarh Muslim University, Aligarh, 202 001 India.

V. G. K. Murti is with the Department of Electrical Engineering, Indian Institute of Technology, Madras, India.

---

[1] If parallel branches are between nodes x and y, then Y_x represents their effective admittance.

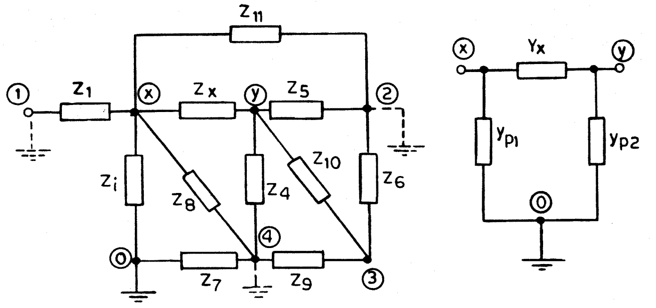

(a) (b)

Fig. 1. (a) Network N, and (b) pi-equivalent of N.

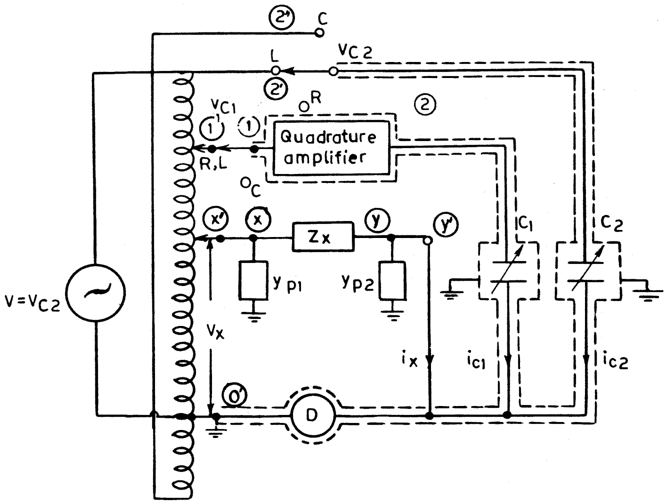

Fig. 2. Bridge scheme for in-circuit measurement.

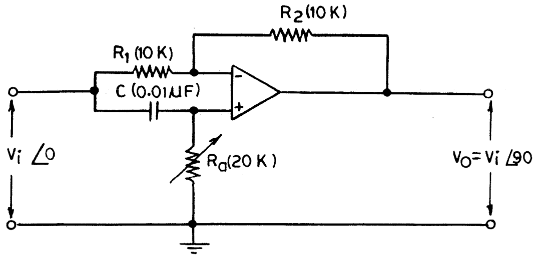

Fig. 3. Active RC realization of QA.

Substitution of circuit parameters in (1) and simplification gives

$$V_xY_x = w(C_1V_{C_1} - jC_2V_{C_2}) \tag{2}$$

where V_{C_1}, V_{C_2}, and V_x are, respectively, the voltages corresponding to the points 1′, 2′, and x' of the TRA. Four cases of practical interest are now considered.

Case 1. Resistor (R_x) Measurement

In the resistance measurement, balance is obtained by the adjustment of C_1 and the corresponding turns-ratio of TRA. With $Y_x = G_x = 1/R_x$, (2) gives

$$R_x = \left(\frac{V_x}{V_{C_1}}\right)\frac{1}{\omega C_1} \tag{3a}$$

or

$$R_x = \left(\frac{N_x}{N_{C_1}}\right)\frac{1}{\omega C_1} \tag{3b}$$

where N_{C_1} and N_x are the turns of the TRA at points 1′ and x', respectively. Note, the approximation (3b) is valid if the leakage impedance of the TRA is negligible. The same argument will also hold for the approximation involved in (4b) and (5b). This will be discussed in detail in Section III. It is observed that the in-circuit resistance in an all-resistor loop, which is commonly encountered in HIC's [1], [2], can easily and conveniently be measured by the technique. Also, only n measurements are required in the determination of n unknowns [4].

Case 2: Capacitance (C_x) Measurement

For an ideal capacitor with $Y_x = jwC_x$, the bridge is balanced by the adjustments of C_2 and the corresponding turns ratio of TRA. In this case, (2) yields

$$C_x = -\left(\frac{V_{C_2}}{V_x}\right)C_2 \tag{4a}$$

or

$$C_x \cong -\left(\frac{N_{C_2}}{N_x}\right)C_2. \tag{4b}$$

The equations indicate that, in C measurements, a phase shift of 180° is required to be introduced. This is practically done by using an appropriate tapping of the TRA (2″), as shown in Fig. 2, or by employing an active inverter [1].

Case 3. Lossy Capacitor Measurement

In a lossy (nonideal) capacitor having $Y_x = G_x + jwC_x$, both the parameters G_x and C_x are required to be determined. The equation at bridge balance is

$$V_x(G_x + jwC_x) = wC_1V_{C_1} - jwC_2V_{C_2}.$$

A comparison of the real and imaginary parts of the equation gives the required expressions for R_x and C_x. These are, respectively, found to be identical to the ones given in (3) and (4). The bridge balance involves adjustments of C_1, C_2, and the turns ratios N_x/N_{C_1} and N_{C_2}/N_x.

Case 4. Lossy Inductor

A lossy inductor has an RL-admittance function of the form $Y_x = G_x + 1/(jwL_x)$. The bridge is balanced with C_1, C_2, and the TRA. The equation at balance is

$$V_x(G_x + 1/(jwL_x)) = wC_1V_{C_1} - jwC_2V_{C_2}.$$

Here, R_x is once again given by (3); L_x is determined from

$$L_x = \left(\frac{V_x}{V_{C_2}}\right)\frac{1}{w^2C_2} \tag{5a}$$

or

$$L_x \cong \left(\frac{N_x}{N_{C_2}}\right)\frac{1}{w^2C_2}. \tag{5b}$$

L measurement is not required in the case of HIC's, but has been included to show the generality of the technique. In the case of ideal L, the balance is achieved with C_2 and N_x/N_{C_2} only.

It is evident from (3) through (5) that the method is suitable for measurements of component values over a wide range. Though the technique is particularly described for in-circuit measurements, the setup can also be used for conventional measurements of *RLC*-components. As the results are in terms of standard capacitors and turns-ratios of TRA, good accuracy is expected in the measurements. Expressions (3) and (5) involve the frequency term w; therefore, a stable drift-free oscillator, along with a frequency counter, is recommended. The salient feature of the technique is that, it not only provides an accurate method of in-cricuit adittance/impedance measurements of *RLC* components of an arbitrary network, but also determines n unknown parameters in n measurements.

III. PRACTICAL CONSIDERATIONS

In this section, some practical aspects of the scheme are critically examined. Particularly, the sources of errors and their minimization, and the range and accuracy of measurements, are considered in detail.

The accuracy of measurement depends upon i) the accuracy of the standards employed in the scheme, such as the capacitors C_1, C_2, and the frequency source, and ii) the errors introduced by the measurement system. The first source of error is directly dependent on the quality of standards employed in the scheme. This, in turn, implies that the overall accuracy desired in the measurement actually influences the choice of the grade of components employed in the realization of the system. The second aspect is concerned with the proper design and fabrication of the system so that the errors are minimized. This aspect shall now be considered in detail.

A. Effect of Leakage Impedance of TRA

In Fig. 2, the unwanted impedances Y_{p1} and Y_{p2} shunt the ratio-arm and the detector, respectively. As the internal impedance of a current detector is generally very low, the shunting effect of Y_{p2} is practically negligible. In case $Z_{p2}(=1/Y_{p2})$ is high, then the detector's sensitivity is decreased. This is, however, not serious and may easily be compensated for by providing an extra stage of amplification. The effect may also be minimized by connecting the detector on the secondary side of a matching transformer so that the reflected impedance of the detector is very small as compared to Z_{p2}.

Ideally, the ratio-arms of a TRA are required to have zero or negligible leakage impedances. Under such conditions, the shunting effect of Y_{p1} does not introduce error, and the expressions in (3b), (4b), and (5b) are valid. However, in case these impedances are not negligible, error is introduced in the measurements [8]. The effects are analyzed as follows.

The equivalent circuit representation of the bridge is shown in Fig. 4. The ratio-arms of the TRA are represented by voltage generators K_1E_1, K_2E_2, and E_x, along with their leakage impedances Z_{01}, Z_{02}, and Z_{ox}. This simplified representation, which does not take into account the coupling that exists between different sections of the secondary, is adequate to establish the order of errors involved due to leakage impedances. The coefficients K_1 and K_2 are included to make the analysis most general by accommodating conditions required for the bridge balance. For example, phase shifting of E_1 by 90° with QA is represented by $K_1 = j1$, and when the C_2 arm is not used in a particular measurement, it is depicted $K_2 = 0$. The shunting effects of the parasitic capacitances C_{s1} and C_{s2}, appearing across the arms having the capacitors C_1 and C_2, are accommodated in Y_{s1} and Y_{s2}, respectively. The effects of shunting capacitance C_{sx} and the shunt-arm admittance of N, Y_{p1} $(=G_{p1} + jwC_{p1})$, are included in Y_{sx}. This is given by $Y_{sx} = G_{p1} + jw(C_{p1} + C_{sx})$. As Y_{p2} appears across the detector, its effect is not considered in the analysis.

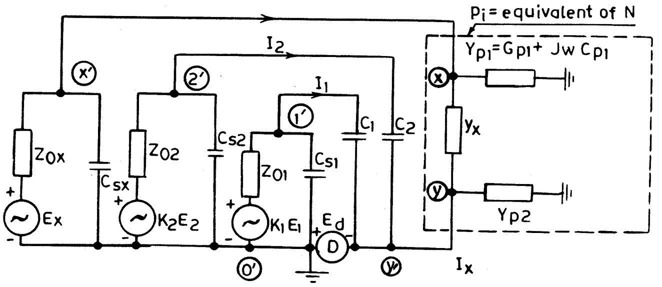

Fig. 4. Equivalent circuit of the scheme.

Nodal analysis at nodes 1′, 2′, and x' gives

$$\begin{aligned} &V_1(Y_1 + Y_{s1} + Y_{01}) - K_1E_1Y_{01} - E_dY_1 = 0\\ &V_2(Y_2 + Y_{s2} + Y_{02}) - K_2E_2Y_{02} - E_dY_2 = 0\\ &V_x(Y_x + Y_{sx} + Y_{0x}) - E_xY_{0x} - E_dY_x = 0 \end{aligned} \tag{6}$$

where E_d is the unbalance voltage across the detector and any admittance is given by $Y_i = (1/Z_i)$. At bridge balance, the detector voltage and current are zero, i.e., $E_d = 0$ and i_d is given by (1). Using (6) with $E_d = 0$, (1) gives

$$\frac{jwK_1E_1C_1Y_{01}}{Y_{01} + jw(C_1 + C_{s1})} + \frac{jwK_2C_2Y_{02}E_2}{Y_{02} + jw(C_2 + C_{s2})} + \frac{E_{x'}Y_{x'}Y_{0x}}{(Y_{0x} + Y_x + Y_{sx})} = 0. \tag{7}$$

The three cases of importance to HIC measurements are considered in the following.

Case 1 (Resistor): In this case, $Y_x = G_{x'}$ and the generator, multipliers are $K_1 = j1$ and $K_2 = 0$. Assuming the leakage impedances (Z_{0i}) to be predominantly resistive, simplification of (7) gives

$$\frac{G_x}{wC_1} = \frac{E_1}{E_x} \frac{1 + Z_{0x}(G_x + Y_{sx})}{1 + Z_{01}\,jw(C_1 + C_{s1})} \tag{8a}$$

$$\cong \frac{N_1}{N_x}\left[(1 + Z_{0x}G_x') + jw\left\{Z_{0x}C_{sx}' - Z_{01}(C_1 + C_{s1})\right\}\right] \tag{8b}$$

where $Y_{sx} = G_{p1} + jw(C_{p1} + C_{sx}) = G_{p1} + jwC_{sx}'$ and $G_x' = G_x + G_{p1}$.

The magnitude of (G_x/wC_1) is given by

$$M_R = \frac{N_1}{N_x}(1 + Z_{0x}G'_x) \cdot \left(1 + \left[\frac{w\{Z_{0x}C'_{sx} - Z_{01}(C_1 + C_{s1})\}}{1 + Z_{0x}G'_x}\right]^2\right)^{1/2}. \tag{9a}$$

Consideration of the actual order of values of the components in (9a) simplifies the expression to

$$M_R \cong \frac{N_1}{N_x}(1 + Z_{0x}G'_x). \tag{9b}$$

The percentage error is

$$\%\epsilon_R = 100\, Z_{0x}G'_x. \tag{10}$$

Note that error is basically a product of the leakage impedance and G'_x. The effective value of G'_x can be reduced to G_x by connecting the point 0 of the pi-section to the ground point 0′ of the bridge through a high resistance (≈100 kΩ).

Case 2 (Capacitor): In capacitance measurement, $Y_x = jwC_x$ and the multipliers are $K_1 = 0, K_2 = -1$. The substitution of conditions in (7) and subsequent simplification gives

$$\frac{C_x}{C_2} = \frac{E_2}{E_x}\,\frac{1 + Z_{0x}G_{p1} + jw(C_x + C'_{sx})Z_{0x}}{1 + jwZ_{02}(C_2 + C_{s2})} \tag{11a}$$

$$\cong \frac{N_2}{N_x}[1 + Z_{0x}G_{p1} + jw\{Z_{0x}(C_x + C'_{sx}) - Z_{02}(1 + Z_{0x}G_{p1})(C_2 + C_{s2})\}]. \tag{11b}$$

The corresponding magnitude is:

$$M_c = \frac{N_2}{N_x}(1 + Z_{0x}G_{p1}) \cdot \left[1 + \left\{w\frac{Z_{0x}(C_x + C'_{sx})}{1 + Z_{0x}G_{p1}} - wZ_{02}(C_2 + C_{s2})\right\}^2\right]^{1/2}. \tag{12a}$$

Once again, consideration of the order of the parameter values (12a) and the grounding of the pi-network through high resistance gives

$$M_c \cong \frac{N_2}{N_x}(1 + \epsilon_r)^{1/2} \cong \frac{N_2}{N_x}\left(1 + \frac{1}{2}\epsilon_r\right) \tag{12b}$$

where

$$\epsilon_r \cong w^2[Zp_x(C_x + C'_{sx}) - Z_{02}(C_2 + C_{s2})]^2 \tag{13}$$

and the percentage error as

$$\%\epsilon_c = 50\epsilon_r. \tag{14}$$

Case 3 (R ‖ C): Direct analysis for this case yields expressions which are difficult to interpret and do not provide insight into the errors involved. However, a fairly good idea regarding the R and C errors in this case is obtained from (10) and (14), respectively.

It is also evident from the equation that errors in R and C measurements are dependent on the leakage impedances of TRA, and should be made as low as practicable. In a well-constructed TRA, these are of the order of 50 mΩ [6]. The range of R and C values in HIC's, in acceptable initial tolerances, are about 100 Ω to 100 kΩ and 100 pf to 40 nf, respectively. The two ranges can conveniently be measured with the given bridge. For the worst-case analysis of errors, the minimum value of resistance (100 Ω) and the maximum value of capacitance (40 nf) are considered in (10) and (14). When the networks (N's) grounding is through a high resistance, the worst-case errors in the R and C measurements at 1 kHz are, respectively, 0.05 percent and 0.01 percent, respectively. The error in C measurement is negligible due to leakage impedances. Though the effect is seen to be more pronounced in R measurement, it is well within the permissible limits for HIC components. Moreover, in the normal range of R measurements, it will be smaller (≈0.005 percent).

IV. Experimental Setup and Results

For the verification of the technique, an experimental model of the bridge was improvised in the laboratory. The salient features of TRA and QA employed in the bridge are described as follows.

A. Transformer Ratio Arms

A considerable volume of literature is already available on the design of a TRA [7]. It has been shown in Section III that the error of measurement is directly dependent upon the leakage impedances of the ratio-arms, which are required to be low. This was achieved by providing a special, low-resistance secondary winding on a low-reluctance core. For the winding, thick, double-enamelled copper wire of 20 swg was used. To provide a maximum turns ratio of 10, the wire was wound on a mumetal core of large cross section (1.25 in^2) in a special manner. Eleven wires were randomly twisted together to form a cable, which was wound on the core in an even layer of 25 turns. The ends of 11 separate sections were then soldered to make a continuous winding of 275 turns. A uniform primary winding of 275 turns of double-enamelled copper wire of 24 swg was provided between the core and the ratio (secondary) winding.

B. Quadrature Amplifier

An active phase shifter, using monolithic operational amplifier and RC discrete elements, was used in the realization of the quadrature amplifier. The circuit is shown in Fig. 3. Its voltage transfer function is

$$T = \frac{V_0}{V_i} = 1\;\underline{|\pi - 2\tan^{-1} wCR}\,. \tag{15}$$

The output voltage remains equal to the input voltage, when the phase shift is varied from about 0° to 180°. Quadrature voltage is obtained when $wCR = 1$.

The circuit was fabricated with a 741-μA operational amplifier, polyester capacitor, and metal film resistors, each of 1-percent tolerance. The values of circuit components, for 1-kHz operation, are included in the figure within brackets. For the resistor R, a variable pot was used. It was adjusted until the desired phase shift of 90° was obtained.

In the experimental set-up, variable capacitors of secondary standard of H. W. Sullivain, Ltd. (London) were employed for C_1 and C_2. An audio range, sine-wave generator, along with a digital counter was used to apply a 10-V signal at 1 kHz. For the determination of bridge balance, the drop across a 50-Ω resistor was measured with a high-sensitivity CRO.

Twin-T configuration is very popular in active RC realizations. For the experiment, such a circuit, shown in Fig. 5, was considered. The components used in the fabrication of the circuit

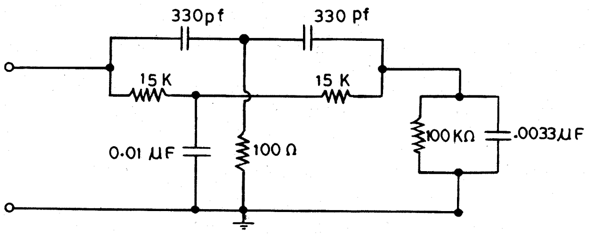

Fig. 5. Twin-T network. (Note: The indicated values are the nominal (marked) values.)

TABLE I
(APPLIED VOLTAGE—10 V: SUPPLY FREQUENCY—1 kHz; TURN-RATIO—1:1 (UNITY))

S.NO.	Value of component from G.R. Bridge	C_1	C_2	Value of component from the TRA Bridge	*% Error with GR-Bridge as reference
1.	14.96 K ohm	0.01063 µf.	–	14.98 K ohm.	0.01
2.	96.40 ohm.	1.655µf	—	96.21 ohm.	-0.20
3.	317 pf		318 pf	318 pf	0.32
4.	9280 pf		9270 pf	9270 pf	-0.10
5.	326 pf		325 pf	325 pf	-0.30
6.	15.18 K ohm	0.0105µf	—	15.16 K ohm	-0.13
7	Parallel RC Circuit: R=36.00K ohm C=3.4 nf	4.4nf	3.3 nf	36.19K ohm 3.35 nf	-0.20 0.30

*% error = (measured value − reference value/reference value) × 100

were initially measured by the GR Bridge (model 1608-A). These were then soldered to realize the network. The in-circuit measurement was performed according to the scheme described earlier. The details of the experiment, along with the results, are included in Table I.

It is observed that the maximum overall errors in R and C measurements are 0.2 and 0.32 percent, respectively. In the case of resistors, measurement of a high-value resistor (14.97 kΩ) yielded a lower error (0.01 percent), which is in conformity with the theory. However, in capacitor measurement, a higher error was obtained in the measurement of low-valued capacitor (317 pf). The deviation in theory may be due to the limited resolution of the capacitors C_1 and C_2 in the range of low-C measurements.

V. CONCLUSION

A bridge technique is given for the in-circuit measurements of passive components in an arbitrary network. Only n measurements are required in finding n unknown elements, without opening the circuit connections. The method is general and may also be adopted for the conventional measurements of R, C, and L components in a high grade of accuracy. The bridge is particularly attractive in the measurement and trimming operations of hybrid IC's. The experimental results on a laboratory model adequately supported the theory presented in the paper. The instrument has two distinct advantages over the automatic circuit test systems. First, it is a low-cost system which can be fabricated for around $1000 as compared to $86 000 for an automatic test system [5]. This feature is particularly attractive for organizations in the Third World countries which cannot easily afford expensive systems. Secondly, the worst-case error analysis, after taking the effects of leakage impedance of TRA and the shunting effects of parasites of the shunt arms of the pi-network into consideration, shows that, in the entire component range of HIC's, the bridge provides accuracies better than 0.05 percent for resistors and 80×10^{-6} parts/10^6 for capacitors at 1 kHz. These figures are superior to the accuracies specified in the automatic test systems [5].

At present, work is in progress towards making the bridge system technique suitable for automatic operation with microprocessor control. Such a system is expected to provide automatic in-circuit testing of active and passive components within reasonable cost.

REFERENCES

[1] G. S. Moschytz, *Linear Integrated Network: Fundamentals.* Princeton, NJ: Van Nostrand Reinhold, 1974, ch. 6.
[2] V. C. Hughes, O. R. Mulkey, and M. A. Williamson, "Thin-film fabrication procedures for complex *R-C* active filters," in *Proc. Electronics Components Conf.*, 1968, pp. 395–403.
[3] P. L. Swart *et al.*, "Resistor loops in hybrid circuits," *Microelectron.*, vol. 7, no. 3(c), pp. 53–55, Mar. 1976.
[4] S. C. Dutta Roy and V. G. Dass, "On resistor loops in hybrid circuits," *Proc. IEEE*, vol. 65, p. 583, 1977.
[5] "Printed circuit board testing with HP 3060A board test system," HP Publ. Manual no. 5952-8778, Aug. 1978.
[6] M. C. McGregor *et al.*, "New apparatus at the NBS for absolute capacitance measurement," *IRE Trans. Instrum.*, pp. 253–261, Dec. 1958.
[7] B. Hague and T. R. Foord, *Alternating Current Bridge Methods.* London: Pitman, 1971.
[8] M. Rehman and V. G. K. Murti, "The reduction of loading errors of a transformer bridge using NICS," *J. Physics E. Instrum.*, vol. 13, pp. 1119–1120, 1980.

Implicit Digital RMS Meter Design

SALEEM M. R. TAHA AND MAJID A. H. ABDUL-KARIM

Abstract—**This paper introduces the design of an implicit-type digital rms-value measurement device. It employs TTL and LSI components throughout the design. It is based on the difference of squares principle. The instrument is simulated and analyzed through the aid of a digital computer program. The software analysis developed reflects the hardware design of the implicit digital rms meter. System accuracy is about (±0.1) percent.**

I. Introduction

Alternating voltages can be measured by the conventional methods of finding the peak, mean, and rms values. The rms value is the most widely accepted representation of an ac signal level. A digital voltmeter is designed here to measure the rms value of a fluctuating voltage utilizing sampling and digital techniques. The technique used is based on the difference of squares principle.

The instrument which measures the rms voltage is shown in block diagram form in Fig. 1. Gilbert [1] uses the same technique, but in analog form. This paper gives a digital counterpart that measures the rms value implicitly.

II. Instrument Principle

Fig. 1 shows the block diagram of the proposed digital system of rms-value measurement. The input voltage V_i is converted to its digital equivalent via the appropriate analog-to-digital converter (ADC) circuit. Then, the sum of the input/output and the difference between them for each input sample are calculated and applied to a digital multiplier. The product will be in the form of the difference between the squares of input and output, i.e., the equivalent of $(V_i^2 - V_o^2)$. The products of all input samples are accumulated by the digital register (accumulator I).

Accumulator II is used to accumulate the output of accumulator I at the end of each input cycle to its contents. A state will be reached when the accumulator II output V_o will force accumulator I output to zero. This condition happens during the recording of the rms value of V_i, i.e.,

$$\sum_{i=1}^{N} (V_i^2 - V_o^2) = 0. \tag{1}$$

Since V_o has been regarded as constant during one input cycle, the above equation becomes

$$\sum_{i=1}^{N} V_i^2 - NV_o^2 = 0 \tag{2}$$

$$\therefore V_o = \left(\frac{1}{N} \sum_{i=1}^{N} V_i^2\right)^{1/2}. \tag{3}$$

A zero logic detector is incorporated in front of the accumulator I output to capture the measurement process. The output will be taken from the accumulator II output digital terminals. This may be converted to its decimal equivalent for readout purposes. The accuracy of measurement is dependent on the word length and number of samples taken per cycle.

This design is supported by an analysis executed by a digital computer program. The computer-aided design (CAD) program simulates the instrument and calculates its error and accuracy [2]. This leads to the appropriate choice of the digital hardware. In this case, $N = 1024$ samples/cycle and $n = 7$ bits (i.e., 7 bits ADC resolution), yielding an error of around 0.056 percent.

III. Conclusions

The inplicit digital rms meter described here (Fig. 2) will measure the rms value of any complex varying signal by computing numerical values of simultaneous samples of the instantaneous input voltage.

Usually, in such systems, the time taken to measure the rms value differs from one input wave shape to another. For instance, if the input is a sine wave of 50-Hz frequency, the rms value is measureable within 0.2 s [3].

The rms value is obtained as five decimal digits. The input frequency range is (30–70) Hz. It is capable of expansion by some simple additional circuitry. The accuracy of measurement is in the (±0.1 percent) class. The described system may be utilized as a multipurpose digital processing unit to measure power, energy, volt-amperes, and volt-amperes reactive. Although there is a commercially available single chip (Burr-Brown Model 4340) that converts the rms to dc, it has a poorer accuracy and has more limited applications compared with the described digital implicit system.

The implicit digital rms-value measurement techniques calculate the rms value implicitly and the system does not need to use a square rooter, as is the case with existing explicit techniques. Hence, it offers less circuit complexity and lower cost. A microprocessor-based implicit system that provides the same capability would be very useful.

Manuscript received April 6, 1983; revised March 30, 1984.

The authors are with the Department of Electrical Engineering, University of Baghdad, Baghdad, Iraq.

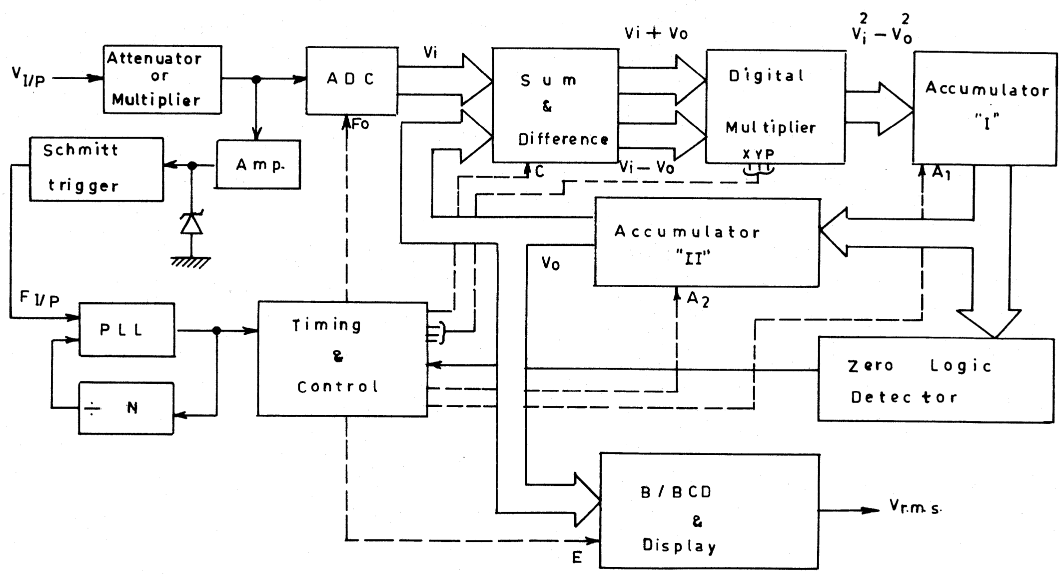

Fig. 1. Block diagram of the implicit digital rms meter.

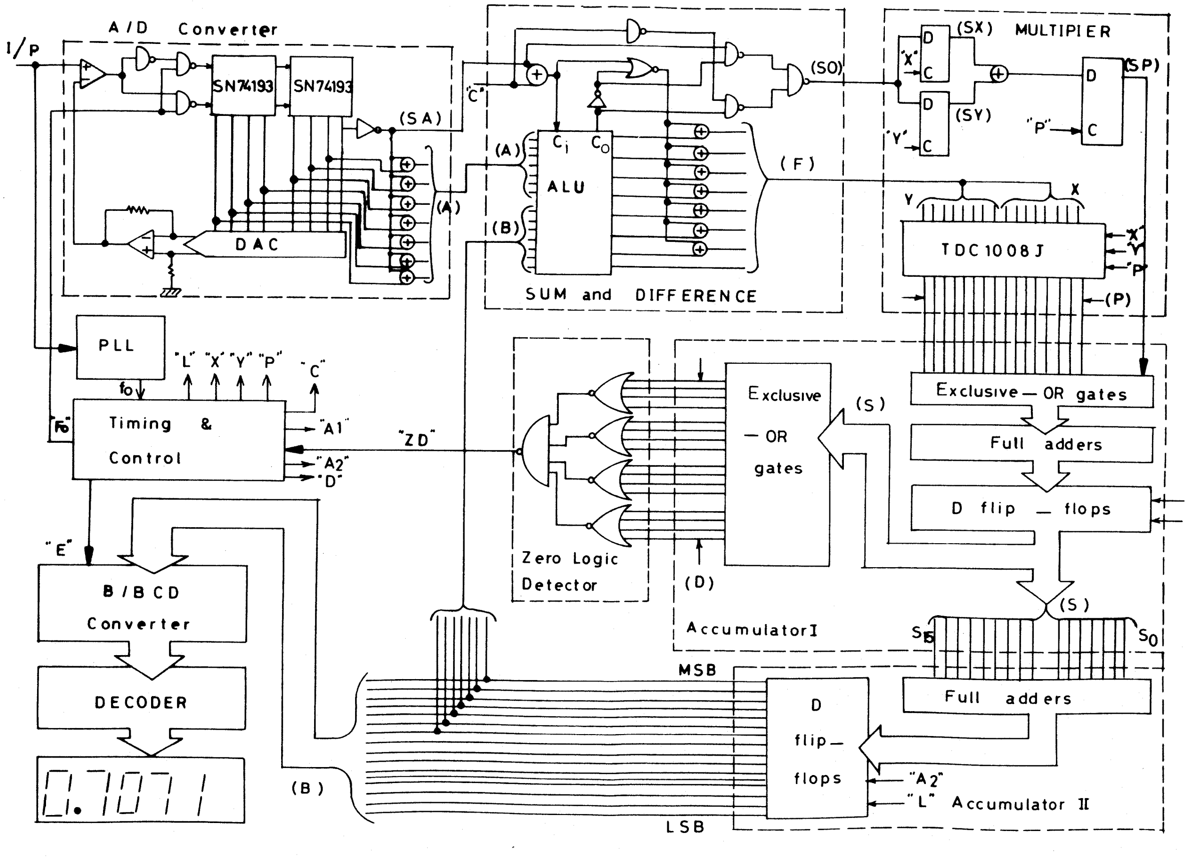

Fig. 2. Complete circuit diagram of implicit digital rms meter.

REFERENCES

[1] B. Gilbert, "Novel technique for R.M.S.-D.C. conversion based on the difference of squares," *Electron. Lett.*, vol. 11, no. 8, pp. 181-182, Apr. 17, 1975.

[2] S. M. R. Taha and M. A. H. Abdul-Karim, "CAD of implicit digital R. M. S. meter," IASTED 84, submitted for publication.

[3] S. M. R. Taha, "Implicit digital R. M. S. voltage measurement," M.Sc. thesis, University of Baghdad, Baghdad, Iraq, Nov. 1981.

A Simple and Low-Cost Personal Computer-Based Automatic Deep-Level Transient Spectroscopy System for Semiconductor Devices Analysis

C. Y. CHANG, SENIOR MEMBER, IEEE, WEI C. HSU, CHII M. UANG,
YEAN-KUEN FANG, AND W. C. LIU

Abstract—**A simple, low-cost, and flexible, automatic, deep-level transient spectroscopy (DLTS) system with an Apple II microcomputer for semiconductor devices analysis is described.**

By using an interactive Basic software program, all the instrument parameters including sampling aperture locations, temperatures, excitation pulse frequency, width and amplitude can be controlled automatically. The transient signals are also averaged by the software program. Furthermore, a linear square regression method is used to calculate the activation energy.

The trap density, capture cross section, activation energy of n-type Si-doped GaAs, grown by molecular beam epitaxy (MBE) system, was measured and compared with conventional boxcar DLTS sytem. In addition, the DLTS signal spectra and the Arrhenius plots can be plotted by a line printer and displayed on a CRT monitor during one thermal scan.

An IEEE-488 interface bus was designed for communication between personal computers and instruments. This configuration provides the advantages of ease of operation and rapid set up, especially for the purpose of data acquisition and processing.

I. INTRODUCTION

IN RECENT YEARS, there has been considerable interest in determining the trap level of semiconductor materials and devices by deep-level transient spectroscopy (DLTS) proposed by Lang [1], [2]. It is sensitive and accurate, for obtaining some physical parameters of deep traps such as majority and minority trap levels, trap concentration, and capture cross section. However, the DLTS takes time in obtaining trap level through multiple thermal scan and is time-consuming for determining peak position and physical parameters. Hence many workers have tried to automate the process [3]-[6]. Automation makes it easy to handle and analyze the measured data, therefore, time per measurement is drastically reduced. But these systems are either expensive or require complex software techniques using a minicomputer [3] or other desktop microcomputers [4], [6] reducing the popularity of these systems. Alternatively, the systems use an A/D converter which is just a semi-automated system since it can't control the instrument parameters automatically [5]. In this paper, we proposed a low-cost, flexible, and easy to operate, personal computer-based, fully automatic control system for DLTS measurement. It includes a low-cost IEEE-488 bus which makes the system more flexibile and able to connect 14 programmable instruments to a personal computer. The system software program has been developed for ease of operation. The system cost is listed in Table I.

TABLE I
THE COST LIST OF CONTROL ASSEMBLIES OF AUTOMATIC DLTS SYSTEM

Control Parts	Cost (US Dollar)
Apple II personal computer (Include keyboard)	$ 1,000
CRT monitor	70
IEEE-488 interface bus	40
Line printer	450
Disk Driver	150

II. PRINCIPLE OF DLTS

The basic idea of the DLTS technique is the rate window concept. If we consider a train of repetitive bias pulses applied to the sample, then there is a signal which consists of the exponential capacitance transient. The DLTS signal is the difference between the transient amplitude at two sampling times selected. During the thermal scan, there is a maximum or minimum peak corresponding to a trap level.

The rate window can be expressed in terms of the transient emission rate giving rise to the maximum or minimum DLTS signal output, namely [1], [2],

$$e_{\max} = l_n(t_2/t_1)/(t_2 - t_1) \tag{1}$$

where $e_{\max}$ is the emission rate of transient, and t_1, t_2 are the preselected sampling times (t_1/t_2 = constant).

The relation between the emission rate and the activation energy ΔE is

$$e_{\max} = \frac{\sigma\langle v\rangle N}{g} \exp(-\Delta E/kT) = AT^2 \exp(-\Delta E/kT) \tag{2}$$

Manuscript received March 17, 1983; revised July 3, 1984.

The authors are with the Semiconductor and System Laboratories, National Cheng Kung University, Tainan, Taiwan, R.O.C.

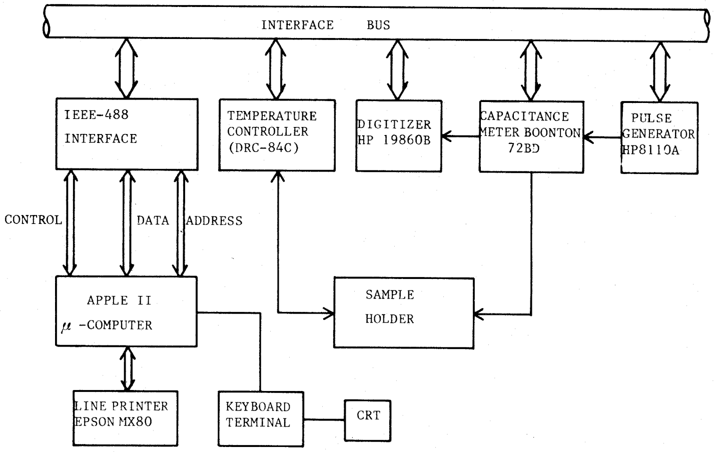

Fig. 1. The system block diagram of Apple II microcomputer-based automatic DLTS system.

where

$\langle v \rangle$ the thermal velocity of carriers,
g the degeneracy factor of the trap level,
k Boltzmann constant,
T the absolute temperature (°K),
N the density of state,
σ the capture cross section.

From (1) and (2), the activation energy can be obtained from the slope of an Arrhenius plot (i.e., $l_n(e_{\max}/T^2)$ versus $1/kT$). The capture cross section can be determined from (2) and the intercept of the Arrhenius plot.

The trap concentration N_T can be determined by

$$N_T = \frac{2\Delta C(0)}{C} \left| N_D - N_A \right| \tag{3}$$

where C is static capacitance, $\Delta C(0)$ is the difference between the capacitance after pulse $C(0)$ and statistic capacitance C, while N_D, and N_A are the donor and acceptor concentration, respectively. It is assumed that $C \gg \Delta C(0)$.

III. System Design

The automatic DLTS system described in this work uses a 6502 CPU with 48K dynamic RAM Apple II microcomputer. The use of a personal computer gives more versatile control over the signal average and can also be utilized as the system manager. In addition, the Apple II computer offers the advantages of low-cost, simplified operation and setup. Rate windows can be set during program initialization through a digitizer.

The main components of this automatic DLTS system, as shown in Fig. 1, are

a) a Boonton 72BD capacitance meter with a resolution of 0.001 pf,
b) an accurate temperature controller and sample holder (DRC-84C), which can cool the temperature of the sample down to 8 K so that the trap level can be detected shallower than 0.1 eV,
c) an HP19860B digitizer; this unit is used for replacing the boxcar averager to sample the capacitance transient signal. It can acquire 500 sample times as well as average the signal to improve the signal/noise ratio. It can detect trap concentration 1/1024 lower than doping concentration,
d) a programmable HP8116A pulse generator,
e) the interface bus between the microcomputer and instruments.

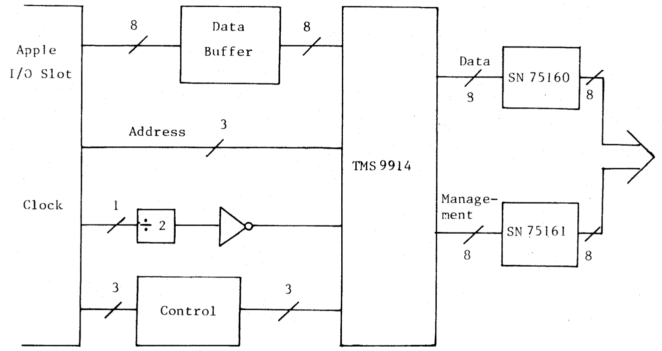

Fig. 2. Schematic diagram of IEEE-488 interface bus circuit.

This interface bus is one of the key units in this system. We designed this GPIB interface bus as a talker/listener/controller. The GPIB interface unit operation centers on the IC TMS9914 which can meet all IEEE-488 protocols automatically, thereby relieving the processor of this job. Fig. 2 shows the diagram of this IEEE-488 interface circuit. The TMS9914 needs two support chips to connect to the IEEE-488 bus: the SN75160 and SN75161. These support chips convert the TTL drive levels of the TMS9914. The SN75160 is the data line transceiver between the TMS9914 and IEEE-488 bus. The SN75161 is the bus management line transceiver. It buffers the bus control and the data transfer direction control lines to drive the 3 handshake line (DAV, NRFD, NDAC) and 5 interface management lines (EOI, IFC, SRQ, ATN, REN). The IC SN74LS245 acts as a bidirectional data bus buffer for bus transceiver between Apple II and the TMS9914 [7], [8]. It is controlled by a microcomputer. The three address lines are connected from the Apple address (A0-A2) to TMS9914 (RS0-RS2). It enables the Apple II to access any one of the TMS9914's thirteen registers. The clock signal is generated from the Apple II microcomputer I/O slot pin 36 through SN74LS93, in which the frequency is divided by 2, and then input to the TMS9914 as time base (3.5 MHz). Both IC SN74LS04 and SN74LS32 are adapted as the control unit. They control the timing of the microcomputer and send READ, WRITE, and RESET signals to TMS9914. This interface bus possesses the capabilities of SH1, AH1, T6, L4, SR1, RL1, PP1, DC1, and DT1. By using only seven IC's, we can construct this powerful and high-reliability interface bus.

As a reference, Table I lists the cost of control parts of the automatic DLTS system. We omit the other instruments since it is optional to choose another comparable instrument apparatus in the DLTS system, either programmable or nonprogrammable, since the digitizer can be used as an A/D converter.

IV. Software Description

The overall system control and interface bus program are implemented in the simple Basic language. Fig. 3 shows the

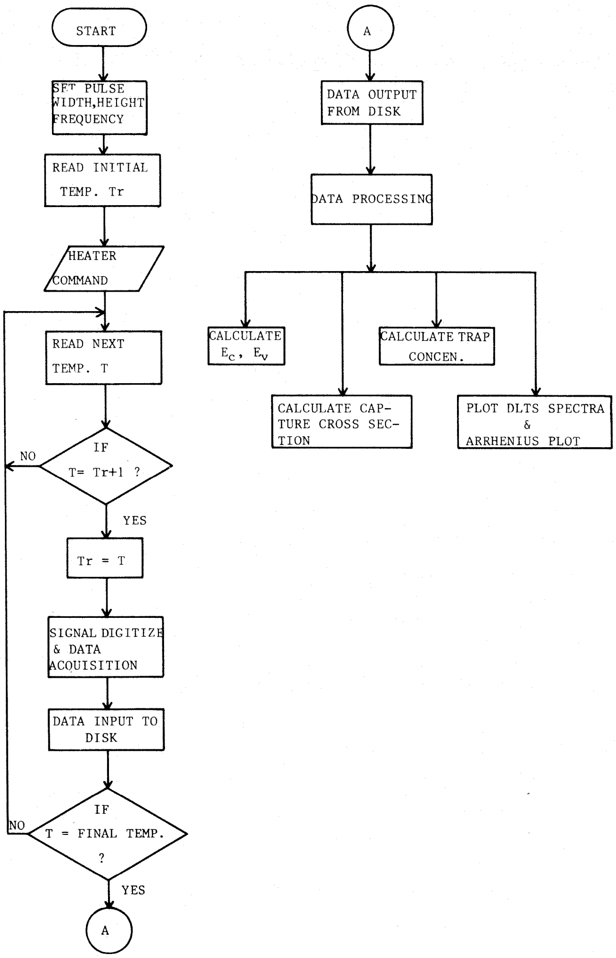

Fig. 3. Flow chart of the acquisition program of Apple II microcomputer-based automatic DLTS system.

flow chart of the system software. The program controls the process and varies parameters for the whole system including:

a) the software of the IEEE-488 interface bus,
b) the speed and range of temperature increase,
c) the pulse frequency, amplitude and width,
d) sampling of the capacitance transient signal and setting of rate windows,
e) improvement of *S/N* ratio,
f) determining the activation energy by using linear least square regression method,
g) determining capture cross section and trap concentration,
h) plotting the DLTS signal spectra and Arrhenius plot.

V. SAMPLE PREPARATION, EXPERIMENTAL RESULTS, AND DISCUSSIONS

The sample structure in this study grown by the molecular beam epitaxy (MBE) technique was an active layer/buffer layer/substrate which is prepared for manufacturing MESFET devices. The active layer was 0.4 μm thick, n-GaAs with silicon as the n-type dopant. The doping concentration was 1×10^{17} cm^{-3} obtained from the *C-V* curve. The thickness of buffer layer was 1.5 μm, which was undoped with a concentration $< 10^{14}$ cm^{-3}. Also the substrate was undoped n-GaAs. All the layers were grown at constant substrate temperature, i.e., *Ts* = 600°C, the ratio of As/Ga = 20 (As-rich). Finally, Schottky contact and ohmic contact were both made on the active layer to study the trap of this layer.

The DLTS spectra (majority carrier traps) of the sample is shown in Fig. 4. In which a −5.5-V reverse bias and a majority carrier injection pulse with width 0.6 ms were applied, and the rate window was 117 s^{-1} ($t_2/t_1 = 2$). Two electron traps at 0.40 and 0.50 eV below the conduction band were observed, and the trap concentrations were 9×10^{15} cm^{-3} and 4.4×10^{15} cm^{-3}, respectively. The E_c-0.50 eV was also found by Lang *et al.* [9], while E_c-0.40 eV is thought to be an oxygen-related defect realized during the growth of MBE system.

Fig. 5 shows the Arrhenius plot of different rate windows as described in (1), which had been processed by least linear regression for higher accuracy and was plotted by line printer. The capture cross section of E_c-0.40 eV and E_c-0.50 eV traps obtained from the intercept of Fig. 5 are 1.46×10^{-17} cm^2 and 1.17×10^{-16} cm^2, respectively. These values are an order larger than actual magnitude [10] due to the temperature-dependent characteristics of capture cross section.

In this experiment, the data acquired by the digitizer has been taken an average of four times. It is implemented by the software program to reduce noise. The DLTS signal is smoother than the signal without averaging. Furthermore, data were sent

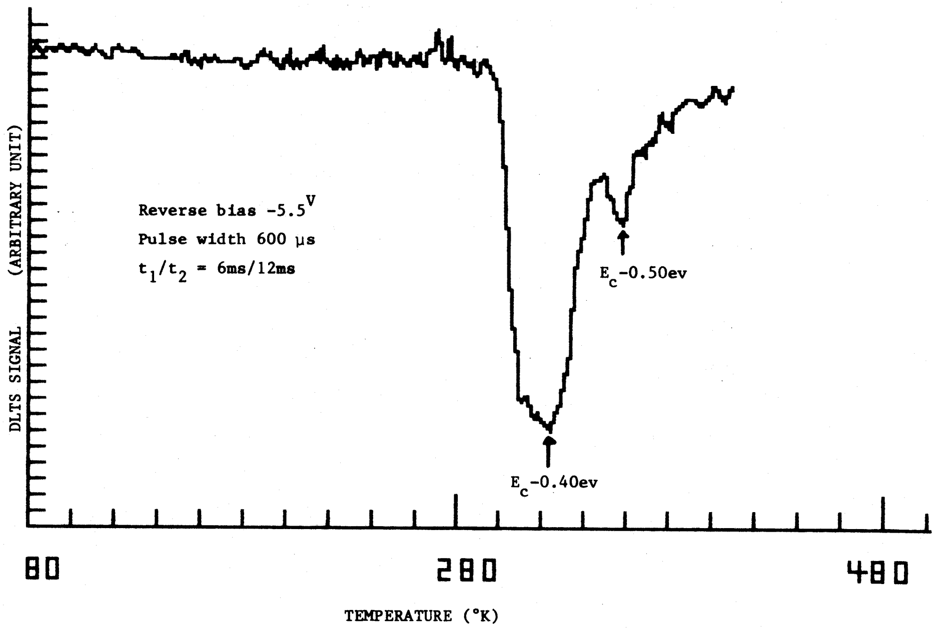

Fig. 4. The DLTS spectra for Si-doped n-GaAs Schottky diode measured by automatic DLTS ($t_2/t_1 = 2$).

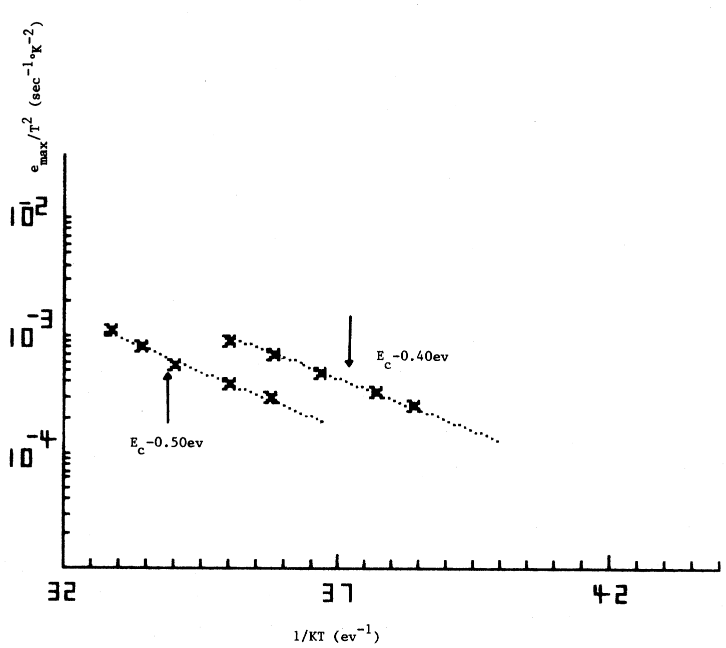

Fig. 5. The Arrhenius plot obtained from the DLTS spectra in Fig. 4.

TABLE II
THE COMPARISON BETWEEN AUTOMATIC DLTS AND BOXCAR DLTS

METHODS / PARAMETERS	AUTOMATIC DLTS		CONVENTIONAL BOXCAR DLTS	
Activation Energy(ev)	E_c-0.40	E_c-0.50	E_c-0.42	E_c-0.51
Trap Concentration(cm^{-3})	9×10^{15}	4.4×10^{15}	8.8×10^{15}	4.6×10^{15}
Capture Cross Section(cm^2)	1.46×10^{-17}	1.17×10^{-16}	1.01×10^{-17}	9.7×10^{-17}

to disk every 10 K during thermal scan to prevent data from occuping too much memory.

VI. CONCLUSIONS

In conclusion, a simple, flexible, low-cost, easily set up, personal computer-based automatic DLTS system has been developed and used for semiconductor devices analysis.

With the interface bus that has been described, the instruments such as the temperature controller, capacitance meter, and digitizer can be appropriately chosen. Furthermore, only the interactive BASIC language is needed for controlling the system and processing the data, thus considerable time is saved in data acquisition, analysis, and system setup. In general, this system can be extended to include another automatic measurement system simultaneously.

In the system, control of all instrument parameters, data acquisition and processing, and the printed results are completely implemented during only one thermal scan. Table II compares the automatic DLTS and boxcar DLTS approaches.

REFERENCES

[1] D. V. Lang, "Fast capacitance transient apparatus: Application to ZnO and O centers in GaP p-n junctions," *J. Appl. Phys.*, vol. 45, no. 7, pp. 3014, July 1974.

[2] D. V. Lang, "Deep level transient spectroscopy: A new method to characterize traps in semiconductors," *J. Appl. Phys.*, vol. 45, no. 7, pp. 3023, July 1974.

[3] M. D. Jack, R. C. Pack, and J. Henriksen, "A computer-controlled deep-level transient spectroscopy system for semiconductor process control," *IEEE Trans. Electron Devices*, vol. ED-27, no. 12, pp. 2226, Dec. 1980.

[4] L. Forbes and U. Kaempt, "Capacitance and conductance deep level transient spectroscopy using HP-IB instruments and a desktop computer," *Hewlett-Packard J.*, pp. 29–32, Apr. 1979.

[5] F. W. Sexton and W. D. Brown, "A low-cost microprocessor-based deep-level transient spectroscopy (DLTS) system," *IEEE Trans. Instrum. Meas.*, vol. IM-30, no. 3, pp. 180, Sept. 1981.

[6] E. E. Wagner, D. Hiller, and D. E. Mars, "Fast digital apparatus for capacitance transient analysis," *Rev. Sci. Instrum.*, vol. 51, no. 9, pp. 1205, Sept. 1980.

[7] Texas Instruments TMS 9914 GPIB Adapter Data Manual, Sept. 1979.

[8] "Tutorial description of the Hewlett-Packard interface bus," Hewlett-Packard Co., Nov. 1980.

[9] D. V. Lang, A. Y. Cho, A. C. Gossard, M. Llegems, and Wiegmann, "Study of electron traps in n-GaAs grown by molecular beam epitaxy," *J.A.P.*, vol. 47, no. 6, pp. 2558, June 1976.

[10] C. H. Henry and D. V. Lang, "Nonradiative capture and recombination by multiphonon emission in GaAs and GaP," *Phys. Rev. B*, vol. 15, pp. 989, 1977.

A Noise Temperature Measurement System for Mismatched Noise Sources

MANFRED SPAUDE, HEINZ-JÜRGEN SIWERIS, REINHARD REINSCHLÜSSEL, AND BURKHARD SCHIEK

Abstract—**A measurement system is described which allows us to determine the noise temperature of mismatched noise sources with unknown reflection coefficients. The system consists of a null-balancing radiometer extended by a circuit to compensate for the reduced noise power emitted by the mismatched one-port. In this circuit, no passive nonreciprocal components are necessary. Special consideration is given to measurement errors that are caused by the correlation of the input and output noise waves of the radiometer preamplifiers. Several methods to eliminate these errors are described. Furthermore, a circuit is given by which the measurement range is extended down to 0 K without the use of cold reference noise sources. Finally, a practical setup, operating in the 20–40-MHz range, is described together with corresponding measurement results.**

I. INTRODUCTION

THE NOISE temperature of a one-port of unknown impedance can be measured with emissivity-balanced radiometers. Measurement systems are described in [1]–[4]. These radiometer circuits need circulators or isolators, i.e., passive, nonreciprocal components to compensate for mismatching effects.

Passive, nonreciprocal components are not available with an acceptable performance in the typical intermediate frequency range, e.g., below 500 MHz. Therefore, reverse noise radiation of the radiometer receiver, which is normally correlated to the output noise of the receiver, will cause measurement errors, if the one-port is mismatched to the radiometer.

To avoid these errors, conventional radiometers use tuning elements between the noise sources and the receiver [5]. This means, however, that every change of the impedance of the unknown one-port requires an individual tuning procedure. Furthermore, this technique is narrow banded.

In this paper, an alternative electronic measurement technique is described, which allows us to measure the noise temperature of a one-port of arbitrary impedance without the use of passive, nonreciprocal components and without any tuning procedure. This technique has been successfully tested at 30 MHz with octave bandwidth, a typical intermediate frequency range of many systems.

II. PRINCIPLE OF OPERATION

The basic configuration of the measurement system is shown in Fig. 1. If the object under test connected to the information channel has a variable, frequency-dependent, and unknown impedance Z_{obj}, unequal to the real characteristic impedance Z_0, a noise power reduced by the factor $(1 - |\rho|^2)$ will be received with ρ being the reflection coefficient as given by

$$\rho = \frac{Z_{\text{obj}} - Z_0}{Z_{\text{obj}} + Z_0}. \tag{1}$$

The reference channel is assumed to be perfectly matched by a load Z_0 at temperature T_{in}. The total noise powers P_1 and P_2

Manuscript received June 17, 1982; revised February 22, 1984.

The authors are with the Institut für Hoch- und Höchstfrequenztechnik, Ruhr-Universität, 4630 Bochum 1, Federal Republic of Germany.

0018-9456/84/0900-0263$01.00 © 1984 IEEE

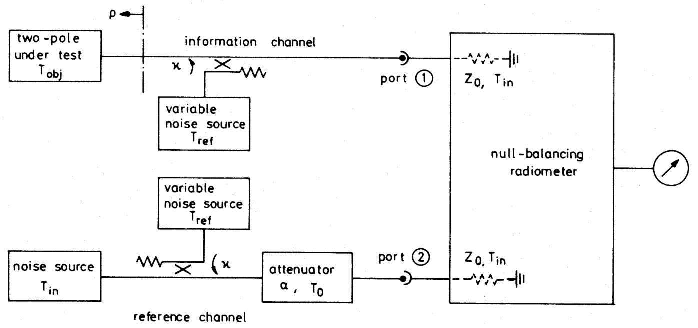

Fig. 1. Basic configuration of the measurement system.

received at port ① and port ②, which are assumed to be matched, are given by

$$\frac{1}{k_B \cdot \Delta f} \cdot P_1 = T_{\text{obj}}(1 - |\rho|^2)(1 - \kappa) + T_{\text{in}}|\rho|^2(1 - \kappa)^2 + T_0 \cdot \kappa + T_{\text{ref}}|\rho|^2\kappa(1 - \kappa)$$

$$\frac{1}{k_B \cdot \Delta f} \cdot P_2 = T_{\text{ref}} \cdot \kappa\alpha + T_{\text{in}}(1 - \kappa)\alpha + T_0(1 - \alpha). \tag{2}$$

In (2), T_{obj} is the temperature of the object under test, T_{ref} is the temperature of a variable reference noise source, T_0 is the ambient temperature, and T_{in} is the noise temperature of the radiometer input ports. Furthermore, κ is the power-coupling factor of the two couplers and α the power attenuation of the matched attenuator.

For a zero output of the null-balancing radiometer, the two input powers P_1 and P_2 need to be equal, which leads to

$$T_{\text{obj}} = \kappa \cdot \frac{\alpha - |\rho|^2(1 - \kappa)}{(1 - |\rho|^2)(1 - \kappa)} \cdot T_{\text{ref}} + \frac{\alpha - |\rho|^2(1 - \kappa)}{1 - |\rho|^2} \cdot T_{\text{in}} + \frac{1 - \alpha - \kappa}{(1 - |\rho|^2)(1 - \kappa)} \cdot T_0. \tag{3}$$

If the attenuation α is related to the coupling factor κ by $\alpha = 1 - \kappa$, which can simply be realized by substituting the attenuator by a coupler with the coupling factor κ, (3) simplifies to

$$T_{\text{obj}} = \kappa \cdot T_{\text{ref}} + (1 - \kappa)T_{\text{in}}. \tag{4}$$

Then, without knowledge of the reflection coefficient ρ, T_{obj} can be determined from the temperature T_{ref} of the calibrated, variable reference noise sources, and the known quantities κ and T_{in}. The reflection coefficient ρ may vary with frequency even within the measurement band.

III. Reduction of Correlation Effects

In (2)-(4), only the reverse radiation of the radiometer input ports, caused by the preamplifiers, has been considered. But, in practice, the preamplifiers also produce output noise waves X_{out}, which normally are correlated to their respective input noise waves X_{in} (Fig. 2).

Therefore, if X_{in} is reflected by a mismatched object, this correlation causes a very strong measurement error, which also depends on both the magnitude and phase of the complex reflection coefficient ρ. In order to account for the correlation of the input and output noise waves of the preamplifiers, an additional term must be added to (4), yielding

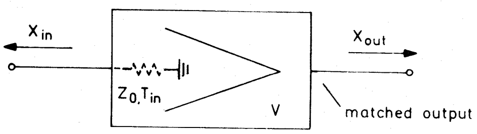

Fig. 2. Preamplifier with noise waves.

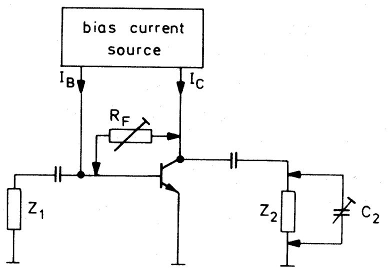

Fig. 3. Transistor amplifier stage with reduced noise correlation.

$$T_{\text{obj}} = \kappa \cdot T_{\text{ref}} + (1 - \kappa)T_{\text{in}} + \underbrace{2 \cdot \frac{1 - \kappa}{(1 - |\rho|^2)k_B \cdot \Delta f} \cdot \operatorname{Re}\left\{\rho^* X_{\text{in}}^* \cdot \frac{X_{\text{out}}}{V}\right\}}_{\text{correlation term}}. \tag{5}$$

The noise waves X_{in} and X_{out} are related to the noise temperatures T_{in} and T_{out} by

$$|X_{\text{in}}|^2 = k_B \cdot T_{\text{in}} \cdot \Delta f$$

$$|X_{\text{out}}|^2 = k_B \cdot T_{\text{out}} \cdot \Delta f.$$

In (5), V is the voltage gain of the preamplifier which is assumed to be matched at the input and at the output and to have perfect reverse isolation. For example, assume $T_{\text{in}} = 300$ K, $T_{\text{out}} = 300$ K, $|\rho| = 0.5$, and a correlation between X_{in} and X_{out} of 50 percent, then a maximum measurement error of T_{obj}, as given by the correlation term in (5), of ±200 K will occur, which is not acceptable for most applications.

In order to limit this measurement error to a sufficiently low level, e.g., 0.2 K, even for large reflection coefficients ρ, the correlation of the amplifier noise waves, or at least its influence on the radiometer output signal, has to be reduced by a factor of about 1000. Experimentally, the effect of the amplifier noise correlation can be measured as follows. The two input ports of the null-balancing radiometer are connected via a variable phase shifter. For a continuous and slow variation of the phase shift, the radiometer output voltage changes between two peak values, the difference of which is a proper measure for the correlation-induced measurement errors. Referring to the example given above, this error voltage has to be reduced by about 60 dB. While at microwave frequencies this reduction can be achieved by the use of passive isolators, one has to look for different solutions at lower frequencies. A number of suitable methods, which have been investigated, are listed below.

1) A proper feedback is applied to the transistor of the preamplifier circuit. For the circuit in Fig. 3, it has been

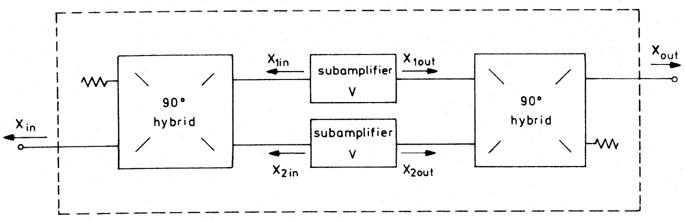

Fig. 4. Balanced amplifier with noise waves.

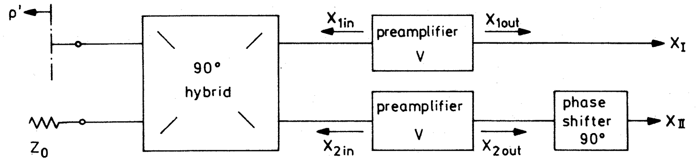

Fig. 5. Correlation error reduction by a 90° hybrid.

found by computer simulations, and measurements as well, that a significant reduction of the correlation is possible by adding the feedback resistor R_F. Only a slight increase of the noise figure was observed.

2) Balanced preamplifiers are used consisting of two identical subamplifiers and two 90° hybrids (Fig. 4). The correlation between X_{in} and X_{out} of the balanced preamplifier is given by

$$X_{\text{in}}^* \cdot X_{\text{out}} = \frac{1}{2} \cdot (jX_{1\,\text{in}} + X_{2\,\text{in}})^* \cdot (X_{1\,\text{out}} + jX_{2\,\text{out}})$$

$$= \frac{j}{2} \cdot (X_{1\,\text{in}}^* \cdot X_{1\,\text{out}} - X_{2\,\text{in}}^* \cdot X_{2\,\text{out}}). \tag{6}$$

This correlation is zero if the two subamplifiers are identical, also with respect to their noise properties. As a further advantage, balanced amplifiers guarantee lower input and output reflection coefficients.

3) Switchable 0°/90°-phase shifters are inserted in front of the preamplifiers. Referring to (5), the correlation term changes its sign if the phase is switched from 0° to 90°, or vice versa. Averaging an equal number of 0° and 90° states eliminates the correlation term.

4) All-pass networks are inserted in front of the preamplifiers. Thereby, the phase of the correlation term in (5) becomes a periodic function of frequency and error contributions from different portions of the measurement band tend to cancel out.

5) Matched attenuators are inserted in front of the preamplifiers. This will reduce the influence of the correlation, but unfortunately, it will increase the system noise figure. Note that the input and output noise waves of a matched attenuator at a homogeneous temperature are not correlated [4].

6) In case of a correlation radiometer, the influence of the correlation on the measurement result is removed by using a 90° hybrid instead of the usual 180° type and inserting a 90° phase shift behind the preamplifier of one of the two channels (Fig. 5). The contribution Y_n of the amplifier noise waves to the radiometer output signal is given by

$$Y_n = \text{Re}\,\{X_{\text{I}}^* \cdot X_{\text{II}}\}$$

with

$$\begin{aligned} X_{\text{I}}^* \cdot X_{\text{II}} &= \{\tfrac{1}{2} \cdot \rho' X_{1\,\text{in}} V + \tfrac{1}{2} \cdot j\rho' X_{2\,\text{in}} V + X_{1\,\text{out}}\}^* \\ &\quad \cdot j \cdot \{\tfrac{1}{2} \cdot j\rho' X_{1\,\text{in}} V - \tfrac{1}{2} \cdot \rho' X_{2\,\text{in}} V + X_{2\,\text{out}}\} \\ &= -\tfrac{1}{4} \cdot |\rho'|^2 |V|^2 \cdot (|X_{1\,\text{in}}|^2 + |X_{2\,\text{in}}|^2) \\ &\quad + \tfrac{1}{2} \cdot (\rho'^* X_{2\,\text{in}}^* \cdot X_{2\,\text{out}} V^* - \rho' X_{1\,\text{in}} \cdot X_{1\,\text{out}}^* V). \end{aligned} \tag{7}$$

The second term of (7) is imaginary if the two amplifiers are identical and thus Y_n is independent of the amplifier noise correlation. Except for the last method, which is restricted to correlation radiometers, each of the correlation error-reduction techniques mentioned above can be applied to any null-balancing radiometer.

IV. A PRACTICAL MEASUREMENT SET UP

In the circuit of Fig. 1 any type of a null-balancing radiometer can be used, e.g., the Dicke radiometer, the Graham receiver, or the correlation radiometer. For the setup described here, the correlation radiometer has been prefered because of a number of advantages. In contrast to the Dicke radiometer or the Graham receiver, the correlation radiometer does not need any switches in front of the preamplifiers. These switches often cause trouble since they produce spikes and introduce additional losses which, moreover, may be different for the two switching states. The complete system is shown in Fig. 6.

In theory, each of the techniques described in the last section provides sufficient correlation error reduction. However, experimental investigations revealed that in a practical system several methods have to be combined. In fact, in the set up of Fig. 6, all techniques except the switchable 0°/90° phase shifters have been incorporated.

a) The preamplifiers have been designed as balanced amplifiers with correlation-reducing feedback applied to the subamplifiers. Amplifier noise correlation has been measured with the circuit shown in Fig. 7.

From the four different switching states of the phase shifters PH_1 and PH_2, one can calculate the correlation of the individual amplifiers 1 and 2 by a linear combination of the Y_n values given in Table I. Using this measurement procedure, the noise correlation of the amplifiers has been minimized by a variation of the feedback resistor R_F and, for fine tuning, the bias currents I_B, I_C, and the small capacitance C_2 (Fig. 3).

Unfortunately, these two techniques, i.e., the techniques described under 1) and 2), are not exactly multiplicative with respect to error reduction. Experimentally, a typical reduction of the preamplifier noise wave correlation by 14 dB has been achieved, which corresponds to an error voltage reduction of 28 dB.

b) A 90° hybrid is used in front of the preamplifiers and a 90° phase shifter (PH in Fig. 6) after one postamplifier. Besides the 6-dB error voltage suppression that any 3-dB hybrid at this position would provide, this particular configuration resulted in an additional reduction of about 11 dB. This value would have been higher if the uniformity of the preamplifiers had not been degraded by the tuning process described above.

c) All-pass networks with about π of phase variation over

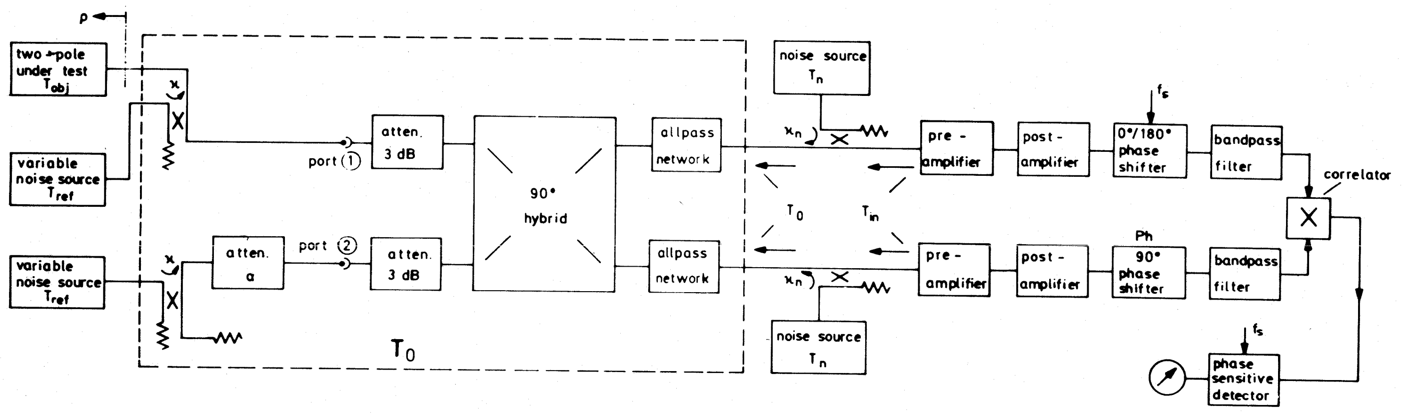

Fig. 6. Block diagram of the measurement system.

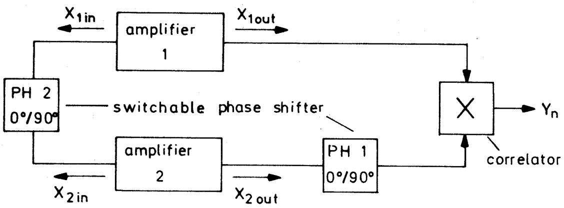

Fig. 7. Determination of the amplifier noise correlation.

TABLE I
OUTPUT SIGNAL Y_n OF THE CORRELATOR (SEE FIG. 7) AS A FUNCTION OF THE SWITCHING STATE OF THE PHASE SHIFTERS

	PH 1	PH 2	Y_n
I	0°	0°	$\text{Re } C_1 + \text{Re } C_2$
II	0°	90°	$-\text{Im } C_1 - \text{Im } C_2$
III	90°	0°	$\text{Im } C_1 - \text{Im } C_2$
IV	90°	90°	$\text{Re } C_1 - \text{Re } C_2$

$C_1 = X_{1in}^* X_{1out}$ $C_2 = X_{2in}^* X_{2out}$

the measurement band 20-40 MHz are inserted (Fig. 6). Depending on the phase variation of the one-port under test, this leads to an error voltage reduction of at least 14 dB. This result was confirmed experimentally. This value is independent of the other error reduction techniques applied.

d) Finally, 3-dB attenuators are inserted in front of the 90° hybrid (Fig. 6). In accordance with the theory, 6 dB of error voltage reduction is observed. This value is also multiplicative to the reduction factors achieved by other methods if the isolation of the 90°-hybrid is high enough. The input matching is improved by the attenuators, but of course the noise figure of the system increases.

To avoid additional noise correlation contributions by the lossy and, in practice, not perfectly matched components in front of the preamplifiers, e.g., the 90° hybrid, it is necessary to keep all these components at one homogeneous temperature, for convenience at ambient temperature T_0 [4, fig. 41]. Therefore, the noise temperature T_{in} of the preamplifiers, which normally is about $T_0/2 \cdots T_0/3$ has to be artificially raised to the ambient temperature T_0. This is done by a proper addition of noise from the noise sources at temperature T_n via 20-dB couplers (Fig. 6). A homogeneous temperature of all components enclosed by the dashed rectangle in Fig. 6 proved to be very important. By combining all the methods described, a total error voltage reduction of approximately 60 dB could be achieved, which meets the requirements specified above.

A switchable 0°/180° phase shifter is inserted in front of the correlator. The switching frequency f_s was chosen as 1 kHz. Thus, the correlator output yields a 1-kHz signal, which, after sufficient amplification, is detected by a phase-sensitive detector. This detection method eliminates offset problems and, as a further advantage, allows us to use a simple mixer instead of a multiplier as correlator. Details will be given in the Appendix. This proves to be an important technical simplification, since a precision multiplier might pose a problem at high frequencies. The switchable 0°/180° phase shifter is uncritical because of sufficient preamplification.

Besides the correlation-induced measurement errors, the nonideal properties of the components may lead to additional minor errors. For the system described in this section, a total temperature resolution better than 1 K could be achieved. The absolute accuracy is determined by the accuracy of the reference noise sources.

V. NOISE MEASUREMENT SYSTEM WITH AN EXTENDED TEMPERATURE RANGE

The measurement system as shown in Fig. 6 needs two uncorrelated calibrated reference noise sources with good tracking and variable temperature T_{ref}. With standard noise sources, the measurement range is limited to noise temperatures above ambient temperature T_0. In the following, a modification of the measurement system will be described which extends the temperature range to 0 K without the necessity of cooling. Although this method will be explained for the mismatch-compensated correlation radiometer, it applies equally well to the Dicke radiometer and the Graham receiver. The measurement system shown in Fig. 1 is extended by an auxiliary noise source at temperature T_{aux}, a matched coupler with the power coupling factor κ_2 in the information channel, and two matched attenuators at ambient temperature T_0 with the power attenuations $\alpha_1 = 1 - \kappa_1$ and $\alpha_2 = 1 - \kappa_2$ (Fig. 8).

Setting $T_{in} = T_0$, the total noise powers P_1 and P_2, received at port ① and port ②, respectively, are given by

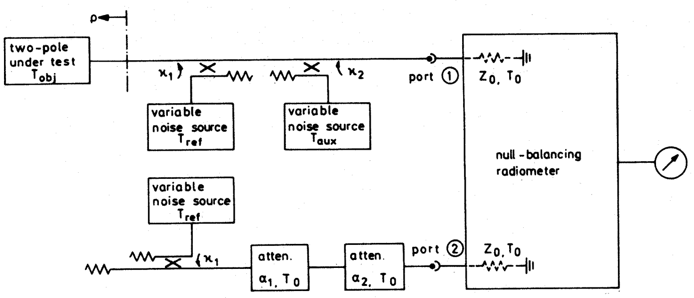

Fig. 8. Measurement system with an extended temperature range.

$$\begin{aligned}\frac{1}{k_B \cdot \Delta f} \cdot P_1 = {} & T_{obj}(1 - |\rho|^2)(1 - \kappa_1)(1 - \kappa_2) \\ & + T_{ref} \cdot |\rho|^2 (1 - \kappa_1)(1 - \kappa_2) \\ & \cdot \kappa_1 + T_{aux} \cdot \kappa_2 + T_0 [|\rho|^2 (1 - \kappa_2)^2 \\ & \cdot (1 - \kappa_1)^2 + (1 - \kappa_2) \cdot \kappa_1 + |\rho|^2 \\ & \cdot (1 - \kappa_1)^2 \cdot (1 - \kappa_2) \cdot \kappa_2] \\ \frac{1}{k_B \cdot \Delta f} \cdot P_2 = {} & T_{ref} \cdot \kappa_1 (1 - \kappa_1)(1 - \kappa_2) \\ & + T_0 [(1 - \kappa_1)^2 \cdot (1 - \kappa_2)^2 + (1 - \kappa_1)^2 \\ & \cdot (1 - \kappa_2) \cdot \kappa_2 + (1 - \kappa_2) \cdot \kappa_1 + \kappa_2]. \end{aligned} \tag{8}$$

Equating the noise powers P_1 and P_2 at ports ① and ② of the radiometer leads to

$$\begin{aligned} T_{obj} = {} & \kappa_1 (T_{ref} - T_0) + T_0 - (T_{aux} - T_0) \\ & \cdot \frac{\kappa_2}{(1 - |\rho|^2)(1 - \kappa_1)(1 - \kappa_2)}. \end{aligned} \tag{9}$$

The measurement is now performed in two steps.

Step I) The reference temperature is set to ambient temperature $T_{ref} = T_0$, the radiometer is balanced by varying T_{aux} resulting in T_{aux}^{I}, and

$$T_{obj} = T_0 - (T_{aux}^{I} - T_0) \cdot \frac{\kappa_2}{(1 - |\rho|^2)(1 - \kappa_2)(1 - \kappa_1)}. \tag{10}$$

Step II) The excess noise temperature $T_{aux} - T_0$ is increased by a factor n giving

$$T_{aux}^{II} - T_0 = n \cdot (T_{aux}^{I} - T_0).$$

The radiometer is balanced by varying T_{ref} to $T_{ref} = T_{ref}^{II}$. Thus, (9) becomes

$$\begin{aligned} T_{obj} = {} & (T_{ref}^{II} - T_0)\kappa_1 + T_0 - n(T_{aux}^{I} - T_0) \\ & \cdot \frac{\kappa_2}{(1 - |\rho|^2)(1 - \kappa_1)(1 - \kappa_2)}. \end{aligned} \tag{11}$$

Multiplying (10) by n and subtracting (11) yields

$$T_{obj} = T_0 - \frac{\kappa_1}{n - 1} \cdot (T_{ref}^{II} - T_0). \tag{12}$$

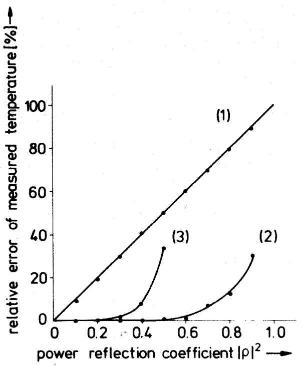

Fig. 9. Relative error of measured temperature versus the power reflection coefficient $|\rho|^2$: 1) Radiometer with no mismatch compensation, 2) Mismatch compensated radiometer at $T_{obj} = 600$ K; 3) Mismatch-compensated radiometer at $T_{obj} = 77$ K.

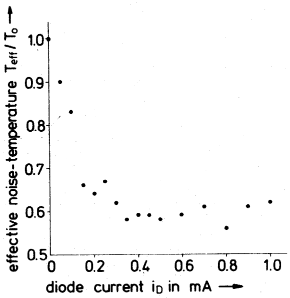

Fig. 10. Effective noise temperature T_{eff} of a Schottky-diode (Siemens BAS 40-02) versus the diode-current i_D.

A suitable factor is $n = 2$, which can be realized by inserting a 3-dB attenuator at ambient temperature T_0 in front of the auxiliary noise source. Then (12) takes the more simple form

$$T_{obj} = T_0 - \kappa_1 (T_{ref}^{II} - T_0). \tag{13}$$

The auxiliary noise source at temperature T_{aux} does not need to be calibrated, but simply has to be variable and stable during the measurement procedure.

If, in Step I), no null-balancing is possible, it follows that the object temperature T_{obj} is above the ambient temperature T_0. Then T_{aux} is set to T_0 and T_{obj} will be determined by (4) with $T_{in} = T_0$

$$T_{obj} = \kappa_1 \cdot (T_{ref}^{II} - T_0) + T_0. \tag{14}$$

VI. MEASUREMENT RESULTS

The noise temperature measurement setup has been tested with a calibrated noise source at temperature T_{obj} as the object under test. The reflection coefficient was varied by a variable parallel capacitance. This will not change the object temperature. Depending on the capacitance, the magnitude of the reflection coefficient $|\rho|$ can take values between 0 and 1.

Measurements have been performed at object temperatures of $T_{obj} = 77$ K and $T_{obj} = 600$ K to prove the applicability of the set up at temperatures below and above the ambient temperature. The relative errors $\Delta T / T_{obj}$ of the measured temperatures versus $|\rho|^2$ at 30 MHz are shown in Fig. 9.

Compared to a conventional radiometer with no mismatch compensation, the improvement is obvious. For example, at $|\rho|^2 = 0.5$, the absolute error ΔT is only 3 K for $T_{obj} = 600$ K. As an example for a practical application, the effective noise temperature T_{eff} of a Schottky diode has been measured as a function of the diode-current i_D (Fig. 10).

The measurement results (Fig. 10) are in agreement with the theory [7], predicting a temperature of $T_0/2$ under ideal conditions, with T_0 being the ambient temperature. The differences are caused by the ideality factor $n > 1$ and the spreading resistance of the Schottky diode.

VII. CONCLUSION

The proposed system for noise temperature measurements on mismatched one-ports has a number of advantages compared with conventional measurement techniques:

1) No nonreciprocal passive components are used.

2) Measurement errors caused by the "reverse noise radiation" of the preamplifiers are independent of the reflection coefficient of a mismatched object and need to be considered only once during the initial calibration of the measurement system.

3) The correlation of the input and output noise waves of the preamplifiers causes no significant measurement errors.

4) The measurement system can be applied in a wide frequency range, even down to a few megahertz.

5) The measurement system can be applied in a wide temperature range, even below the ambient temperature without the use of "cold" reference noise sources.

Thus, the proposed system is expected to be useful for a number of applications in the industrial, scientific, and medical fields.

APPENDIX

The correlator of the correlation radiometer has to produce a zero output if its two input signals $x_1(t)$ and $x_2(t)$ are not correlated. Theoretically, this is easily achieved by using a multiplier followed by a low-pass filter or an integrator yielding the mean value $\langle y\rangle$ of the multiplier output signal. However, besides the product $x_1 \cdot x_2$, the output signal of a real multiplier usually contains additional terms, and the mean value, which in general may be described as

$$\langle y\rangle = \sum_{m=0}^{\infty} \sum_{n=0}^{\infty} C_{mn} \cdot \langle x_1^m \cdot x_2^n\rangle \tag{A1}$$

is not necessarily zero for uncorrelated input signals, as will be shown in the following.

The mean values $\langle x_1^m \cdot x_2^n\rangle$ can be computed from the characteristic functions of the input signals, e.g., [6]. For uncorrelated Gaussian noise, this leads to

$$\langle x_1^m \cdot x_2^n\rangle = \frac{1}{j^{m+n}} \cdot \left[\frac{d^m}{dv_1^m} \exp\left(-\frac{1}{2}\cdot\langle x_1^2\rangle \cdot v_1^2\right) \cdot \frac{d^n}{dv_2^n} \exp\left(-\frac{1}{2}\cdot\langle x_2^2\rangle \cdot v_2^2\right)\right]\Bigg|_{v_1=v_2=0} \tag{A2}$$

with j denoting the imaginary unit.

The nth order derivative of a function e^{av^2} is given by

$$\frac{d^n}{dv^n} e^{av^2} = e^{av^2} \cdot \sum_{k=0}^{\hat{k}} \frac{a^k}{k!} \cdot \frac{n!}{(n-2k)!} \cdot (2av)^{n-2k} \tag{A3}$$

with

$$\hat{k} = \begin{cases} \dfrac{n}{2}, & \text{if } n \text{ is even} \\ (n-1)/2, & \text{if } n \text{ is odd.} \end{cases}$$

From this, it follows that $\langle x_1^m \cdot x_2^n\rangle$ is zero for all combinations of m and n, except those where both m and n are even. Setting $m = 2k$ and $n = 2l$, the final result for the value $\langle y\rangle$ is

$$\langle y\rangle = \sum_{k=0}^{\infty} \sum_{l=0}^{\infty} C_{2k2l} \cdot \frac{(2k)! \cdot (2l)!}{2^{k+l} \cdot k! \cdot l!} \cdot (\langle x_1^2\rangle)^k \cdot (\langle x_2^2\rangle)^l. \tag{A4}$$

Thus, in the case of a nonideal multiplier, a dc error signal will occur at the correlator output, which depends on the power level of the input signals.

Now, if a periodically switched 0°/180° phase shifter is inserted in one of the radiometer channels, the cross-correlation coefficient $\langle x_1 \cdot x_2\rangle$ of the input signals and, as a consequence, the associated correlator output signal are periodic functions of time. On the other hand, the dc error signal given by (A4) remains unchanged. If a phase-sensitive detector is used to detect the ac part only, the error signal is eliminated and, even with a nonideal multiplier, the output of the correlator is exactly zero for uncorrelated input signals. Moreover, it is not necessary to use a multiplier. Any circuit relating the input signals according to the very general expression in (A1), e.g., a Schottky diode mixer, can be used. This simplifies the realization of the correlator, particularly at high frequencies.

ACKNOWLEDGMENT

The authors wish to thank K. M. Lüdeke and J. Köhler of the Philips GmbH Forschungslaboratorium Hamburg and H. Severin of Institut für Hoch- und Höchstfrequenztechnik, Ruhr-Universität, Bochum, who have supported the work.

REFERENCES

[1] D. F. Wait and T. Nemoto, "Measurement of the noise temperature of a mismatched noise source," *IEEE Trans. Microwave Theory Tech.*, vol. MTT-16, pp. 670–675, Sept. 1968.

[2] K. M. Lüdeke, B. Schiek, and J. Köhler, "Radiation balance microwave thermograph for industrial and medical application," *Electron. Lett.*, vol. 14, p. 194, Mar. 1978.

[3] K. M. Lüdeke, J. Köhler, and J. Kanzenbach, "A radiation balance microwave thermograph for medical applications," *Acta Electron.*, vol. 22, p. 65, Jan. 1979.

[4] W. Schilz and B. Schiek, "Microwave systems for industrial measurements," in *Advances in Electronics and Electron Physics*, vol. 55. New York: Academic Press, 1981, pp. 346–355.

[5] P. I. Somlo, "A noise doubling radiometer for the absolute calibration of high-frequency noise sources," *IEEE Trans. Instrum. Meas.*, vol. IM-26, pp. 85–87, June 1977.

[6] H. E. Rowe, *Signals and Noise in Communication Systems.* Princeton, NJ: Van Nostrand, 1965, pp. 30–34.

[7] A. R. Kerr, "Shot-noise in resistive-diode mixers and the attenuator noise model," *IEEE Trans. Microwave Theory Tech.*, vol. MTT-27, pp. 135–140, Feb. 1979.

The Precise Measurement of RF Power and Voltage Using Coaxial Calorimeters and Microcalorimeters

DAVID L. HOLLWAY, SENIOR MEMBER, IEEE, AND WALTER MULLER, MEMBER, IEEE

Abstract–**Automated calorimeters and microcalorimeters used by the CSIRO Division of Applied Physics as primary standards of radio frequency power and voltage and for measuring the effective efficiency of bolometer mounts are described. Methods for evaluating corrections from computer models of the thermal and electrical circuits and results of measurements and intercomparisons are presented.**

I. INTRODUCTION

THE DEVELOPMENT of primary standards of RF power and voltage at the Division of Applied Physics began in 1972 with the construction of a twin-load calorimeter based on existing designs [1]-[6]. This, and the later microcalorimeters, were designed to be fully automated, with software replacing hardware wherever possible. A full description of these systems is beyond the scope of this paper, but is available elsewhere [7].

The invention by MacPherson and Kerns [8] in 1955 of the microcalorimeter [9], [10] method for measuring the efficiency of waveguide power mounts was an important innovation in RF calorimetry, but its advantages still are not widely recognized. It is a single-step procedure–the efficiency is found in a simple way from temperature measurements and as the power mount remains in one position, fully automated measurements may be continued for long periods without intervention.

It is more difficult to use the microcalorimeter method for the calibration of coaxial-line power mounts than for waveguide mounts, because corrections for heat flow in the inner line must be evaluated. Possibly for this reason, coaxial microcalorimeters do not appear to have been used previously.

Seven- and 14-mm coaxial line microcalorimeters have been used by the Division, chiefly for calibrating standard power mounts. The coaxial calorimeter power standard is used for calibrating standard thermal converters and standard power mounts. Comparisons between calibrations made with the microcalorimeters and the power standard provide a valuable check for systematic errors.

II. COAXIAL MICROCALORIMETERS

Power-measuring mounts incorporating thermistor or barretter elements[1] which are held at a constant resistance by an external circuit, may be calibrated by the microcalorimeter method. Usually the circuit is a self-balancing dc bridge having the thermistor element in one arm, so that when RF is fed in, the bridge reduces the dc power by an amount almost equal to the RF. Usually, more RF than dc power is lost in the mount before reaching the thermal element, so that the mount temperature tends to rise slightly when RF is applied. This increased heating is balanced by the microcalorimeter system and used to evaluate the *effective efficiency*, defined as the retracted dc power divided by the total RF power flowing into the mount.

A coaxial microcalorimeter [11] is shown diagrammatically in Fig. 1. Two similar thermistor mounts, attached to 100-mm lengths of thin-walled 7-mm precision coaxial lines, are contained in a cylindrical aluminum chamber divided by a central partition. The thin lines are of nickel–silver, 0.125 mm thick, dimensioned to match APC-7 connectors. The inner chamber is surrounded by a cylindrical copper container having hollow walls filled with water and sealed. Thin-walled coaxial lines 150 mm long join connectors in the top cover. The container is surrounded by a layer of foam thermal insulation and by walls and floor built from rectangular plastic containers filled with water and sealed. The whole construction is housed in a wooden box about 1 m high, which is lined with thermal insulation and an electrostatic screen.

The RF and dc cables provide a thermal path between the microcalorimeter and the outside environment. To reduce temperature variations caused by changes in the ambient temperature, the cables within the box are coiled between layers of sealed, water-filled containers (Fig. 1). As errors can be caused by moisture [13], the humidity of the interior is monitored.

The temperature difference between the mounts is measured by a 252-junction thermopile in thermal contact with the shells of the RF input connectors of the mounts and a thermal shunt is provided where the thermopile conductors pass through the

Manuscript received February 28, 1983; revised April 6, 1983 and January 25, 1984.

The authors are with the CSIRO Division of Applied Physics, Sydney, Australia, 2070.

---

[1] The methods described in this paper apply to the calibration of power-measuring mounts incorporating either thermistors, which have a negative, or barretters which have a positive, temperature coefficient. For brevity, only thermistors will be referred to throughout the text.

0018-9456/84/0900-0269$01.00 © 1984 IEEE

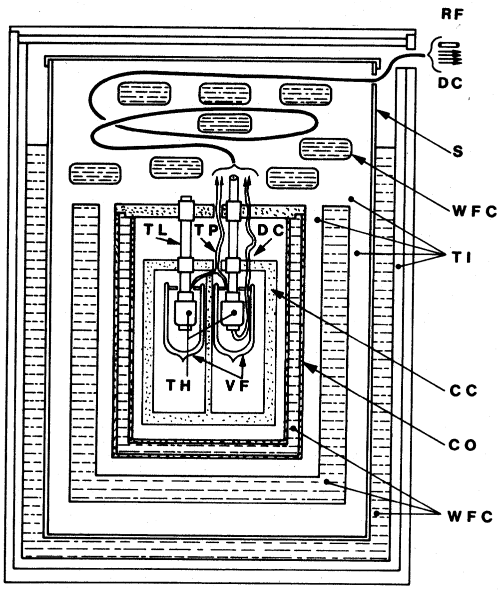

Fig. 1. The coaxial microcalorimeter shown diagrammatically in cross-section. (The thermistor heads TH are in vacuum flasks VF in separate compartments of a thick aluminium cylinder CC, in an outer, water-filled cylinder CO surrounded by water-filled containers WFC and thermal insulation TI. TC—Thermopile leads. TL—Thin-walled coaxial lines. S—Metal screen.)

central partition, to prevent transfer of heat between the mounts. A wide-mouthed vacuum flask is positioned around the mount as shown in Fig. 1 to ensure that all the heat produced in different parts of the mount can escape only through the coaxial line connector, where the temperature rise is sensed by the thermopile. The dc leads are thermally shunted to the walls of the inner and outer chambers.

Microcalorimeter calibrations are made by the automated equipment shown in Fig. 2. The active thermistor forms one arm of a precise, self-balancing bridge. When switch $S1$ is closed, the resistor R_s shunts the upper arm and so augments the power fed to the mount. At all times during measurements, the thermopile voltage is kept backed-off by the computer as shown in Fig. 2. The null is sensed by a galvanometer nanovoltmeter and precautions are taken to shield the low-level circuits and to avoid thermals. All dc measurements are made by a multiplexed seven-digit DVM interfaced to the computer.

Before beginning a calibration, the system is run for 24 h to reach a steady temperature. A calibration is made by supplying RF to the mount for 3 h, followed by 3 h off, for a total of 18 periods. Bridge voltage, thermopile voltage, ambient temperature, and RF level are measured at 1-min intervals. The dc power fed to the mount is computed from the bridge voltage. Mean values are stored 12 times/h. The computer also provides an expanded chart record of the key quantities.

The bridge shunt R_s (Fig. 2), which is switched on when the RF is off, is chosen so that there is very little change in the temperature of the mount between the RF-on and RF-off conditions. The bridge voltage when unshunted is measured twice every hour. The results are analyzed in a separate program which applies the necessary corrections and computes the effective efficiency.

A. Computing the Effective Efficiency

The powers, thermopile voltages, and thermistor bridge voltages for the three conditions measured are shown in Table I. When the RF is applied, the total power heating the mount and contributing to the thermopile voltage U_r is the RF power P_t entering the mount, the remaining dc power P_r from the bridge, and a fraction q of the RF power P_l which heats the thin-walled lines. Therefore

$$U_r = k(P_r + P_t + qP_l) \tag{1}$$

where k is a constant of proportionality.

When the RF is off, only P_b contributes to the thermopile reading U_b and therefore $U_b = kP_b$. The shunt resistance R_s (Fig. 2) is chosen so that U_b is almost equal to U_r. Therefore, when the microcalorimeter temperature has become stable and the system is free from drift, $(U_r/U_b)P_b = P_r + P_t + qP_l$.

If we define $d = qP_l/P_t$, then

$$P_t = \frac{(U_r/U_b)P_b - P_r}{1 + d}. \tag{2}$$

The dc power retracted by the bridge in order to keep the thermistor resistance constant is $P_d - P_r$, and the effective efficiency η_e is defined as

$$\eta_e = (P_d - P_r)/P_t. \tag{3}$$

Therefore, on substituting (2) into (3)

$$\eta_e = (P_d - P_r)(1 + d)/\{(U_r/U_b)P_b - P_r\}. \tag{4}$$

The dc powers P_b, P_d, and P_r are computed from measurements of the bridge voltages and a knowledge of the loop resistance R_b of the leads between the bridge and the thermistor mount. If R_a is the bridge arm resistance and $b = R_b/R_a$, then when the switch $S1$ is open, $P_d = (E_d^2/4R_a)(1 - b)$ and $P_r = (E_r^2/4R_a)(1 - b)$. When $S1$ is closed, $E_b/2$ appears across the shunt R_s in parallel with R_a. If $a = R_a/R_s$, the dc power in the thermistor becomes

$$P_b = (E_b^2/4R_a)(1 + a)\{1 - b(1 + a)\}. \tag{5}$$

If we define $s = (1 + a)\{1 - b(1 + a)\}/(1 - b)$ and the expressions for P_d, P_r, and P_b are substituted in (4), then

$$\eta_e = \frac{(E_d^2 - E_r^2)(1 + d)}{(U_r/U_b)\, sE_b^2 - E_r^2}. \tag{6}$$

B. Corrections for Losses in the Input Coaxial Lines

Unlike a waveguide microcalorimeter in which most of the heat flowing towards the mount in the input guide may be diverted to a large thermal sink, the coaxial line microcalorimeter has an inner conductor which not only provides a path for heat flow from the outside environment but is heated by RF losses. A correction must be made for that part of the heat produced by losses in both the inner and outer thin-walled lines which reaches the mount. The task is to evaluate d ((4) and (6)) from dc to the highest frequency.

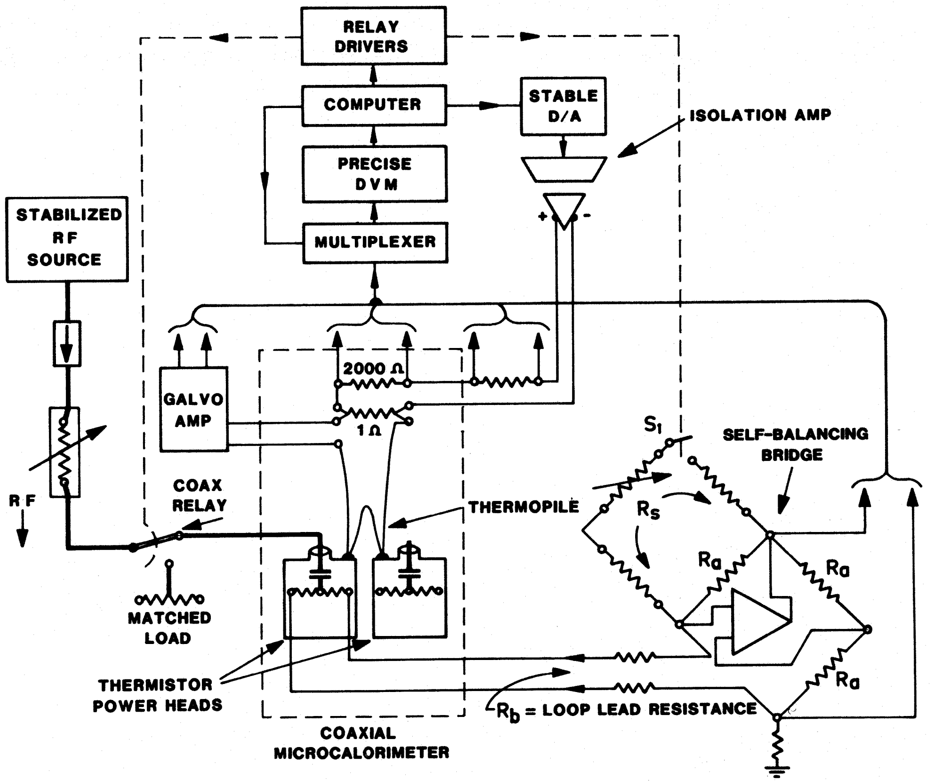

Fig. 2. Simplified diagram of equipment used for calibrating power-measuring heads using the automated microcalorimeter.

TABLE I
Some Symbols Used in Determining the Effective Efficiency

QUANTITY.	DC ONLY, RF OFF.		RF ON.
	S1 OPEN.	S1 CLOSED	S1 OPEN
Thermopile voltage:	-	U_b	U_r
Voltage across thermistor bridge:	E_d	E_b	E_r
Dc power in thermistor:	P_d	P_b	P_r
Rf power into thermistor mount.	-	-	P_t

The attenuation α_r of the input lines is the ratio of the RF power entering the mount to that entering the input port of the microcalorimeter, therefore

$$\alpha_r = P_t/(P_t + P_l)$$

and we may write d in terms of α_r as

$$d = q(1 - \alpha_r)/\alpha_r.$$

The attenuation α_r has been measured by conventional methods between dc (or 50 Hz) and 6 GHz for the 14-mm, and 12 GHz for the 7-mm microcalorimeters.

In order to calculate q as a function of frequency, the input lines, connectors, insulating beads, and air spaces are considered to be divided into small elements termed "segments," and the thermal circuit is modeled by a network composed of the thermal resistances of the segments [7]. In the model representing the 7-mm microcalorimeter, there are 94 segments conducting heat between 49 nodes. Fifty of the 94 segments carry RF current and these both generate and conduct heat. The segments are made sufficiently small to be regarded as "lumped" elements for both thermal and electrical computations and to allow heat flow to be considered either purely axial, as in segments of the thin-walled lines, or purely radial, as in the annular insulators and spaces between the lines.

The RF segments may have up to three conducting layers. Up to 13 items of data are associated with each segment, including the dimensions, the thicknesses of the layers, and references to their thermal and electrical conductivities. The thermal resistances of all the segments are computed and then, from the resistive network, a "thermal gain" is computed for each RF segment. The thermal gain of a segment is defined as the fraction of the heat developed in that segment which reaches the mount being calibrated. Thermal gains vary from almost zero for segments near the input, to nearly unity for those near the mount.

The next step is to compute the RF resistance of each conducting segment, and the total resistance of each line. For this, use is made of a skin-effect program [12]. The resistances are computed first at 50 Hz and compared with measured values. The two are brought into agreement by a change (of a few percent) in the selected value of the resistivity of the material of the thin lines. Segment and line resistances are then computed

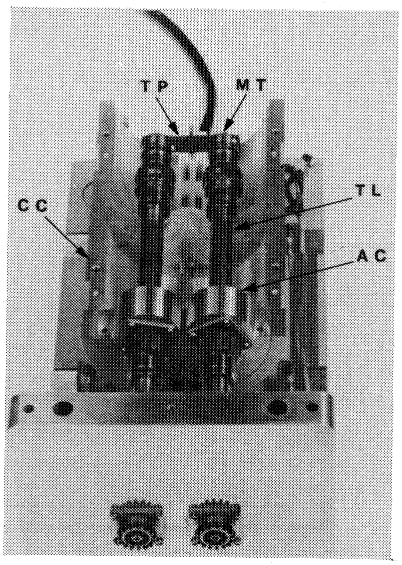

Fig. 3. The coaxial power standard shown partially dismantled. (MT—Matched terminations. TP—200-junction thermopile. CC—Cylindrical aluminium chamber containing terminations shown with upper half and end removed. AC—Aluminium cylinders surrounding connectors. TL—Thin-walled coaxial lines.)

for 30 or 40 frequencies. Measured values of the resistances of the two lines R_1 and R_2 are derived from the power ratios α_1 and α_2 by the approximations[2]

$$R_1 = -Z_0 \ln(\alpha_1)$$

and

$$R_2 = -Z_0 \ln(\alpha_2).$$

The computed resistances of segments in line 1 then are multiplied by a correction $C_1 = 1 + k_1\sqrt{f}$ and those in line 2 by $C_2 = 1 + k_2\sqrt{f}$, where k_1 and k_2 are chosen to make the computed line resistances equal to R_1 and R_2 at the highest frequency. In practice, only small corrections are needed and these provide agreement over the whole frequency range; for example, for the 14-mm microcalorimeter $k_1 = 0.00066$ and $k_2 = 0.0012$ when f is in megahertz. Finally, the line resistance effective in heating the mount R_{eff} is computed. This is the sum over all the segments, of the products: segment resistance x thermal gain.

The following results for the 14-mm microcalorimeter show the magnitudes of these quantities at 6 GHz. For the 100-mm nickel-silver line connected to the mount, $R_1 = 0.46\ \Omega$, $R_{\text{eff}} = 0.229\ \Omega$, $q_1 = 0.498$, and for the 150-mm stainless-steel input line $R_2 = 1.27\ \Omega$, $R_{\text{eff}} = 0.0057$, and $q_2 = 0.0045$. For both lines in tandem, the value of q is: 0.136 and $R_{\text{eff}} = 0.234$.

III. CALORIMETER POWER STANDARDS

One of the twin-load coaxial calorimeter power standards is shown partially dismantled in Fig. 3. It consists of two similar resistive matched loads enclosed in a thick-walled cylindrical aluminum chamber of which only the lower half is shown. Coaxial lines composed of nickel-silver tubes 0.126 mm thick, dimensioned to match GR-900 lines, connect the loads to the input ports. A 200-junction copper-constantan thermopile is attached between the loads, which are separated by a thermal barrier. The lines and inner chamber are enclosed in a thick-walled aluminum case.

Before construction began, the thermal performances of different designs were computed from models composed of networks of thermal resistors and capacitors. An objective was to reduce the thermopile output produced by heat from the environment flowing to just one of the input ports or to parts of the outer case. The results showed that good thermal contact between the outer shells of the Type-900 connectors and the bulkheads was essential. To achieve this, while still allowing for the line assemblies to be removed intact for attenuation measurements, the connectors have been machined to increase their area of contact with aluminum cylinders, shown in Fig. 3.

When the RF loads fitted originally were operated on dc, problems were caused by the Peltier effect. This was overcome by changing to loads electrically similar to GR-1641 50-Ω terminations. In these, the resistors are small, coated prisms, about 2 mm wide, pressed into thermal and electrical contact with the end face by an extension of the inner conductor. Small tuning screws allow the reflection coefficient to be reduced below 0.007 at frequencies up to 7.5 GHz. The power standard will accept input powers of up to 100 mW. It is used in a screened laboratory held to a constant temperature within ±0.5°C and is protected from air currents by a wooden enclosure. When connected to fixed devices, it is floated on springs to avoid stressing the connectors.

A. *Operation of the Power Standard*

In a typical measurement, a highly stabilized RF source of 10 mW is connected through the two coaxial relays to the measurement port as shown in Fig. 4 and the computer begins a procedure to establish a fine three-way thermal balance between the RF, the periodically reversed dc (prdc) substituted for the RF in the measurement load, and the dc fed to the balance load.

As the first step, the computer switches RF into the measurement port and adjusts the balance dc for nearly zero output from the thermopile. The next step is to switch the measuring port from RF to prdc and, with the balance dc constant, to adjust the prdc for zero thermopile output. The power changes needed to balance the system are predicted from the slopes and positions of straight lines fitted by least squares through the thermopile voltages.

Having established a coarse balance, it now begins alternating between RF and prdc into the measuring port while adjusting the prdc for equal heating of the measuring load and trimming the dc in the balance load for zero thermopile output. This stage lasts until the whole system settles down to a steady temperature distribution, which may take one-half h, or more, if conditions are unsteady. As the system approaches balance, the cycle times are gradually increased until they equal those used during calibrations.

When the balance has been held within limits for a given period, the dc into the balance load is held constant and the com-

---

[2] The (voltage) attenuation constant of a uniform line of resistance R' Ω/unit length, negligible conductance, and characteristic impedance Z_0 is approximately: $R'/2Z_0$) Np/unit length. Therefore, the output/input power ratio $\alpha_1 \simeq \exp(-R_1/Z_0)$.

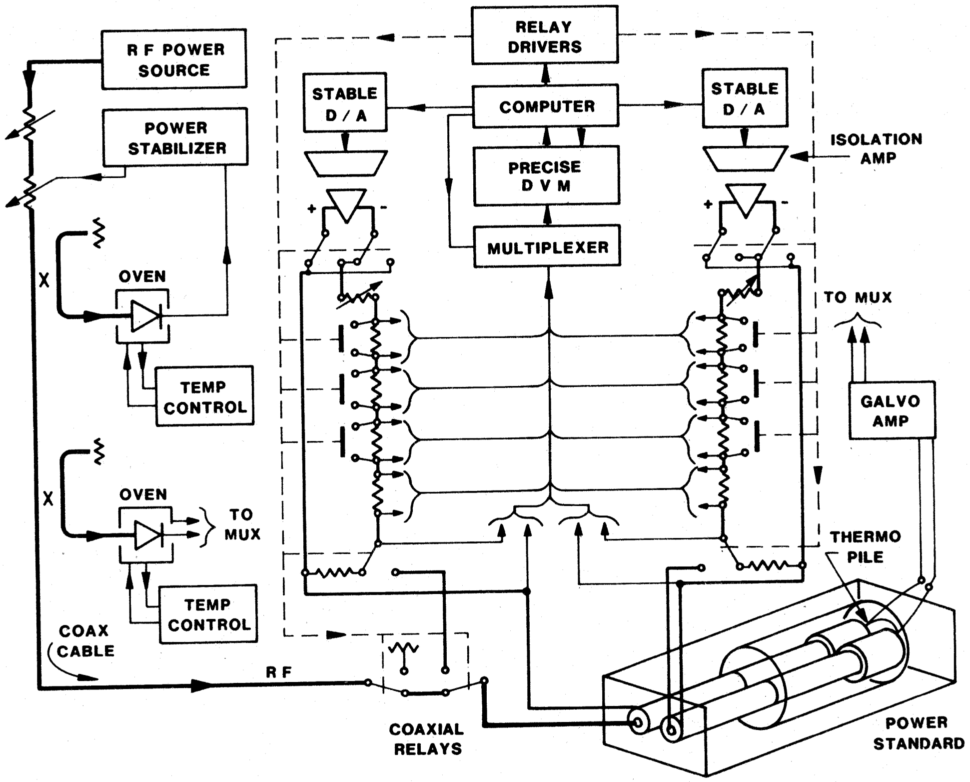

Fig. 4. Simplified diagram of equipment used for the measurement of RF power with the coaxial calorimeter power standard shown in Fig. 3.

TABLE II
SYMBOLS USED IN EVALUATING CORRECTIONS TO POWER MEASUREMENTS

Quantity	Prdc half-cycle	Rf half-cycle
Power at coaxial line input:	P_{id}	P_{ir}
Power entering termination:	P_{td}	P_{tr}
Power lost in coaxial line:	P_{ld}	P_{lr}
Attenuation (power ratio):	$\alpha_d = P_{td}/P_{id}$	$\alpha_r = P_{tr}/P_{ir}$
Thermopile voltage:	U_d	U_r

puter begins the calibration by establishing a fine balance between the prdc and RF applied to the measuring load. Typically, in this condition the dc and RF powers and the thermopile voltage are measured every 6 s, the dc in the measuring load is reversed every 36 s, and a dc/RF substitution cycle occupies 720 s. Mean values of the RF and prdc powers are printed out and stored after each cycle. A correction, which is usually less than 1 μW, is made for any changes in the thermopile voltage between the RF and prdc heating periods. If possible, calibrations are performed overnight when conditions are more stable.

B. Corrections to Power Measurements

To find the RF power at the input to the measuring line in terms of the measured prdc input, let the variables shown in Table II denote conditions during the prdc and RF half cycles.

To reduce the time needed for each power measurement, a cycle time of 12 min is used for the calorimeter power standard, compared with 360 min for the microcalorimeter. In this shorter period, the heat flow to the termination from the thin lines does not reach a steady state during either the prdc or RF half cycles. If q is (as before) the fraction of the heat flow from the line loss which would reach the termination in the steady state, let qh denote that fraction of the heat produced during one-half cycle which reaches the termination during the same and later half cycles of the same kind. The remainder $q(1 - h)$ arrives during half cycles of the other kind.

The thermopile voltages U_d and U_r are proportional to the total amounts of heat reaching the termination during the prdc and RF half cycles respectively, therefore

$$[P_{tr} + P_{lr}qh + P_{ld}q(1 - h)]/U_r = [P_{td} + P_{ld}qh + P_{lr}q(1 - h)]/U_d.$$

On substituting $P_{ld} = P_{id}(1 - \alpha_d)$ and $P_{lr} = P_{ir}(1 - \alpha_r)$, the input RF power is given by

$$P_{ir} = P_{id}\left[\frac{\alpha_d U_r + (1 - \alpha_d)\{qhU_r - q(1 - h)U_d\}}{\alpha_r U_d + (1 - \alpha_r)\{qhU_d - q(1 - h)U_r\}}\right]. \quad (7)$$

At thermal balance, U_d differs from U_r by less than 1 part in 10 000, which may be neglected in the $q(1 - h)$ terms, giving

$$P_{ir} = P_{id}\frac{U_r}{U_d}\left[\frac{\alpha_d + (1 - \alpha_d)q(2h - 1)}{\alpha_r + (1 - \alpha_r)q(2h - 1)}\right]. \quad (8)$$

If R_t is the resistance of the termination and R_{ld} is the dc resistance of the loop formed by the inner and outer coaxial lines, then $\alpha_d = R_t/(R_t + R_{ld})$. The values used at present are:

$R_t = 50.094\ \Omega$, $R_{ld} = 0.034\ \Omega$, and $q = 0.170$. For a cycle time of 12 min, $h = 0.64$.

The value of q has been found by the methods already described for the microcalorimeter and by experiment. In one measurement of q and h, a thin silver disk shortcircuit was interposed between the load and the input line and a thin wire was connected to the inner line of the termination. Prdc or 50 Hz was then fed to the loop formed by the input lines during the half-cycle normally heated by RF. The power in the termination, needed for balance, was then found by the computer.

In other tests to find h as a function of cycle time, a constant RF power was measured with cycle times ranging from 200 to 2000 s and similar tests were made using the thermal converter technique, described later. High frequencies were used because there is less heating from the input lines at lower frequencies. This work is continuing, for at present there is a discrepancy at 6 GHz which increases smoothly to 0.1 percent when the cycle time is reduced from 1200 to 240 s.

Corrections to the power measurements resulting from instrument and component calibrations are included in the control program. These include a small correction for the heating time lost in switching during dc reversals. For the mercury-wetted relays used, this is 1.12 ms/cycle.

IV. Calibration of Thermal Converters

A major function of the power standard is the calibration of the Division's standard thermal converters. The use of a calorimetric power meter as a primary standard of RF voltage is not new [14]; however, in the present method the power standard is not used as a calibrated voltmeter, but is maintained in the condition of dynamic balance already described, to establish a known ratio between the RF and prdc voltages at the measuring port of the power standard. During calibration, the thermal converter is connected in parallel with the power standard by means of a coaxial tee connector and the same RF and prdc inputs are fed to both the power standard and thermal converter.

The central plane of the tee, perpendicular to the symmetrical arms, is the common *voltage reference plane* and corrections must be made for the coaxial line elements between this plane and the measuring port of the power standard.

The RF-dc difference of a thermal converter is defined as

$$\delta = (E_{\mathrm{RF}} - E_u)/E_u \tag{9}$$

where E_u is the prdc input at a specified reference plane which would give the same output from the converter thermocouple as the RF input E_{RF}.

During calibration, the voltages applied to the reference plane of the converter are E_{RF}, and the prdc input E_{dc} needed to balance the calorimeter. U_{RF} and U_{dc} are the corresponding voltages from the converter thermocouple (Fig. 5).

The relationship between E_u and E_{dc} must be established by making a dc calibration of the thermal converter, which copies the dynamic conditions existing during calorimeter balance, but with E_u replacing E_{RF} to produce output U_{RF}. This calibration evaluates a parameter N where

$$\begin{aligned} N &= (\Delta U/U)/(\Delta E/E) \\ &= (U_{\mathrm{RF}} - U_{\mathrm{dc}})E_u/(E_u - E_{\mathrm{dc}})U_{\mathrm{RF}} \end{aligned} \tag{10}$$

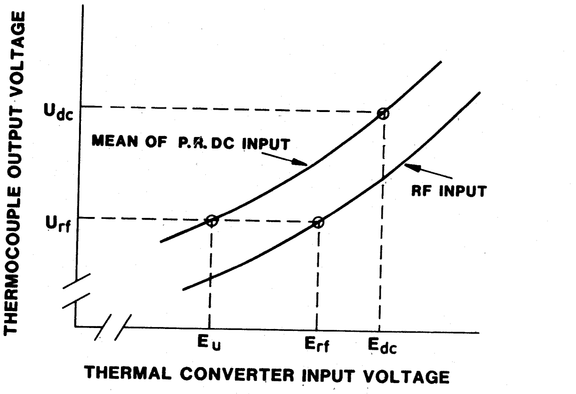

Fig. 5. Relationship between quantities used for finding the RF-dc difference of thermal converters from measurements made with the power standard.

so that

$$E_u = N U_{\mathrm{RF}} E_{\mathrm{dc}}/(U_{\mathrm{dc}} + (N-1)U_{\mathrm{RF}}).$$

On substituting E_u in (9), the RF-dc difference is given by

$$\delta = \left[1 + \frac{U_{\mathrm{dc}} - U_{\mathrm{RF}}}{N U_{\mathrm{RF}}}\right] \frac{E_{\mathrm{RF}}}{E_{\mathrm{dc}}} - 1. \tag{11}$$

The parameter N is used in the normalized form (10) because it is less sensitive to changes in operating conditions than $\Delta U/\Delta E$ would be. Thus, only one value of N is needed for each cluster of results.

In practice, one or more adaptors must be used to connect the thermal converter to the power standard. The RF voltage at the reference plane E_{RF} then must be computed from the RF voltage at the input port E_{ir} and a knowledge of the parameters of the adaptors. E_{ir} is found from the input power P_{ir} (see (8)) and the measured value of the impedance of the input port $R_i + jX_i$. On substituting $P_{ir} = E_{ir}^2 R_i/(R_i^2 + X_i^2)$ and $P_{id} = E_{id}^2/(R_{ld} + R_t)$ into (8)

$$E_{ir} = \frac{E_{id}}{(R_{ld} + R_t)} \sqrt{\frac{U_r (R_i^2 + X_i^2)\{R_t + q(2h-1)R_{ld}\}}{U_d Ri\{\alpha_r + q(2h-1)(1-\alpha_r)\}}}. \tag{12}$$

A. Adapator Corrections

E_{id} is found from the measured prdc voltage E_{dc} by correcting for the dc resistance of the adaptor R_{ad}

$$E_{id} = E_{\mathrm{dc}}(R_{ld} + R_t)/(R_{ad} + R_{ld} + R_t). \tag{13}$$

To find E_{RF}, the adaptor parameters are entered in a program used to analyze the results, which then selects an algorithm for the particular configuration and includes minor corrections for step capacitances and the change in characteristic impedance caused by skin effect. If the adaptor consists only of a length x of uniform line, the major part of the correction is given by

$$E_{\mathrm{RF}} = E_{ir}(\exp(\gamma x) + \Gamma \exp(-\gamma x))/(1 + \Gamma) \tag{14}$$

where Γ, the reflection coefficient at the calorimeter input, and γx are found by measurement. The RF-dc difference is then found by substituting E_{RF} and E_{dc} in (11).

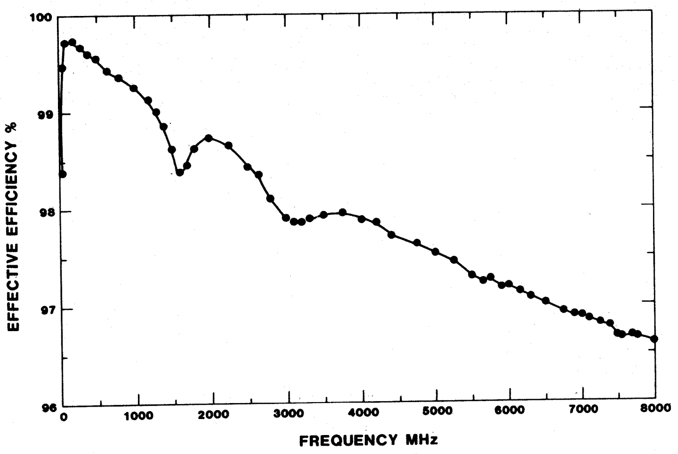

Fig. 6. The effective efficiency of a typical thermistor power-measuring head. The measurements were made in the coaxial microcalorimeter.

V. Accuracy and Results

The uncertainty associated with RF power measurements increases rapidly with frequency, and is difficult to estimate. The thermal balance, thermopile, and dc measurements contribute little to the uncertainty in the gigahertz range, but intercomparisons between the calorimeters show that an adequate allowance must be made for systematic errors. For example, although measurements of the same mount made at 8 GHz by the 7- and 14-mm microcalorimeters agree within ±0.1 percent at the 10-mW level, in some tests these have differed from the power standard by 0.4 percent. At 8 GHz, the estimated uncertainty is ±0.5 percent when not limited by the performance of the instrument being calibrated.

An example of the calibration of a thermistor mount (HP 8478B and Type 900/N adaptor), made in the 14-mm calorimeter, is shown in Fig. 6. As described earlier, each measurement requires at least 18 three-hour periods and the complete calibration takes some months.

The methods described for thermal converter measurements were used in International Intercomparisons of voltage: at 1 MHz [15] in 1974 and 1977 and at 100, 250, 500, and 1000 MHz [16] in 1981. The estimated uncertainties for these measurements varied from 0.01 percent at 1 MHz to 1 percent at 1 GHz.

VI. Conclusions

Calorimeters and microcalorimeters have been designed and constructed as standards of RF and microwave power and voltage. They are used with associated equipment of high precision to form the basis of the Division's calibration service. The equipment is computer controlled and after initial setting-up can be left unattended. Corrections and sources of error have been analyzed and evaluated. From the results of intercomparisons between the calorimeters and microcalorimeters and from International Intercomparisons, it appears that there are no large systematic errors.

Acknowledgment

The authors acknowledge contributions made to the design and construction of these calorimeters by W. H. Reid, who also built the thermopiles. P. I. Somlo produced general-purpose skin-effect and network programs which have been incorporated into our correction programs. The late J. A. Harvey set up automated equipment for the intercomparison of power mounts and the measurement of impedance and made the line attenuation measurement. J. E. Peters performed measurements of reflection coefficient and power mount efficiency. The accuracy and stability of the calorimeters owes much to the skill of P. Campbell who built the 14-mm microcalorimeter and all the thin lines.

References

[1] A. Jurkus, "A coaxial radio-frequency power standard," *IEEE Trans. Instrum. Meas.*, vol. IM-15, pp. 338-342, Dec. 1966.

[2] M. Sucher and H. J. Carlin, "Broad-band calorimeters for the measurement of low and medium level microwave power. I. Analysis and design," *IRE Trans. Microwave Theory Tech.*, vol. MTT-6, pp. 188-194, 1958.

[3] A. V. James and L. O. Sweet, "Broad-band calorimeters for the measurement of low and medium level microwave power II. Construction and performance," *IRE Trans. Microwave Theory Tech.*, vol. MTT-6, pp. 195-202, Apr. 1958.

[4] R. F. Clark, "A coaxial calorimeter for use as a microwave power standard," *IEEE Trans. Instrum. Meas.*, vol. IM-14, pp. 59-63, Mar.-June 1965.

[5] R. Bostrom, "Coaxial microcalorimeter," in *Proc. IMEKO Symp. Microwave Meas.* FOA 3 Rapport, B 3030-E1 (E2), 1972. (Forsvarets Forskningsanstalt, Avdelning 3, 104, 50, Stockholm 80). (Note: Bostrom describes a twin-load power standard, not a microcalorimeter in the sense used in the present paper.)

[6] P. A. Hudson and C. M. Allred, "A dry, static calorimeter for rf power measurement," *IRE Trans. Instrum.*, vol. I-7, pp. 292-296, Dec. 1958.

[7] D. L. Hollway, "Coaxial calorimeters and microcalorimeters for RF power measurement: Operation and the evaluation of line loss corrections," CSIRO Division of Applied Physics, tech. memo. 4, 1982. First published: DAP-P156, July, 1980.

[8] A. C. MacPherson and D. M. Kerns, "A microwave microcalorimeter," *Rev. Sci. Instrum.*, vol. 26, pp. 27-33, Jan. 1955.

[9] G. F. Engen, "A refined *X*-band microwave microcalorimeter," *J. Res. NBS*, vol. 63C, pp. 77-82, July-Sept., 1959.

[10] H. Bayer, "Experiences and results on the microwave power and attenuation measuring equipment in the PTB," in *Proc. IMEKO Symp. Microwave Meas.* (Budapest, Hungary), May 10-13, 1972.

[11] W. H. Reid, "7 mm Coaxial Microcalorimeter. Details of constrution and assembly," CSIRO Division of Applied Physics, Tech. Memo. 6, 1982. First published: DAP-R2, June, 1980.

[12] P. I. Somlo, "The computation of the surface impedance of multi-layer cylindrical conductors," CSIRO Division of Applied Physics, Rep. APR 12, Nov. 1966.

[13] P. I. Somlo and D. L. Hollway, "The Australian NSL X-band radiometer for the calibration of noise sources," *IEEE Trans. Microwave Theory Tech.*, vol. MTT-16, pp. 664-669, Sept. 1968.

[14] R. F. Clark and A. P. Jurkus, "Calibration of thermal transfer standards of RF voltage," *IEEE Trans. Instrum. Meas.*, vol. IM-16, pp. 232-237, Sept. 1967.

[15] A. E. Fantom, "Rapport final sur la comparaison internationale de tensions á 1 MHz," Annexe E13, Comité International des Poids et Mesures, Comité Consultatif d'Électricité 15e Session, Sept. 13-14, 1978, pp. E70-E76.

[16] H. Bayer and D. Janik, "Results of an international intercomparison of RF voltage at some frequencies between 100 MHz and 1 GHz in coaxial guide systems," in *Proc. INSYMET'82, The Sixth Int. Symp. on Metrology* (Bratislava, CSSR), Sept. 21-24, 1982, pp. 202-206.

Optimum Form of Capacitive Transducer for Displacement Measurement

MASAHIDE HIRASAWA, MITSUNOBO NAKAMURA, AND
MAKOTO KANNO, FELLOW, IEEE

***Abstract*—A comb-shaped capacitive transducer for displacement measurement is used as a manufacturing machine controller, a step-and-repeat camera, and an electrical micrometer. In this transducer one of the comb-shaped electrodes is fixed and the other is moved parallel to it. For an accurate measurement it is desirable to increase the difference between the maximum and the minimum values of the capacitance. It has been reported that putting dielectric protective layers on the surfaces of the electrodes effectively increases that difference. To find the optimum form of the transducer, a simulation based on the finite-element method is introduced, and the simulation is experimentally verified. To achieve the optimum form, the distance between the electrode must be made as narrow as possible, and the width of the tooth should be 20 ~ 30 percent of one pitch. The effect of dielectrics put in the capacitor is also discussed.**

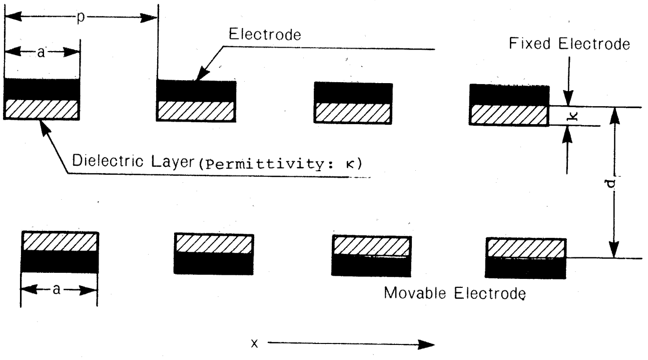

Fig. 1. Cross section of a comb-shaped capacitor.

I. Introduction

DISPLACEMENT MEASUREMENT with a comb-shaped capacitive transducer depends on purely electrical means [1]. It is simpler in structure and more economical than an optical method [2] or a microwave interferometer [3]. The transducer is composed of two comb-shaped electrodes. One of them is fixed and the other is movable. While the movable electrode moves parallel to the fixed one, the measured capacitance value changes nearly sinusoidally. The displacement measurement is primarily derived by counting the number of the peaks caused by the change. Therefore, the resolving power of the transducer is determined by the pitch of the teeth of the comb. To obtain the best signal-to-noise ratio, the amplitude of the capacitance change should be as large as possible.

In this paper, the optimum form of the transducer is discussed. The best width for the teeth of the comb, previously set at half of the pitch [1], is investigated. The effect of the gap size between the two electrodes and the effect of dielectric protective layers are also considered.

For these purposes, a simulation based on the finite-element method (FEM) was performed to get the optimum form of the comb-shaped capacitor. The experiments on the macro scale design were carried out and the results are discussed. A large model is used to simplify the measurement.

II. Finite-Element Method (FEM) for Calculation of Capacitance

Several references are presented on the FEM for electromagnetic field problems [4]-[7]. Here the calculation of capacitance is briefly discussed. For simplicity, only the two-dimensional (2D) problem is dealt with, because the model for the comb-shaped capacitor can be treated two dimensionally.

The total energy W of a capacitor with capacitance C is given by

$$W = \frac{1}{2} CV^2 = \frac{1}{2} \iint \epsilon (\text{grad}\, \phi)^2 \, ds \qquad (1)$$

where V is the voltage applied to the capacitor, ϵ is the permittivity, ϕ is the potential, and the integration is over the entire 2D space. By the variational principle the upper bound C' on C is

$$C \leqq C' = \frac{\iint \epsilon (\text{grad}\, \phi_t)^2 \, ds}{V^2} \qquad (2)$$

where ϕ_t is a trial function for ϕ.

The 2D domain is divided into many triangular elements and a linear trial function for each element is used. Then an approximate upper value C' for C is computed.

III. Numerical Results

The cross section of a comb-shaped capacitor is shown in Fig. 1. Of the two comb-shaped electrodes, one is fixed and the other is movable. Both have the same pitch. Here a and b are, respectively, the width of one tooth of the fixed electrode and the width of one tooth of the movable electrode, p is the length of one pitch, and d is the distance of the gap between the electrodes. The movable electrode moves parallel to the fixed one. The discussion begins with the electrodes which have no dielectric layers.

In this model the potentials u on the electrodes are given as follows:

Manuscript received February 16, 1984; revised July 2, 1984.

The authors are with the Department of Electronics, Tamagawa University, Machida, Tokyo 194, Japan.

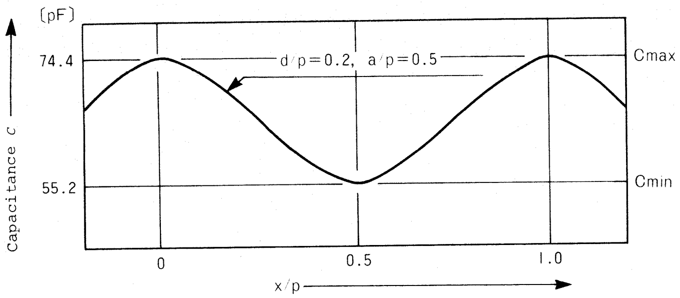

Fig. 2. Representative example for the change of capacitance versus the displacement of the movable comb.

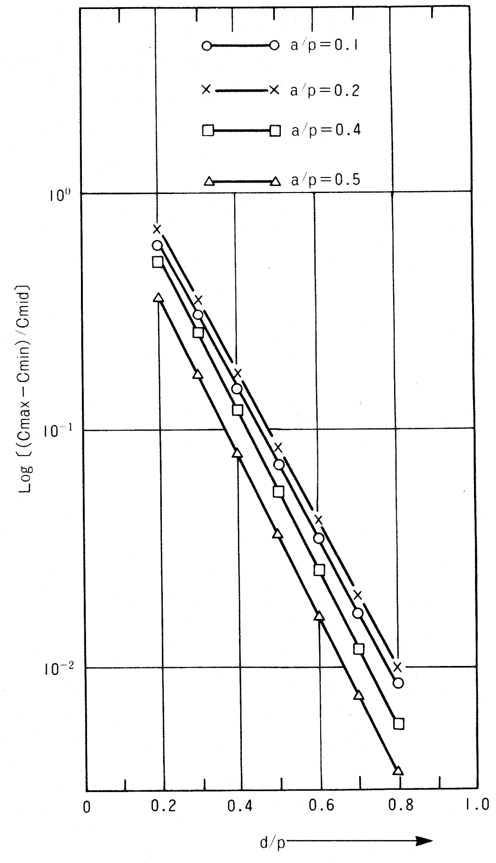

Fig. 3. β versus d/p taking a/p as the parameter. (Here d, a, and p are, respectively, the distance between the electrodes, the width of the tooth and the length of one pitch of the comb, $\beta = (C'_{\max} - C'_{\min})/C'_{\mathrm{mid}}$ where $C'_{\max}$, $C'_{\min}$, and C'_{mid} are, respectively, the maximum, the minimum, and the middle value of the change of capacitance.)

$$\begin{aligned} u &= 1 \quad \text{on the fixed electrode} \\ u &= 0 \quad \text{on the movable electrode.} \end{aligned} \tag{3}$$

The amplitude of the capacitance difference is decided by the ratios a/p, b/p, and d/p. Therefore, in the discussions the sizes a, b, and d are normalized by p to dimensionless quantities. To omit the edge effect of the capacitor, the capacitance C' was calculated by the FEM for one tooth located sufficiently far from the ends of the comb, where the capacitance for each tooth was equal.

Initially the calculations were carried out at $a = b$. A typical curve showing change of capacitance as a function of displacement of the comb is shown in Fig. 2. The curve is very close to a sinusoidal curve. The result agrees with the results of the experiment of Kosel *et al.* [1].

For an accurate displacement measurement it is desirable that the quasisinusoidal amplitude be as large as possible. The sizes a, b, d, and p are basic parameters used to decide the best performance of the transducer for the displacement. To determine the best performance, the effect of the distance d between the comb-shaped electrodes was investigated.

Here another dimensionless quantity for sensitivity β is introduced as follows:

$$\beta = (C'_{\max} - C'_{\min})/C'_{\mathrm{mid}} \tag{4}$$

where $C'_{\max}$, $C'_{\min}$, and C'_{mid} are, respectively, the maximum, the minimum, and the middle value of the change of the capacitance. The quantity β makes it easier to analyze the calculated results.

In Fig. 3, β is plotted against d/p with a/p as the parameter. When d/p increases by 0.3, β becomes 1/10 of each original value. The quantity β increases exponentially as the value d/p approaches zero, therefore, the gap distance d should be as small as possible for the optimum design. Thus the movable comb slides on the fixed one with minimal intervening insulation.

Next, the characteristics of the capacitor for the width $a(=b)$ are investigated. In Fig. 4 representative β values are plotted against a/p with d/p as the parameter. The magnitude of β reaches its highest value at $a/p = 0.2$ for every d/p.

Next, the calculations are performed for the best width of the tooth for $a \neq b$. The results are shown in Fig. 5, where β is plotted versus b/p at $d/p = 0.5$ taking a/p as the parameter. The magnitude of β reaches its highest value at $b/p = 0.2$ for every a/p. Also for every b/p, the curve of $a/p = 0.2$ yields the highest value. These results are common for every d/p. From these facts, β is determined to be the best for the width of the tooth at $a/p = b/p = 0.2$.

Filling a dielectric with specific permittivity κ in the whole of the space between the electrodes effectively increases the amplitude because it makes the numerator of (4) increase by κ times. As the denominator of (4) also becomes κ times greater, the magnitude of β is not changed. Therefore, the shape remains the same.

Kosel *et al.* showed that putting protective dielectric layers only on the metallic part of the comb electrode is an effective method for increasing the value β [1]. To investigate this premise, dielectric layers of thickness κ are put on the electrodes of the calculated model as shown in Fig. 1. Here κ is the specific permittivity of the layers. In this model the quantity β is also considered. The value $\beta(\kappa)$ is shown as β for the electrodes with protective layers of specific permittivity κ, and $\beta(1)$ is considered as β for the electrodes with the exposed metallic surfaces. From the result of Fig. 5 the calculation is carried out for the model of $a/p = b/p$. In Fig. 6, $\beta(\kappa)/\beta(1)$ versus κ is plotted, where $a/p = 0.2, d/p = 0.5$, and $k/p = 0.05$. In many calculations for other sizes, the results are the same, i.e., the protective layers are effective in improving β, but this effect is small. For instance, $\beta(\kappa)$ is only 1.6 times greater than $\beta(1)$, even though κ is equal to 20.

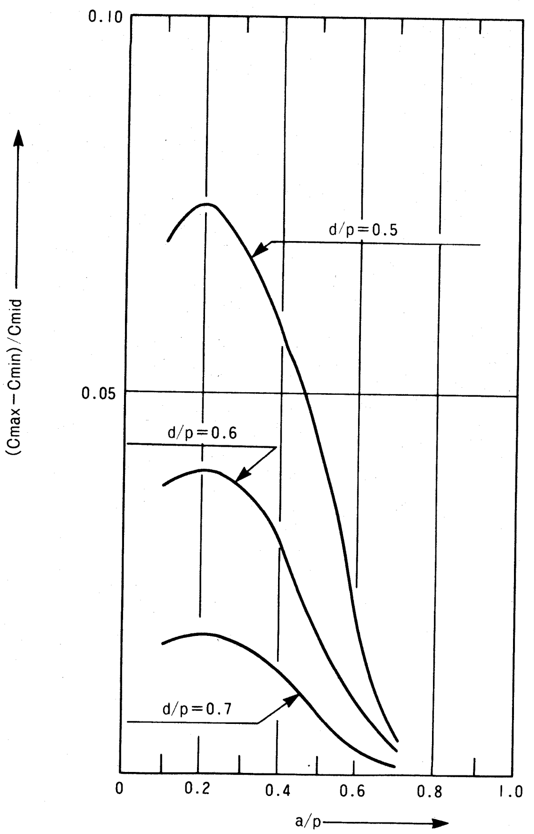

Fig. 4. β versus a/p taking d/p as the parameter.

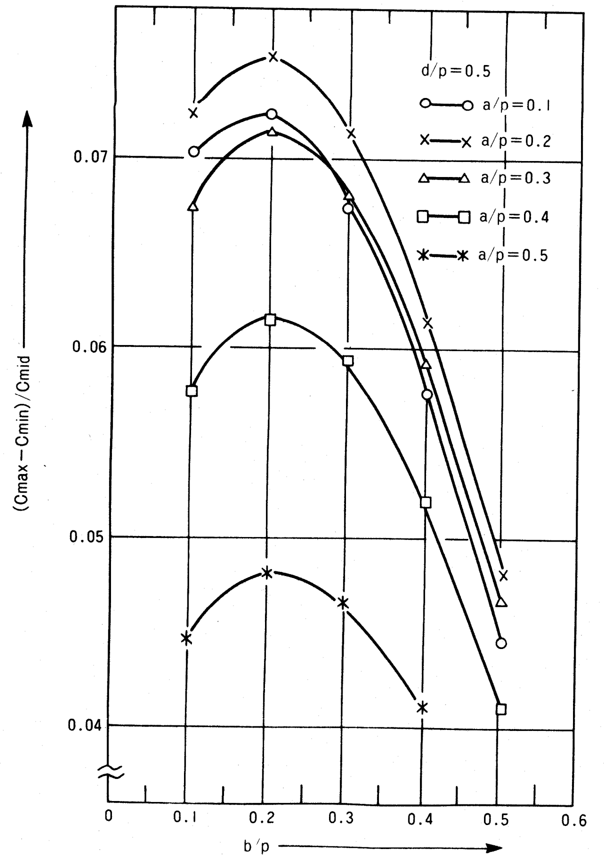

Fig. 5. β versus b/p at $d/p = 0.5$ taking a/p as the parameter. (Here a and b are, respectively, the width of the tooth on the fixed and the movable electrode.)

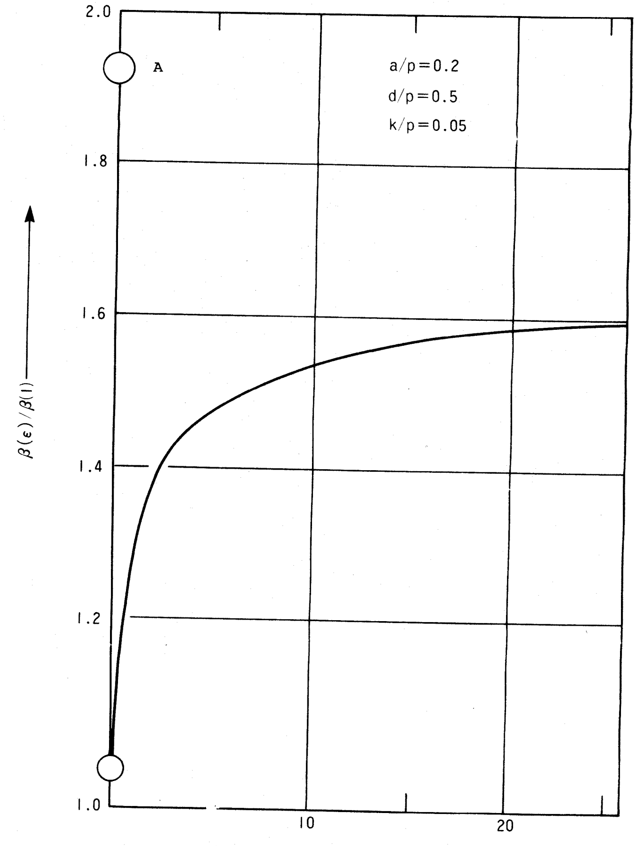

Fig. 6. $\beta(\kappa)/\beta(1)$ versus specific permittivity κ, at $a/p = 0.2$, $d/p = 0.5$, and $k/p = 0.05$ (Here $\beta(\kappa)$ and $\beta(1)$ are, respectively, β for the capacitor with the dielectric protective layers and β for the capacitor whose electrodes expose their metallic surfaces.)

Let $\beta(A)$ be defined as β for the capacitor with exposed electrodes whose distance between the electrodes is $d - 2k$. In Fig. 6, $\beta(A)/\beta(1)$ is plotted at the point A. Here the distance between the electrodes corresponding to $\beta(1)$ is d. The quantity $\beta(A)$ is about 20 percent larger than the maximum value of $\beta(\kappa)$. Therefore, it is better to make the gap between the electrodes smaller by the distance $2k$ than to put the protective layers with a thickness of k on the both surfaces of the electrodes.

IV. EXPERIMENTAL RESULTS

To verify the results of the simulation based on the FEM, several experiments were performed. Fig. 7 shows a prototype of a comb-shaped capacitor for the experiment. A large-sized macro model was used to permit simple construction and measurement. There are two comb-shaped electrodes: the longer one is fixed and the other is movable. To keep the face-to-face area of the capacitor constant while the movable electrode moves, the length of the latter is made shorter than the fixed one. The teeth are formed of a thin copper plate on a substrate of bakelite. The length of the fixed electrode is 1000 mm and that of the movable electrode is 500 mm. The distance between the fixed and movable electrodes is changeable. The movable electrode is able to move for a seven-pitch distance along the fixed one. There are 20 teeth on the fixed electrode and ten on the movable one. The length of one pitch is 50 mm and the height of the electrode is 245 mm. The width of the tooth

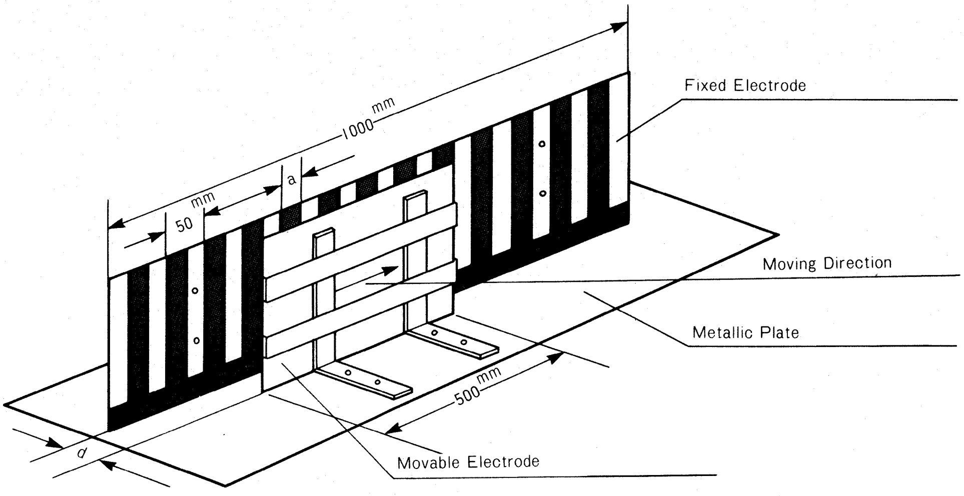

Fig. 7. Prototype of comb-shaped capacitor experiment.

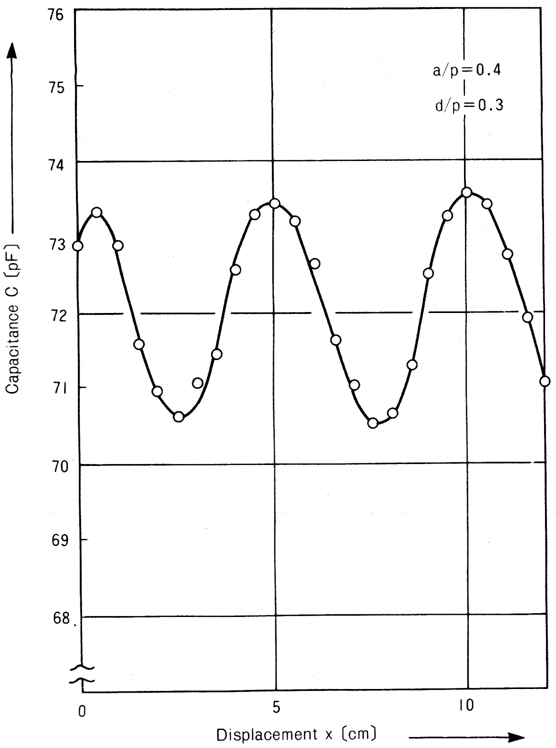

Fig. 8. One of the representative changes of capacitance versus the displacement of movable electrode at $a/p = 0.4, d/p = 0.3$.

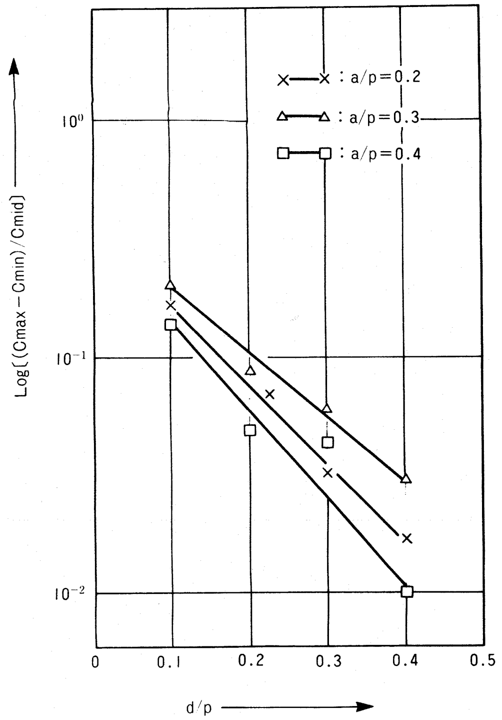

Fig. 9. β versus d/p for the experimental results taking a/p as the parameter.

may be decreased by etching. Here the tooth widths of the two electrodes are equal to each other.

The capacitance value was measured by a Yokogawa Hewlett Packard 4192A LF Impedance Analyzer. The electrostatic shield system, which is now shown in Fig. 7, was applied to prevent stray capacitance effects.

The typical change of capacitance versus the displacement of a movable electrode parallel to the fixed one is plotted in Fig. 8, where $a/p = 0.4, d/p = 0.3$. In agreement with the results of the calculation by the FEM and those of Kosel *et al.*, the capacitance changes sinusoidally as the movable electrode moves [1]. Fig. 9 represents β versus d/p for the experimental results taking a/p as the parameter, where β is defined by (4). The result agrees with the numerical result, i.e., and d/p increases, β decreases exponentially. For instance, d/p increases 0.3 then β becomes $\frac{1}{10}$ of the original value.

Fig. 10 represents experimental β versus a/p with d/p as the parameter. In Fig. 10, β reaches the highest value when a/p in 0.25 ~ 0.30. Although the results in Fig. 10 include some errors caused by the residual stray fields, these results agree with the results of Fig. 4. The results are treated as dimensionless quantities, therefore, they can be applied even for a small, comb-shaped capacitor.

V. CONCLUSIONS

The suitability of the simulation based on the FEM for the analysis of the comb-shaped capacitor has been validated by

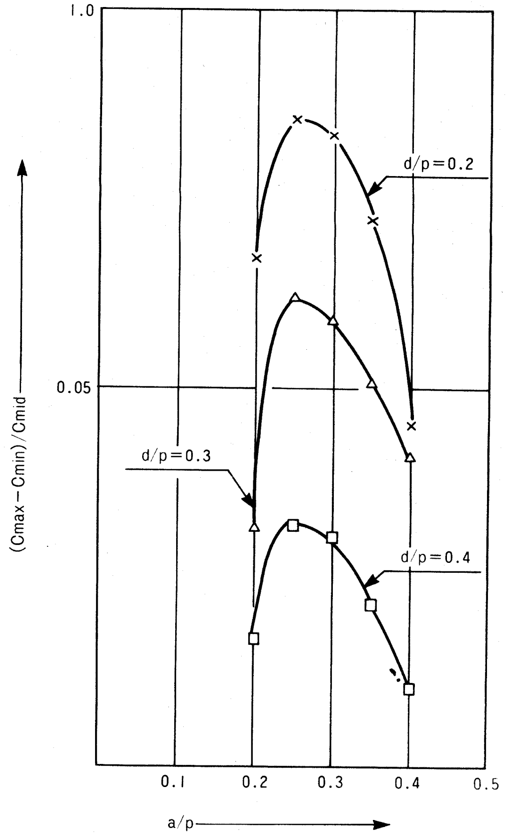

Fig. 10. β versus a/p for the experimental results taking d/p as the parameter.

experimentation. The change of capacitance with respect to the displacement of the movable electrode parallel to the fixed one is very close to a sinusoidal curve. When the gap between the two electrodes decreases, the value of the sensitivity β in (4) increases exponentially. When the normalized widths of the teeth a/p and b/p are each $0.2 \sim 0.3$ and $a/p = b/p$, β is maximized. Hence, displacement measurements are most accurate, and the design of the electrode approaches the optimum, when the gap between the two electrodes is as narrow as possible and the width of a tooth is $20 \sim 30$ percent of the length of one pitch. It is better to use exposed electrodes with close spacing than to sacrifice the gap width by using dielectric protective layers on the surfaces of the electrodes. After the distance between the electrodes is made as narrow as possible, filling a dielectric in the space effectively increases the amplitude.

The simulation, based on the finite-element method, is useful in finding the optimum forms of comb-shaped capacitive transducers for displacement measurement.

ACKNOWLEDGMENT

The authors wish to thank R. Asaba, O. Nomura, O. Nose, and K. Wada for their valuable assistance with the numerical calculations and measurements. The authors also greatly appreciate Mrs. and Mr. Moss with their effective suggestions. The numerical computations were carried out on the M-28OH at the Computer Center, University of Tokyo, Tokyo, Japan.

REFERENCES

[1] P. B. Kosel, G. S. Munro, and R. Vaughan, "Capacitive transducer for accurate displacement control," *IEEE Trans. Instrum. Meas.*, vol. IM-30, no. 2, pp. 114–123, June 1981.

[2] H. De Lang and G. Bouwhuis, "Displacement measurement with a laser interferometer," *Philips Tech. Rev.*, vol. 30, no. 6/7, pp. 160–165, 1969.

[3] A. Thansandote, S. S. Stuchly, and J. S. Wight, "Microwave interferometer for measurements of small displacements," *IEEE Trans. Instrum. Meas.*, vol. IM-31, no. 4, pp. 227–232, Dec. 1982.

[4] M. V. K. Chari and P. P. Silvester, *Finite Elements in Electrical and Magnetic Field Problems*. New York: Wiley, 1980.

[5] M. Nakamura and M. Mizuno, "Bounds for effective conductivity of heterogeneous materials by the finite element method," *J. Math. Phys.*, vol. 23, no. 6, pp. 1228–1230, June 1982.

[6] M. Nakamura and M. Hirasawa, "Bounds on the effective conductivity of a composite by the finite element method," *J. Appl. Phys.*, vol. 54, no. 7, pp. 4216–4217.

[7] M. Hirasawa, M. Nakamura, and M. Kanno, "Optimum design of capacitive transducer for displacement measurement," in *Proc. Association for the Advancement of Modelling and Simulation Techniques in Enterprises Bermuda Symp.*, Mar. 1983, pp. 131–135.

IEEE TRANSACTIONS ON INSTRUMENTATION AND MEASUREMENT, VOL. IM-33, NO. 4, DECEMBER 1984

Study and Performance Evaluation of Two Iterative Frequency-Domain Deconvolution Techniques

BIDYUT PARRUCK, STUDENT MEMBER, IEEE, AND SEDKI M. RIAD, SENIOR MEMBER, IEEE

Abstract—**The performance of two iterative frequency-domain deconvolution techniques, the optimum compensation and the Guillaume-Nahman, is evaluated. The study involved the characterization of the adaptive filters utilized to reduce the deconvolution noise. Comparisons between the two techniques are performed for various classes of signals having different levels of acquisition noise. It is found that the Guillaume-Nahman technique is potentially more accurate but more sensitive to acquisition noise. It is also found that the optimum compensation deconvolution technique uses an adaptive filter with the passbands coinciding with the frequency bands of the signal, thus optimizing noise filtration, while the Guillaume-Nahman technique utilizes a low-pass filter for all signals.**

I. INTRODUCTION

DECONVOLUTION of time domain waveforms is used to determine the impulse response of a linear time invariant system. If $h(t)$ is the impulse response of such a system whose input is $x(t)$, then the output $y(t)$ is given by the convolution

$$y(t) = x(t) * h(t) \tag{1}$$

where $*$ denotes the convolution operation. In the frequency domain, convolution transforms into multiplication, thus

$$Y(j\omega) = X(j\omega) \cdot H(j\omega) \tag{2}$$

where $Y(j\omega)$, $X(j\omega)$, and $H(j\omega)$ are the frequency domain representations of $x(t), y(t)$, and $h(t)$, respectively.

Ideally, the impulse response $h(t)$ can be determined by evaluating the transfer function, $H(j\omega)$ using (2), i.e.

$$H(j\omega) = Y(j\omega)/X(j\omega) \tag{3}$$

to which the inverse Fourier transform can be applied to give $h(t)$. The process of obtaining $h(t)$, knowing both $x(t)$ and $y(t)$, is called deconvolution. Thus (3) performs a deconvolution process through frequency-domain division. To date, there is no well-known time-domain representation for (3), in particular, the deconvolution symbol. In this paper, it is proposed to use the symbol : to denote the deconvolution operation. Consequently, the proposed time-domain representation of (3) is

$$h(t) = y(t) : x(t). \tag{4}$$

In general, the zeroes of $X(j\omega)$ are also zeroes of $Y(j\omega)$. At these zeroes, (3) becomes indeterminate. Hence applying (3) blindly (as in a computer algorithm) will result in noise-like errors at and around these zeroes. When $H(j\omega)$ is transformed to the time domain, the noise-like errors, which were present only in the neighborhood of zeroes of $X(j\omega)$, will cover the entire transform window, swamping the useful information content (waveform detail).

Hence, the deconvolution operation needs to be modified, beyond the simple division, in order to yield a low-noise "good" estimate of $h(t)$. Numerous approaches to the deconvolution problem have been developed. One thing all these approaches have in common is the use of iterations to design an optimum "filter" to reduce the deconvolution noise. *The optimum filter interpolates $H(j\omega)$ at the zeroes of $X(j\omega)$, where it is indeterminate, to yield $H_e(j\omega)$; the "best" estimate of $H(j\omega)$.*

It is important here to emphasize that the simple division (3) accurately describes the deconvolution result. Such a result is not practically usable due to its large noise content. The use of noise-reduction filters causes the deconvolution result to become inaccurate. The introduced inaccuracy can not be determined due to the lack of knowledge of the true result. In other words, only *estimates* to a filtered deconvolution result can be obtained, and the accuracy of such results can only be *estimated* using some accuracy *indicator.*

Two iterative frequency domain deconvolution techniques are to be discussed in this paper. They are:

1) The automated optimum compensation deconvolution [1], [3], which defines

$$H_e(j\omega) = Y(j\omega) \cdot X^*(j\omega)/[|X(j\omega)|^2 + \lambda]. \tag{5}$$

In this technique, the criterion for selecting the optimum value of the parameter λ is based on a compromise between deconvolution accuracy and noise content indicators. The indicators are defined for the step-response waveform $w_e(t)$ obtained by integrating the deconvolved impulse response $h_e(t)$ as follows [3]:

$$\text{accuracy indicator } A(\lambda) = \text{av } [w_e(t)], \qquad t > T_1$$

$$\text{noise indicator } N(\lambda) = \text{rms } [w_e(t) - A(\lambda)], \qquad t > T_1$$

where T_1 is a time instant beyond which $w(t)$ is expected to be constant.

2) The Guillaume-Nahman (automated-regularization) technique [5], utilizes the form [2]

$$H_e(j\omega) = Y(j\omega) \cdot X^*(j\omega)/[|X(j\omega)|^2 + \gamma\omega^4] \tag{6}$$

which is similar to (5) except for replacing λ by $\gamma\omega^4$. The optimum γ is chosen as the value for which the standard devi-

Manuscript received July 25, 1983; revised February 29, 1984.

B. Parruck is with the Advanced Technology Center, ITT, Shelton, CT 06484.

S. M. Riad is with the Department of Electrical Engineering, Virginia Polytechnic Institute and State University, Blacksburg, VA 24061.

ation in the imaginary part of the deconvolved impulse response is minimized [5]. For voltage waveforms, if the mean value of the imaginary part is negligible, then the standard deviation is equal to the energy in a 1-Ω load.

In this paper, the performance of these two iterative frequency-domain deconvolution techniques is evaluated. The next section describes the method used for this purpose. Section III considers the effect of acquisition noise on the performance of these techniques. Section IV considers the effects of the signal type. Finally, Section V concludes the paper.

II. Performance Evaluation Procedure

Studies [4] showed that the performance of a deconvolution method can be best assessed by analyzing the effects of its filter. The deconvolution's filtering effects are expected to give not only an idea of the deconvolution's performance quality, but also a qualitative idea of the mechanics of the deconvolution process. This is particularly helpful in the case of the two iterative deconvolution techniques under study, where the operations of the compensation and the regularization operators (filters) are not obvious. The proposed method evaluates the transfer function of these filters. And it involves studying the variations of the filter characteristics with the type (class) of the deconvolution signals and their noise content.

The method involves the generation of an analytical input signal $x(t)$ which may belong to any general class of signals—low-pass, wide-band, or narrow-band. The system assumed is an ideal attenuator with a transfer function magnitude of 0.5 and a propagation delay τ. Consequently, the output $y(t)$ is given by

$$y(t) = 0.5x(t - \tau). \tag{7}$$

At this point, in order to simulate the presence of acquisition noise in measured waveforms, white random Gaussian noise components are added to both $x(t)$ and $y(t)$. The deconvolution technique under test is then applied to deconvolve $x(t)$ from $y(t)$ to give $h_e(t)$. Ideally, using (3) and (4), the expected result for $h(t)$ should take the form

$$h(t) = 0.5\delta(t - \tau) \tag{8}$$

where $\delta(t)$ is the Dirac delta function. And, the corresponding frequency domain representation of $h(t)$ takes the form

$$H(j\omega) = 0.5 \exp(j\omega\tau). \tag{9}$$

The magnitude of this transfer function, $|H(j\omega)| = 0.5$, should be flat over the entire frequency range. Clearly, if either of the deconvolution techniques (5) or (6) is used, the result would be different. Rewriting (5) and (6) in the form

$$H_e(j\omega) = [Y(j\omega)/X(j\omega)] \cdot F(j\omega) \tag{10}$$

gives (10) where $F(j\omega)$ is the deconvolution's noise reduction filter. From (5) and (10), the optimum compensation filter $F_c(j\omega)$ is of the form

$$F_c(j\omega) = 1/[1 + \lambda/|X(j\omega)|^2]. \tag{11}$$

While, from (6) and (10), the regularization filter $F_r(j\omega)$ is the form

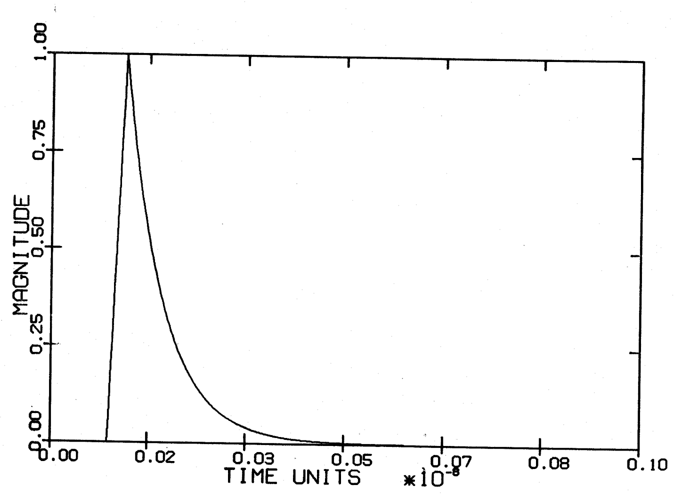

Fig. 1. Low-pass analytical input waveform.

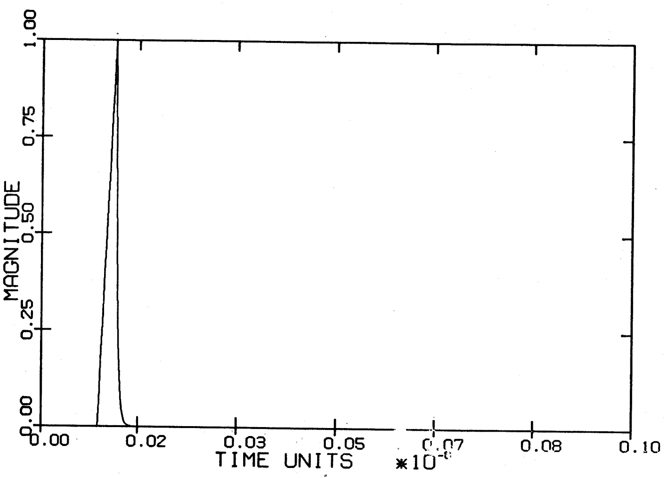

Fig. 2. Wide-band analytical input waveform.

$$F_r(j\omega) = 1/[1 + \gamma\omega^4/|X(j\omega)|^2]. \tag{12}$$

Using the ideal deconvolution form (3), the best estimate deconvolution result (10) takes the form

$$H_e(j\omega) = H(j\omega) \cdot F(j\omega). \tag{13}$$

For the particular $H(j\omega)$ used in this paper and given by (9), $F(j\omega)$ as derived from (13) can be written as

$$F(j\omega) = 2 \exp(-j\omega\tau) H_e(j\omega). \tag{14}$$

Rewriting (14) in its magnitude form yields

$$|F(j\omega)| = 2|H_e(j\omega)|. \tag{15}$$

Consequently, it can be stated that the magnitude of the deconvolution result, in the frequency domain, is a representation of the filtering effects of the technique itself [6].[1]

As stated earlier, three classes of signals will be used to test the deconvolution techniques performance. The three classes are the low-pass, the wide-band, and the narrow-band signals. The three signals are analytically generated and their waveforms are shown in Figs. 1, 2, and 3, respectively. Their correspond-

---

[1] A method for obtaining the regularization filter's impulse and transfer function responses was developed independently by Nahman in April 1982. His work was not disclosed to the authors or the public until January 1983 [5].

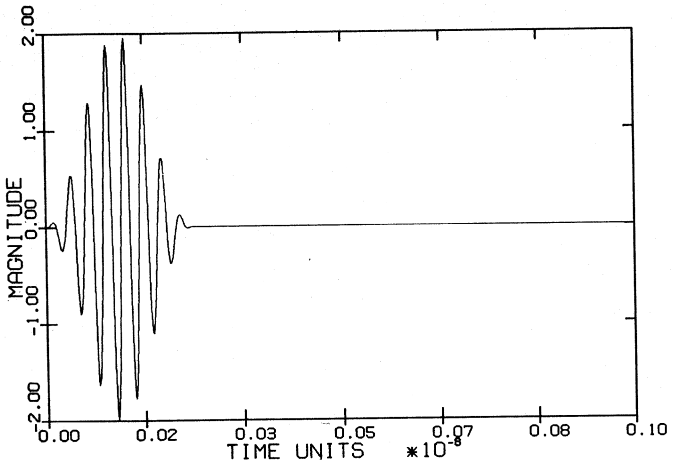

Fig. 3. Narrow-band analytical input waveform.

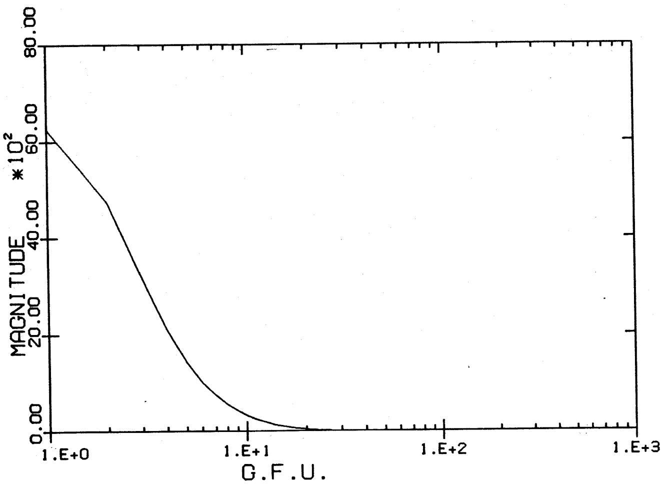

Fig. 4. Magnitude response of low-pass analytical pulse.

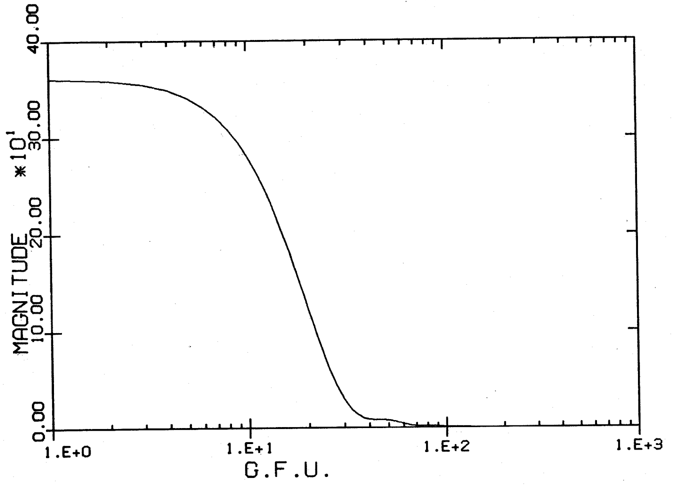

Fig. 5. Magnitude response of wide-band analytical pulse.

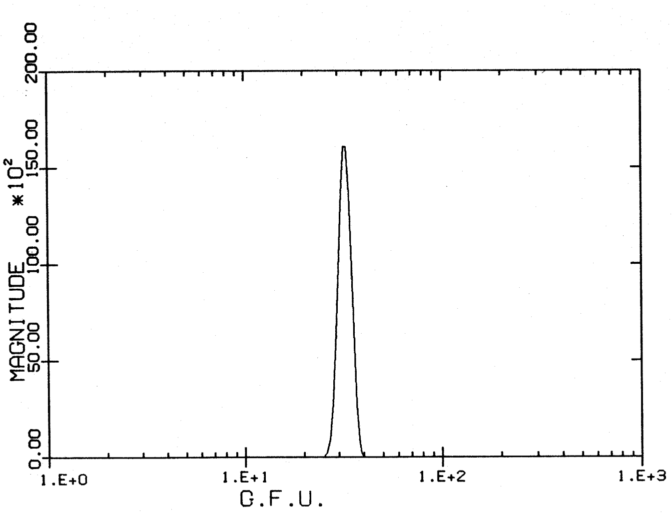

Fig. 6. Magnitude response of narrow-band analytical pulse.

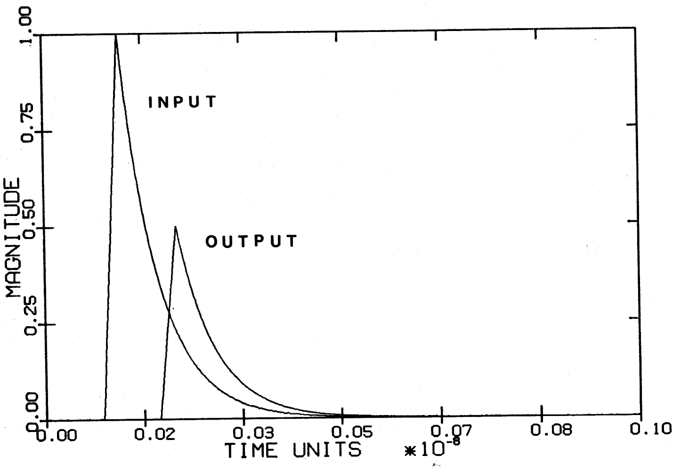

Fig. 7. Input and output waveforms with -45-dB noise.

ing magnitude spectrums $|X(j\omega)|$ are shown in Figs. 4, 5, and 6, respectively. In these figures, the time and frequency indicated on the horizontal axes are in arbitrary units (an arbitrary unit/scale factor can be applied without affecting the results of this study). The abbreviation fu (frequency unit) will be used throughout this paper to indicate the frequency's arbitrary unit. As shown in Figs. 4, 5, and 6, the significant bands for the signals spectrums are DC-20 Gfu,[2] DC-70 Gfu, and 25-40 Gfu for the low-pass, wide-band, and narrow-band signals, respectively.

III. THE EFFECT OF ACQUISITION NOISE

In this section, the effect of the acquisition noise, present in the acquired waveforms $x(t)$ and $y(t)$, on the deconvolution process is studied. The low-pass signal is used as the test signal in this study, while the acquisition noise is simulated by an additive white random Gaussian component added to both $x(t)$ and $y(t)$. In the following, the additive noise power will be expressed in decibels with respect to the signal power. In order to study its effect, various degrees of the simulated acquisition noise are added to the test signals. Three different levels of noise will be used in this study: -45, -40, and -30 dB. Figs. 7 and 8 show the noisy input and output waveforms for both the -45 and -30-dB noise levels.

Fig. 9 shows the magnitude of the deconvolved transfer function $|H_e(j\omega)|$ obtained as a result of application of the two techniques on low-pass signals with -45 dB of additive

---

[2] Gfu = 10^9 fu = 10^9 frequency unit.

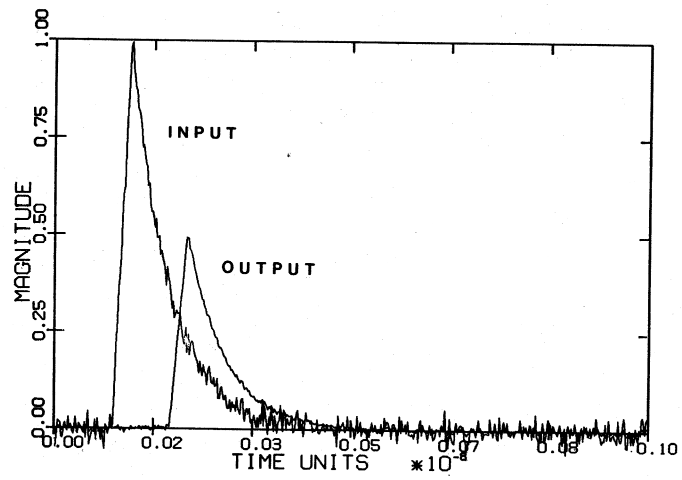

Fig. 8. Input and output waveforms with -30-dB noise.

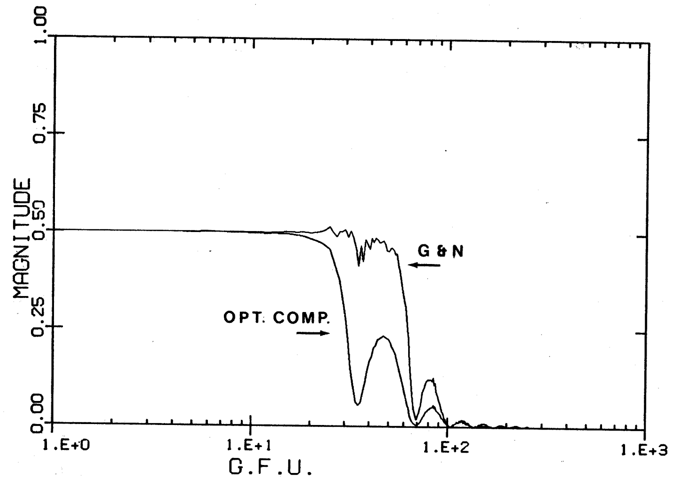

Fig. 9. Magnitude response of the adaptive filters in deconvolution of low-pass signals with -45-dB noise.

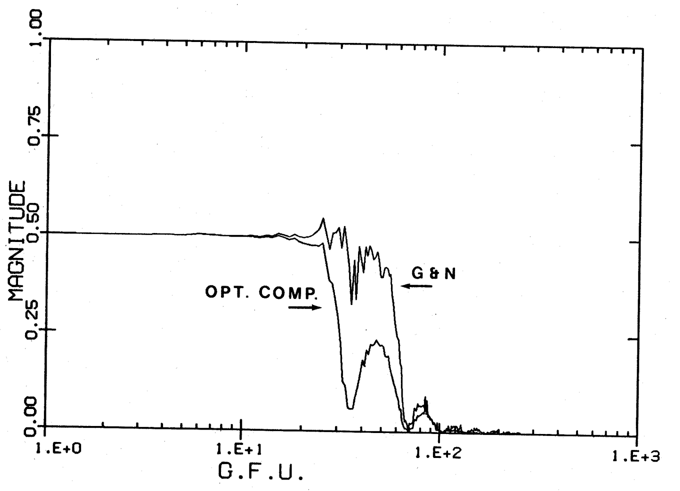

Fig. 10. Magnitude response of the adaptive filters in deconvolution of low-pass signals with -40-dB noise.

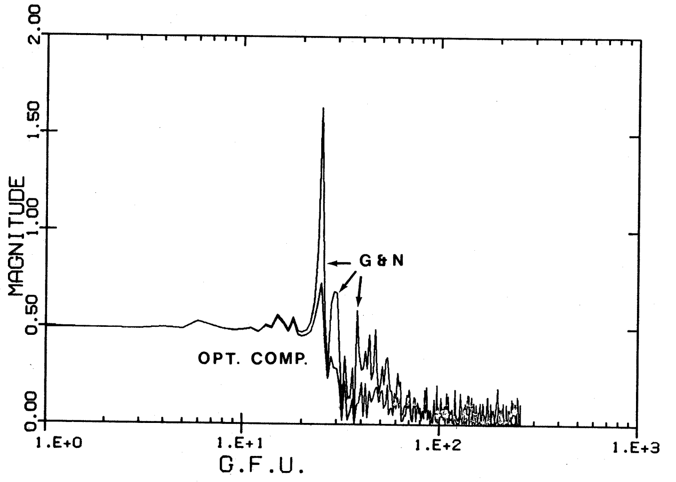

Fig. 11. Magnitude response of the adaptive filters in deconvolution of low-pass signals with -30-dB noise.

noise. The obtained $|H_e(j\omega)|$ gives an indication of the deconvolution filter's performance. By virtue of (15), $|F(j\omega)|$ is double $|H_e(j\omega)|$. From the figure, it is observed that both techniques utilize low-pass type filters with different bandwidths. The bandwidth for $F_r(j\omega)$ extends to 60 Gfu compared to 30 Gfu for $F_c(j\omega)$. This implies that $F_r(j\omega)$ is capable of yielding more accurate deconvolution results for $h_e(t)$ than those obtained using $F_c(j\omega)$. However, $F_r(j\omega)$ is expected to produce more noise in $h_e(t)$ since it displays error-noise components in the range 20 Gfu $< f <$ 60 Gfu.

Recalling from Fig. 4 that the significant band of the test signal (the low-pass $X(j\omega)$ is 20 Gfu), it is to be noticed that the optimum compensation filter has a closer matching bandwidth to that of $X(j\omega)$ as compared to the Guillaume-Nahman filter. This is due to the nature of the optimum compensation filter as presented earlier—the filter's effect is dominant at the zeros of $X(j\omega)$.

These observations are verified for deconvolution of low-pass signals with higher noise content. The low-pass signals used for obtaining transfer functions in Fig. 10 had -40 dB of noise added to them. The two transfer functions, representing the optimum filters are plotted. It is observed that the error noise present on the Guillaume-Nahman filter has increased. Fig. 11 shows the filter characteristics of the two techniques, while deconvolving low-pass signals with -30 dB of noise. With the increased noise content in $X(j\omega)$, the error noise has increased further affecting both techniques. However, it is apparent that the Guillaume-Nahman technique is more sensitive to signal noise content than the optimum compensation technique.

Another way of comparing the two filters performance is by examining their impulse responses as obtained by applying the inverse Fourier transform to $F(j\omega)$. The obtained impulse responses are shown in Figs. 12, 13, and 14 for the three cases with noise levels -45, -40, and -30 dB, respectively. Ideally, as can be seen from (3) and (10), $F(j\omega)$ should be equal to unity at all frequencies, which corresponds to a Dirac delta function for the filter's ideal impulse response.

Examining the impulse response figures, it is apparent that the Guillaume-Nahman filters contain more ringing as compared to the corresponding optimum compensation filters. This phenomenon corresponds to the larger bandwidth observed in the frequency-domain forms and discussed earlier. It is also observed that the ringing level in both sets of filters is increased with the increase of acquisition noise level.

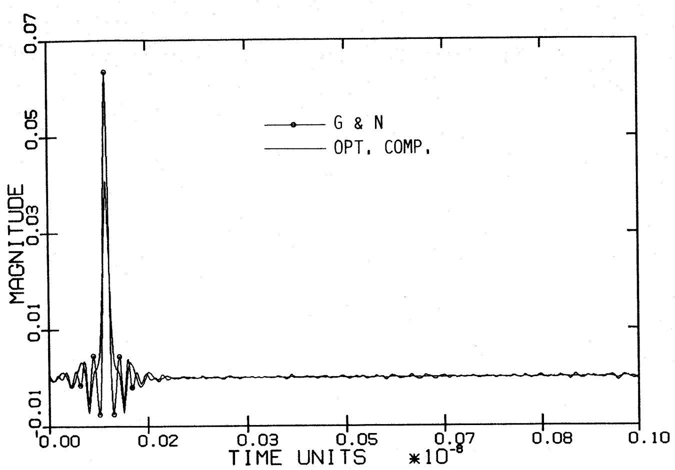

Fig. 12. Deconvolution filters' impulse response for the case of a low-pass signal with -45-dB noise.

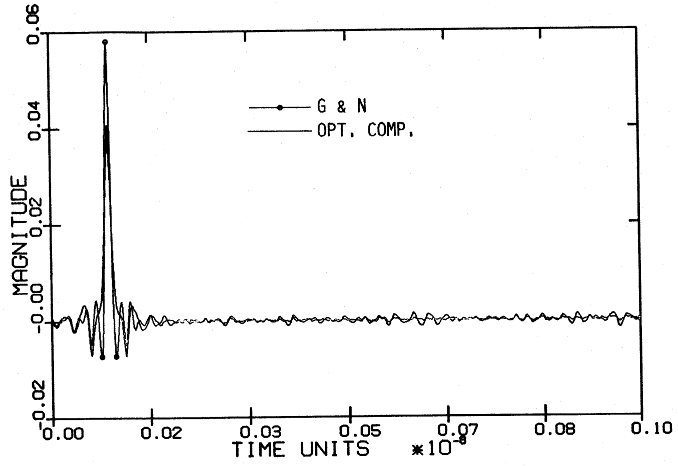

Fig. 13. Deconvolution filters' impulse response for the case of a low-pass signal with -40-dB noise.

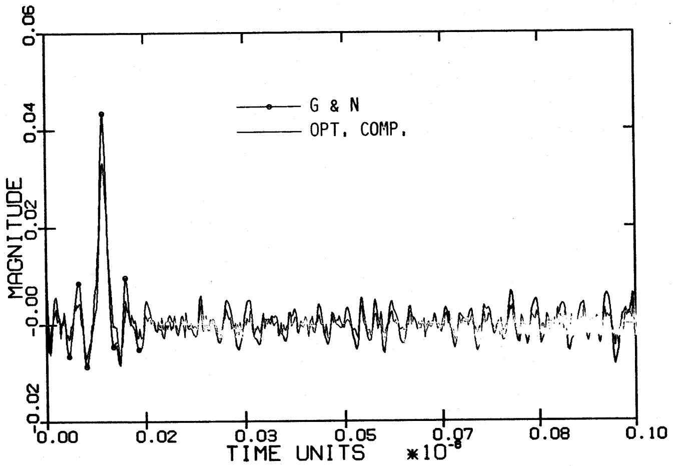

Fig. 14. Deconvolution filters' impulse response for the case of a low-pass signal with -30-dB noise.

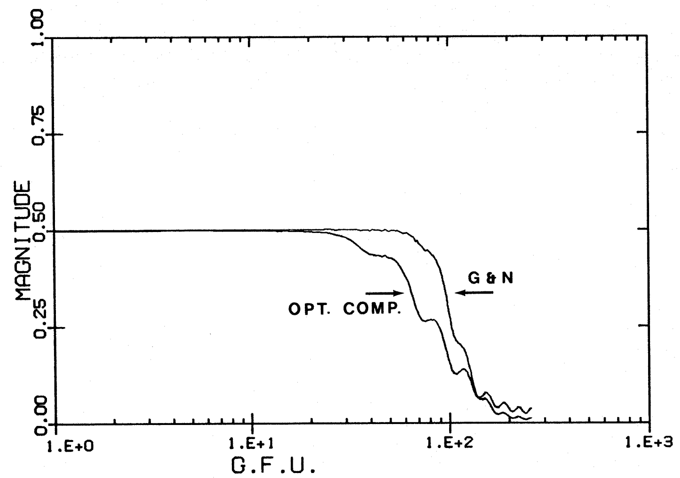

Fig. 15. Magnitude response of the adaptive filters in deconvolution of wide-band signals with -45-dB noise.

IV. The Effect of Signal Type

In this section the effect of signal type on the two deconvolution techniques is studied. The different classes of signals considered in this study are low-pass, wide-band, and narrow-band signals. The difference between the low-pass and the wide-band signals is essentially the bandwidth. In a way, comparison between the two cases is expected to show the effect of the sampling rate on the performance of the deconvolution technique. The narrow-band signal is helpful in studying the adaptive nature of the two deconvolution techniques. In order to isolate the effect of signal type on deconvolution, only signals with low noise content are considered in this study.

As discussed in the last section, Fig. 9 shows the deconvolved transfer functions obtained from the deconvolution of low-pass pulses with -45 dB additive noise using the two techniques of deconvolution. Fig. 15 shows the two transfer functions obtained by the deconvolution of the wideband pulses with -45 dB of additive noise using the two techniques. These filters are compared to the magnitude response of the input pulse, presented in Fig. 5. The $|X(j\omega)|$ becomes small only at frequencies above 30 Gfu. The optimum compensation filter starts a gradual cutoff at about the same frequency (30 Gfu), while the Guillaume-Nahman one starts the gradual cutoff at about 60 Gfu. Since $|X(j\omega)|$ never becomes extremely small, the two adaptive filters never cut off completely. Also neither of the filters shows the presence of error noise. However, the passband gain of the optimum compensation filter is smaller than the ideal 0.5. The Guillaume-Nahman technique has a wider passband and cuts off sharper. Hence, the Guillaume-Nahman technique is potentially more accurate in this case, too.

Rather interesting results are observed for the deconvolution of narrow-band signals. Fig. 16 shows the deconvolved magnitude responses for the two techniques. These are compared to the magnitude response of the input pulse, shown in Fig. 6. The nature of $|X(j\omega)|$ is narrow-band, and exists only in the band 25-40 Gfu. The adaptive filter resulting from the Guillaume-Nahman technique is still a low-pass one—cutting off at about 50 Gfu. The optimum compensation technique utilizes a bandpass filter with passband ~20-45 Gfu. Both the techniques generate stopband ripples. The difference between the two techniques' filters is striking—one uses a low-pass filter with cutoff at the highest frequency component

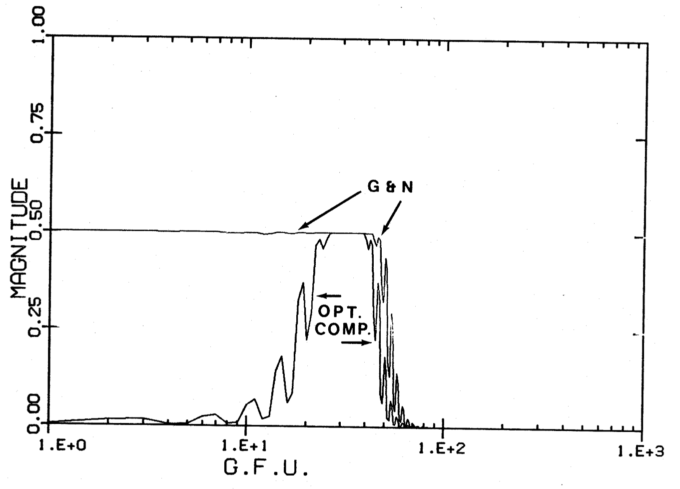

Fig. 16. Magnitude response of the adaptive filters in deconvolution of narrow-band signals with −85-dB noise.

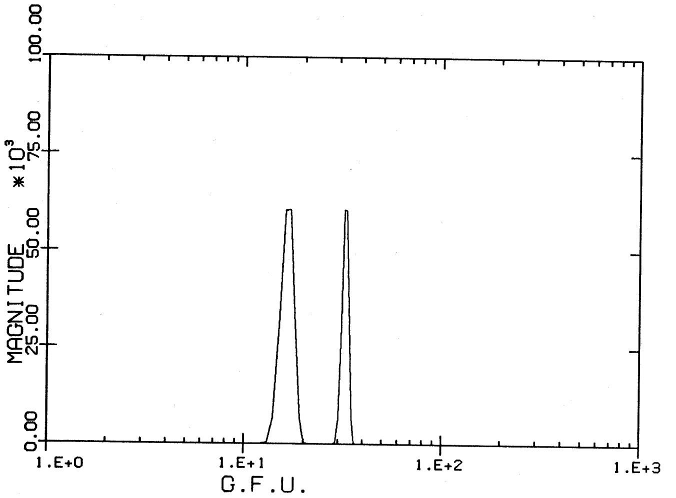

Fig. 17. Magnitude response of narrow-band analytical pulse with two bands.

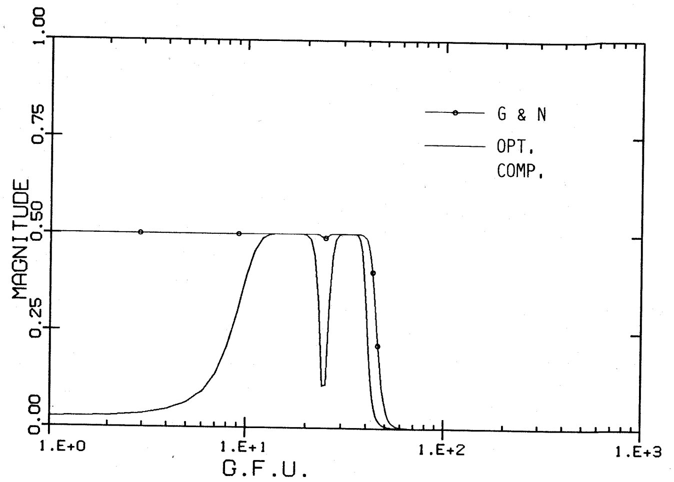

Fig. 18. Magnitude of the adaptive filters in deconvolution of the narrow-band signal with two bands.

of the signal, while the other utilizes a bandpass filter to adapt to the narrow-band signal. This difference in the adaptive nature of the filters can be anticipated and is explained in the following.

Using (11) and (12), the filters utilized in both techniques can be represented by the form

$$F(j\omega) = 1/[1 + \lambda(j\omega)/|X(j\omega)|^2] \qquad (16)$$

where $\lambda(j\omega)$ is constant for the optimum compensation technique and is a function of frequency ($\gamma\omega^4$) for the Guillaume-Nahman technique. From (16) it is clear that $F(j\omega)$ has stopbands where $\lambda(j\omega)/|X(j\omega)|^2$ is large.

In the optimum compensation technique, $\lambda(j\omega)$ is constant and hence the stopbands exist wherever $|X(j\omega)|$ is small. Consequently, it utilizes an adaptive filter of the same type as the signal, i.e., the filter is bandpass for bandpass signals and low-pass for low-pass signals, etc. Whereas the Guillaume-Nahman technique emphasizes the low-frequency components due to the ω^4 term in $\lambda(j\omega)$, this is because $\gamma\omega^4$ is very small at low frequencies resulting in $F(j\omega) \simeq 1$. As a result, it always utilizes a low-pass filter with passband extending up to the highest frequency component in $|X(j\omega)|$. This notion is further illustrated in the next experiment.

The test pulses used in this experiment have two bands, 12-20 Gfu and 30-35 Gfu, Fig. 17. The deconvolution yielded the two transfer functions shown in Fig. 18. The Guillaume-Nahman technique forms a low-pass filter extending up 50 Gfu, while the optimum compensation technique adapts to the signal and has a filter with passbands 10-22 Gfu, 25-40 Gfu.

V. SUMMARY AND CONCLUSIONS

This paper presents a performance evaluation of both the Guillaume-Nahman and the optimum compensation iterative frequency-domain deconvolution techniques. Comparisons between the two techniques are made when applied to the deconvolution of noisy low-pass, wide-band, as well as narrow-band signals. These comparisons helped demonstrate the adaptive nature of the two filters. The effect of waveform acquisition noise was studied by comparing the deconvolution results with various degrees of simulated noise.

To summarize the results of the study carried out in this paper, the following conclusions are drawn:

1) The Guillaume-Nahman technique is potentially more accurate, but more sensitive to noise, too.

2) The optimum compensation technique is more robust and can tolerate higher levels of acquisition noise.

3) The Guillaume-Nahman technique uses a low-pass filter to reduce the error-noise regardless of the signal class. Hence it cannot filter out low-frequency error-noise components which occur in the deconvolution of bandpass-type signals.

4) The optimum compensation deconvolution technique uses an adaptive filter with passbands that coincide with the frequency bands where $|X(j\omega)|$ is significant.

REFERENCES

[1] S. M. Riad, "Optical fiber impulse response evaluation using frequency domain optimal compensation deconvolution," in *Proc. FOC '80, Int. Fiber Optic and Communication Exposition* (San Francisco, CA), Sept. 1980, pp. 210-213.

[2] N. S. Nahman and M. E. Guillaume, "Deconvolution of time domain waveforms in the presence of noise," NBS Tech. Note 1047, NBS, Boulder, CO, Oct. 1981.

[3] B. Parruck and S. M. Riad, "An optimization criterion for iterative deconvolution," *IEEE Trans. Instrum. Meas.*, vol. IM-32, Mar. 1983.

[4] B. Parruck, "Study and performance evaluation of some iterative frequency domain deconvolution techniques," M.S. thesis, Virginia Polytech. Inst. State Univer., Blacksburg, VA, Mar. 1983.

[5] N. S. Nahman and M. E. Guillaume, "Some results using the Guillaume–Nahman automated deconvolution method," presented at URSI, U.S. National Radio Science Meeting (Boulder, CO), Jan. 5–7, 1983, digest paper, p. 148.

[6] B. Parruck and S. M. Riad, "Performance evaluation of frequency domain techniques," presented at URSI, U.S. National Radio Science Meeting (Boulder, CO), Jan. 5–7, 1983, digest paper, p. 149.

High-Accuracy Spectrum Analysis of Sampled Discrete Frequency Signals by Analytical Leakage Compensation

H. RENDERS, J. SCHOUKENS, AND G. VILAIN

***Abstract*—A method is presented which estimates the spectrum of a uniform sampled signal, which is sinusoidal, periodic, or composed of sinusoids of arbitrary frequencies. The proposed algorithm uses the Fast Fourier Transform algorithm. If frequency resolution is sufficient to distinguish different tones, the algorithm eliminates leakage and gives unbiased and highly accurate estimates for the amplitudes, phases, and frequencies.**

I. INTRODUCTION

ESTIMATION OF the spectrum of a sampled process is usually based on procedures employing the Fast Fourier Transform (FFT) [1]. This approach to spectrum analysis is computationally efficient but has two major disadvantages, due to the data windowing.

1) The frequency resolution is inversely proportional to the measurement time interval.

2) Leakage effects can appear. This means that the energy of the main lobe leaks into "sidelobes."

The latter can be reduced, by the selection of windows with nonuniform weighting. This, however, decreases the resolution of the spectral estimates and causes a loss of phase information.

The modeling approach to spectral estimation can make more realistic assumptions concerning the nature of the measured signal outside the measured interval, other than when assuming a cyclic signal. The Prony's Spectral Line Estimation is in this way a very appropriate method for signals composed of a finite number of sinusoids, if only a small amount of data are available.

This paper deals with a method of the last modeling type: FFT. The FFT is used as a numerical tool and leakage is eliminated, so that the frequencies, the amplitudes, and the phases are unbiasedly estimated, if the noise on the measured signals is uncorrelated.

If the unknown frequencies can not be distinguished from the FFT estimation, the use of narrow-band FFT's can extend the application of the proposed method.

The main idea of the algorithm is to solve the multifrequency problem iteratively, using a subalgorithm where the single sinusoid is identified.

II. PRELIMINARY CONSIDERATIONS

Consider a sampled multifrequency signal

$$x(k\Delta t) = \sum_{m=1}^{M} A_m \sin(2\pi f_m k\Delta t + \phi_m), \qquad k = 0, 1, 2, \cdots, N-1 \quad (1)$$

where f_m is the frequency of sinusoid m, A_m is amplitude of sinusoid m, and ϕ_m is the phase of sinusoid m.

It is assumed that the sampling frequency ($f_s = 1/\Delta t$) obeys the theorem of Shannon

$$f_s > 2f_M.$$

Using the representation

$$f_m = (L_m + \delta_m) f_0 = \lambda_m f_0 \quad (2)$$

with L_m an integer, $-0.5 \leqslant \delta_m \leqslant 0.5$, and $f_0 = 1/T\ (T = N\Delta t)$, it can be shown [2] that the Discrete Fourier Transform (DFT) of (1) at the frequency $f_i = if_0$ (with i an integer) is

$$P(i) = -0.5j \sum_{m=1}^{M} A_m \left\{ \exp(ja(\lambda_m - i) + \phi_m) \cdot \frac{\sin(\pi(\lambda_m - i))}{\sin(\pi(\lambda_m - i)/N)} - \exp(-j(a(\lambda_m + i) + \phi_m)) \cdot \frac{\sin(\pi(\lambda_m + i))}{\sin(\pi(\lambda_m + i)/N)} \right\} \quad (3)$$

Manuscript received December 15, 1982; revised March 1, 1984.

H. Renders is an Independent Researcher in Brussels, Belgium.
J. Schoukens is with the National Fund for Scientific Research, Brussels, Belgium.
G. Vilain is with the Department of General Electricity and Measurement Techniques, University of Brussels, Brussels, Belgium.

0018-9456/84/0900-0287$01.00 © 1984 IEEE

$$a = \pi(N - 1)/N.$$

Define

$$\begin{aligned} S(z) &= \sin(az) \cdot \{\sin(\pi z)/\sin(\pi z/N)\} \\ C(z) &= \cos(az) \cdot \{\sin(\pi z)/\sin(\pi z/N)\} \end{aligned} \tag{4}$$

and

$$\begin{aligned} P(i) &= U_i + jV_i \\ A_m \exp(j\phi_m) &= X_m + jY_m. \end{aligned}$$

Then equating the real and imaginary parts of (3), we obtain

$$\begin{aligned} &\sum_m \{\{C(\lambda_m - i) - C(\lambda_m + i)\} X_m \\ &\qquad - \{S(\lambda_m - i) - S(\lambda_m + i)\} Y_m\} = -2V_i \\ &\sum_m \{\{S(\lambda_m - i) + S(\lambda_m + i)\} X_m \\ &\qquad + \{C(\lambda_m - i) + C(\lambda_m + i)\} Y_m\} = 2U_i \end{aligned} \tag{5}$$

with

$$0 \leqslant i \leqslant N/2.$$

The functions C and S are a function of the frequency of the studied signal but independent of the amplitude and phase. The last information is represented in X and Y. From (5) it is possible to evaluate, by matrix inversion, the quantities X_m and Y_m which are in direct relation with A_m and ϕ_m if the frequencies are known.

III. DETERMINATION OF THE FREQUENCY, REAL, AND IMAGINARY PARTS OF A SINGLE SINUSOIDAL SIGNAL

The prime factors of interest are the estimates of X, Y, and f from the knowledge of $P(i)$. The equations given by (5) must be solved for two values of i, to ensure identifiability. So the largest two spectral lines, $P(i)$ and $P(i + 1)$, are chosen so that the signal-to-noise ratio is at a maximum there.

The following notation will be used:

$$\begin{aligned} C(\lambda - i) &= a_i \\ C(\lambda + i) &= b_i \\ S(\lambda - i) &= c_i \\ S(\lambda + i) &= d_i. \end{aligned} \tag{6}$$

A. Estimation of the Frequency

Quite often the frequency f is known *a priori*, so that the estimates of X and Y can be found by the simple inversion of (5). The problem of estimating f is treated separately, so that even in this case the same formulas for X and Y can be used.

Analytical Formulas for $i > 0$: After the elimination of X and Y in (5), (if $i > 0$) two equations remain which relate the unknown λ to V_i, U_i, V_{i+1}, and U_{i+1}. In fact, after some manipulations, they are

$$\frac{\cos ni - \cos n\lambda}{\cos n(i+1) - \cos n\lambda} \cdot \frac{\sin n(i+1)}{\sin ni} = \frac{U_{i+1} \sin n(i+1) - V_{i+1} \cos n(i+1)}{U_i \sin ni - V_i \cos ni} = \frac{V_{i+1}}{V_i} \tag{7}$$

where $n = 2\pi/N$.

A class of solutions for λ will be given by solving

$$\frac{\cos ni - \cos n\lambda}{\cos n(i+1) - \cos n\lambda} \cdot \frac{\sin n(i+1)}{\sin ni} = \frac{U_{i+1} \sin n(i+1) - V_{i+1} (\cos n(i+1) - K)}{U_i \sin ni - V_i (\cos ni - K)} \tag{8}$$

for an arbitrary value of K.

If there is no noise on the studied signals, the value of K doesn't affect the estimate of λ. This is a rather unrealistic supposition because measurements are always disturbed by measurement noise (e.g., digitalization noise). Suppose the noise $e(k\Delta t)$ is a white sequence. This is a realistic supposition if Δt is chosen to be greater than one-half the autocorrelation width (as defined in [3]) of the noise $e(t)$, which can be known from *a priori* analysis. Then it can be easily shown that the variances, σ_i^2, of all the estimates, U_i, V_i are equal, except the variance of U_0 which is twice as much.

Although the mean of the estimates of λ, which are obtained from estimates of U_i, V_i, U_{i+1}, V_i is unaffected by K, the variance σ_λ^2 strongly depends on K. It is thus obvious to minimize the variance with respect to K.

An approximation of $K_{\min}$, for which σ_λ is minimal, can be determined analytically

$$K_{\min} \simeq K_{\text{opt}} = \frac{(\sin ni)(V_{i+1} - V_i) + (\cos ni)(U_{i+1} - U_i)}{U_{i+1} - U_i}. \tag{9}$$

Analytical Formulas for $i = 0$: If less than a whole period of the sinusoid has been recorded during the measurement, the two spectral lines with greatest signal-to-noise ratio are 0 to 1. From a DFT of the signal the value of V_0 will always be equal to zero, so only three equations of (5) must be considered, the fourth being an identity.

Eliminating X and Y, the following equation relates the unknown λ to U_1, V_1, and U_0

$$V_1(1 - \cos n) + U_1 \sin n = U_0 (\sin n) \cdot \frac{1 - \cos n\lambda}{\cos n - \cos n\lambda}. \tag{10}$$

General Solution: Equations (8) and (10) can be rewritten in a more suitable form valid for $i = 0, 1, \cdots, N - 1$

$$\cos n\lambda = \frac{Z_2 \cos n(i+1) - Z_1 \cos ni}{Z_2 - Z_1}$$

with

$$Z_1 = V_i \left(\frac{K_{\text{opt}} - \cos ni}{\sin ni} \right) + U_i$$

$$Z_2 = V_{i+1}\left(\frac{K_{\mathrm{opt}} - \cos n(i+1)}{\sin n(i+1)}\right) + U_{i+1} \tag{11}$$

for $i = 0, K_{\mathrm{opt}} = 1$ which also agrees with (9).

B. Estimation of the Imaginary and Real Components

If the frequency is known, either *a priori* or from (11), different procedures can lead to reasonable estimates of X and Y. One of them is to choose the spectral line with the most information and, if $i \neq 0$, to invert (5). In this case, the variances of X and Y depend on the position of the frequency in the interval $i, i+1$ as shown in Fig. 2, (Full line 1 and 2) and also on the value of i.

If X and Y are estimated by a least-squares [5], [6] based on (5) for i and $i+1$, the dependence of the standard deviation on δ is much lower. The influence of the value of i on the standard deviation is also very low for $1 < i < N/2 - 1$.

Using the following notations, with $(P(i), P(i+1))$ the couple of largest spectral lines

$$A_M = \begin{pmatrix} a_i - b_i & d_i - c_i \\ c_i + d_i & a_i + b_i \\ a_{i+1} - b_{i+1} & d_{i+1} - c_{i+1} \\ c_{i+1} + d_{i+1} & a_{i+1} + b_{i+1} \end{pmatrix} \quad B_M = \begin{pmatrix} -2V_i \\ 2U_i \\ -2V_{i+1} \\ 2U_{i+1} \end{pmatrix}$$

$$\alpha = \begin{pmatrix} X \\ Y \end{pmatrix}. \tag{12}$$

The result of the least-squares is [6]

$$\hat{\alpha} = \{A'_M A_M\}^{-1} A'_M B_M. \tag{13}$$

For $i = 0$, a weighted least-squares will do.

Using the following definitions:

$$A_0 = \begin{pmatrix} 0 & 0 \\ (c_0 + d_0)/\sqrt{2} & (a_0 + b_0)/\sqrt{2} \\ a_1 - b_1 & d_1 - c_1 \\ c_1 + d_1 & a_1 + b_1 \end{pmatrix}$$

$$B_0 = \begin{pmatrix} 0 \\ \sqrt{2}\, U_0 \\ -2V_1 \\ 2U_1 \end{pmatrix} \tag{14}$$

the result is

$$\hat{\alpha} = \{A'_0 A_0\}^{-1} A'_0 B_0. \tag{15}$$

Both results (13) and (15), can be considered to be similar in form.

IV. EFFECT OF ADDITIVE NOISE ON THE MEASUREMENTS

A. Influence on the Estimation of λ

The solution of (11) is given by

$$\lambda = \frac{\arccos x}{n}. \tag{16}$$

Using the Taylor expansion of arc cos (x) in (16), it is possible to find the following relations:

1) The bias on λ is given by

$$B_\lambda = \frac{\sigma_\lambda^2}{\dfrac{tg\, 2\lambda(\pi/N)}{(\pi/N)}}. \tag{17}$$

This means $B_\lambda < \sigma_\lambda^2$ for $0.5 < \lambda < N/2 - 0.5$ which is negligible in a practical situation, even when the signal-to-noise ratio is relatively high.

2) The variance on λ was calculated and found to be a function of δ and the phase of the signal. The influence of the value of i turned out to be small for values of $i > 1$.

An upper limit for σ_λ is given by

$$\sigma_\lambda < \frac{1}{\sqrt{N}} \cdot \frac{\sigma_{\mathrm{noise}}}{V_{\mathrm{eff}}} \tag{18}$$

with V_{eff} the effective value of the sinusoid.

In Fig. 1, the upper and lower limits of σ_λ are plotted as a function of the frequency (full line), with

$$N = 1024$$

$$\sigma_{\mathrm{noise}} = 0.07 V_{\mathrm{eff}}.$$

These results are verified by the use of simulations. The variance on λ is shown in Fig. 1, with a dotted line and it coincides completely with the previous calculations. Fig. 1 shows that the standard deviation on the estimate of the frequency is quite uniform and very low. An exception exists for λ between 0 and 1 where no further improvement can be made if only two spectrum lines (0 and 1) are used.

B. Influence of Adaptive Noise on the Estimation of the Real and Imaginary Parts

Using the supposition of white noise, it is easy to prove the following relations [4]:

$$\sigma_U = \sigma_V = \sigma_{\mathrm{FFT}} = \sqrt{N/2} \cdot \sigma_{\mathrm{noise}} \tag{19}$$

with σ_U—the standard deviation on the real part and σ_V—the standard deviation on the imaginary part. Starting from the result obtained by the FFT algorithm, the real and imaginary parts, X and Y, are estimated.

If the frequency is known, it is possible to calculate the ratio between σ_X, σ_Y, and σ_{FFT}. The results are given in Fig. 2. The full lines 1 and 2 give the ratios $\sigma_X/\sigma_{\mathrm{FFT}}$ and $\sigma_Y/\sigma_{\mathrm{FFT}}$ if the inversion of (5) is used to calculate X and Y. The dotted line 3 gives the same ratios, if (13) is used. In the last case σ_X and σ_Y are about the same.

It was found from simulations that, if the frequency is also estimated, the standard deviations σ_X and σ_Y are less than twice σ_{FFT}.

V. SPECTRUM ANALYSIS OF THE MULTIFREQUENCY SIGNAL

The spectrum of the multifrequency signal is found by an iteration technique. Approximate values, as well as the num-

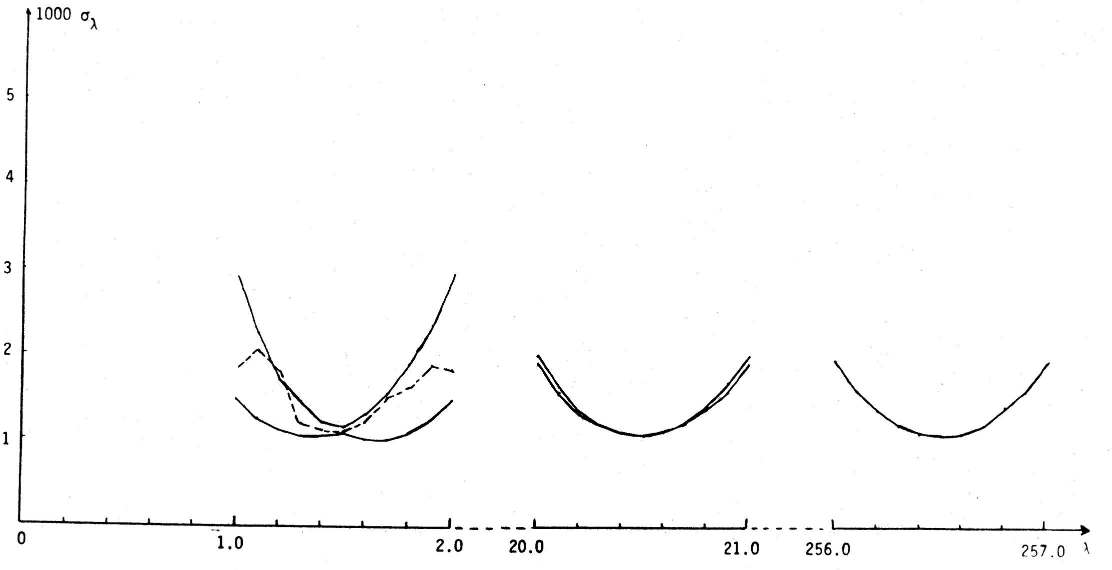

Fig. 1. Standard deviation of frequency. Full line: the upper and lower limit for σ_λ as a function of the frequency. Dotted line: result of a statistical analysis after 20 simulations at each frequency–$N = 1024$, $\sigma_{\text{noise}} = 0.07 V_{\text{eff}}$.

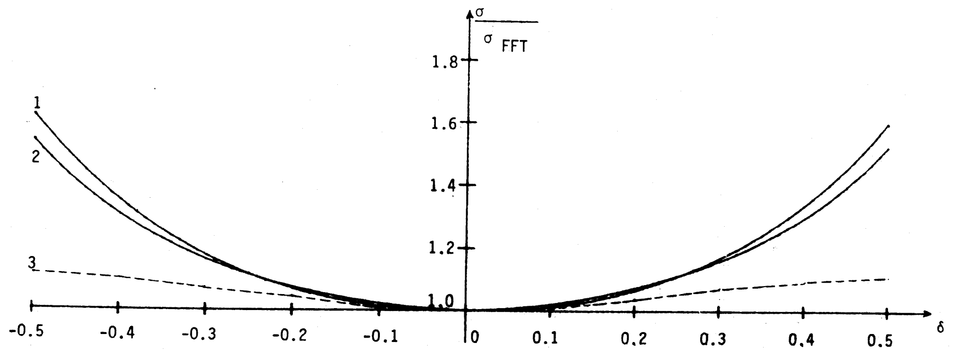

Fig. 2. Ratio of the standard deviations on real and imaginary parts and σ_{FFT} for $N = 1024$ and $i = 5$ (1: $\sigma_X/\sigma_{\text{FFT}}$, 2: $\sigma_Y/\sigma_{\text{FFT}}$ using the inversion of (5), and 3: $\sigma_X/\sigma_{\text{FFT}} = \sigma_Y/\sigma_{\text{FFT}}$ using the least-squares expressions (13) and (15)).

ber of the unknown frequencies, are detected by simple inspection of the DFT spectrum. This gives a limit on the frequency resolution. To ensure identifiability, the minimal accepted mean distance between 2 unknown spectrum lines is 3/2 times the resolution of the DFT. The principle used to find the solution of the set of nonlinear equations by iteration can be summarized as follows.

Consider a signal consisting of three sinusoids which has a DFT spectrum as shown in Fig. 3(a). The largest peak is selected and is identified first with the algorithm for a single frequency signal. This peak and its effect on the other peaks is then subtracted (Fig. 3(b)). Then the second largest peak is estimated and subtracted (Fig. 3(c)). This procedure is repeated until the last peak is processed (Fig. 3(d)). So approximate values for the frequency, amplitude, and phase are found to begin with. Consecutively, an improved estimation is done on each peak, by adding first the influence on the spectrum of a previous estimation, and then by estimating and subtracting again. This is done until convergence is reached. All calculations are only done on the three most important lines describing each peak. From those three lines, the largest couple $(P(i), P(i+1))$ is selected each time. The algorithm is quite robust and converged in all the test examples to the correct solution.

VI. EXAMPLES

Firstly, the method was tested by simulations where each experiment was repeated 100 times. The results are given in Tables I-V.

In Tables I-IV, a monofrequency signal is studied with an amplitude of 1. The noise on the time signal was generated with a uniform random generator with amplitude 0.1 ($\sigma_{\text{noise}} = 0.029$).

In Tables I and II, the following values were used:

$\lambda = 3.5$ $\quad A = 1$

$\phi = \pi/4$ $\quad \sigma_{\text{noise}} = 0.029$

while Table I gives the result if the frequency is unknown, and Table II gives the result if the frequency is known.

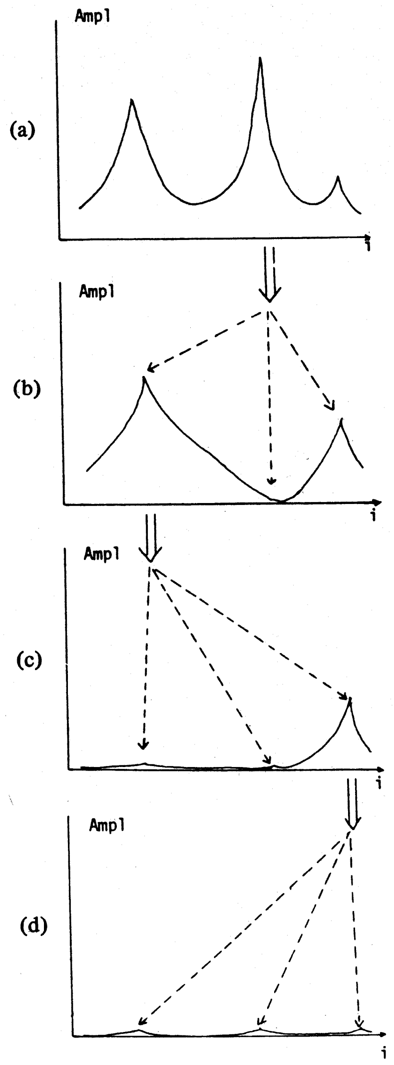

Fig. 3. Schematical representation of the iteration algorithm to solve the multifrequency problem.

TABLE I
RESULTS OF THE STATISTICAL ANALYSIS OF THE IFFT AFTER 100 SIMULATIONS

	mean	standard dev. (measured)	Δ	standard dev. (theoretical)
F	3.50008	6.1E-4	8.2E-5	6.4E-4
X	0.70728	0.0019	1.7E-4	
Y	0.70706	0.0020	3.8E-5	
A	1.00010	0.0015	1.0E-4	
ϕ	0.78525	0.0023	1.5E-4	

F unknown, $\sigma_{\text{noise}} = 0.029, F = 3.5, A = 1, \phi = \pi/4, N = 1024$

Tables III and IV give the result for

$\lambda = 0.4 \qquad A = 1$

$\phi = \pi/4 \qquad \sigma_{\text{noise}} = 0.029.$

From these results it is seen that the accuracy of the method is very high, even for a low signal-to-noise ratio. The results are also unbiased as was proven in the theory.

TABLE II
RESULTS OF THE STATISTICAL ANALYSIS OF THE IFFT AFTER 100 SIMULATIONS

	mean	standard dev. (measured)	Δ	standard dev. (theoretical)
X	0.70721	0.0016	1.0E-4	0.0014
Y	0.70723	0.0013	1.2E-4	0.0014
A	1.00016	0.0016	1.6E-4	
ϕ	0.78568	0.0014	2.8E-4	

F known *a priori*, $\sigma_{\text{noise}} = 0.029, F = 3.5, A = 1, \phi = \pi/4, N = 1024$

TABLE III
RESULTS OF THE STATISTICAL ANALYSIS OF THE IFFT AFTER 100 SIMULATIONS

	mean	standard dev. (measured)	Δ
F	0.40008	8.6E-4	8.E-5
X	0.7073	0.0032	2.E-4
Y	0.7067	0.0026	4.E-4
A	0.9999	0.0015	1.E-4
ϕ	0.7850	0.0039	4.E-4

F unknown, $\sigma_{\text{noise}} = 0.029, F = 0.4, A = 1, \phi = \pi/4, N = 1024$

TABLE IV
RESULTS OF THE STATISTICAL ANALYSIS OF THE IFFT AFTER 100 SIMULATIONS

	mean	standard dev. (measured)	Δ
X	0.7073	0.0011	2.E-4
Y	0.7067	0.0019	4.E-4
A	0.9999	0.0014	2.E-4
ϕ	0.7850	0.0016	4.E-4

F known *a priori*, $\sigma_{\text{noise}} = 0.029, F = 0.4, A = 1, \phi = \pi/4, N = 1024$

In Table V, a multifrequency signal is analyzed

$$x(t) = \sum_{i=1}^{5} A_i \sin(2\pi f_i t + \phi_i)$$

with

$$\begin{array}{lll} A_1 = 1 & \lambda_1 = 4.3 & \phi_1 = 0.20 \\ A_2 = 10 & \lambda_2 = 11.7 & \phi_2 = 0.35 \\ A_3 = 3 & \lambda_3 = 26.8 & \phi_3 = 0.70 \\ A_4 = 2 & \lambda_4 = 33.1 & \phi_4 = 1.10 \\ A_5 = 0.1 & \lambda_5 = 45.8 & \phi_5 = -0.30. \end{array}$$

The noise was generated with a uniform generator with amplitude 1.

The standard deviation of the noise ($\sigma_{\text{noise}} = 0.3$) is three times larger than the amplitude of the smallest component ($A_5 = 0.1$). The results in Table V show again that the estimates of the IFFT are unbiased. The measured and predicted standard deviations also coincide very well.

Secondly, the method was also verified by experiments. The

TABLE V
RESULTS OF THE STATISTICAL ANALYSIS OF THE IFFT AFTER 100 SIMULATIONS

	mean	standard dev. (measured)	standard dev. (theoretical)
F1	4.299	0.010	0.008
F2	11.700	0.001	0.0009
F3	26.7998	0.004	0.003
F4	33.0993	0.006	0.006
F5	45.743	0.25	0.13

	mean	standard dev. (measured)		mean	standard dev. (measured)
A1	1.0004	0.016	ϕ_1	0.202	0.03
A2	10.0020	0.015	ϕ_2	0.349	0.003
A3	3.0002	0.014	ϕ_3	-0.701	0.01
A4	2.0005	0.012	ϕ_4	1.102	0.02
A5	0.148	0.18	ϕ_5	-0.23	0.5

F unknown, $\sigma_{\text{noise}} = 0.3$, $N = 1024$ (amplitudes, frequencies and phases are given in the text)

results of the experiments coincide completely with the above-mentioned results.

VII. CONCLUSION

An algorithm has been proposed, which can be used on different practical problems, where the principal aim is to very accurately estimate the spectrum of digitized signals which can be periodic or combinations of sinusoids with arbitrary amplitudes, phases, and frequencies. An important contribution is that the estimates of the frequency are unbiased and the accuracy is analytically known from the standard deviation of the noise on the signal and from the number of measurement points. These results are independent of the unknown frequency. This is not the case with the results obtained by Jain *et al.* [2] where λ has to be greater than 20 to obtain acceptable results. Measurements of less than one period can also be handled, but with decreasing accuracy. The algorithm has been used by the authors for frequency determination, for fault localization in time domain reflectometry (TDR), for harmonic analysis, and for transfer function identification of continuous systems. It can also be used in other application fields such as astronomy, quality control of high-fidelity products, etc.

ACKNOWLEDGMENT

The authors wish to thank Prof. J. Renneboog and Dr. R. Dearnley for critical reading of the manuscript and Ir. D. Sergeant for the implementation on a microprocessor system.

REFERENCES

[1] M. K. Steven and S. L. Marple, Jr., "Spectrum analysis—A modern perspective," *Proc. IEEE*, vol. 69, no. 11, pp. 1380–1419, Nov. 1981.

[2] V. K. Jain, W. L. Collins, and D. C. Davis, "High-accuracy analog measurements via interpolated FFT," *IEEE Trans. Instrum. Meas.*, vol. IM-28, no. 2, pp. 113–122, June 1979.

[3] P. C. Kelly and W. E. Harris, "Estimation of chromatographic peaks with consideration of effects of baseline noise," *Anal. Chem.*, vol. 43, no. 10, pp. 1170–1195, Aug. 1971.

[4] A. Papoulis, *Probability Random Variables Stochastic Processes.* New York: McGraw Hill, 1965, ch. 5, pp. 116–153.

[5] H. W. Sorenson, *Parameter Estimation, Principles and Problems.* New York and Basel: Marcel Dekker, 1980, append. C, pp. 353–375.

[6] P. Eyckhoff, *System Identification, Parameter and State Estimation.* New York: Wiley, 1974, ch. 6, pp. 180–223.

Standard-Cell Intercomparison Using a Calculator-Controlled Galvanometer in an Integral-Control Feedback System

ROBERT B. FRENKEL

Abstract—**The ability of integral-control feedback to produce a zero-error steady state, in response to a step input, is exploited for the purpose of automatically nulling a galvanometer in a standard-cell intercomparison system. The precision of the null is determined by the quantization error of an analog-to-digital converter and is about ±0.1 pA. As the zero-error property of integral control is independent of gain, reducing the gain after the null is obtained can reduce system noise without affecting the null. Changes in gain are conveniently programmed into the calculator incorporated into the system. Mechanical vibration is the dominant component of the 2-nV standard error of the intercomparison.**

I. Introduction

The MANUAL intercomparison of the electromotive force (emf) of standard cells to high precision has been a frequent, routine, and exacting procedure in standards laboratories. Several of these have therefore investigated and developed automatic intercomparison systems [1]-[5].

The difference in emf of any two standard cells at the same nominal temperature is usually less than 100 μV, and may approach 1 mV when their respective temperatures are near opposite extremes of the useful range, 20-37°C. The circuit for measuring these differences contains essentially three components in series: the pair of cells connected back-to-back, a low-voltage source which is variable within the expected range of the emf differences and which is normally the output of a potentiometer, and a null detector. In manual intercomparison, the potentiometer output is manually adjusted until the detector is nulled. As this nulling is the most tedious part of the measurement, automating it is desirable and is the subject of this paper.

In the present feedback system, the null detector, a moving-coil galvanometer, sends information on its coil deflection to a desk-top calculator, which accordingly adjusts the output of the potentiometer to control the coil deflection. The potentiometer output has a range of about ±100 μV. A calculator in a feedback system offers a wealth of possibilities, since a great variety of desired dynamics can be imparted to the controlled unit, in this case the galvanometer coil, by programming, a much simpler technique than wholly analog feedback systems permit.

Since the ideal steady-state coil current is exactly zero, in response to a step-voltage input, integral-control is the natural type of feedback to consider. The feasibility of its application to automated standard-cell intercomparisons has been examined in the prototype system to be described. Integral-control produces a coil movement which in the absence of mechanical vibration ceases in about 6 s at a steady state corresponding to about 0.1 pA, set by the quantization error of an analog-to-digital converter (ADC). In effect, the integral-control sets the potentiometer output equal to the unknown emf difference, thereby automatically nulling the galvanometer. Since the resistance of a pair of standard cells is of the order of 1000 Ω, the small null current offers subnanovolt precision in the measurement of their emf difference. The vibration normally affecting the galvanometer in the present system limits the standard error of each comparison to a typical 2 nV. A single galvanometer with display screen may be used, even though its damping may be much greater than the effective damping of the two-galvanometer combination (an amplifying and a display galvanometer) commonly used in manual high-precision dc measurements.

At null, the smallness of the cell current, and its independence of the emf difference measured, are attractive and simplifying features of integral control. In systems where the emf difference is the input to an electronic low-noise high-impedance (~50 MΩ) dc amplifier, a voltage offset must be generated in series with the cells in order to ensure a small steady-state cell current, and both the voltage offset and the amplifier gain must be known with some accuracy in order that the cell emf difference may be deduced. A further advantage of integral-control is that the precision of the null is independent of loop gain. The loop gain can therefore be set high initially so that null is approached relatively quickly, and can then be reduced without degrading the precision of the null. The gain reduction maintains stability during the period of longer sampling intervals when the digital voltmeter (DVM) is taking readings, and decreases the readout noise. On the other hand, integral control, as used here, with a moving-coil galvanometer is slower than the above-mentioned dc amplifier systems. The total time for one measurement of emf difference, from initial reading of galvanometer zero to final calculator print-out, varies from 20 to 40 s. However, when all the emf differences during a run of measurements vary slightly near a high constant value, as for example when the comparisons are between cells at two different nominal temperatures, nulling can be speeded up if this value is the programmed initial output of the potentiometer as an offset in series with the cells. There is no need to know this

Manuscript received February 28, 1983; revised March 12, 1984.

The author is with CSIRO Division of Applied Physics, Sydney, Australia 2070.

0018-9456/84/0900-0293$01.00 © 1984 IEEE

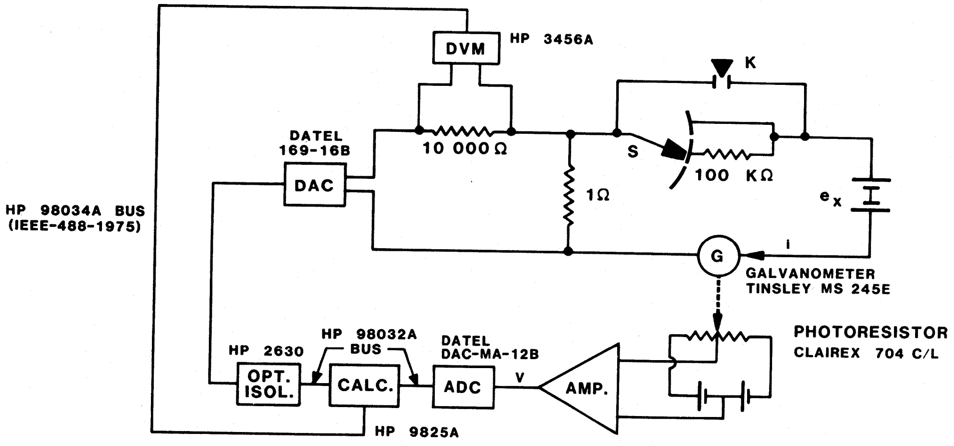

Fig. 1. Adaptation of the Lindeck-type potentiometer.

offset value with any accuracy, and of course it will also serve to reduce the transient cell current during the approach to null.

II. Description of System

Fig. 1 shows the Lindeck-type potentiometer adapted for the present purpose. In manual intercomparison of a pair of standard cells, the coil deflection of the galvanometer G is nulled by manually adjusting the input voltage to the voltage divider, consisting here of the 10 000:1-Ω ratio. The unknown standard-cell difference e_x, together with any thermal emf, is then equal to the voltage across the 10 000-Ω resistor, easily measured, since it is generally well above the millivolt level, multiplied by the known 1:10 000-Ω ratio. This method has the advantage that e_x is multiplied by the simple ratio of two resistors, each of which is provided with externally accessible current and potential terminals (not shown in Fig. 1), has a known temperature coefficient, and can therefore be regularly and conveniently recalibrated to fix the multiplication ratio within about 10 ppm.

In the present automatic system, the galvanometer is a modified unit [6] whose lamp is masked so as to project a narrow (2 mm) vertical strip of light onto its screen, on which a dc-energized center-tapped photoresistor is mounted and connected as a bridge. In steady state, the amplified bridge output voltage V is proportional to the galvanometer current i for a range of about ±1 nA. A 12-bit ADC digitizes the voltage V for delivery to the calculator, which provides a 16-bit output via a set of optical isolators to the digital-to-analog converter (DAC). The DAC input is determined by the history of ADC inputs according to the strategy of integral control. The manual make-before-break switch S engages a protective 100-kΩ resistor for initial coarse nulling, a precise final null being obtained with the low-thermal key K in circuit. The digital data from the ADC to the calculator and from the calculator to the optical isolators are transferred along a 16-bit interface cable, which also carries the calculator signal that initiates analog-to-digital conversion. After a final null has been reached, a signal from the calculator to the DVM, over an IEEE-488 interface bus, instructs the DVM to take readings of the voltage across the 10 000-Ω resistor. 25 DVM readings are generally sufficient, and the calculator evaluates the mean of these. As the DVM accuracy exceeds 10 μV, the attainable accuracy in the measurement of the standard-cell emf difference exceeds 1 nV.

Apart from the very strict temperature control of the cells (within ±0.0001°C, necessary in view of their temperature coefficient near −50 μV/°C), strict control of the ambient (within about ±0.2°C or so) is essential in two respects. First, it makes possible the necessary high stability of the galvanometer zero. When the system is thermally stabilized, the drift of the zero is equivalent to less than about 10 pA in an hour. Since the zero level is determined afresh before each measurement, as described below, errors due to drift of the zero are rendered negligible. Secondly, it stabilizes the thermal emf's in the low-voltage part of the circuit, including the key K. A run of measurements always follows an experimental design in which half of the readings are on forward polarity and the other half on reverse polarity, that is with the leads to the cells reversed. Polarity reversal, a standard procedure in high-precision dc measurements, both measures the net thermal emf, in this case a few tenths of a microvolt, and eliminates it as a systematic error from the final results. A similar, normally lesser systematic error, can arise as an effect of earth leakage in the low-voltage part of the circuit and is also eliminated by polarity reversal.

III. Application of Integral Control

Fig. 2 shows the flow diagram of the program stored in the calculator. This program contains a loop, at each traversal of which the calculator initiates analog-to-digital conversion by means of a signal to the ADC. The ADC samples the galvanometer coil deflection every 20 ms approximately. The first loop traversal (or first set of traversals) is used to measure the galvanometer zero, Z V, while on subsequent traversals the variable position V volts is measured, so that the deflection is $(V - Z)$ V. During each of these subsequent traversals the DAC is instructed by the program to produce the voltage $V_{\mathrm{DAC}} = K(V - Z) + K\alpha\Sigma(V - Z)$, where the first term is a proportional-control term to ensure stable feedback, the second is the integral-control term with integral-control factor α, and K is a gain figure. A suitable practical value for α is 0.02.

Initially the switch S (Fig. 1) is set at the off position and the average Z is measured over a set of loop traversals. Then

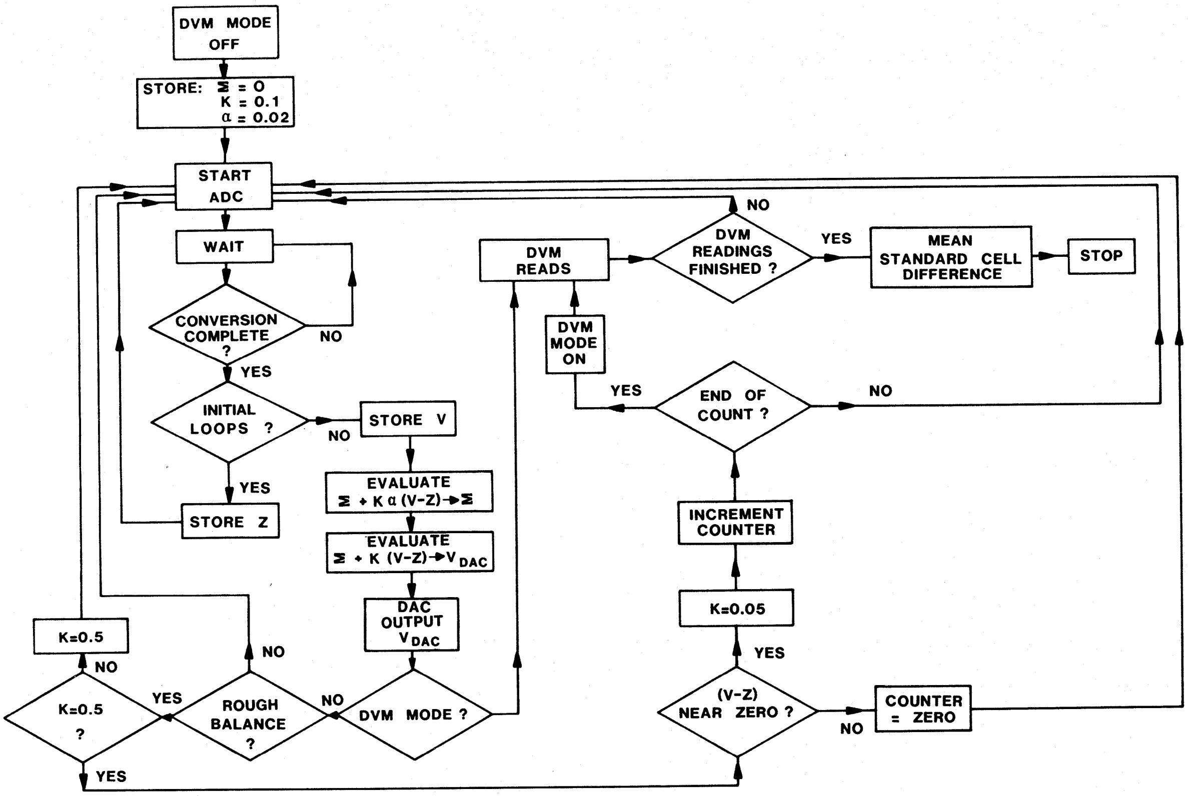

Fig. 2. Flow diagram of control program.

integral control is initiated, by manually pressing the appropriately programmed function key of the calculator, S is set at the 100-kΩ position and a coarse null is reached in about 2-3 s with $K = 0.1$. For a cell emf difference of 50 μV, the galvanometer current is about 30 pA at 3 s. S is then set to the shorting position, the low-thermal key is closed, and the gain K is increased to 0.5. When $(V - Z)$ has reached near zero (in practice, corresponding to a deflection equivalent to about 0.6 pA) K is reduced to 0.05 and a counter is initiated. The counter is incremented each time the measured deflection is near zero and is reset each time the measured deflection exceeds this bound. When the counter reaches a preset value the steady-state deflection has therefore been near zero. The DVM is now instructed to take a number of readings, the interval between successive readings and hence the sampling interval being 170 ms. Feedback stability, which is discussed in Section IV, is still assured in spite of this longer sampling interval, since the gain has been reduced.

IV. System Response

The essential function of the calculator is to provide an output voltage sequence $\{y_k\}$ from the DAC in response to the input sequence $\{x_k\}$ to the ADC in accordance with the relation

$$y_k = K\left(x_k + \alpha \sum_{j=0}^{k} x_j\right) \tag{1}$$

where the x_j, y_k occur at times jT, kT, respectively, T being the sampling interval. $\{x_k\}$ represents the sequence of samples of V, and $\{y_k\}$ the sequence of samples of V_{DAC}. The effect of α is to produce a steady state in which the inputs x_j, and hence the deflection of the galvanometer coil, are as close to zero as the resolution of the ADC permits. The 12-bit ADC has a ± 5-V input range, so that its resolution is 5 V/2^{11} = 2.44 mV. The amplifier in Fig. 1 provides an output voltage V, in response to a steady galvanometer current i, given by $V = iR_m$ with $R_m = 1.25 \times 10^{10}$ Ω. The ADC resolution is therefore equivalent to a steady-state current error of magnitude about ± 0.1 pA.

It may be shown that in terms of the variable $z = e^{sT}$, where s is the complex angular frequency, (1) implies a pulse transfer function $D(z)$ of the ADC-calculator-DAC system given by $D(z) = KC(z)$ where

$$C(z) = (\beta z - 1)/(z - 1) \tag{2}$$

and $\beta = 1 + \alpha$. The relation between the output transform $Y(z)$ and the input transform $X(z)$ is therefore

$$Y(z) = D(z)\, X(z) = KC(z)\, X(z). \tag{3}$$

The output of the DAC is held constant between successive samples, so that $D(z)$ may be considered followed by a zero-order hold with transfer function $(1 - e^{-sT})/s$. The calculator program provides an output sequence delayed by a time γT $(0 < \gamma < 1)$ with respect to the input sequence, so that a transfer function $e^{-\gamma sT}$ is included. We define $R(s)$ to be the transfer function of the galvanometer-photoresistor combination, $r = 1$ Ω and R_1 = 10 000 Ω are the resistors dividing the DAC output, and R' is the combined resistance of the galvanometer coil (about 500 Ω), standard cells, and any protective resistor. $g = r/(R'R_1 + R_1 r + R'r) \approx r/R'R_1$ is therefore the factor by

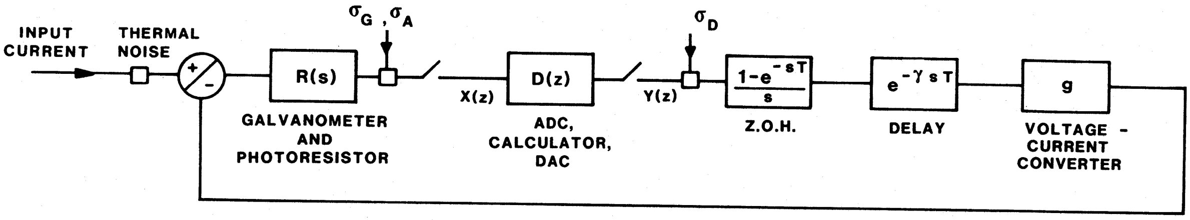

Fig. 3. Block diagram of feedback loop, including noise sources.

which the DAC output voltage is multiplied to give the steady-state current into the galvanometer coil. For $R' = 1500\ \Omega$, $g \sim 6.7 \times 10^{-8}\ \Omega^{-1}$, and for $R' = 100\ \text{k}\Omega$, $g \sim 10^{-9}\ \Omega^{-1}$. The feedback system can now be adequately represented by the block diagram in Fig. 3, in which $X(z)$ and $Y(z)$ describe the sample sequences at the input and output, respectively, of the ADC-calculator-DAC system. Fig. 3 also shows noise sources, to be discussed in Section V.

An approximate expression for $R(s)$ is derived as follows. If J is the moment of inertia of the coil, N the flux linkage through it, b a mechanical damping constant, and c the suspension torque constant, the angular deflection θ of the coil in response to an input current i is given by

$$J\ddot{\theta} + (b + N^2/R_0)\dot{\theta} + c\theta = Ni. \tag{4}$$

R_0 is the parallel combination of R' and a 100-kΩ shunt resistor permanently connected internally to the galvanometer terminals, to provide a convenient amount of damping when the galvanometer is disconnected from an external circuit.

The conductivity of the photoresistor when illuminated rises with a time constant t_L, and when it is darkened drops with a time-constant t_D, with $t_L \sim 3t_D$ under the present conditions where the illumination of the photoresistor by the galvanometer lamp is about 1 lux. The inequality of t_L and t_D complicates the analysis, but it may be shown that for small deflections of the coil the photoresistive-bridge output voltage V obeys an effective time-constant t_p given by $t_p = 2t_Lt_D/(t_L + t_D)$. As observed experimentally, a sinusoidal oscillation of the galvanometer coil produces an approximately sinusoidal oscillation of V. For a fixed amplitude of coil oscillation, the observed variation of the amplitude of V with frequency is consistent with an effective time-constant t_p, and this consistency holds for larger deflections, comparable to the width of the light-slit on the galvanometer screen. We may therefore write

$$V + t_p\dot{V} = M\theta \tag{5}$$

where M is an amplification factor in volts/radian. In the present case $t_p \sim 80$ ms.

In terms of the galvanometer critical damping resistance R_c, about 72 000 Ω, sensitivity S (in radians of coil deflection per amp, so that $R_m = MS$) and galvanometer open-circuit time-constant τ, 2.5 s, the constants in (4) may be written

$$\begin{aligned} J &= R_c\tau^3/4\pi^3S^2 \\ N &= R_c\tau/\pi S \\ c &= R_c\tau/\pi S^2 \end{aligned} \tag{6}$$

assuming that $b \ll N^2/R_0$. Since $R_m = MS$, the transfer function for the galvanometer-photoresistor combination can then be written

$$R(s) = 4\pi^2R_m/[(1 + t_ps)(4\pi^2 + 4\pi R_c\tau s/R_0 + \tau^2s^2)]. \tag{7}$$

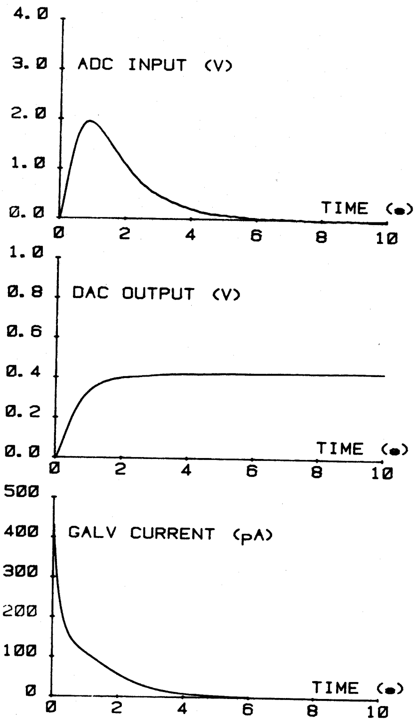

Fig. 4. System response during approach to null, with $R' = 100$ kΩ and applied emf difference $e_x = 43\ \mu$V.

Fig. 3 may now be analyzed using conventional sampled-data techniques to give the overall loop transfer function and therefore the responses $\{x_k\}$ and $\{y_k\}$ at the sampling instants. This procedure is outlined in Appendix I. The system is reliably stable for each stage of the galvanometer nulling, as indicated in the following table by the available phase and gain margins. Gain margin is calculated as $(1/m) - 1$, where m is the open-loop gain magnitude at 180° phase shift.

Stage	R'	T	γ	K	PM	GM
Approach to null	100 kΩ	20 ms	0.5	0.1	60°	4
High sensitivity	~1500 Ω	20 ms	0.5	0.5	35°	3.3
DVM readout	~1500 Ω	170 ms	0.12	0.05	70°	10

Fig. 4(a) and (b) shows, respectively, the experimentally observed sequences $\{x_k\}$ and $\{y_k\}$, plotted as smooth functions of time $V(t)$ and $V_{\text{DAC}}(t)$, during the approach to null, with $K = 0.1$, $R' = 100$ kΩ, and an applied emf difference $e_x = 43\ \mu$V. $V(t)$ has a peak value $V_0 = 2.0$ V at time $t_0 = 1.0$ s, followed by a decay with time-constant $t_d = 1.7$ s. Fig. 4(c) shows the galvanometer current $i(t)$, deduced from the relation (using the approximation $R', R_1 \gg r$)

$$i(t) = (1/R')\{e_x - V_{\mathrm{DAC}}(t)\,(r/R_1) - (R_c\tau/\pi R_m)\,(\dot{V}(t) + t_p\ddot{V}(t))\} \tag{8}$$

where the third term on the right is the induced coil voltage $N\dot{\theta}$. The current drops to one-third of its initial value in about 0.6 s.

During the approach to null the two smallest roots of the system are the galvanometer roots $4\pi R_c/R_0\tau = 7.2$ s^{-1} and $\pi R_0/R_c\tau = 0.9$ s^{-1}. A useful estimation of the response is therefore possible neglecting t_p and assuming a continuous system with $\sum_j x_j$ in (1) replaced by $(1/T)\int^t V(t')\,dt'$. The deflection of the galvanometer coil is then described by

$$J\ddot{\theta} + (N^2/R_0)\dot{\theta} + c\theta = (N/R')(e_x - V_{\mathrm{DAC}}(t)(r/R_1)) \tag{9}$$

and combining (9) with the relations (6) and

$$V(t) = M\theta(t) \tag{10}$$

and

$$V_{\mathrm{DAC}}(t) = KV(t) + (K\alpha/T)\int^t V(t')\,dt' \tag{11}$$

we obtain for the voltage $V(t)$ at the input to the ADC

$$\ddot{V}/\omega_0^2 + (2R_c/\omega_0 R_0)\dot{V} + (1 + KA)V + (KA\alpha/T)\int^t V dt' = e_x AR_1/r \tag{12}$$

where $A = gR_m$ and $\omega_0 = 2\pi/\tau$.

Solving this third-order equation gives values of V_0, t_0, and t_d which differ from the observed values by 1, 1, and 7 percent, respectively. Some further insight into the dynamics may be obtained by noting that the initial rise of $V(t)$ to V_0 is governed by the first three left-hand terms in (12), the contribution of the fourth being small during this period. These three terms constitute a second-order equation whose coefficients have numerical values giving near-critical damping. After $V(t)$ has passed its peak, a rough measure, within 10 percent, of t_d may be obtained from (12) by noting that during this period the dominant left-hand terms in (12) are the third and fourth, so that neglecting the first two and differentiating gives

$$\dot{V}(1 + KA) + KA\alpha V/T = 0 \tag{13}$$

implying a decay time-constant t_d given by

$$t_d = (T/\alpha)(1 + KA)/KA. \tag{14}$$

V. LIMITATIONS DUE TO SYSTEM NOISE

The DAC output voltage is contaminated by noise, whose three main sources are considered here for the period after balance has been reached and the DVM is taking readings. They enter the feedback loop at the points shown in Fig. 3 and are: a) thermal-agitation noise, dominated by the current noise with spectral density $4kT'/R'$ A^{2}Hz^{-1} in the galvanometer series resistance R' (k and T' being, respectively, Boltzmann's constant and the absolute temperature); b) vibration of the galvanometer mount, producing relative motion of coil and photoresistor and hence an effective noise voltage rms value σ_G volts at the input to the ADC; and c) quantization noise of the ADC and DAC, represented by rms values σ_A and σ_D, respectively. The resultant noise voltages appearing at the sampling instants at the DAC output are evaluated by numerical integration using the noise variance integrals given in Appendix II, and are stated here for $T = 170$ ms, $\gamma = 0.12$, $K = 0.05$, and $R' = 1500\ \Omega$. Closed-form approximate expressions are also given here, obtained by neglecting t_p and using the fact that now $R' \ll R_c$.

A. Thermal Noise

Its rms value, denoted by $\sqrt{|V_T^2|}$ and obtained by numerical integration of (A15), is 16 μV and varies roughly as the square root of the gain K. The closed-form approximation to (A15) predicts a value differing by about 6 percent and is

$$\sqrt{|V_T^2|} = R_m(KkT'/R_c\tau A)^{1/2}(1 + u) \tag{15}$$

where the correction term $u = \pi KAR'T/4R_c\tau$ is about 0.047.

The equivalent rms noise in the measured standard-cell emf difference is therefore about 1.6 nV.

B. Vibration Noise

In the present case, the input spectrum extended mainly from 10 to 150 Hz with several peaks, including one at 24 Hz (the effect of 1440 rev/min air-conditioning plant in the building), and another at 100 Hz. The amplitude at any particular frequency varied from one time to another. The sampling interval $T = 170$ ms gives a folding frequency $1/2T$ of about 3 Hz, so that to a rough approximation the sampled spectrum may be taken as white. Numerical integration of (A16) shows that the rms value of vibration noise $\sqrt{|V_G^2|}$ is roughly proportional to K for a constant σ_G. The closed-form approximation to (A16) is

$$\sqrt{|V_G^2|} = \sigma_G K(1 + u). \tag{16}$$

Where vibration noise dominates the other sources, as in the present case, reducing the gain therefore significantly reduces the net noise at the DAC output.

C. Quantization Noise

The quantization steps of 2.44 mV in the ADC output are a possible source of noise in the DAC output. The DAC input is another possible source of quantization noise, since numbers are stored in the calculator to 12-decimal-digit precision, yet must be coarsened to 15 bits plus sign for delivery to the 16-bit DAC. The quantization steps of the DAC, which has a ± 5-V output range, are 5 V/2^{15} = 153 μV.

When the quantization steps q of a digitizer are fine enough to satisfy $q < 1/2f_0$, where f_0 is the highest frequency (in volts^{-1}) contained in the spectrum of the probability density function $w(V)$ of the digitizer input voltage V, the quantization noise is white (confined in magnitude within $\pm q/2$) with variance $q^2/12$. This figure for the variance can therefore be used with high confidence when the digitizer input varies over several quantization levels. Moreover, as discussed by Widrow [7], the requirement regarding the fineness of q can be considerably relaxed without materially affecting the variance. Thus for Gaussian signals whose variance σ^2 is small enough to satisfy $\sigma = q/3$, the noise variance differs from $q^2/12$ by only 13 percent. In the following analysis, the noise at the DAC output will be evaluated on the assumptions that i) the quantization noise from each of the two sources is white with variance $q^2/12$, and ii) the only other source of noise is thermal. It will then be shown that i) and ii) are mutually inconsistent, even when accepting the above relaxed requirement, and that the $q^2/12$ result for both digitizers is valid only when there is additional extraneous noise such as vibration.

We therefore assume white noise from the ADC with $\sigma_A = 2.44/\sqrt{12} = 0.704$ mV. The rms noise voltage $\sqrt{|\overline{V_A^2}|}$ at the DAC output from this source is then given by (A17). Numerical integration of (A17) yields the rms value 38 μV at the DAC output, or an equivalent 3.8-nV rms noise in the measured standard-cell difference. The approximate expression for $\sqrt{|\overline{V_A^2}|}$ is

$$\sqrt{|\overline{V_A^2}|} = \sigma_A K (1 + u). \tag{17}$$

Similarly, if σ_D is assumed to be $153/\sqrt{12} = 44.2\,\mu$V of white noise, the rms noise voltage $\sqrt{|\overline{V_D^2}|}$ at the DAC output from this source is obtained by numerical integration of (A18) and is 46 μV (4.6 nV equivalent). This noise is roughly independent of the gain K. The approximate expression for $\sqrt{|\overline{V_D^2}|}$ is

$$\sqrt{|\overline{V_D^2}|} = \sigma_D (1 + u). \tag{18}$$

The root-sum-square noise at the DAC output, on the above two assumptions, would therefore be $\sqrt{(16^2 + 38^2 + 46^2)}$ or about 62 μV (6.2 nV standard-cell equivalent).

We now estimate the combined input noise to the ADC from the thermal source and from the calculator-DAC source. The rms noise value at the ADC input from the thermal source may be roughly evaluated by noting that since the thermal source rms value at the DAC output is 16 μV as found above, the thermal noise at the ADC input is about $\sqrt{|\overline{W_T^2}|} = 16\,\mu\text{V}/K$ or about 0.3 mV for $K = 0.05$.

The contribution from the calculator-DAC source has a variance given by (A19) and its rms value may be approximately written as

$$\sqrt{|\overline{W_D^2}|} = \sigma_D (\pi A R' T / 2 K R_c \tau)^{1/2}. \tag{19}$$

The rms value given by (19) is also about 0.3 mV. Thus the combined effect at the ADC input of thermal noise and calculator-DAC noise amounts to no more than about 0.4 mV, or one-sixth of an ADC quantization step. This magnitude fails to meet the relaxed requirement by a factor of two, and the assumption that the ADC generates white quantization noise with variance $q^2/12$ is clearly untenable when extraneous noise such as vibration is excluded. In general, with an n_A-bit ADC and an n_D-bit DAC, it may be shown that unless there is extraneous noise, there is no combination of n_A and n_D which gives white noise with variance $q^2/12$ from both sources. However, a small amount of vibration will suffice to produce quantization noise with approximate variance $q^2/12$ from the digitizers. For $K = 0.05$ this amount is about 0.7 mV rms. The net rms noise at the DAC output will then be about 71 μV (7 nV equivalent).

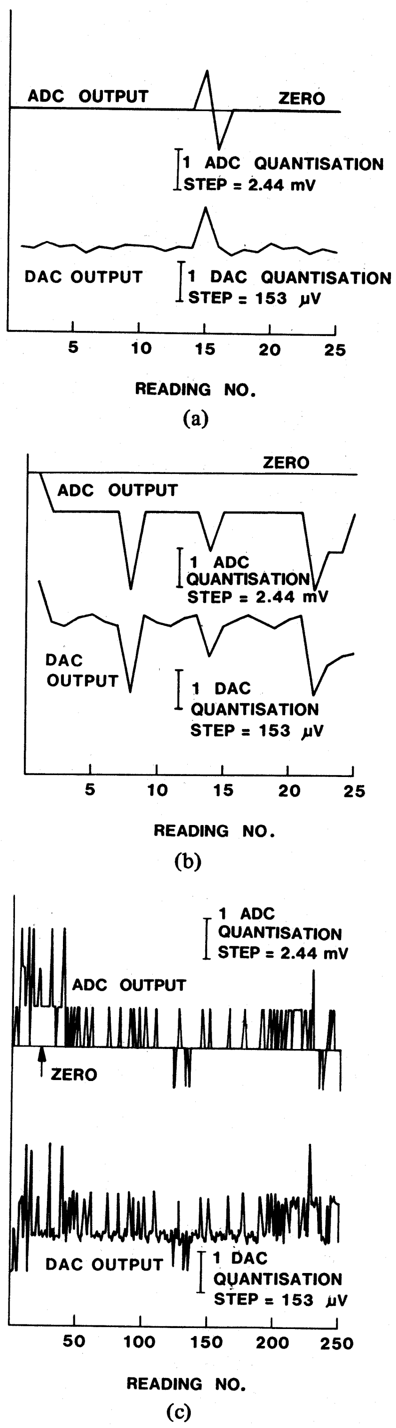

Fig. 5. Examples of noise observed at the ADC and DAC outputs during DVM readout time.

Fig. 5(a) and (b) show, respectively, the noise observed at the sampling instants over an exceptional run of 25 DVM readings (lasting about 4 s), and over a more typical run of the same duration. A prolonged run of 250 readings (about 40 s) is shown in Fig. 5(c). The galvanometer was screened to some extent from vibration by an isolation table. In each figure the upper record is the output of the ADC as recorded by the calculator, and the lower record is the output of the DAC as measured by the DVM. These are generally highly correlated, the ratio of their two standard deviations being of course approximately the gain K. The standard deviations of the DVM readings are 35 μV in Fig. 5(a), 104 μV in Fig. 5(b), and 90 μV in Fig. 5(c), showing that vibration was negligible in the first case only. The initial zero of the galvanometer is shown on the ADC record in each case, and implies an effective direct current at null of: 0.0 pA in Fig. 5(a), -0.2 pA in Fig. 5(b), and +0.1 pA in Fig. 5(c). The standard error of the mean of the 25 readings in each of Fig. 5(a) and (b), referred to the measured standard cell emfs, is 0.7 nV in Fig. 5(a) and 2.1 nV in Fig. 5(b).

VI. CONCLUSION

Integral control, which independently of gain produces zero steady-state error in a feedback system, can be used for standard-cell intercomparisons to null a galvanometer automatically. The dominant component of the typical 2-nV standard error observed is mechanical vibration, which in turn gives rise to $q^2/12$ quantization noise from the digitizers. A higher degree of mechanical isolation should therefore reduce the standard error to very low levels.

APPENDIX
DERIVATION OF THE PULSE TRANSFER FUNCTION

To derive the pulse transfer function (PTF) for the system shown in Fig. 3, we define the following dimensionless quantities, noting that in the case $R' > R_c$, which arises when high-valued protective resistors are in series with the galvanometer, the quantities b_1, b_2 are complex conjugates:

$$\begin{aligned}
A &= gR_m \\
a &= R_c/R' \\
w &= \tau/t_p \\
\mu &= e^{-T/t_p} \\
\epsilon_0 &= e^{-T(1-\gamma)/t_p} \\
b_1 &= 2\pi\{a - (a^2 - 1)^{1/2}\} \\
b_2 &= 2\pi\{a + (a^2 - 1)^{1/2}\} \\
\lambda_1 &= e^{-b_1 T/\tau} \\
\lambda_2 &= e^{-b_2 T/\tau} \\
\kappa &= 4\pi^2/\{(w - b_1)(w - b_2)\} \\
\epsilon_1 &= \lambda_1 e^{\gamma b_1 T/\tau} \\
\epsilon_2 &= \lambda_2 e^{\gamma b_2 T/\tau} \\
c &= \{b_2 \epsilon_1 (w - b_2) - b_1 \epsilon_2 (w - b_1)\}/w \\
c' &= \{b_2 \lambda_2 \epsilon_1 (w - b_2) - b_1 \lambda_1 \epsilon_2 (w - b_1)\}/w \\
h &= \{b_2 (1 - \lambda_1)(w - b_2) - b_1 (1 - \lambda_2)(w - b_1)\}/w \\
h' &= \{b_1 \lambda_1 (1 - \lambda_2)(w - b_1) - b_2 \lambda_2 (1 - \lambda_1)(w - b_2)\}/w.
\end{aligned} \tag{A1}$$

Then the combination $gR(s)e^{-\gamma sT}(1 - e^{-sT})/s$ has the transform $F(z)$ given by

$$F(z) = (A/z)\{1 + \kappa(z - 1) \cdot [((w/2\pi)^2(cz - c')/f(z)) - (\epsilon_0/(z - \mu))]\} \tag{A2}$$

where $f(z) = (b_1 - b_2)(z - \lambda_1)(z - \lambda_2)$. For a galvanometer step-current input $i_0 = ge_x(1 + R_1/r) \sim e_x/R'$ when a standard-cell emf difference e_x is applied, the sequences $X(z)$ and $Y(z)$ are described by

$$X(z) = i_0 R_m P(z)(z/(z - 1)) \tag{A3}$$

and

$$Y(z) = KC(z)X(z) \tag{A4}$$

where $P(z)$ is the overall dimensionless PTF, given by

$$P(z) = \kappa \left\{ \frac{(1 - \mu)}{(z - \mu)} - \frac{(w/2\pi)^2(hz + h')}{f(z)} \right\} \Big/ U(z) \tag{A5}$$

and

$$U(z) = 1 + KC(z)F(z). \tag{A6}$$

$X(z)$ may be written as a ratio of two polynomials $G(z)$ and $H(z)$

$$X(z) = i_0 R_m G(z)/H(z) \tag{A7}$$

where $H(z)$ is of fifth degree with unity as the coefficient of z^5, and has roots z_i ($i = 1$ to 5) found using standard library root-extraction routines. The voltage x_k at time kT at the input to the ADC is then given by

$$x_k = i_0 R_m \sum_{i=1}^{5} A_i z_i^k \tag{A8}$$

where

$$A_i = G(z_i) \Big/ \prod_{i \neq k} (z_i - z_k). \tag{A9}$$

The voltage y_k at the output of the DAC is then found using (A4) and (A7).

APPENDIX II
NOISE VARIANCE INTEGRALS

The following notation is used for brevity: for any function $H(z)$, defined everywhere on the unit circle $|z| = 1$, we write $HH^* = H(e^{j\phi})H(e^{-j\phi})$.

A. Thermal Noise

If a current with continuous transform $I(s)$ is applied to the galvanometer input, the sampled voltage at the DAC output has the z transform given by

$$N(z) = \{KC(z)/U(z)\} \times Z\{I(s)R(s)\} \tag{A10}$$

where $Z\{I(s)R(s)\}$ denotes the z transform corresponding to $I(s)R(s)$, and $R(s)$ is defined in (7), $C(z)$ in (2), and $U(z)$ in (A6). In this case the current is thermal and so has the spectral density (in angular units) $(2/\pi)kT'/R'$. The continuous spectral density of the transform $I(s)R(s)$ is therefore $(2/\pi)(kT'/R')\,|R(j\omega)|^2$. The corresponding sampled spectral density $S_i(z)$ can then be shown to be

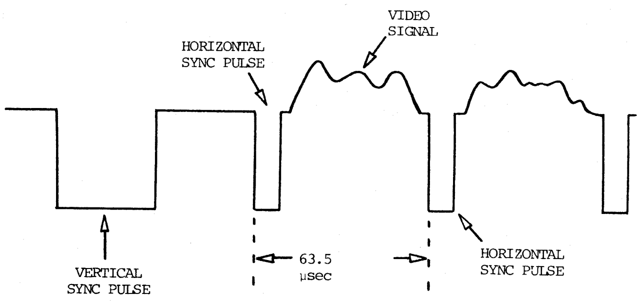

Fig. 2. Video waveform.

used as the video input with a 12-in black and white monitor available for initial setup.

The heart of the system is the video camera computer interface (VCCI) which was required to sample and buffer the image information from the camera. The structure of the VCCI is based on two major decisions. The first is that only binary intensity information will be extracted from each pixel and that coordinate information will be stored in the computer for pixels exceeding a given threshold. Secondly, image information will only be extracted on one field of each frame with the other field being reserved for data transmission to the computer. As a consequence, the maximum y-axis resolution is one part in 256 and the transfer time is limited to 16.7 ms.

Typical video digitizers sample the time sequence and transmit the grey level or binary information to the host computer. The computer then reconstructs the two-dimensional image from this data and can extract various pieces of information from it by knowing the data structure within the computer. Large image arrays such as generated by the 256 × 256 sampling grid used in this system require a large amount of memory even if data compaction is done. For special purpose systems such as this application where the data in the image is very sparse and the grey level resolution is binary, it is more efficient to generate the coordinate information in the interface and transmit it to the computer. This not only minimizes the amount of data storage needed, but also decreases the amount of time required to transmit the image to the host computer. The major drawback is that if the data is buffered in the interface, the size of the buffer will determine the number of pixels that can be recorded.

The VCCI has been designed to determine the position coordinates of light spots in the camera field by dividing each horizontal sweep into 256 pixels (x coordinate) of 0.2-μs duration and dividing the vertical scan into approximately 256 sweeps (y coordinate). Position in the camera field is determined by use of x- and y-position counters which count the x-axis pixels and the y-axis sweeps. The horizontal sync is used to synchronize a 5-MHz oscillator which provides the horizontal pixel sampling rate. The vertical (y axis) sampling signal is also derived from the horizontal sync pulse. The vertical sync pulse rate from the camera is divided by two to eliminate the interlace scan and is used to manage the x and y counters and the memory address counter. It is also used to signal the computer that a frame is completed and data is ready to be transferred to the computer during the 16.7-ms interlace period.

A 16-bit by 128-word buffer memory stores each x–y coordinate for every pixel which exceeds a preselected threshold. The active low signal from a lighted sample generates a memory write which causes the contents of the x and y counters to be written to the memory as one 16-bit word. This transfer occurs during the 200-ns duration of the pixel. The following rising edge of this signal is also used to increment the memory address counter in preparation for the next data word. The interface was therefore designed to accommodate only 128 pixels per image before overflowing.

Interaction between the VCCI and the computer occurs during the 16.7-ms interlace period. The data transfer is initiated by the occurrence of the vertical sync pulse at the beginning of the interlace perod. A logic "1" signal is output to the computer at the beginning of this period and the computer responds by the software generation of a series of clock pulses which are used to decrement the address counter as the contents of each memory location are transferred to the computer. Thus only those x–y coordinate words loaded during the preceding 16.7-ms scan are now transferred to the computer. Although the high speed buffer memory in the prototype consisted of 128 × 16-bit words, this memory could be expanded provided that the computer could accept and store this data within the allotted time.

IV. VCCI Hardware

A. Sampling Control System

A block diagram of this subsystem is shown in Fig. 3 with a complete circuit diagram presented in Fig. 4. It should be noted that no sync separation circuitry is included in the design. The camera chosen provided outputs for horizontal and vertical synchronization signals and required only level shifting circuitry to make them logic compatible.

The video output of the camera is input to the VCCI through a threshold comparator to convert the video output to uncoded TTL logic level signals. During each horizontal sweep this signal is divided into 256 pixels by the NAND gate G1.

Sampling of the thresholded video signal by G1 is accomplished by driving the other input of G1 with a 5-MHz squarewave $\phi 2$ which is the inversion of the output $\phi 1$ of the relaxation oscillator. Synchronization of this oscillator is accomplished by the camera horizontal sync signal. Prior to applying this sampling signal to G1 it is passed through AND gate G2, where it is blanked during the retrace time period by blanking counter C1. The blanking counter counts the 5-MHz squarewave beginning at the end of each horizontal sweep when the camera outputs a horizontal sync pulse. This sync pulse is used to provide the load pulse to reset C1 and initiate the count, starting at a preset value. When counter overflow occurs, the counter output goes high thus enabling G2. Because the interlaced sweep is not to be used for data taking, the blanking delay counter is disabled on alternate vertical sweeps by the output of FF1. By disabling the blanking counter, G1 is disabled, interrupting the sampling process during the interlace period. The output of FF1 is also used to signal the host computer that data is available to be read out during this interlace period. This same data available signal is used to place the memory address counter C2 in a down count mode.

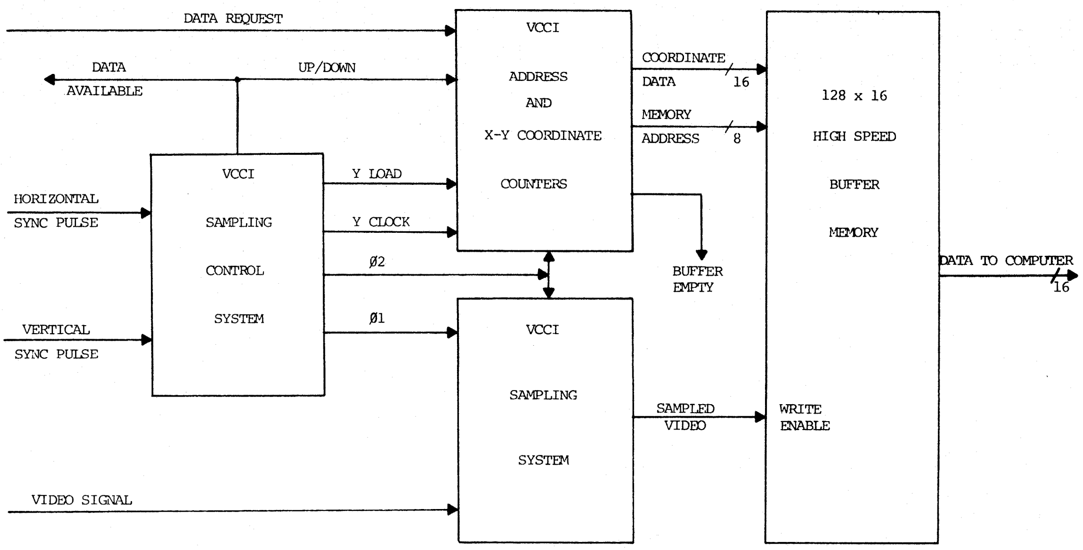

Fig. 3. VCCI block diagram.

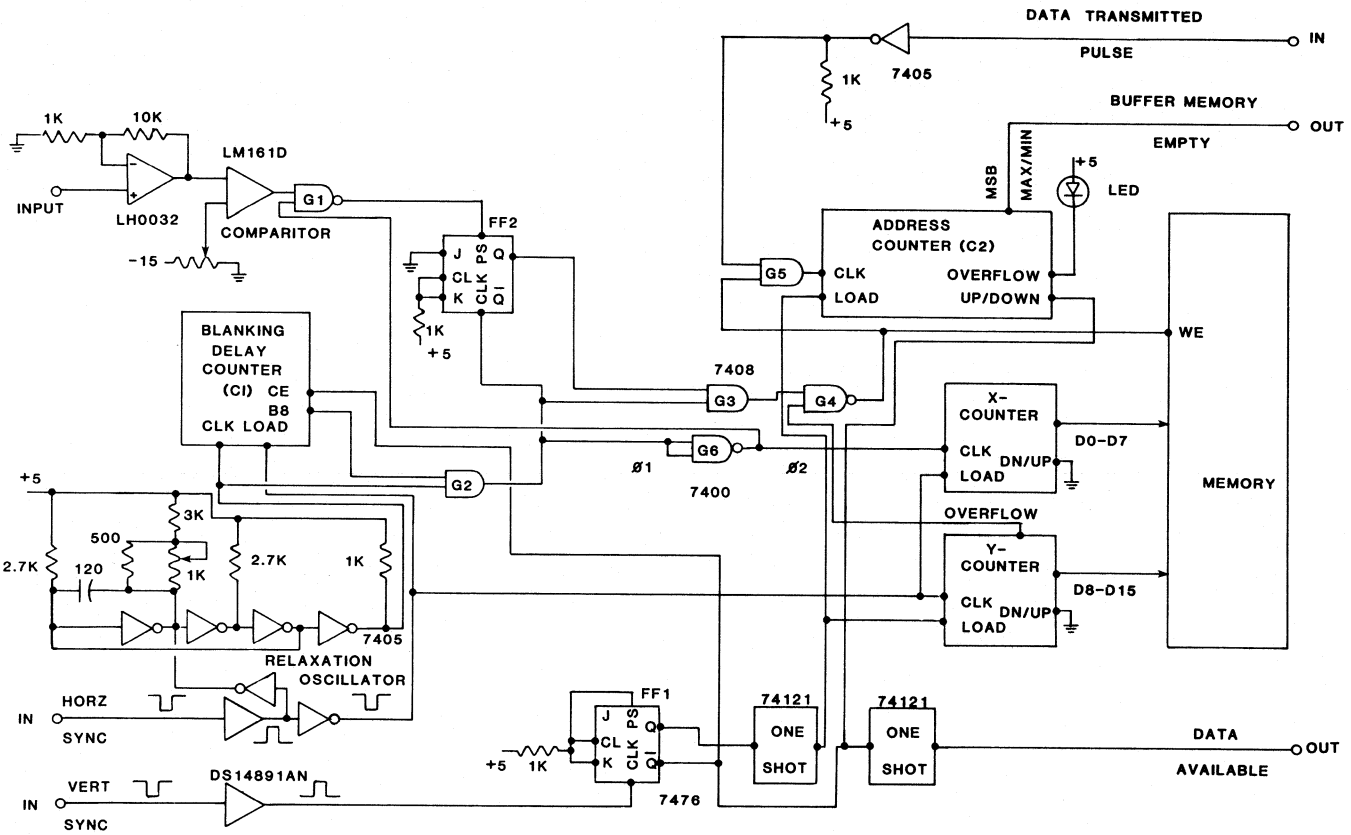

Fig. 4. VCCI circuit diagram.

B. Sampling System

The NAND gate G1 performs the sampling of the threshold level video signal at the times specified by the clock signal $\phi 2$; however, the output of G1 cannot be used to clock in the x-y coordinates to the memory because the video signal may change states several times during the period that G1 is enabled. To eliminate the problem, a flip-flop FF2 has been provided to store the state of the sampled video during the time that $\phi 1$, is low. Fig. 5 is the sample timing diagram. The sampling interval is initiated when the falling edge of $\phi 1$ occurs and flip-flop FF2 is reset to a zero output. During the period in which $\phi 1$, is low, gate G1 is enabled and the video signal is sampled, causing the output of G1 to go low if a bright spot occurs. This results in the output of FF2 being set to one. During the time that $\phi 1$ is high, AND gate G3 is enabled, and if FF2 is high a one is output to NAND gate G4. If G4 is enabled, a write command is issued to the high-speed memory and the corresponding x-y addresses are loaded. Flip-flop FF2 is then reset to zero on the falling edge of $\phi 1$.

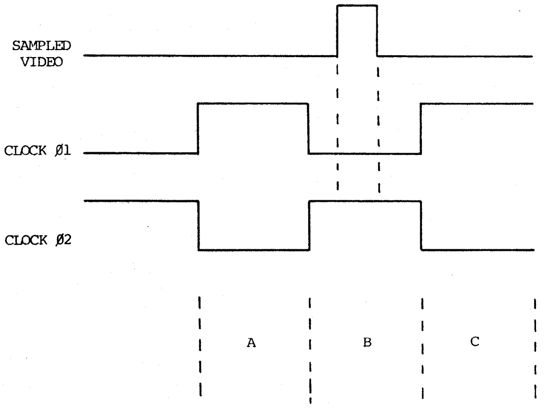

Fig. 5. Sampling timing diagram. (A: Gate G3 is enabled and G1 is disabled. B: Enable G1 and sample video signal. If video is high, direct set flip-flop to store video information. C: Enable G3. If video exceeded threshold during period B, write coordinate information to memory. Reset storage flip-flop on falling edge of $\phi 1$. A, B and C are 100 ns in duration.)

C. Address and Position Counters

The coordinates of each lighted pixel are stored in memory as one 16-bit word. Two 8-bit counters are used to acquire the x–y coordinates of each pixel, with the x counter being incremented by $\phi 2$ and the y counter being advanced by the occurrence of a horizontal sync pulse. Thus the x and y counters contain the updated digitized position of the beam in the vidicon camera's raster scan. Although the x and y counters are continually outputting coordinate information, no write to memory occurs unless a memory write signal is generated by the sampling system.

x and y coordinate information is stored consecutively in memory at an address which is determined by a single 8-bit counter. This counter is incremented after a storage occurs such that the current value of the counter corresponds to the next location to be loaded. When data is being taken, the address counter is set to up count by the output of FF1. During the interlace, however, the address counter is placed in the down count mode so that the host computer can sequentially decrement through each address and read the corresponding contents of each memory location. The address counter is clocked by successive write enable signals while the host computer holds the READ/WRITE line high. Information is written to the high-speed buffer memory when the write enable line goes low. The output of AND gate G5 is now low, but will return high on the rising edge of the write enable signal, thus incrementing the memory address counter.

The vertical sync pulse, which occurs at the end of the data collection scan, signals the host computer that data is ready to be transferred from the VCCI. Just prior to the occurrence of the vertical sync pulse, the y counter will overflow interrupting the sampling process by means of NAND gate G4. The high output of G4 enables G5, thus allowing the host computer to generate clock pulses to decrement the address counter.

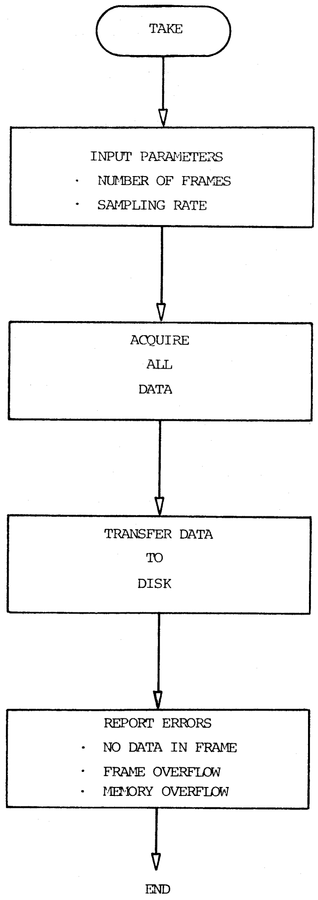

Fig. 6. Data acquisition program flowchart.

V. Image Processing Software

The software required to acquire and process the image is currently contained in two separate programs. One program is used to acquire the images and record them on disk. The other program processes the images from disk to produce such information as light spot centroid locations and harmonic analysis of motion. It is necessary to operate in this mode because the host computer contains only 28K words, and a large portion of this memory must be reserved for pixel storage in order to maintain real-time system operation.

A flow chart for the data acquisition program is shown in Fig. 6. The operator must input the number of image frames to be acquired along with the number of frames to skip between acquisitions. This allows the sampling rate to be variable in increments of 33.3 ms with the maximum rate being 30/s. The number of possible frames per acquisition is a function of the number of lamps used and the number of pixels needed to represent each lamp or the total number of pixels acquired. Error reporting is also included for such conditions as no image in a particular frame due to insufficient lighting or threshold setting, too many pixels per frame resulting in an interface buffer overflow and too many total pixels resulting in a host computer memory overflow.

The image data is processed by a second program which sequentially reads each frame from disk. Because the data have been extracted from a raster-scan device, pixel coordinates from multiple lamps are interspersed throughout the data. The first task for this routine, as shown in the flowchart of Fig. 7, is to reassociate each pixel with its respective lamp within each frame. The algorithm which accomplishes this task centers a mask, as shown in Fig. 8, over each pixel in the frame and tests to see if the other coordinates contained within the mask are

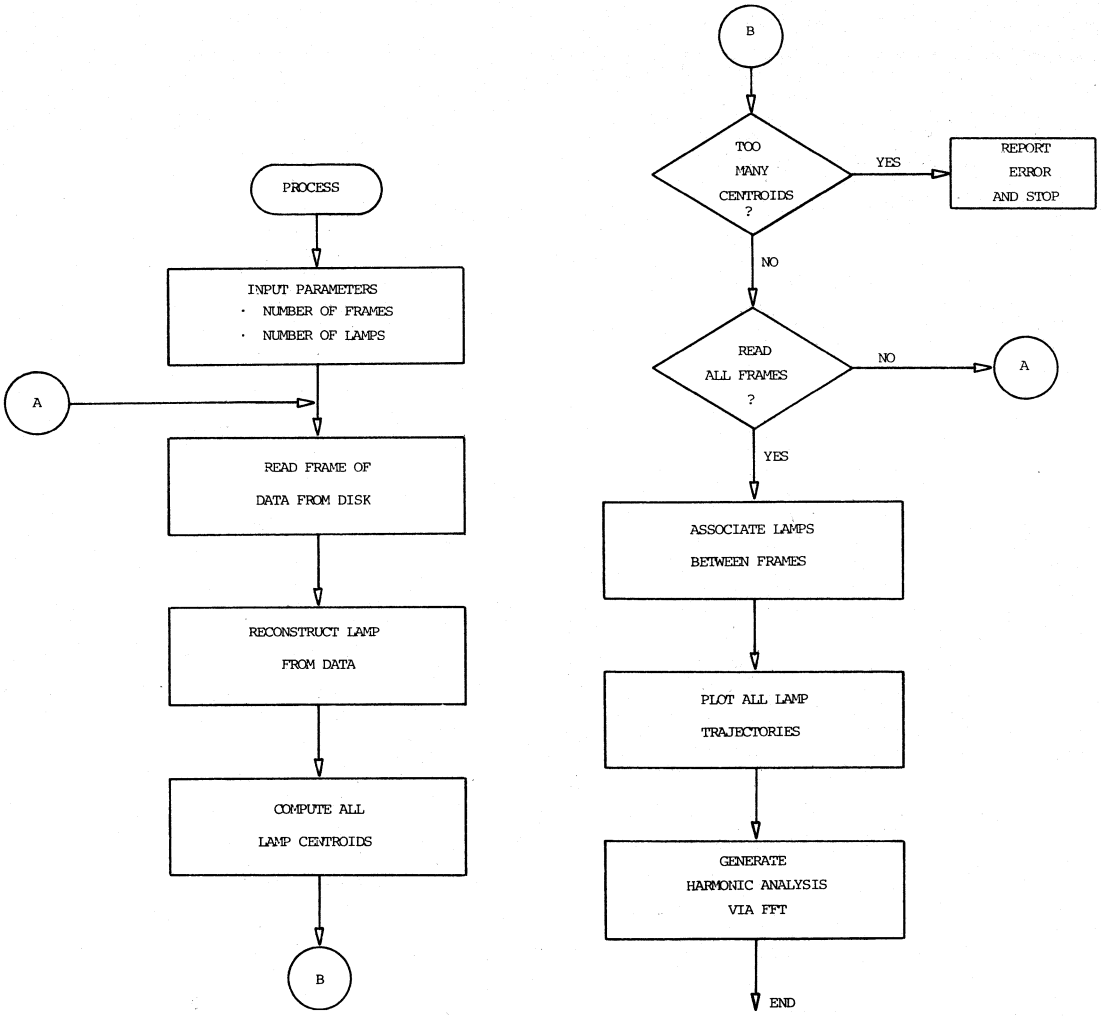

(a) (b)

Fig. 7. Data processing program flowchart.

in the data array. The process is started by selecting, at random, the first pixel and assigning it lamp 1. Coordinates of the other pixels in the mask are calculated and the data is scanned searching for their occurrence. If the coordinates are found then the pixel is assigned to lamp 1. The mask is then centered consecutively over the neighboring pixels identified by the initial mask position. The process is repeated until no new pixels can be found that should be associated with lamp 1. The algorithm now searches the data for any unassigned pixels and makes a designation of lamp 2 to the first one it encounters. The masking process is repeated in order to find lamp 2 pixels with the entire process being repeated for additional lamps until all pixels in the current frame of data have been assigned lamp numbers.

Once the lamps have been reconstructed, the center of gravity or centroid is calculated for each lamp. Centroid locations are used to remove variations in lamp size due to misalignment and motion artifacts. An option is available such that the centroids are output at the end of each frame of data. If too many lamps are found in the masking algorithm, it is also reported.

Another frame of data is read from disk and processed as described above, and the process is repeated until all data have been processed. The centroid results are retained in memory from each frame of data. In order to calculate a trajectory for each lamp, centroids between frames must be associated. The routine accomplishes this task by calculating the Euclidean distance between the centroid of a lamp and all of the centroids in the next frame. The lamp pairs with the minimum distances are associated. The process is then repeated. This scheme does require that the sampling rate be much faster than the motion.

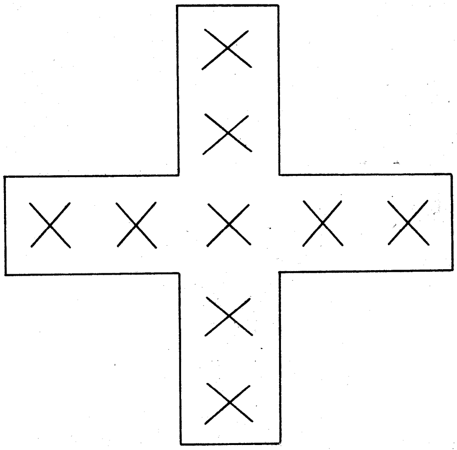

Fig. 8. Mask used for lamp reconstruction.

Output from the routine can take several forms. The simplest is a plot of the trajectory of the lamp on a multipen plotter.

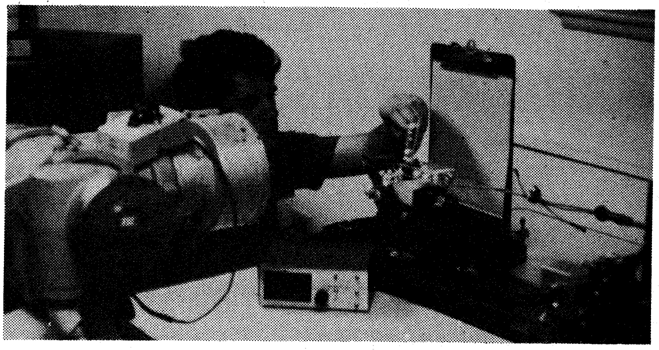

Fig. 9. Spinal stability experimental setup.

Software is also available for the harmonic analysis of the motion using the Fast Fourier Transform.

VI. PERFORMANCE

The system has been utilized successfully in several applications. It has been used extensively to measure load deformation of the *in vitro* cervical spine [7]. The test shown in Fig. 9 uses two *in vitro* vertebral segments from the canine cervical spine. The distal vertebra is embedded in a polymethyl-methacrylate base and securely clamped in a holding fixture. A cable is attached to the body of the proximal vertebra. A load is then applied to the spine through the cable and is recorded by the computer through an instrumented load bar.

The displacement of the segments are determined using six lamps. Two lamps are attached to the proximal vertebra to record its deflection. Two lamps are attached to the load cable to indicate the vector force. Because of possible specimen motion, two lamps are attached to the bench as a reference.

Fig. 10 shows the resulting motion of a two-segment spine section under load. The actual motion of four of the lamps (excluding the reference lamps) are shown with the actual deformation of segment C4 relative to C5 shown on the bottom right portion of the figure. Failure information (load versus deformation) can be obtained from the acquired data.

The system has been operational and in use for four years. It has proven to be long term stable and capable of repeatable results. The static resolution is

$$R_s = D/256$$

units where D is measured in the field of view. The maximum velocity in field of view for minimum R_s is

$$V_{\max} = R_s/(1/60) = 0.234D$$

units/s.

VII. CONCLUSIONS

The system has proven to be versatile and reliable. A buffer size of 128 words has been sufficient in all of the applications so far. Since the design of the VCCI, a large-scale integrated (LSI) circuit in the form of a first-in-first-out (FIFO) buffer has become available which could be used to replace the current memory and memory address counter. Using the FIFO's would make the job of expanding the buffer extremely easy. Also, the PDP-11/03 could be replaced by any of the 16-bit microcomputer systems currently on the market such as the IBM-PC. Actually, an 8-bit system could be used as long as the transfer rate from the VCCI is sufficient to obtain all of the coordinate information in the 16.7 ms.

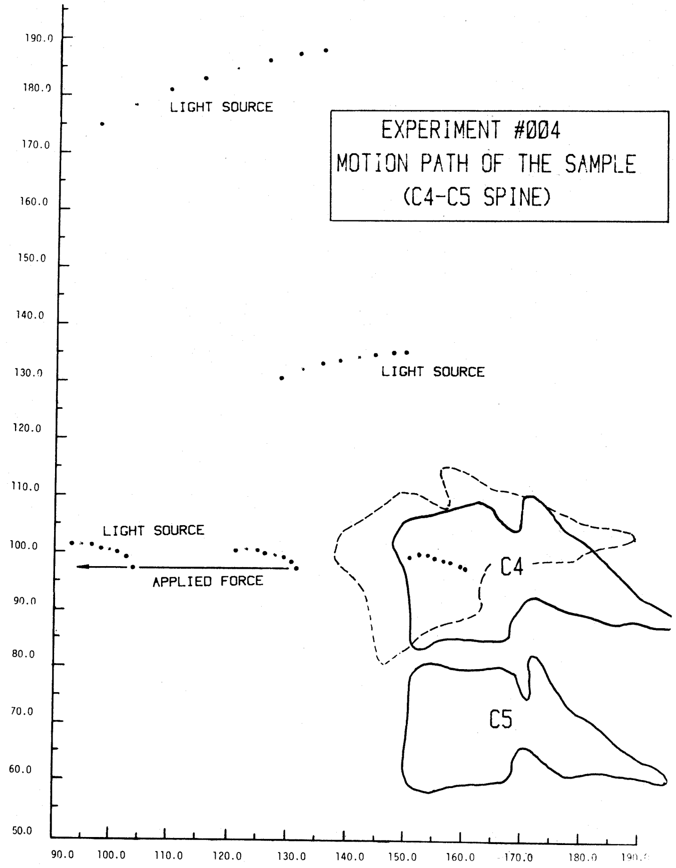

Fig. 10. Load deformation results from a two-segment spine section.

Several enhancements could be easily incorporated into design of the VCCI. Increased resolution could be accomplished by including data acquisition on the interlace sweep as well. By using two buffers in a ping-pong configuration, an acquisition rate of 30 Hz can be maintained. Absolute motion measurements can be provided by using two cameras in synchronization. Only the buffer memory portion and video thresholding must be added since the synchronization will be accomplished by letting one camera drive the other.

REFERENCES

[1] H. Hatze, "Optimization of human motion," in *Biomechanics III*. Baltimore: University Park, and Basel: S. Karger, pp. 138-142.

[2] H. Hatze, "A model of skeletal muscle suitable for optimal motion problems," *Biomechanics IV*. Baltimore: University Park and New York: Macmillan Press, pp. 417-422.

[3] K. Soudau and P. Durckx, "Calculation of derivatives and Fourier coefficients of human motion data, while using spline functions," in *Journal Biomechanics*, vol. 12. London: Pergamon Press Ltd., pp. 21-26.

[4] W. Bauman, "New chronophotographic methods for three dimensional movement analysis," in *Biomechanics IV*. Baltimore: University Press and New York: Macmillan, pp. 463-468.

[5] P. Lappalainen and M. Tervonen, "Instrumentation of movement analysis by raster-scanned image source," *IEEE Trans. Instrum. Meas.*, vol. IM-24, no. 3, pp. 217-221, Sept. 1975.

[6] L. E. Lindholm, "An optoelectronic instrument for remote on-line movement monitoring," in *Biomechanics IV*. Baltimore: University and New York: Macmillan, pp. 510-512.

[7] R. L. Kett, *et al.*, "Motion analysis and load deformation testing of the in-vitro cervical spine," in *Proc. 5th Annual Conf. on Rehabilitation Engineering* Houston, TX, 1982, pp. 83.

General Formulas for the Average Magnetic Field at a Receiving Circular-Loop Antenna Placed Arbitrarily to a Radiating Loop

HIROSHI NAKANE

Abstract—**For testing the sensitivity of receivers having loop antennas, radiating and receiving loops have been located either coplanar or coaxial to each other. Theoretical analyses of the magnetic fields have been carried out for such alignments of loops. It is often necessary in the actual tests to estimate the effects of deviations from these ideal arrangements of the loops.**

In this paper, the radiating and receiving circular loops are located arbitrarily in direction, and a formula is derived to obtain the average normal component of the magnetic-field strength incident on the receiving loop using the Eulerian angles. The theory is applied to the design of a generator in which a rotating field is used as the standard field. In this case, the calculated values of the magnetic field are in agreement with the measured ones to within ±0.1 dB.

I. INTRODUCTION

THE NEAR-ZONE magnetic field radiated by a small circular loop antenna has been used for testing the sensitivity of receivers and field-intensity meters having loop antennas [1]. In these tests, it is necessary to adjust the direction of the receiving loop (test loop) so that the loop has the maximum sensitivity at a fixed position. The author has already proposed a method of using a rotating field in order to obtain a constant magnetic field without influence of the test loop's direction at the test point [2].

The voltage induced in the receiving antenna is measured and the result is compared with a value obtained by Faraday's law of induction from the average magnetic-field intensity normal to the plane of the receiving loop and enclosed by it, H_{av}. For coaxial and coplanar alignments of loops, which are commonly used in the test, the formulas for H_{av} are given in [3] and [4], respectively. In the analysis of the generator radiating a rotating field, a formula for H_{av} is required in which the receiving loop is placed in an arbitrary direction relative to the radiating loop.

In this paper, a formula for this arbitrary alignment of loops is derived by using the Eulerian angles [5]. A generator with the rotating magnetic field was designed by using the above theory and an experiment was carried out to confirm the theory. The measured values obtained in the experiment are compared with those calculated from theory.

II. FORMULATION

As shown in Fig. 1, a small circular loop C_T of radius r_T and carrying current $I(\gamma)\exp(j\omega t)$ lies in the x-y plane with its center at the origin of the rectangular coordinate system. A receiving loop C_R of radius r_R is located in an arbitrary plane with its center at the point of $P(0, L, D)$. It is assumed that the radius of the wires of the loop winding is negligibly small compared with the loop radius. Let us obtain the average value of the axial component of magnetic-field intensity in the area enclosed by the receiving loop, H_{av}. From [3], H_{av} is given by

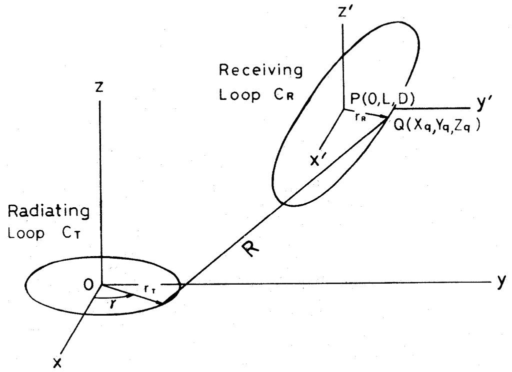

Fig. 1. Geometry when radiating and receiving loops are located arbitrarily.

$$H_{\text{av}} = \frac{1}{\pi\mu r_R^2}\int_{C_R}\vec{A}\cdot\overrightarrow{dC_R}$$

$$= \frac{1}{4\pi^2 r_R^2}\int_{C_T}\int_{C_R} I(\gamma)\frac{e^{-j\beta R}}{R}\,\overrightarrow{dC_T}\cdot\overrightarrow{dC_R} \tag{1}$$

where $\vec{A}$ is the magnetic vector potential, μ is the permeability of the medium, β is the wave number, and R is the distance from a point on C_T to a point on C_R. $\overrightarrow{dC_T}$ and $\overrightarrow{dC_R}$ show the segment of the arc on C_T and C_R, respectively.

In order to find specific formulas for R and $\overrightarrow{dC_R}$, let us carry out the analysis of the arrangement in terms of the loop C_R. Consider the rectangular coordinate axes x', y', and z' shown in Fig. 2. These have the origin at the point of $P(0, L, D)$ in Fig. 1, and are parallel to the axes x, y, and z, respectively. One can carry out the transformation from the loop in the coordinate system $x'y'z'$ (shown by the broken line in Fig. 2) to another loop in the coordinate system $x''y''z''$ (by the solid line in Fig. 2) by means of three successive rotations performed in a specific sequence. The Eulerian angles are used as the three successive angles (ϕ, θ, ψ) of rotation. The relations, in matrix

---

Manuscript received July 5, 1983; revised July 2, 1984.

The author is with the Department of Electrical Engineering, Science University of Tokyo, 1-3, Kagurazaka, Shinjuku-ku, Tokyo, Japan.

0018-9456/84/0900-0307$01.00 © 1984 IEEE

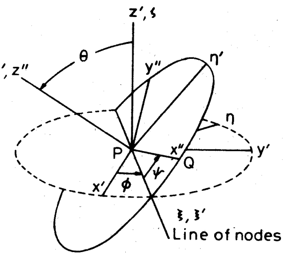

Fig. 2. Arrangement of receiving loop C_R in terms of Eulerian angles.

form, between the coordinate systems $x'y'z'$ and $x''y''z''$ are [5]

$$\begin{bmatrix} x' \\ y' \\ z' \end{bmatrix} = \begin{bmatrix} \cos\phi\cdot\cos\psi - \cos\theta\cdot\sin\phi\cdot\sin\psi & -\cos\phi\cdot\sin\psi - \cos\theta\cdot\sin\phi\cdot\cos\psi & \sin\theta\cdot\sin\phi \\ \sin\phi\cdot\cos\psi + \cos\theta\cdot\cos\phi\cdot\sin\psi & -\sin\phi\cdot\sin\psi + \cos\theta\cdot\cos\phi\cdot\cos\psi & -\sin\theta\cdot\cos\phi \\ \sin\theta\cdot\sin\psi & \sin\theta\cdot\cos\psi & \cos\theta \end{bmatrix} \begin{bmatrix} x'' \\ y'' \\ z'' \end{bmatrix}. \tag{2}$$

The intersection point $Q(x_q, y_q, z_q)$ of the axis x'' with the circle of C_R shown by the solid line in Fig. 2 is obtained by substituting $x'' = r_R$, $y'' = 0$, and $z'' = 0$ into (2) and by considering the coordinates at the point of $P(0, L, D)$. In the coordinate system xyz, the intersection point is

$$\left.\begin{aligned} x_q &= r_R\,(\cos\phi\cdot\cos\psi - \cos\theta\cdot\sin\phi\cdot\sin\psi) \\ y_q &= L + r_R\,(\sin\phi\cdot\cos\psi + \cos\theta\cdot\cos\phi\cdot\sin\psi) \\ z_q &= D + r_R\cdot\sin\theta\cdot\sin\psi. \end{aligned}\right\} \tag{3}$$

Since the loop C_R is symmetrical around the axis z'', ψ (the fixed coordinate) can be rewritten as the angle of the current coordinate. From (3) and the definition of the R, $\vec{R}$ and $\overrightarrow{dR}$ are obtained

$$\begin{aligned} \vec{R} &= \hat{x}(-r_T\cos\gamma + r_R\cos\phi\cos\psi \\ &\quad - r_R\cos\theta\sin\phi\sin\psi) + \hat{y}\,(L - r_T\sin\gamma \\ &\quad + r_R\sin\phi\cos\psi + r_R\cos\theta\cos\phi\sin\psi) \\ &\quad + \hat{z}(D + r_R\sin\theta\sin\psi) \end{aligned} \tag{4}$$

$$\begin{aligned} \overrightarrow{dC_R} &= \frac{\partial\vec{R}_{(L=D=r_T=0)}}{\partial\psi}\,d\psi \\ &= [-\hat{x}\,(\cos\phi\sin\psi + \cos\theta\sin\phi\cos\psi) \\ &\quad + \hat{y}\,(-\sin\phi\sin\psi + \cos\theta\cos\phi\cos\psi) \\ &\quad + \hat{z}\,(\sin\theta\cos\psi)]\; r_R\cdot d\psi \end{aligned} \tag{5}$$

where $\hat{x}$, $\hat{y}$, and $\hat{z}$ are the unit vectors on the x, y, and z axes, respectively. As $\overrightarrow{dC_T}$ has previously been given by [3] and [4], the inner product between $\overrightarrow{dC_T}$ and $\overrightarrow{dC_R}$ is

$$\begin{aligned} \overrightarrow{dC_T}\cdot\overrightarrow{dC_R} &= [\sin\psi\sin(\gamma-\phi) + \cos\theta\cos\psi\cos(\gamma-\phi)] \\ &\quad \cdot r_T\cdot r_R d\gamma\cdot d\psi. \end{aligned} \tag{6}$$

From (4), R is given by

$$R = \sqrt{R_0^2 + 2\Delta R} \tag{7}$$

where

$$R_0^2 = r_T^2 + r_R^2 + D^2 + L^2$$

and

$$\begin{aligned} \Delta R = [&-r_T L\sin\gamma + r_R L(\cos\theta\cos\phi\sin\psi \\ &+ \sin\phi\cos\psi) - r_T r_R \\ &\cdot\{\cos\theta\sin\psi\sin(\gamma-\phi) + \cos\psi\cos(\gamma-\phi)\} \\ &+ r_R D\sin\theta\sin\psi]. \end{aligned} \tag{8}$$

Let us use the sum of spherical Hankel functions of the second kind [3], $h_k^{(2)}(\beta R_0)$, to rewrite the term $\exp[-j\beta R]/R$ in (1), and substitute (6) for the expression $\overrightarrow{dC_T}\cdot\overrightarrow{dC_T}$

$$\begin{aligned} H_{\text{av}} = &-\frac{j\beta r_T}{4\pi^2 r_R}\sum_{k=0}^{\infty}\frac{h_k^{(2)}(\beta R_0)}{k!} \\ &\cdot\left(-\frac{\beta}{R_0}\right)^k \int_{-\pi}^{\pi}\int_{-\pi}^{\pi} I(\gamma)\cdot(\Delta R)^k \\ &\cdot[\cos\theta\cos\psi\cos(\gamma-\phi) + \sin\psi\sin(\gamma-\phi)]\; d\gamma\cdot d\psi \end{aligned} \tag{9}$$

where k is an integer.

Applying binomial expansion to $(\Delta R)^k$ in (9) gives

$$\begin{aligned} (\Delta R)^k = &\sum_{l=0}^{k}\sum_{m=0}^{l}\sum_{n=0}^{m}\sum_{s=0}^{n}\sum_{t=0}^{s} \\ &\cdot\frac{k!(-r_T)^{k-l+n-t}{r_R}^{l}L^{k-n}D^t(\sin\gamma)^{k-l}(\sin\theta)^t}{(k-l)!(l-m)!(m-n)!(n-s)!(s-t)!t!} \\ &*(\cos\theta)^{l-m+n-s}(\sin\phi)^{m-n} \\ &\cdot(\cos\phi)^{l-m}(\sin\psi)^{l-m+n-s+t} \\ &**(\cos\psi)^{m-n+s-t}\{\sin(\gamma-\phi)\}^{n-s} \\ &\cdot\{\cos(\gamma-\phi)\}^{s-t} \end{aligned} \tag{10}$$

where l, m, n, s, and t are integers.

It is assumed that the current distribution $I(\gamma)$ on the radiating loop is uniform and is equal to I. In the equation obtained by substituting (10) into (9), the integrals for γ and ψ in the range of $-\pi$ to π becomes zero when the powers for the sinusoidal and cosinusoidal terms are odd. Therefore, the remaining integrals only contain even powers. The integrals in the expression for H_{av} can be evaluated using a definite integral formula from [6]:

$$H_{\text{av}} = -\frac{j\beta r_T I}{r_R}\sum_{k=0}^{\infty} F(k) \tag{11}$$

TABLE I
COMPARISON AMONG VARIOUS ARRANGEMENTS OF LOOPS

Arrangement of loops	Reference	Values to be substituted in Eq.(11)
Coaxial	[3]	$L = 0$ $D = d$ $\theta = 0$, $\phi = 0$
Coplane	[4]	$D = 0$, $\theta = 0$, $\phi = 0$
Intersecting at right angle	[7]	$L = a$ $D = b$ $\theta = \frac{\pi}{2}$, $\phi = 0$

where

$$F(k) = \sum_{l=0}^{k} \sum_{m=0}^{l} \sum_{n=0}^{m} \sum_{s=0}^{n} \sum_{t=0}^{s} \left(\frac{\beta}{R_0}\right)^k \frac{(-1)^{-(l+s+t)} h_k^{(2)}(\beta R_0)\, r_T^{k-l+n-t} r_R^{l}}{(k-l)!(l-m)!(m-n)!(n-s)!}$$

$$\cdot \frac{L^{k-n} D^t (\sin\theta)^t (\cos\theta)^{l-m+n-s} (\sin\phi)^{m-t+1} (\cos\phi)^{l-m}}{(s-t)!t!(k-l+n-t+1)!!(l+1)!!} \left[\cos\theta \sum_{a=0}^{n-s} \sum_{b=0}^{s-t+1}\right.$$

$$\cdot \frac{(-1)^{-a}(n-s)!(s-t+1)!(k-l+s-t+a-b)!!}{(\tan\phi)^{a+b}\, a!b!(n-s-a)!} \; \frac{(n-s-a+b-1)!!(m-n+s-t)!!(l-m+n-s+t-1)!!}{(s-t-b+1)!}$$

$$+ \sum_{c=0}^{n-s+1} \sum_{d=0}^{s-t} \frac{(-1)^{-c+1}(n-s+1)!(s-t)!(n-s-c+d)!!}{(\tan\phi)^{c+d}\, c!d!\,(s-t-d)!}$$

$$\left.\cdot \frac{(k-l+s-t+c-d-1)!!(m-n+s-\mathrm{t}-1)!!(l-m+n-s+t)!!}{(n-s-c+1)!}\right]$$

where a, b, c, and d are integers

$$k \geqq l \geqq m \geqq n \geqq s \geqq t$$

$$n - s \geqq a, \quad s - t + 1 \geqq b, \quad n - s + 1 \geqq c, \quad s - t \geqq d$$

$$-1!! = 0!! = 0! = 1.$$

Let us rewrite the condition as abovementioned (the integrals obtained by substituting (10) into (9) only contain even powers) into the following specific expression. It is necessary in (11) that all terms of ( )!! included in the numerator of the first term, which is concerned with the summations of a and b, and/or the second term, which is concerned with the summations of c and d, be odd. These requirements are

1) the first term exists when all terms of l, $(k + n - t + 1)$, $(m - t - a + b)$, and $(m - n + s - t)$ are odd.

2) the second term exists when all terms of l, $(k + n - t + 1)$, $(m - t - c + d)$, and $(m - n + s - t - 1)$ are odd.

According to the characteristic of a spherical Hankel function of the second kind [3], (11) converges for

$$R_0^2 > 2|\Delta R|. \qquad (12)$$

III. DISCUSSION

The conventional formulas for special arrangements of loops are obtained by substituting the specific values of L, D, θ, and ϕ in the Table I into (11). A comparison shows that (11) is in agreement with the conventional formulas for these special arrangements.

IV. ANALYSIS OF ROTATING FIELD

A specific application of (11) is reported in this section. In a sensitivity test, in order to make it easier to set the receiving loop (test loop) at the test point, a method was developed in which a rotating field was used as the standard magnetic field. The rotating field is formed by intersecting, at a right angle (at the test point), two magnetic-field components which have the same amplitude and a phase difference of $\pi/2$ rad. This method takes advantage of the fact that the magnetic field detected by a receiving loop is nearly constant when the radius of the loop is small compared with the distance between the center of the radiating loop and the test point.

A generator was designed in which the standard magnetic field around the test point was obtained independently of the direction and the location (by using the uniform field [8]) of the receiving loop. As shown in Fig. 3, the centers of the four radiating loops are placed on the y or z axes. Radiating loops 1 and 2, and loops 3 and 4 lie on the planes formed by the x-y axes and x-z axes, respectively. It is assumed that the properties of these loops are the same, and that the currents in these loops have the same amplitude and a phase difference of $\pi/2$ rad between loops 1 and 2 and loops 3 and 4. When the receiving loop, the plane of which is kept perpendicular to the plane involving the y-z axes, rotates about the axis which goes through the center of the loop and is parallel to the x axis, the magnetic-field strength detected by the receiving loop H_T is given by

$$H_T = \left| \sum_{n=1}^{4} K_n(x', y', z') \cdot I_n \right| \qquad (13)$$

where

$$I_1 = I_2 = I \cdot \exp(j\omega t)$$

$$I_3 = I_4 = I \cdot \exp[j(\omega t - \pi/2)].$$

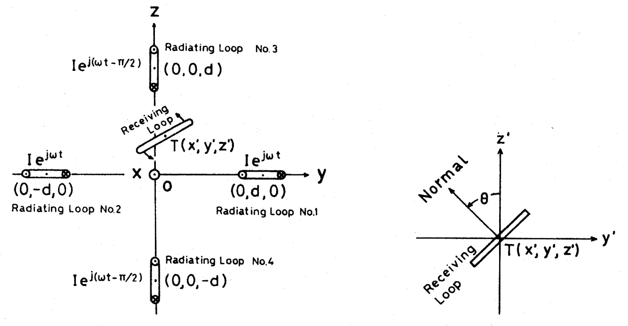

(a) (b)

Fig. 3. (a) Geometry of radiating loops which generate a rotating field and receiving loop. (b) Rotation of a receiving loop at test point T.

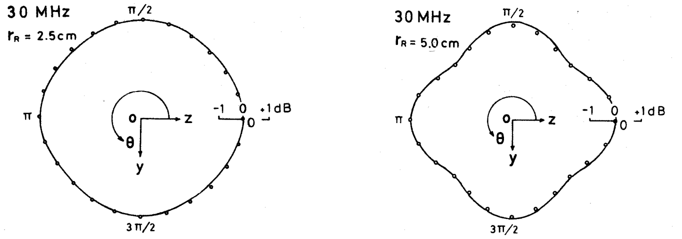

(a) (b)

Fig. 4. Uniformity of magnetic-field strength of rotating field. (a) r_R = 2.5 cm at origin. (b) r_R = 5.0 cm at origin.

TABLE II
VALUES TO BE SUBSTITUTED IN (11) TO OBTAIN $K_n(x', y', z')$ IN (13)

$k_n(x',y',z')$	Values to be substituted in Eq.(11)		
$k_1(x',y',z')$	$L=-\sqrt{(y'-d)^2+x'^2}$ $D=\ z'$	$\theta=\theta$	$\phi=0$
$k_2(x',y',z')$	$L=\sqrt{(y'+d)^2+x'^2}$ $D=\ z'$		
$k_3(x',y',z')$	$L=-\sqrt{(z'-d)^2+x'^2}$ $D=\ y'$	$\theta=-\theta-\frac{\pi}{2}$	
$k_4(x',y',z')$	$L=\sqrt{(z'+d)^2+x'^2}$ $D=\ y'$		

K_n is obtained by substituting the relations as shown in Table II for H_{av}/I which is derived from (11).

In the cases of frequency = 30 MHz, d = 30 cm, r_T = 5.0 cm, and r_R = 2.5 and 5.0 cm, the solid lines in Fig. 4 show the results of calculated H_T (normalized by the value of $\theta = 0$) when the receiving loop was rotated at the origin. Equation (11), which is used in the calculation of H_T, must be approximated by a finite series. The convergence in (11) was investigated by calculating the convergence error C_E ($C_E = 1 - (\Sigma_{k=0}^{i} F(k)/\Sigma_{k=0}^{\infty} F(k))$) [4]. For the parameters treated in Fig. 4, H_{av} for each radiating loop was obtained within allowable error ($C_E \leqq \pm 10^{-3}$) by retaining terms up to k = 11 for r_R = 2.5 cm and k = 15 for r_R = 5.0 cm.

Experiments were carried out to confirm the validity of the calculations shown in Fig. 4. The measured values are indicated by the white dots, and agree with the calculated values to within ±0.1 dB.

Note that the rotational characteristic at the origin in Fig. 4 deviates from a circle when the radius of the receiving loops becomes large. This deviation occurs because the assumption (that two magnetic-field components with the same amplitude and a phase difference of $\pi/2$ rad, which is detected by the receiving loop, intersect on the plane of the loop) is no longer valid as the radius of the loop becomes large.

V. CONCLUSION

In this paper, a new formula was obtained for the average normal component of magnetic-field strength incident on the receiving loop when the radiating and receiving circular-loop antennas are located arbitrarily. Formulas for special arrangements of the loops have already been derived. These were compared with the new formula by substituting appropriate values for the parameters. It was confirmed that the formulas agree with each other.

By applying this new formula, a generator was devised in which a rotating field was used as an RF standard magnetic field and an experiment with this generator was carried out. The measured values agreed with the ones calculated by the new equation to within ±0.1 dB.

ACKNOWLEDGMENT

The author would like to thank Prof. Dr. K. Futami, Prof. Dr. S. Omori, and Dr. I. Yokoshima for their helpful discussions and S. Obuki and H. Adachi for their helpful assistance.

REFERENCES

[1] F. M. Greene, "NBS field-strength standards and measurements (30 Hz to 1000 MHz)," *Proc. IEEE*, vol. 55, pp. 970-981, June 1967.

[2] H. Nakane, "RF standard magnetic field generating method using rotating field," *Trans. IEE of Japan*, vol. 102-A, pp. 678, Dec. 1982.

[3] F. M. Greene, "The near-zone magnetic field of a small circular-loop antennas," *J. Res. Nat. Bur. Stand.*, vol. 71c, pp. 319-326, June 1967.

[4] H. Nakane, S. Omori, and I. Yokoshima, "Studies of magnetic field for transmitting and receiving loop antenna placed in a coplane," *IEEE Trans. Instrum. Meas.*, vol. IM-30, pp. 206-209, Sept. 1981.

[5] H. Goldstein, *Classical Mechanics*, Reading, MA: Addison-Wesley, 1950, pp. 107-109.

[6] I. S. Gradshteyn, *Table of Integrals, and Products*. New York and London: Academic Press, 1965, p. 369.

[7] I. Yokoshima and H. Nakane, "Analysis of average magnetic field on circular plane intersecting at right angle with a transmitting loop," *Bull. Electrotech. Labora.*, vol. 43, pp. 609-612, 1967, in Japanese.

[8] N. Nakane, S. Obuki, S. Omori, and I. Yokoshima, "Standard magnetic field radiated by two loop antennas in a coplane," *IEEE Trans. Instrum. Meas.*, vol. IM-32, pp. 238-240, Mar. 1983.

Microwave-Induced Constant Voltage Steps at Series Arrays of Josephson Tunnel Junctions with Near-Zero Current Bias

JURGEN NIEMEYER, JOHANN H. HINKEN, SENIOR MEMBER, IEEE, AND
WOLFGANG MEIER

Abstract—Microwave-induced, constant-voltage steps in the current-voltage characteristics of Josephson tunnel junctions are used as a reference voltage in cryogenic voltage standards. This relatively low reference voltage of a few millivolts could be increased by using series arrays of tunnel junctions instead of a single junction. Series arrays consisting of 2, 6, 14, and 54 tunnel junctions were tested at a frequency of 70 GHz. The use of this relatively high frequency and of lead-alloy base electrodes allows zero crossing steps of up to 34 mV to be observed for an array with only 54 junctions when irradiated by an RF power of 32 mW. The measurements were performed at 4.2 K.

I. INTRODUCTION

IF A MICROWAVE signal is coupled to a current-biased Josephson junction the dc current-voltage characteristic shows ranges of constant quantized voltages at

$$V_n = n \frac{\hbar}{2e} f \tag{1}$$

where ($n = 0, 1, 2, \cdots$) [1], f is the frequency of the microwave, $\hbar$ is Planck's constant, and e is the elementary charge. One of these constant voltage steps in the millivolt region can be used as the reference voltage in a voltage standard [2].

In the case of superconductor-insulator-superconductor junctions with a highly hysteretic dc current-voltage characteristic, the constant voltage steps appear in the reverse switching characteristic at relatively low microwave power. In this region the steps cross the zero-current axis, reaching small negative currents [3] (Fig. 1). It has been proposed by Levinsen *et al.* [4] to increase the reference Josephson voltage of a voltage standard from a few millivolts to a considerably higher level by using series arrays of tunnel junctions in the zero-crossing mode. In principle, no dc current supply would be needed for such an arrangement. Experimental results were presented by Kautz and Costabile [5]. They tested series arrays of 100 tunnel junctions operated with a 20-GHz microwave signal and reached stable quantized voltages up to 27 mV.

There are two limiting conditions which determine the optimum single junction parameters to get stable and large zero-current voltage steps. The plasma frequency should be smaller than the operating frequency [4]-[7]

$$(2eI_c/\hbar C)^{1/2} < \omega \tag{2}$$

where I_c denotes the critical current, C the capacity of the junction, and $\omega = 2\pi f$.

To exclude spatial variations of the supercurrent density, the junction length should be smaller than 4 λ_J [8]. λ_J is the Josephson penetration depth

$$\lambda_J = (\phi_0/2\pi\mu_0 j_c d)^{1/2} \tag{3}$$

where d is the sum of the thickness of the oxide barrier and the London penetration depths in both adjacent superconducting electrodes and j_c is the critical current density of the junction. ϕ_0 denotes the flux quantum.

The total current amplitude of the nth constant voltage step is given by

$$2J_c\left|J_n(2eV_{\mathrm{RF}}/\hbar\omega)\right|. \tag{4}$$

V_{RF} is the amplitude of the RF voltage and J_n the nth-order Bessel function.

II. EXPERIMENTAL PROCEDURES

Different series arrays of 2, 6, 14, and 54 single junctions are fabricated using a normal, photoresist stencil, lift-off process as described, for instance, by J. H. Greiner *et al.* [9]. A single inline type junction has an area of $10 \times 30 \mu\mathrm{m}^2$. A 54-junction array is shown in Fig. 2(a). The arrays consisting of a smaller number of single junctions are formed by only one row of junctions connecting the two superconducting current leads. In no case did the length of one row exceed 1.2 mm.

The base electrodes of the junctions are patterned from a lead alloy film containing 12 weight-percent In and 4.4 wt-% Au. The layer is deposited onto Corning glass 7059 substrates (thickness 0.5 mm) at a pressure of 10^{-4} Pa. During this process the substrate is kept close to a temperature of 77 K [10].

The total film is evaporated in two sequential steps. At first, lead and gold are evaporated from one boat followed by a second coevaporation of lead and indium. Each evaporation contributes half of the total film thickness of about 200 nm. The evaporation boats contain just as much material as needed to obtain the desired film thickness by complete evaporation.

The tunneling barriers are grown on the RF-plasma-cleaned base electrode layer by a low pressure RF-oxidation process

---

Manuscript received September 19, 1983; revised September 28, 1983, and January 24, 1984.

The authors are with the Physikalisch-Technische Bundestalt, Bundesalle 100, Germany.

0018-9456/84/0900-0311$01.00 © 1984 IEEE

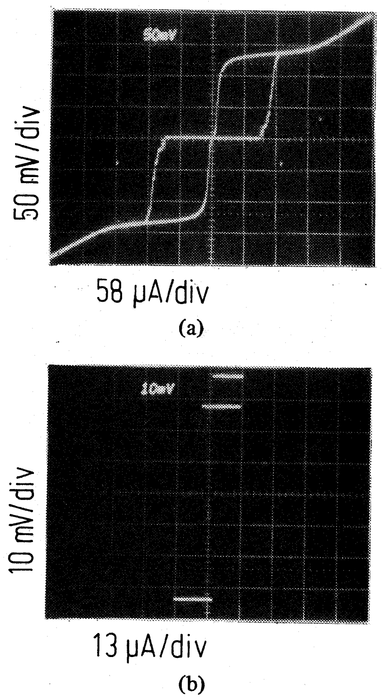

Fig. 4. (a) Current–voltage characteristic of a 54-junction array with RF power lacking (single junction area: 300 μm^2; mean critical current: $I_c = 105$ μA; mean critical current density: $j_c = 35$ A/cm^2). (b) Stability range of two zero crossing steps at +28 mV and −34 mV and a near zero current step at 37 mV of the same I–V characteristic under the influence of an RF power of 32 mW at the sample holder.

shows a stable step range of 50 μA at $V = 10$ mV. With 9 percent of 2 I_c, this value is only slightly smaller than that of the samples with smaller critical current densities. This example demonstrates that it is possible to use samples with a critical current density which is rather close to the maximum value following from condition (2). This is important when series arrays are used in a voltage standard because the constant reference voltage from the RF-induced steps has to be compared with the voltage of a Weston cell. For this operation, a sufficiently large step amplitude is required; otherwise switching over from one step to another would take place during operation.

The 54-junction arrays provide stable, RF-induced steps at a maximum voltage level of about 30 mV. This is 56-percent of the expected value of 54 mV. The maximum, stable-step amplitude at this voltage level attains only 7.4 percent of the mean value of 2 I_c (see Fig. 4). The measured maximum-step amplitude amounts to 10-percent of the mean value of 2 I_c.

These results demonstrate that with an increasing number of single junctions in an array, the maximum RF-induced step voltage per junction and the maximum step amplitude decrease. The same tendency, even to a greater degree, is found in [5].

IV. CONCLUSIONS

To operate the series arrays we used a different arrangement, as described in [5], to couple the RF power to each junction. This eliminates any need for additional circuit elements. We chose the relatively high frequency of 70 GHz, so the low-order steps reach the maximum voltage level of 1 mV (e.g., $V_7 \simeq 1$ mV at 70 GHz or $V_{24} \simeq 1$ mV at 20 GHz). From the Bessel function dependence of (4), it follows that low-order steps have a larger current amplitude than high-order steps. These advantages, and the rather high subgap resistance of the junctions with the PbInAu base electrodes, make it possible to reach stable RF-induced steps at 34 mV with only 54 junctions in a series array. However, the voltage level at the 14- and 54-junction arrays was not reached as would have been expected from the results of the arrays with a smaller number of junctions. This would have been 14 and 54 mV, respectively. There are at least two reasons for this difference. Firstly, the external electromagnetic noise is more effective in the high ohmic arrays. Secondly, the single junctions do not receive the same RF power. This depends on the differences between the capacitances of the single junctions, (the impedance of the junctions is mainly capacitive with respect to the microwave of 70 GHz so that the RF current to operate the junction at V_n is mainly $\omega C V_n$), and in particular on a nonuniform distribution of the RF current along the series array caused by standing waves, especially in the larger arrays.

It should be possible to minimize the influence of these disturbing factors by using high-frequency filters and a series coupling circuit which avoids any reflection of the RF power at the ends of an array.

Furthermore, the junction fabrication process should be optimized to arrive at a small dispersion of the junction parameters. An electrode material with a large subgap resistance and gap voltage can be used; for instance NbN [14]. Another way to overcome the difficulties is to operate the arrays at even higher frequencies.

ACKNOWLEDGMENT

The authors wish to thank V. Kose for stimulating discussions and L. Grimm for the design of the current source.

REFERENCES

[1] A. Barone and G. Paternò, *Physics and Applications of the Josephson Effect.* New York: Wiley, 1982, ch. 11, pp. 291–309.

[2] V. Kose, "Recent advances in Josephson voltage standards," *IEEE Trans. Instrum. Meas.*, vol. IM-25, pp. 483–489, Dec. 1976.

[3] J. T. Chen, R. J. Todd, and Y. W. Kim, "Investigation of microwave-induced dc voltages across unbiased Josephson tunnel junctions," *Phys. Rev. B*, vol. 5, pp. 1843–1849, Mar. 1972.

[4] M. T. Levinsen, R. Y. Chiao, M. J. Feldman, and B. A. Tucker, "An inverse ac Josephson effect voltage standard," *Appl. Phys. Lett.*, vol. 31, pp. 776–778, Dec. 1977.

[5] R. L. Kautz and G. Costabile, "A Josephson voltage standard using a series array of 100 junctions," *IEEE Trans. Magn.*, vol. MAG-17, pp. 780–783, Jan. 1981.

[6] R. L. Kautz, "On a proposed Josephson-effect voltage standard at zero current bias," *Appl. Phys. Lett.*, vol. 36, pp. 386–388, Mar. 1980.

[7] N. F. Pedersen, O. H. Soerensen, B. Dueholm, and J. Mygind, "Half-harmonic parametric oscillations in Josephson junctions," *J. Low Temp. Phys.*, vol. 38, pp. 1–23, Jan. 1980.

[8] A. Barone, W. J. Johnson, and R. Vaglio, "Current flow in large Josephson junctions," *J. Appl. Phys.*, vol. 46, pp. 3628–3632, Aug. 1975.

[9] J. H. Greiner, C. J. Kirchner, S. P. Klepner, S. K. Lahiri, A. J. Warnecke, S. Basavaiah, E. T. Yen, J. M. Baker, P. R. Brosious, H.-C. W. Huang, M. Murakami, and I. Ames, "Fabrication process for Josephson integrated circuits," *IBM J. Res. Devel.*, vol. 24, pp. 195–205, Mar. 1980.

[10] M. Murakami and C. M. Serrano, "Thermal stability of Pb-alloy Josephson junction electrode materials. III. Correlation of

microstructure and strain in Pb-In-Au base electrodes," *J. Appl. Phys.*, vol. 53, pp. 326-336, Jan. 1982.

[11] J. H. Greiner, "Oxidation of lead films by rf sputter etching in an oxygen plasma," *J. Appl. Phys.*, vol. 45, pp. 32-37, Jan. 1974.

[12] M. Murakami, H.-C. W. Huang, and C. J. Kirchner, "Thermal stability of Pb-alloy Josephson junction electrode materials. VIII. Effects of Au addition to Pb-Bi counter electrodes," *J. Appl. Phys.*, vol. 54, pp. 743-747, Feb. 1983.

[13] J. M. Baker, and J. H. Magerlein, "Tunnel barriers on Pb-In-Au alloy films," *J. Appl. Phys.*, vol. 54, pp. 2556-2568, May 1983.

[14] M. Hikita, K. Takei, T. Iwata, and M. Igarashi, "Fabrication of high quality NbN/Pb Josephson tunnel junctions with plasma oxidized barriers," *Japan. J. Appl. Phys.*, vol. 21, pp. L724-L726, Nov. 1982.

Short-Term Frequency Stability of Relaxation Crystal Oscillators

DRAGAN M. VASILJEVIĆ

Abstract—**Due to the need for stable frequency rectangular wave signals, various relaxation quartz crystal oscillators were designed. Therefore it is of interest to have data on their short-term frequency stability. The generally accepted definitions of measures for short-term frequency stability and measurement procedures are reviewed in this paper. Measurement results for the short-term frequency stability of quartz crystal multivibrators in time and frequency domains show a high spectral purity of the multivibrator output signal. The single-sideband-to-carrier phase noise has values lower than −90 and −120 dB on the offset frequencies of 1 and 10 Hz, respectively. The white phase noise is about −160 dB. The power law spectral density model of fractional frequency fluctuations for the quartz multivibrators is established and a discussion on the noise sources is given.**

I. Introduction

Sinusoidal quartz oscillators are used as secondary frequency standards, due to low cost, small size, and good short-term frequency stability. Recently, many relaxation quartz oscillators [1]-[9] have appeared. They are simply designed, with a small number of elements and insensitive to temperature changes. In this paper the short-term frequency stability of relaxation crystal oscillators is examined.

The definition of frequency stability was provided by the IEEE Subcommittee on Frequency Stability [10]. The general expression for the instantaneous output voltage $v(t)$ of a high-quality signal generator is

$$v(t) = (V_0 + \epsilon(t)) \sin (2\pi \nu_0 t + \phi(t)) \tag{1}$$

where V_0 and ν_0 are the nominal amplitude and frequency, while $\epsilon(t)$ and $\phi(t)$ are random amplitude and phase fluctuations, respectively. The fractional instantaneous frequency deviation from the nominal frequency ν_0, is defined as

$$y(t) = \frac{1}{2\pi\nu_0} \frac{d\phi(t)}{dt} = \frac{\nu(t)}{\nu_0} - 1 \tag{2}$$

where $\nu(t)$ is the instantaneous frequency.

1) The proposed definition of measure for frequency stability in the frequency domain is the one-sideband power spectral density $S_y(f)$ on a per Hertz basis of the instantaneous fractional frequency fluctuations [10]. It was shown [11] that the one-sideband power spectral density $S_\phi(f)$ on a per Hertz basis of the instantaneous phase fluctuations (phase noise) and $S_y(f)$ satisfy the relation

$$S_y(f) = \frac{f^2}{\nu_0^2} S_\phi(f) \tag{3}$$

where f is the offset frequency defined as a time-independent Fourier frequency calculated with respect to the nominal frequency value ν_0.

When AM noise $\epsilon(t)$ is negligible and the root-mean-square value of $\phi(t)$ is much smaller than 1 rad, there exists the relationship between the $\mathcal{L}$ function $\mathcal{L}(f)$ [12] and $S_\phi(f)$

$$\mathcal{L}(f) \simeq \tfrac{1}{2} S_\phi(f). \tag{4}$$

The function $\mathcal{L}$ is defined as the ratio of the one-side-band power spectral density on a per Hertz basis at an offset frequency f, to the total power of the output signal. The function $\mathcal{L}(f)$ can be measured directly on a spectrum analyzer if the aforementioned conditions for the existence of (4) are satisfied. On the basis of (3) and (4), we get the relationship between $S_y(f)$ and $\mathcal{L}(f)$

$$S_y(f) = 2\frac{f^2}{\nu_0^2} \mathcal{L}(f). \tag{5}$$

The most sensitive method for measuring the close-in carrier phase noise is a time-domain technique based on the Hadamard

---

Manuscript received August 1, 1983; revised January 23, 1984.

The author is with the Faculty of Electrical Engineering, University of Belgrade, 11000 Belgrade, Yugoslavia.

0018-9456/84/0900-0315$01.00 © 1984 IEEE

TABLE I
COMPONENTS OF THE ALLAN VARIANCE FOR THE POWER-LAW SPECTRAL DENSITY MODEL (ADAPTED FROM [12]).

Designation	$S_y(f)$	$S_\phi(f)$	$\sigma_y^2(\tau)$	Slope of $\sigma_y^2(\tau)$ vs. τ on log-log plot
Random walk frequency noise	$\frac{h_{-2}}{f^2}$	$\nu_o^2 \frac{h_{-2}}{f^4}$	$\frac{2\pi^2 h_{-2}\tau}{3}$	+ 1
Flicker frequency noise	$\frac{h_{-1}}{f}$	$\nu_o^2 \frac{h_{-1}}{f^3}$	$2\ln 2 h_{-1}$	0
White frequency noise	h_o	$\nu_o^2 \frac{h_o}{f^2}$	$\frac{h_o}{2\tau}$	- 1
Flicker phase noise	$h_1 f$	$\nu_o^2 \frac{h_1}{f}$	$\frac{h_1}{4\pi^2\tau^2}(1.038 + 3\ln 2\pi f_h\tau)$	between -2 and -1
White phase noise	$h_2 f^2$	$\nu_o^2 h_2$	$\frac{3h_2 f_h}{4\pi^2\tau^2}$	- 2

variance [13] and realized by a frequency counter. The counter is a linear system that measures phase fluctuations of the input signal over the gate time τ and divides the result by $2\pi\tau$ to give the frequency

$$\nu(t) = \frac{1}{2\pi\tau}(\phi(t) - \phi(t-\tau)). \tag{6}$$

Starting from the weighted combination of $N = (M+1)/2$ pairs of counter measurements taken at different times t_i as

$$m(t) = \frac{1}{2\pi\tau}\sum_{i=0}^{M} \alpha_i \nu(t_i), \qquad \alpha_i = (-1)^i \tag{7}$$

we define the variance of the process $m(t)$, called the Hadamard variance, as

$$\sigma_m^2(\tau, \tau_d, N) = \left\langle \frac{1}{K-1}\left(\sum_{i=1}^{K}\left(m_i - \frac{1}{K}\sum_{j=1}^{K} m_j\right)^2\right)\right\rangle \tag{8}$$

where $\langle g \rangle$ denotes the infinite time average of g. K is the number of measurement sequences $m(t)$ and τ_d is the time between consecutive measurements, called dead time.

Near the frequency $f_0 = (1/2(\tau + \tau_d))$, for large N and $\tau = 2\tau_d$, the power spectral density of the input signal phase fluctuations is calculated as [13]

$$S_\phi(\omega_0) \simeq 0.183 \frac{\sigma_m^2(\tau, \tau_d, N)}{N f_0} \tag{9}$$

where $|\omega \pm \omega_0| \ll \omega_0$.

A system which measures the sequence $m(t)$ (7), in the time domain has, in the frequency domain, a transfer function [12] which corresponds to a filter with many passbands centered on the frequencies Pf_0, where P's are prime numbers except three [13]. The bandwidth of each band is $BW = 1/N\tau$.

Due to many passbands in the transfer function, an error appears in the estimation of the phase noise value $S_\phi(\omega)$. The value of the error depends on the presence of flicker phase noise (f^{-1}) and white phase noise (f^0) (Table I). For example, in the presence of the flicker phase noise only, the measured phase noise value is about 5 dB higher than the actual one [14].

The most sensitive and direct method of phase noise measurement for higher offset frequencies is based on the phase demodulation of the signal under test and spectrum examination of the phase detector output by a low-frequency spectrum analyzer [10], [15]. In this method, the signal under test is mixed with a low-noise reference source in a double-balanced mixer. The signals are set in phase quadrature using a phase-locked loop (PLL). To avoid phase noise cancellation by loop tracking [15], the bandwidth of the PLL must be much less than the lowest offset frequency of the measurements. If the phase of the oscillators is adjusted so that their phase difference $\Delta\phi$ satisfies the condition $|\Delta\phi| \ll 1$ rad, the signal V at the output of the mixer is

$$V_{\mathrm{rms}} = K_\phi \Delta\phi_{\mathrm{rms}} \tag{10}$$

where V_{rms} is a noise level measured by the spectrum analyzer in a 1-Hz bandwidth, and K_ϕ is a phase detector constant. Using (4) we get

$$\mathcal{L}(f) = \frac{S_\phi(f)}{2} = \frac{1}{2}\frac{V_{\mathrm{rms}}^2}{K_\phi^2}. \tag{11}$$

The noise measured by this technique represents the combined noise of the source under test and the reference source. Consequently, the phase noise of the reference must be known.

2) The accepted definition of measure for frequency stability in time domain is the zero-dead-time, two-sample variance (the Allan variance $\sigma_y^2(\tau)$) [10] of the fractional frequency. The average fractional frequency

$$\bar{y}_i = \frac{1}{\tau}\int_0^\tau y(t)\,dt = \frac{\bar{\nu} - \nu_0}{\nu_0} \tag{12}$$

is measured by the counter over an interval of time τ followed by a dead time τ_d. If the measurement process is repeated until $N+1$ values of $\bar{y}_i$ are reached, the estimation of the Allan variance is obtained as

$$\hat{\sigma}_y^2(\tau) = \frac{1}{2N} \sum_{j=1}^{N} (\bar{y}_{j+1} - \bar{y}_j)^2. \tag{13}$$

For higher resolution of the measurement system, a heterodyne technique [10] is used. The signal under test is mixed with a reference signal in a double-balanced mixer and filtered by a sharp low-pass filter with the cutoff frequency f_h. To allow meaningful comparisons of measurement results in the time domain, the value of f_h must be specified [12]. The down-converted frequency is referred to as the beat frequency ν_b.

When an almost linear drift of frequency in time exists (i.e., $y(t) = d_1 t$), the direct calculation from (13) gives an increase of the Allan variance value by the amount

$$\sigma_y^2(\tau)_{\mathrm{LD}} = \frac{d_1^2}{2} \tau^2. \tag{14}$$

This means that, in the plot $\sigma_y(\tau)$ versus τ, there exists a τ^{+1}-law for greater values of τ. The error introduced by deterministic variations of frequency in estimates of short-term frequency stability can be eliminated by using a structure function approach [16], [17].

3) Relationships for translation among frequency and time domain measures of the short-term frequency stability are known [10], [12]. Using the power-law spectral-density model for $S_y(f)$ in the form

$$S_y(f) = \sum_{i=-2}^{2} h_i f^i \tag{15}$$

the relationship between components of the Allan variance and power spectral density of $S_y(f)$ were derived (see Table I).

The methods described are developed for sinusoidal signals. In relaxation oscillators the output signal is a train of rectangular pulses, phase modulated in such a way that the deviation of pulse edges from the equilibrium position at some moment is proportional to the modulating signal (noise) at the same moment (the first type phase modulation [18]). The question arises whether the spectra in the side bands of the basic frequency harmonics overlap. If the one-test-tone analysis is performed (the test tone is a sinusoid which serves as the modulating signal), under the assumption that the greatest phase deviation is much smaller than 1 rad, we obtain a spectrum around each harmonic of the basic frequency which is determined by the Bessel functions of the first kind and the nth order from the small argument. Therefore, amplitudes of the spectrum decay quickly. The overlapping of side ranges is thus proportional to the phase deviation made by the noise and is negligible.

II. MEASUREMENT INSTRUMENTATION AND OSCILLATORS

A. Instrumentation

Short-term frequency stability in the time domain was estimated by the Allan variance ($\sigma_y^2(\tau)$). Measurements were realized on the frequency stability analyzer HP 5390A which uses the heterodyne down-conversion technique. A test oscillator is connected to the system via the isolation amplifier realized on the basis of Walls *et al.* [19]. Using this amplifier, frequency pulling caused by insufficient isolation of the reference and test oscillators is suppressed [20]. As a reference oscillator, a quartz frequency standard HP 105B [21] was used. It has an Allan deviate as in Table II and an aging rate of order of 5×10^{-10}/24 h [21]. The frequency stability analyzer has a system software controlling the measurement process and computing the Allan variance. The system sensitivity [23] is given by

TABLE II
THE ALLAN DEVIATE FOR CRYSTAL OSCILLATOR HP105B [21]

τ (s)	0.01	0.1	1
$\sigma_y(\tau)$	1.5×10^{-10}	1.5×10^{-11}	5×10^{-12}

$$\sigma_y(\tau)_{\mathrm{sens}} = \frac{1.155 \times 10^{-9}}{\tau} \frac{\nu_b}{\nu_0}. \tag{16}$$

In the frequency domain, the spectral density of the phase fluctuations near a carrier frequency was measured on the basis of the Hadamard variance. Measurements were also realized on the frequency stability analyzer 5390A with the same hardware as for the Allan variance. On the basis of the input data (offset frequencies and filter bandwidth, (9)), the system software calculates the values of the measurement time τ, dead time τ_d, and the number of measurement pairs N. The single-sideband-to-carrier phase-noise-power per Hertz $\mathcal{L}(f)$ is calculated for S measurement sweeps in the measurement band of offset frequencies. The mean value of $\mathcal{L}(f)$ is the output result. To eliminate the error in phase-noise measurement due to the responses of the Hadamard filter at frequencies higher than the measuring frequency f_0 [14], the system has a low-pass filter with the cut-off frequency f_h between f_0 and $5f_0$. The filter is connected between the mixer and counter. The sensitivity of this system is derived in [13] and is given for the HP5390A by the following equation:

$$\mathcal{L}(f)_{\mathrm{sens}} = -173 + 20 \log_{10} \nu_b - 10 \log_{10} f \quad [\mathrm{dB}]. \tag{17}$$

The maximum value of the offset frequency in the spectral analysis performed by the frequency stability analyzer 5390A is $\nu_b/6$ [13]. Therefore, measurement of $\mathcal{L}(f)$ in the wider range of offset frequencies is not possible. Any increase of the beat frequency ν_b is useless because of the decrease in the system sensitivity.

The estimation of the phase noise in the wider range of offset frequencies may be given on the basis of the measurement data for the Allan variance for small values of τ. Using the relationships between $\sigma_y^2(\tau)$ components and the power law spectral density model (see Table I, last two rows), we may estimate the existence and level of the flicker and white phase noise. Sensitivity limits of the frequency stability analyzer 5390A for $\sigma_y(\tau)$ measurements, make it possible to estimate white phase noise down to the level of -175 dB, if the beat frequency ν_b and measurement bandwidth f_h are 100 Hz and 100 kHz, respectively [13]. However, the reference oscillator's

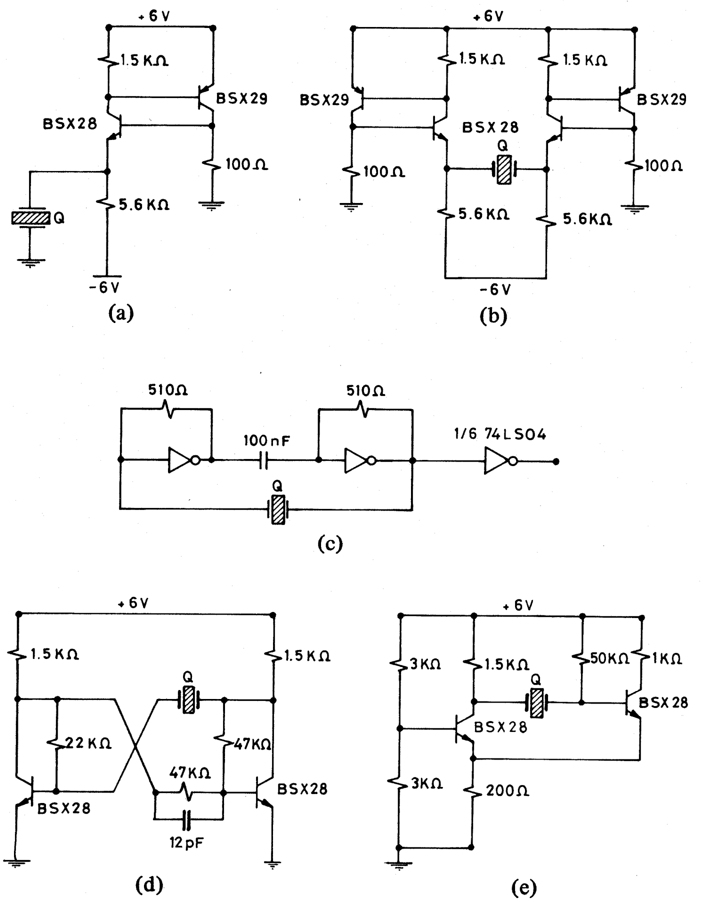

Fig. 1. Tested oscillators: (a) complementary switch multivibrator [7]; (b) two complementary switch multivibrator [6]; (c) TTL multivibrator [1]; (d) collector-coupled multivibrator [9]; and (e) emitter-coupled multivibrator [4].

(HP 105B) noise (Table II), limits the white phase noise floor of measurement system to the value of about -165 dB.

B. Circuits and Operating Conditions

The tested oscillators are shown in Fig. 1. The circuits were realized on the basis of data from [1], [4], [6], [7], and [9]. Metal-film resistors, styroflex capacitors, switching transistors, LS TTL integrated circuits, and stabilized power supplies of 6 V were used. Experiments were performed with a general purpose AT-cut crystal, in a soldered case, labeled as IMP, whose parameters are listed in Table III. The aging rate of this crystal is about 5 Hz/MHz per year. In order to examine the dependence of the oscillator's characteristics versus crystal features, a high-quality crystal labeled as JK was used (see Table III).

The environmentally induced component of the frequency stability is minimized by keeping constant operating conditions. The oscillators were tested at constant temperature, load, and power supply voltage.

III. Measurement Results and Discussion

The measurements were realized with the oscillators shown on Fig. 1. The components used had the values labeled on this figure.

TABLE III
Measured Characteristics of the Quartz Crystal Units Used

Quartz crystal unit characteristics	IMP crystal TYPE 5111	JK crystal TYPE G-12AS
Series resonant frequency [Hz]	999893	999982
Series resonant resistance [Ω]	128	5
Inductance [H]	3.995364	1.524630
Series capacitance [pF]	0.006341	0.016615
Parallel capacitance [pF]	2.4	11.3
Quality factor	195642	1878000
Package	soldered case	vacum-glass case

A. Measurements in the Frequency Domain

All measurements were performed at the carrier frequency $\nu_0 = 1$ MHz with the beat frequency $\nu_b = 105$ Hz in the range of offset frequencies from 0.1 to 20 Hz. The bandwidth of the Hadamard filter was chosen as 10 percent of the offset frequency. The number of measurement sequence repetitions was $K = 10$ for three sweeps over the range of offset frequencies ($S = 3$).

1) Noise Analysis in Various Oscillators: Results for single-side-band to carrier phase noise $\mathcal{L}(f)$ for circuits in Fig. 1 are given in Table IV and in Fig. 2. (solid line). The IMP crystal was used. It seems that the best results are obtained for the complementary switch crystal oscillators (Fig. 1(a), (b)). The TTL crystal oscillator has almost identical characteristics (Fig. 1(c)) with a somewhat higher level of $1/f^2$ noise. Collector- and emitter-coupled multivibrators (Fig. 1(d), (e)) have a very high level of the flicker frequency noise (Fig. 2, Table IV).

2) Noise Analysis of the Complementary Switch Multivibrator with Various Circuit Modifications: In order to analyze phase noise dependence in this multivibrator on various circuit modifications, some experiments were conducted. Results are given in Table V. The basic configuration of the circuit is as in Fig. 1(a). Experiment I (the first column in Table V) was performed with low-noise amplifier transistors BC 318, BC 321 instead of switching transistors BSX 28 and BSX 29. In the experiment labeled II (Table V), the capacitor $C = 12$ pF was added between the collectors of the switching transistors to provide a slower operation of the complementary switch. In experiment III (Table V), the output sinusoidal signal was taken from the capacitor ($C = 56$ pF) connected in series with the quartz crystal unit (Fig. 1(a)). In Experiment IV, the rectangular output signal, taken from the collector of the p-n-p transistor (Fig. 1(a)) is first shaped by six Schmitt triggers, and then measured. In this way, the influence of the

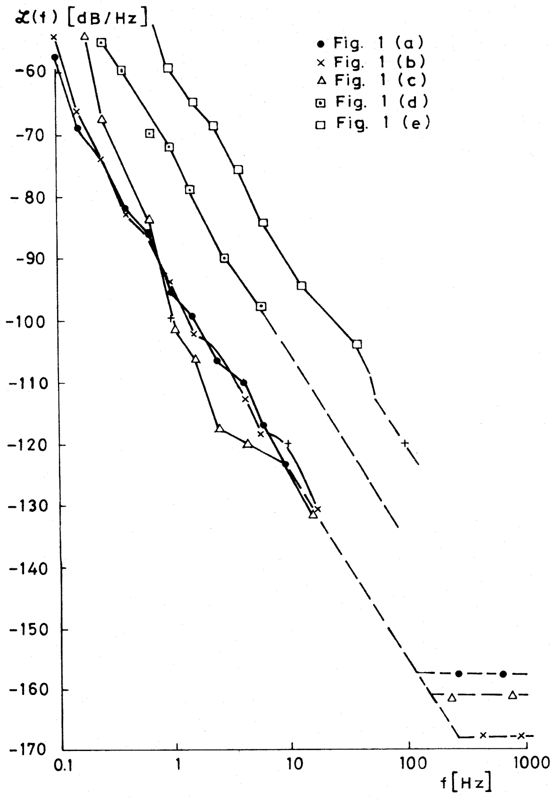

Fig. 2. Phase noise $\mathcal{L}(f)$ of quartz multivibrators from Fig. 1.

TABLE IV
PHASE NOISE $\mathcal{L}(f)$ OF OSCILLATORS FROM FIG. 1

Offset frequency f[Hz]	Single-sideband to carrier phase noise $L(f)$ [dB/Hz]				
	Oscillator from Fig.				
	1(a)	1(b)	1(c)	1(d)	1(e)
0.1	-57.1	-54.5	-35.2	-	-
0.25	-74	-74.2	-67.8	-55.5	-38
0.63	-86.2	-87.3	-84.4	-70.5	-48.4
1.53	-99.6	-102.1	-106.8	-79.2	-65.1
3.67	-102.3	-108	-118	-90.3	-75.6
9.17	-116.7	-119.5	-121.8	-98	-83.3
18.33	-121.4	-130.3	-132.8	-	-93.9

wave shaping on the oscillator noise was explored. Experiment V was performed by filtering the fifth harmonic from the rectangular output signal and measuring its phase noise. All the mentioned experiments were realized with the IMP quartz crystal unit. The effect of the quartz crystal unit on the noise of the oscillator was investigated using the high-quality JK quartz crystal. Results are given in the column denoted by VI in Table V.

B. Measurements in Time Domain

Carrier and beat frequency in the measurements were $\nu_0 =$ 1 MHz and $\nu_b = 105$ Hz, respectively. The bandwidth of the low-pass filter was $f_h = 100$ kHz and the number of samples $N = 50$. Measurement time was varied from 0.01 to 10 s.

1) The Allan Deviate for Various Quartz Multivibrators: Values of two-sample, zero-dead-time, deviate for circuits in Fig. 1 are shown in Fig. 3 and in Table VI. All measurements were carried out with the IMP quartz crystal unit. The best results were obtained for the complementary switch multivibrators and the TTL oscillator (Fig. 1(a)-(c)). The very characteristic increase of the Allan deviate for large values of τ is due to the high-level of the random walk frequency noise (see Table I and measurement results for phase noise in Section III-A). Due to the mean frequency drift in the order of $5 \cdot 10^{-8}$/day,[1] enlargement of the $\sigma_y(\tau)$ for large τ is $4 \cdot 10^{-13}$.

---

[1] The data were obtained experimentally by monitoring the multivibrator mean frequency during one month.

TABLE V
PHASE NOISE $\mathcal{L}(f)$ FOR VARIOUS MODIFICATIONS OF THE COMPLEMENTARY SWITCH MULTIVIBRATOR

Offset frequency f [Hz]	Single-sideband to carrier phase noise $\mathcal{L}(f)$ [dB/Hz] Experiment labeled as: I	II	III	IV	V	VI
0.25	-	-	-72.3	-	-59.4	-
0.5	-79.4	-84.8	-83	-85.1	-68.9	-73.4
1.25	-93.6	-102.3	-94.3	-94.8	-81.8	-89.5
3.3	-106.9	-108.1	-105.9	-107.6	-95.3	-103.4
9.89	-116.7	-119.7	-117.7	-115	-103.8	-119.5
19.78	-118.7	-123.5	-121.7	-123.8	-110.4	-124.3

TABLE VI
THE ALLAN DEVIATE FOR MULTIVIBRATORS FROM FIG. 1

Measurement time τ [s]	The Allan deviate $\sigma_y(\tau)$ Oscillator from Fig. 1(a)	1(b)	1(c)	1(d)	1(e)
0.01	$8 \cdot 10^{-10}$	$2.6 \cdot 10^{-10}$	$2.9 \cdot 10^{-10}$	-	$3.5 \cdot 10^{-9}$
0.1	$3.6 \cdot 10^{-11}$	$6 \cdot 10^{-11}$	$5.5 \cdot 10^{-11}$	$2.3 \cdot 10^{-10}$	$2 \cdot 10^{-9}$
1	$4.5 \cdot 10^{-11}$	$1.3 \cdot 10^{-10}$	$1.1 \cdot 10^{-11}$	$3 \cdot 10^{-10}$	$2 \cdot 10^{-9}$
10	$2.1 \cdot 10^{-10}$	$1.2.10^{-9}$	$1.1 \cdot 10^{-9}$	$2.7 \cdot 10^{-10}$	$2.3 \cdot 10^{-9}$

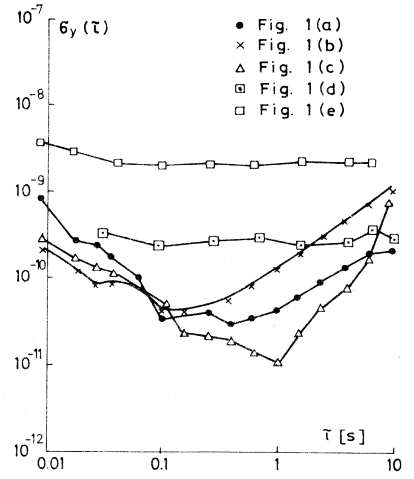

Fig. 3. The Allan deviate $\sigma_y(\tau)$ of quartz multivibrators from Fig. 1.

This is a much lower value than the one generated by random-walk frequency noise. Flicker frequency noise determines the low level of the Allan deviate. On the basis of the measurement data of the Allan deviate for low values of τ, an estimate of the white phase noise floor was made (see Table I). Results are plotted on Fig. 2 by dashed lines. The high level of the flicker frequency noise for the collector and emitter-coupled multivibrators Fig. 1(c), (d), determines the constant value of the Allan deviate in the range of measurement time τ.

2) The Allan Deviate of the Complementary Switch Quartz Multivibrator with Various Circuit Modifications: The same experiments as in Section III-A-2 were carried out. Results for the Allan deviate are given in Table VII.

C. Discussion

On the basis of the previous experimental data, the power-law spectral density model for relaxation crystal oscillators is defined in the form

$$S_y(f) = \frac{h_{-2}}{f^2} + \frac{h_{-1}}{f} + h_2 f^2. \tag{18}$$

Coefficient values for various oscillators are given in Table VIII.

It is known [11] that random-walk frequency noise usually relates to oscillator environment (temperature, shocks, vibration). In our experiments the circuits under test were placed in a thermos. We believe that $1/f^2$ noise would be much lower if the circuits had been situated in a high-precision thermostat.

The quantity of the relaxation crystal oscillators white phase noise is determined by the simplicity of these circuits.

In such oscillators there are no parts of the circuit beyond the oscillator loop and therefore additive white noise sources causing white phase noise do not exist [11].

Flicker frequency noise sources in quartz oscillators are related to the quartz resonator [12]. Recently, the nature of this noise has been explored on the basis of the general quan-

TABLE VII
THE ALLAN DEVIATE FOR VARIOUS MODIFICATIONS OF THE COMPLEMENTARY SWITCH MULTIVIBRATOR

Measurement time τ [s]	The Allan deviate $\sigma_y(\tau)$					
	Experiment labeled as:					
	I	II	III	IV	V	VI
0.01	$6\cdot10^{-10}$	$3.8\cdot10^{-10}$	$4.9\cdot10^{-10}$	$4.1\cdot10^{-10}$	$2.6\cdot10^{-10}$	$5\cdot10^{-10}$
0.1	$6\cdot10^{-11}$	$5.1\cdot10^{-11}$	$8\cdot10^{-11}$	$6.2\cdot10^{-11}$	$6.99\cdot10^{-11}$	$7.2\cdot10^{-11}$
1	$4\cdot10^{-11}$	$3.4\cdot10^{-11}$	$5.2\cdot10^{-11}$	$6.9\cdot10^{-11}$	$1.7\cdot10^{-10}$	$8.5\cdot10^{-11}$
10	$2.7\cdot10^{-10}$	$1.5\cdot10^{-10}$	$3.7\cdot10^{-10}$	$2.5\cdot10^{-10}$	$1.4\cdot10^{-9}$	-

TABLE VIII
POWER-LAW SPECTRAL DENSITY MODEL COEFFICIENTS FOR VARIOUS CRYSTAL MULTIVIBRATORS

Oscillator from Fig.	Coefficients		
	h_{-2}	h_{-1}	h_2
1(a)	$3.3\cdot10^{-22}$	$2.5\cdot10^{-21}$	$8.6\cdot10^{-28}$
1(b)	$2\cdot10^{-22}$	$9\cdot10^{-22}$	$9.1\cdot10^{-29}$
1(c)	$1.4\cdot10^{-21}$	$3.6\cdot10^{-22}$	$1.13\cdot10^{-28}$
1(d)	-	$7.2\cdot10^{-20}$	-
1(e)	-	$3.5\cdot10^{-18}$	-

tum theory of $1/f$ noise [23]. It is concluded that fractional frequency fluctuations are caused by fluctuations of the oscillator dissipative constant γ. The constant γ is defined as a real part of the root of the oscillating system's characteristic equation [24]. The value of γ depends on the quartz crystal unit parameters and on circuit characteristics. This explains the unequal flicker frequency noise in various multivibrator circuits with the same quartz crystal unit. Deterministic analyses must be carried out in further work to determine dissipative constants of crystal multivibrators for the purpose of noise sources identification.

The measurement results, obtained in the time domain, are in agreement with the results measured in the frequency domain. The comparison is made on the basis of the relationships from Table I.

The examination of the influence of circuit modifications on the complementary quartz multivibrator (Fig. 1(a)) noise gives the following results. The use of low-noise amplifier transistors instead of switching transistors, does not yield substantial differences in the oscillator noise (Experiment I, Tables V and VII). The same result is valid for longer switching times of the complementary switch (Experiment II). Experiments III and IV confirm the known result that waveshaping of the oscillator output signal does not change its noise. It is well known that frequency doubling increases the noise level of the oscillator output signal by 6 dB per octave [16]. This result is confirmed by Experiment V. In Experiment VI the same noise level is obtained using a general-purpose quartz crystal unit or a high-quality unit. This means that the primary component of noise in relaxation crystal oscillators is due to the circuit's characteristics.

IV. CONCLUSION

Relaxation quartz crystal oscillators containing a small number of elements are simply designed. The complementary switch multivibrators (Fig. 1(a), (b)) and the TTL multivibrator (Fig. 1 (c)), have good spectral purity in the sense that in the output signal spectrum there are small, nonharmonic components.

The level of the flicker frequency noise is mainly determined by the multivibrator circuit structure. The low white-phase noise floor is a consequence of the circuit simplicity. The mean frequency drift of the crystal multivibrators is more pronounced than that in harmonic oscillators due to a higher level of the quartz-crystal unit excitation.

REFERENCES

[1] J. H. Kolataj, "Linearise your TTL gates—then build useful circuits with them," *Electron. Des.*, vol. 17, pp. 640–641, Mar. 1, 1969.
[2] W. I. Fletcher, *An Engineering Approach to Digital Design.* Englewood Cliffs, NJ: Prentice Hall, 1980, ch. 5.
[3] H. R. Newhoff, "Crystal-controlled multivibrators," *Electron.*, vol. 36, pp. 60–62, Apr. 12, 1963.
[4] D. Vasiljević and S. Tesic, "An emitter-coupled quartz multivibrator," *Int. J. Electron.*, vol. 42, pp. 551–558, June 1977.
[5] D. Vasiljević, "Stabilization of multivibrator frequency by means of quartz," in *Proc. ETAN* (Opatija, Yugoslavia), June 1–4, 1976, (in Serbocroat).

[6] D. Vasiljević, "A quartz multivibrator using two regenerative switches," *Proc. IEEE*, vol. 65, pp. 166–167, Jan. 1977.

[7] D. Vasiljević, "A quartz complementary multivibrator," *Proc. Inst. Elec. Eng.*, vol. 123, pp. 851–854, Sept. 1976.

[8] D. D. Damljanović, "New quartz multivibrator," *Proc. IEEE*, vol. 62, pp. 640–641, May 1974.

[9] J. Freeman, "Crystal controlled multivibrator," in *Circuit Design Idea Handbook*, B. Furlow, Ed. Boston, MA: 1980, p. 138.

[10] J. A. Barnes, A. R. Chi, L. S. Cutler, D. J. Healy, D. B. Leeson, T. E. McGunigal, J. A. Mullen, W. L. Smith, R. L. Sydnor, R. Vessot, and G.M.R. Winkler, "Characterization of frequency stability," *IEEE Trans. Instrum. Meas.*, vol. IM-20, pp. 105–120, May 1971.

[11] D. W. Allan, "Statistics of atomic frequency standards," *Proc. IEEE*, vol. 54, pp. 221–230, Feb. 1966.

[12] J. Rutman, "Characterization of phase and frequency instabilities in precision frequency sources: Fifteen years of progress," *Proc. IEEE*, vol. 66, pp. 1048–1074, Sept. 1978.

[13] L. Peregrino and D. W. Ricci, "Phase noise measurement using a high resolution counter with on-line data processing," in *Proc. 30th Ann. Frequency Control Symp.* (Atlantic City, NJ), June 2–4, 1976.

[14] "Measuring phase spectral density of synthesized signal sources exhibiting f_0 and f^{-1} noise characteristics with the 5390A frequency stability analyzer," Hewlett-Packard application note 225.

[15] "Applications and measurements of low phase noise signals using the 8662 A synthesized signal generator," Hewlett-Packard application note 283-1, Nov. 1981.

[16] W. C. Lindsey and C. M. Chie, "Theory of oscillator instability based upon structure functions," *Proc. IEEE*, vol. 64, pp. 1652–1666, Dec. 1976.

[17] W. C. Lindsey and C. M. Chie, "Identification of power-law type oscillator phase noise spectra from measurements," *IEEE Trans. Instrum. Meas.*, vol. IM-27, pp. 46–53, Mar. 1978.

[18] P. F. Panter, *Modulation, Noise and Spectral Analysis.* New York: McGraw Hill, 1965, ch. 7.

[19] F. L. Walls, S. R. Stein, J. E. Gray, and D. J. Glaze, "Design considerations in state-of-the-art signal processing and phase noise measurement systems," in *Proc. 30th Annu. Frequency Control Symp.* (Atlantic City, NJ), June 2–4, 1976.

[20] "Measurement considerations when using the 5390 A option 010," Hewlett-Packard application note 225-1.

[21] Hewlett-Packard catalog 1982, p. 307.

[22] "Users Manual for 5390 A frequency stability analyzer," Hewlett-Packard, Dec. 1977.

[23] P. H. Handel, "Nature of $1/f$ frequency fluctuations in quartz crystal resonators," *Solid-State Electron.*, vol. 22, pp. 875–876, Oct. 1979.

[24] A. A. Andronov, A. A. Witt, and S. E. Chaikin, *Theory of Oscillations.* Moscow: Fizmatgiz, 1959, ch. 10 (in Russian).

An Approach to Automatic FLIR Video Assessment

MALLORY J. BOYD AND ALFRED G. SUTTON

***Abstract*—This paper describes an approach to automatic video assessment of military infrared imaging systems by employing automated analysis techniques on measured system responses. Included are a description of the developmental test configuration and methodology, and a description of the activity with initial findings and conclusions.**

I. INTRODUCTION

PERFORMANCE and diagnostic testing of Navy-deployed electro-optical (EO) avionics equipment and, in particular, forward looking infrared (FLIR) weapons replaceable assemblies (WRAs) is one of the major intermediate maintenance level test requirements which has not been automated, or implemented in automatic test equipment (ATE). At present, a human operator must subjectively evaluate a FLIR-displayed image to assess WRA performance. This is a time-consuming process which is proving to be unacceptable due to: the increasing number (and mix) of deployed systems at a single site, the decreasing availability of highly trained maintenance personnel, the increasing throughput demand on deployed test equipment, and the ambiguous test results which can often occur from a subjective operator evaluation of displayed imagery.

In recognition of these problems, the Naval Weapons Center (NAVWPNCEN), China Lake, CA, has been tasked by the Naval Air Systems Command (NAVAIR) to investigate and develop test concepts and technology applicable to the automatic testing of EO WRA's.

II. APPROACH

Automatic test of an FLIR WRA constitutes a significant ATE systems design problem in which all elements of a typical ATE architecture may be impacted. A critical component of the overall automation problem is the computer processing of WRA output video signals as a means to ascertain WRA imagery performance (or lack of it) while subjecting the WRA to optical input stimulus under ATE control.

Consequently, as part of our investigations, the various laboratory and system specification performance parameters normally used to define the imaging performance of a typical FLIR system were analyzed to determine which were most

---

Manuscript received August 31, 1983. This paper was originally presented at Autotestcon 83 (Ft. Worth, TX), November 1–3, 1983.

M. J. Boyd is with the Naval Weapons Center, China Lake, CA 93555.

A. G. Sutton is with Comarco, Inc. (Simutech Division), Ridgecrest, CA 93555.

0018-9456/84/0900-0322$01.00 © 1984 IEEE

essential (must be tested in the field) and, of those, which constitute the greatest technical risk to implement in an automatic processing test equipment architecture. Those parameters deemed both critical and difficult to implement were selected to form a baseline test requirement for further investigation.

A preliminary trade-off study was then conducted to determine what test technique(s) appeared most suitable for each requirement. Typical factors considered in this trade-off included: target complexity and numbers of targets required, test software complexity, algorithm and processor complexity, and memory and data acquisition requirements. Also considered was whether parameters could be grouped and processed in a single test, or if a dedicated test for a single parameter was required. Inputs to the trade-off study included: a literature search, an industry survey, the test techniques in use at contractor facilities or existing military deployed EO test equipment, and new concepts based upon airborne system and processing system expertise available in-house.

A laboratory facility was established to further trade off and evaluate concepts by experimentation. Upon selection of a test concept to be evaluated, detailed test structure and desired outputs were specified and implemented in the EO test facility. The development of test algorithms into modular software packages was accomplished and experiments were conducted to exercise the software design and identify design changes, as required. This iterative cycle of design, evaluation and change was continued until a satisfactory level of performance was achieved.

For each parameter evaluated, a parallel effort of measurement by traditional manual (subjective) methods was also conducted to provide control and traceability for the automated processing results.

III. Discussion

The following provides a detailed discussion of our effort. Three major subject areas are discussed: a description of the EO test facility, a summary of the test requirements established in initial trade-off studies, and a test concept trade-off example, for one requirement, to illustrate methodology.

A. Test Facility

The EO test facility is based upon a Digital Equipment Corporation PDP 11/44 minicomputer, programmable commercial test equipment, an independent exploratory development (IED) FLIR WRA similar to an S-3A FLIR architecture (OR-89), an AAM-60(V)-1 manual test set and various ancillary equipment. Fig. 1 illustrates the facility hardware configured to process single lines of FLIR or TV WRA video output data. In that configuration, data is collected and digitized by a Tektronix 7612D and transferred to the PDP-11/44 via an IEEE 488 buss for storage and processing. Over 1 Mbyte random access memory and 20 Mbytes of disc storage is available. Processing results can be displayed on a terminal or hard copied on an ancillary *X–Y* plotter.

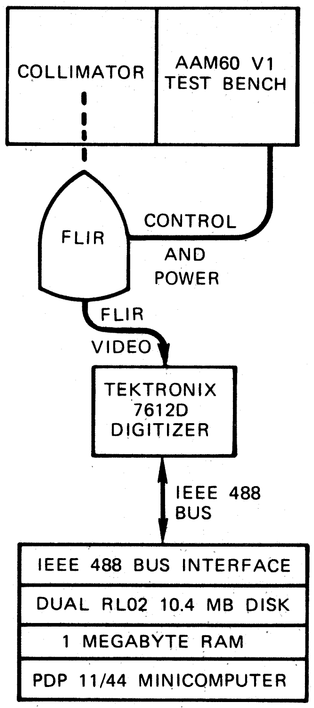

Fig. 1. Hardware configuration for processing single lines of FLIR or TV video output.

Facility software consists of an RSX-11M operating system and processing is implemented in Fortran 77. To date, approximately 5000 lines of Fortran code have been developed for experimental processing purposes, which comprise 96 software modules or submodules. Fig. 2 illustrates typical software module partitioning and flow necessary to evaluate FLIR WRA performance parameters.

B. Test Requirements

Three basic image test requirements have been established: Spatial Resolution, Thermal Sensitivity, and Image Quality. The first two requirements relate, in general, to a FLIR system operator's ability to detect an object in the field of view of the system. The third requirement can be related to the system's general response and the overall "goodness" of the displayed image and raster. It is postulated that each test requirement can be satisfied by evaluation of a measurable test parameter or group of test parameters related to that requirement. Table I summarizes the requirements and related critical and/or high risk parameters selected for evaluation.

C. Test Concept Trade-Off

As previously mentioned, the test concept trade-off of one test requirement, spatial resolution, is presented here to illustrate the methodology applied to all Table I requirements.

Spatial resolution represents a FLIR systems ability to resolve small objects within the system's field of view. The smaller an object that can be resolved, the better the spatial resolution. Spatial resolution is a critical test requirement which must be tested in the field. Test equipment design is impacted by this requirement since, as spatial resolution increases, test equipment processing becomes more complex (increased data rates and bandwidth) and optical stimulus requirements become more stringent. In general, spatial resolution parameters are field tested in only one detector scan direction (along scan) by placing test targets, oriented perpendicular to the scan direction, in the WRA field of view.

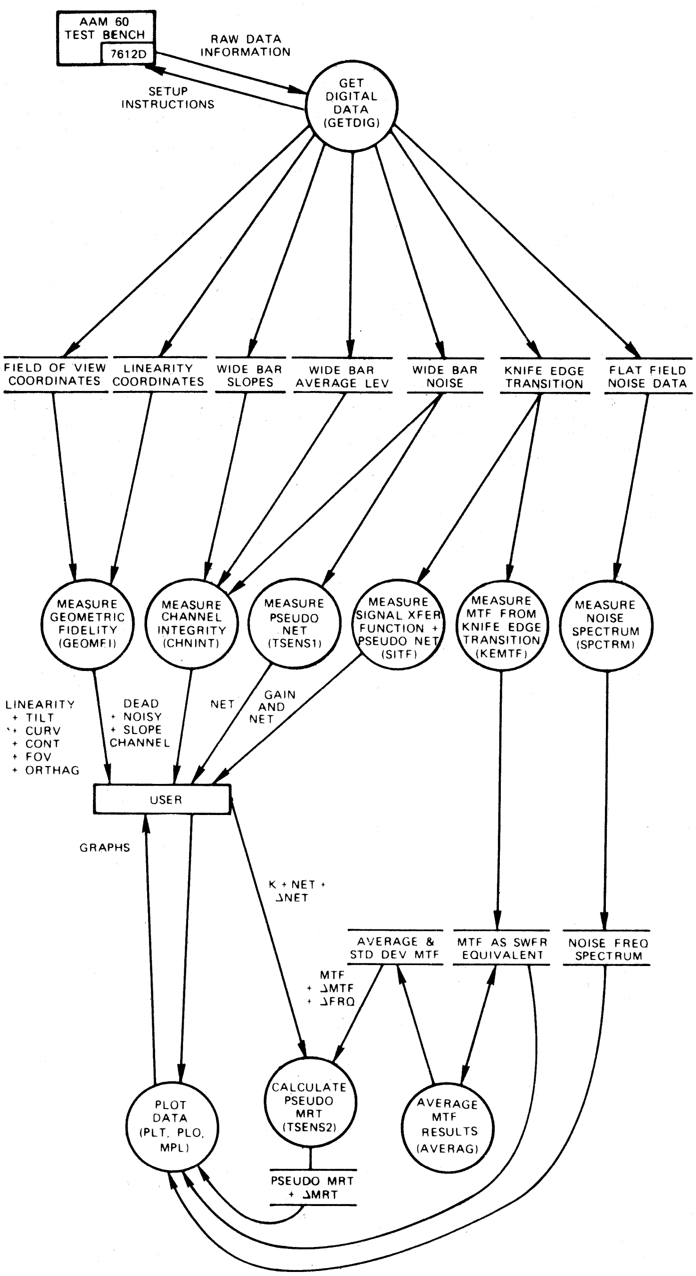

Fig. 2. Software module partitioning and flow for performance parameter evaluation.

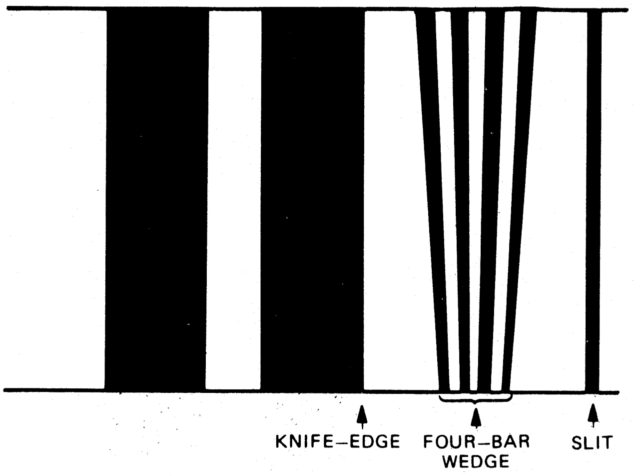

Fig. 3. Compare modulation transfer function (CMPMTF) program evaluation target.

TABLE I
TEST REQUIREMENTS SUMMARY

REQUIREMENT	MEASUREMENT PARAMETERS
Spatial Resolution	1. Modulation Transfer Function (MTF) 2. Square Wave Frequency Response (SWFR)
Thermal Sensitivity	1. Minimum Resolvable Temperature Difference (MRTD) 2. Video Noise Equivalent Temperature (VNET)
Image Quality	1. Geometric Fidelity 2. AC and DC Uniformity 3. Signal Transfer Function 4. Channel Integrity 5. Field of View

A commonly accepted parameter that can be used to describe the spatial resolution of a system is the modulation transfer function (MTF), which is the system frequency response. There exists a number of ways to evaluate and test MTF. Current Navy-deployed test equipment indirectly tests MTF using a traditional SWFR method. This manual test utilizes a four-bar target of specified width and 7:1 aspect ratio as a test stimulus. Modulation (response) at the spatial frequency represented by a four-bar set is determined by an operator from the oscilloscope display of WRA output signals. This method of spatial resolution measurement has significant drawbacks in that only a few discrete frequencies can be tested on any given target configuration. In addition, each frequency requires an individual measurement, thus requiring numerous tests to approximate a system frequency response curve. Although the measured SWFR values are not mathematically equivalent to MTF, discrete MTF values can be calculated from SWFR values by utilizing a standard Fourier expansion.

Another method for determining MTF is to Fourier transform the systems response to impulse stimulation. The system response is the line-spread function (LSF) which is a two-dimensional equivalent of a three-dimensional point-spread function (PSF). Impulse stimulation can be approximated by a hot wire, or slit, placed in the WRA field of view and oriented perpendicular to WRA detector scan direction.

As an alternative approach, the system LSF can be obtained by differentiating the system response to a step function stimulus which can be obtained from a knife-edge target oriented in the WRA field of view as previously described. The derivative of the WRA output step function is the LSF which, when processed by the test system using a Fast Fourier Transform (FFT), yields MTF.

Analytical evaluation of the above methods of measuring spatial resolution does not clearly identify a preferred concept. Therefore, an experiment was conducted, using an 875-line Vidicon TV camera from a FLIR system and a comprehensive software program CMPMTF (CoMPare MTF) to evaluate each method. CMPMTF evaluates MTF from a slit stimulus, knife-edge stimulus, and four-bar stimulus by processing digitized camera output signals. A special target was constructed for this experiment and is shown in Fig. 3. The four-bar wedge pattern shown in Fig. 3 provides a SWFR frequency continuum as a function of the horizontal TV line selected for processing. Thus, numerous operator verifiable SWFR check points are available to compare and evaluate processing results. CMPMTF outputs can be listed or plotted for comparison using additional data-handling software.

IV. RESULTS

This summary of the results of our studies and experiments to date is given with respect to both the test requirements previously described and test set stimulus/measurement capabilities. It should be noted that thermal sensitivity and image quality investigations are still in an early experimental stage. Consequently, results in these areas are more akin to problems being investigated than to definitive observations and comments.

A. Spatial Resolution

A computer measurement of SWFR that simply emulates current manual methods is easy to automate, yields test repeatability improvements of up to 8:1 over operator interpretation of an oscilloscope display and can be done in a fraction of the time. However, only a single frequency can be tested from each averaged data sample and target. On the other hand, the FFT of the system line-spread function (from a slit or knife-edge target) yields a complete system response, for a nearly unlimited number of frequencies within the system bandpass, from a single averaged data sample and target. However, repeatability of test results is less certain due to the sensivity of FFT analysis to defects in target construction, WRA noise, and test system noise. Nonetheless, these contributors to measurement uncertainty can be reduced by proper target construction and noise filtering techniques. In fact, the measurement of spatial resolution using a slit stimulus provided the best overall repeatability when the width of the slit was accurately known and WRA output data was truncated, to remove major signal distortions, prior to FFT processing.

Slit width uncertainty was found to be the major contributor to measurement uncertainty and error. This occurs since the input stimulus is not an infinitely narrow impulse, but is rectangular in shape. As a consequence, the FFT output must be corrected by a slit correction factor which is accurately known. By experimental observation, variances in slit width of only 2 percent resulted in a variance in calculated MTF of up to 23 percent.

When processing MTF with a knife-edge stimulus, a software differentiator is required to obtain the LSF from step response prior to performing an FFT. This technique is less sensitive to target construction defects, yet the differentiator can be extremely noise sensitive which results, again, in measurement error and uncertainty. Given proper hardware filtering and differentiator design, the knife-edge stimulus method yields equally good MTF results as a slit stimulus, with the additional hardware/software penalty.

Experimental data has shown that the detection of certain "soft" WRA failures may be possible using LSF measurement concepts that are not practical using SWFR methods. "Soft" failures in this context are those WRA failures, commonly caused by optical or electronic maladjustments, which would not be readily noticed by a FLIR system operator or cause WRA built-in test to fail. This "soft" failure capability is due to the fact that the FFT output (MTF) contains many data points throughout the WRA bandwidth from a single WRA output data sample. The shape of the resultant frequency response curve can be utilized (in conjunction with selected discrete data point values) to assess WRA performance. To obtain equivalent fault detection capability using SWFR methods, a target must be provided for each frequency of interest, an SWFR test must be done from each target, and a sufficient number of frequencies must be tested to detect all anticipated failure modes.

The major test time contributor, in any parameter measurement method investigated, was found to be the time required for data handling. Contributors to this problem include: IEEE-488 Bus transfer speed, associated IEEE-488 Bus control software execution time, and disk storage transfer speed. Empirically derived results indicate approximately three seconds to perform processing of the MTF while data handling time ranged between 65 to 70 s.

B. Thermal Sensitivity

Two major thermal sensitivity parameters are initially being investigated in this development effort: minimum resolvable temperature difference (MRTD) and video noise equivalent temperature (VNET). The method used to determine MRTD was suggested by Lloyds [1] model expressed as

$$\mathrm{MRTD}(f) = K * \mathrm{NET}/\mathrm{MTF}(f) \tag{1}$$

where K is a function of detector dwell time, display monitor response and human eye response. Since NET is not available at a typical FLIR WRA I/O interface, (1) is not directly useable and the parameter VNET (measured at the WRA output) was established. The use of (1) requires a library of K values for each type WRA to be tested. Also, (1) assumes that K remains constant for all WRA's of a specific type. Early experimental results have shown that significant test uncertainties occur with making these kinds of assumptions and work is proceeding to identify and reduce the major error sources, particularly in the VNET measurements.

VNET is measured as the rms value of a digitized video noise signal. Poor repeatability of initial VNET measurements was found, by spectral analysis, to be the result of significant nonrandom noise characteristic of the WRA and associated test equipment. Additionally, the spectral values of the video level noise were not uniform with respect to frequency. Since VNET measurement is a time-domain measurement process, data obtained from a digital "snapshot" of time domain noise values will vary significantly from test to test as a result of these two observed conditions.

Additional problems in the VNET concept were noted. For example, no industry standard exists for this parameter and there is no accepted method of verifying the quality of the parameter, or traceability.

Although the initial results of MRTD and VNET measurements indicate numerous problems, work is continuing to resolve these issues and investigate viable alternative approaches.

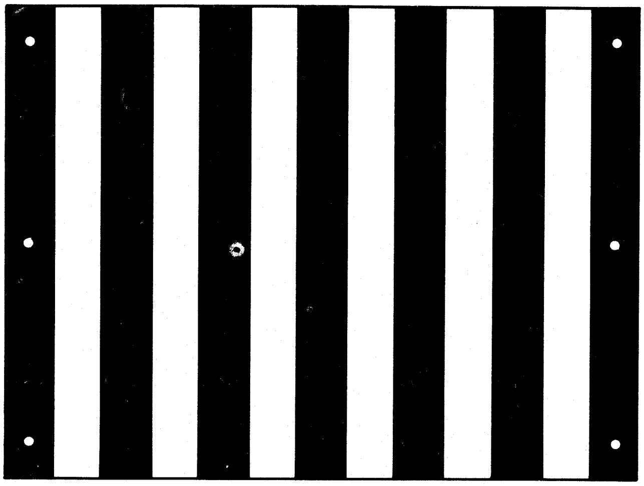

Fig. 4. Prototype target for experimental evaluation.

Analysis of WRA output noise spectrum and noise spectral density appears promising at this point (although the exact relationships to thermal sensitivity have not been established). Noise spectrum measurements by ensemble averaging (magnitude averaging of noise spectral values) do not exhibit the uncertainty problems observed in time-domain measurements if a sufficient number of averages is chosen. Desirable results have occurred as a result of 128 averages of noise spectral data.

It must be noted that the fundamental issue in the automatic measurement of thermal sensitivity parameters (such as MRTD) is that most accepted techniques tested manually today involve a parameter which includes operator perception and other uncontrolled or not fully defined variables. The ultimate goal of our thermal sensitivity investigation is to develop a measurement parameter that is totally independent of the display/operator complex and acceptable to industry as a standard for testing purposes. Nevertheless, our first approach was to attempt to utilize a parameter that is widely used and could provide some traceability to manual testing and WRA specifications.

C. Image Quality

Early investigations of the image quality parameters, noted in Table I, indicated desirability of a single generalized target capable of providing most of the required WRA input stimulus in one target structure. Processing of WRA output data obtained using frame grab and/or broadband single line sampling techniques could then yield a variety of image quality test parameter values in a single test. If possible, the same target would be used to satisfy spatial frequency and thermal sensitivity stimulus requirements as well.

A prototype target was designed and constructed for experimental evaluation and is shown in Fig. 4. Parameters considered testable using an automated computer process with this target include spatial resolution (MTF), thermal sensitivity (VNET and MRTD), ac uniformity, geometric fidelity, signal transfer function, and IR channel integrity. MTF is measured by differentiating the knife-edge response, determining the Fourier transform, and converting to SWFR equivalence using Fourier series expansion techniques. VNET is measured as the video level rms noise voltage from bar to bar, and MRTD from MTF and VNET as noted in (1); ac uniformity is measured by comparing the intensity levels of all the TV lines within a hot vertical bar. Geometric fidelity refers to the system's ability to accurately reproduce an apparent two-dimensional image from three-dimensional object space. Geometric fidelity includes such parameters as spatial fidelity, tilt, field of view size, and image orthogonality. Knowing the position of points in object space, spatial fidelity can be tested by checking the relationship of the corresponding points in image space. This parameter is measured by checking the index values of the preselected voltage threshold level at each of the bar transitions. Other parameters such as image orthogonality, tilt, and field of view size are tested by making geometric calculations on the array index values of the digitized image. Signal transfer function (SiTF), is represented by the video voltage level as a function of stimulus delta temperature. IR channel integrity refers to the measurement of dead or noisy IR channels. Noisy channels are detected as wide variances in the line-by-line NET analysis and dead channels are detected as wide variances in the ac uniformity measurements.

Evaluation of this prototype target is well underway, however, significant problems have been observed. For example, one difficulty encountered in processing imagery that has been generated through multiplexing techniques is dealing with the artifacts that result from these processes. As an example, in typical FLIR systems the display scan lines will relate to IR scan lines in some format. This mapping has been particularly difficult for the electro-optical multiplexed FLIR we have been using because of the curved IR scan path compared to the horizontal scan of the TV camera. This particular IR scan format exists in the early S3-type systems still deployed in the Navy. Newer systems do not present this identical problem, however, the correlation of TV lines to the IR scan lines remains a function of image tilt. Thus a correlation problem exists for all systems and the relationship between TV and IR scan lines may not remain constant over the horizontal scan period. The resulting distortion of the waveform has made it difficult to extract information about dead and/or noisy IR channels. A partially effective solution for the S3 FLIR system has been to look at narrow vertical slices of data near the center of the field of view. The relationship of the video line data to the IR channels in this region is better due to the near parallelism of the TV lines to the IR channels.

Image quality test precision and accuracy capability using the prototype target has been established by statistical methods (means and standard deviations for repeated tests). In general, repeated test results are observed to be within two standard deviations of manually measured values. However, at the present time, to achieve a high degree of confidence in the automatically processed image parameters, it is necessary to take many samples with statistically valid pass/fail criteria established for each test parameter.

V. CONCLUSIONS

The development of processing techniques, as described in this paper, is expected to continue through the end of fiscal year 1984 as a parallel effort with other investigations of EO avionics test automation. However, at this time, several conconclusions can be drawn.

1) The processing of FLIR WRA output video, to automatically determine imaging system performance, is feasible for both fault detection and diagnostics. As used here, the word automatic denotes that no operator interpretation of the displayed imagery is required.

2) A combination of TV line and frame grab processing capability is essential in any ATE that would truly accommodate FLIR video test requirements. The amount, acquisition rate and near real-time manipulation requirements of data, inherent in the frame grab process and required to interpret test results, may dictate a specialized image (video) processor design in any ATE architecture regardless of core capability.

3) Noise and artifacts present in a FLIR video output signal, even in a properly operating WRA, may require significant hardware and software filtering or preprocessing of data prior to processing for test results. Despite a carefully designed processor system, statistical data collection and test reiteration may be necessary to determine WRA pass/fail conditions.

4) FLIR test parameters, such as MRTD which are based upon an operator(s) ability to percieve or recognize objects in a FLIR system field of view, are not readily usable for automatic test purposes. New parameters may be required which can be directly translated to electrical signals available at the WRA output. Acceptance by the EO avionics community is the critical issue in development of more testable performance parameter definitions.

5) Spatial resolution tests using discrete frequency four-bar targets and SWFR measurements, as used in the field today, need not be duplicated in future deployed EO test equipment. Test techniques using line spread function analysis (from slit or knife-edge targets) provide a significant improvement in fault detection capability and simplifies test equipment design by reducing the number of targets required.

REFERENCES

[1] J. M. Lloyd, *Thermal Imaging Systems.* New York: Plenum, Mar. 1979, p. 188.

Short Papers

A Simple Fast Frequency Detector for a Constant Amplitude Sinusoid

MAHIR K. MAHMOOD, MEMBER, IEEE, JANAN E. ALLOS, MEMBER, IEEE, AND MAJID A. H. ABDUL-KARIM

Abstract—**The frequency of a constant-amplitude sinusoidal signal is measured within a small fraction of a cycle. This is accomplished by carrying out computations on two successive samples of the input signal. System delay expressed in a fraction of a cycle is given by two times the ratio of the input-to-sampling frequencies. An inverse sine function is computed using digital hardware, giving a digital output representing the frequency.**

I. INTRODUCTION

Fast frequency detection has many applications in power system control, and automatic frequency control. In general, applications are most appropriate where the frequency is very low [1], or where the transient variation of the frequency is to be detected. For the first case, using the conventional time interval counter method, the counting time becomes excessively long for a reasonable accuracy, while in the latter case, the transient variation may be lost due to averaging. In such cases, it becomes necessary to measure the frequency within a small fraction of a cycle.

As an example of the urgent need for the fast frequency measurement in less than a cycle, consider the Doppler method of velocity measurement, in which the difference frequency (Δf) between two sinusoids is to be measured. If Δf is so small as to be of the order of few hertz, then the conventional time interval counter method will take many seconds for a reasonably accurate measurement. However, it is quite probable that Δf may change many times during the measurement time, yielding a reading that is completely incorrect.

In general, the fastest detection speed is one cycle, or half a cycle for a symmterical waveform. However, if the signal is mathematically well defined, as in the case of a sinusoid, then detection can be achieved in a small fraction of a cycle.

In this paper, the frequency of the constant-amplitude sinusoid is measured within a small fraction of a cycle. The speed of the system can be easily increased simply by increasing the sampling frequency.

In the proposed system, it is assumed that the amplitude of the input signal is constant and known to the designer. However, if that is not the case, then other methods [2], [3] of fast amplitude detection within a small fraction of a cycle are to be used together with the proposed system.

II. MATHEMATICAL RELATIONSHIP

Assuming the input signal is a pure and distortionless sinusoid, then

$$v_i = V \sin \omega_i t \tag{1}$$

Manuscript received April 1, 1983; revised June 4, 1984.

The authors are with the University of Baghdad, College of Engineering, Electrical Department, Baghdad, Iraq.

0018-9456/84/0900-0327$01.00

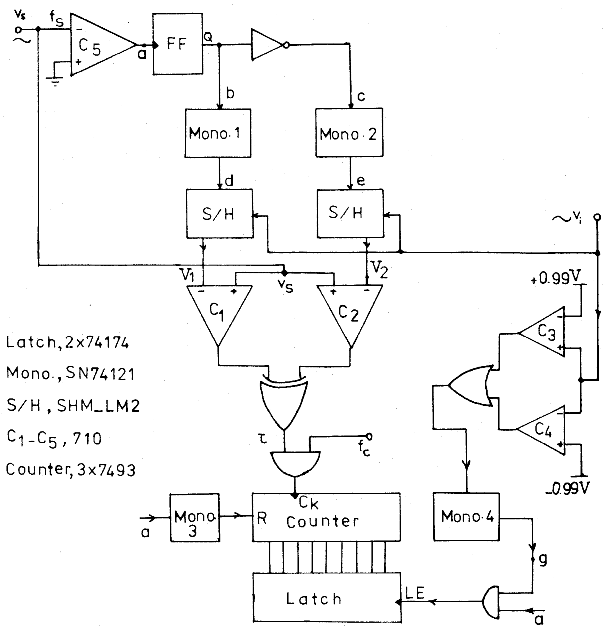

Fig. 1. System block diagram.

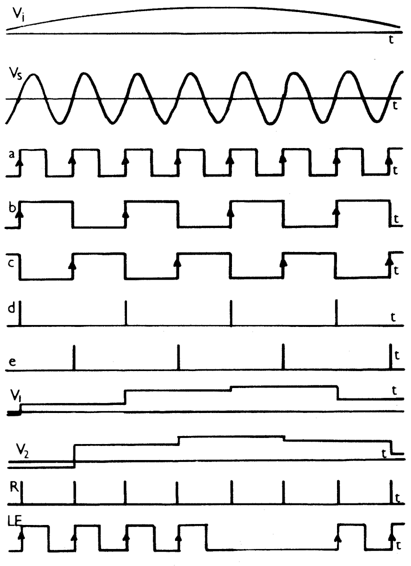

Fig. 2. Timing waveforms of the system.

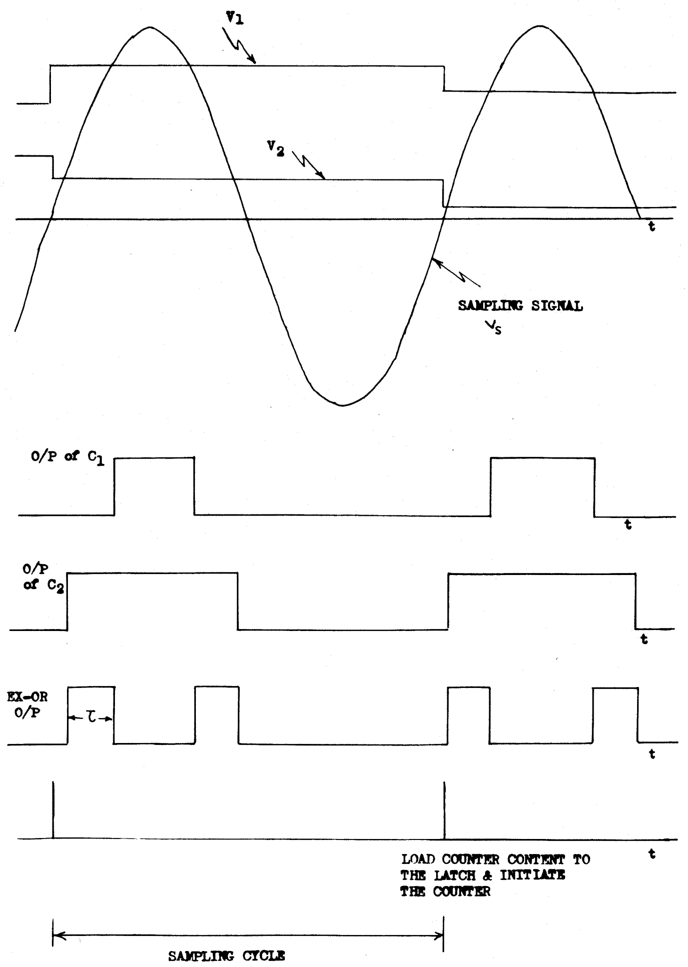

Fig. 3. Computation of the inverse sine using the sampling sinusoidal signal as the nonlinear time function.

and at $t = t_1$, the first sample is taken, then

$$V_1 = V \sin \omega_i t_1. \tag{2}$$

At $t = t_2 = t_1 + \Delta t$, the second sample V_2 is taken, then

$$V_2 = V \sin \omega_i (t_1 + \Delta t). \tag{3}$$

Subtracting (2) from (3) after taking the inverse sine, then

$$\omega_i \Delta t = \sin^{-1}\left(\frac{V_2}{V}\right) - \sin^{-1}\left(\frac{V_1}{V}\right). \tag{4}$$

Equation 4 gives the value of ω_i for the given value of V and Δt.

III. SYSTEM DESCRIPTION

Fig. (1) shows the block diagram of the system, and Fig. 2 shows the timing waveforms. The input signal v_i is applied to the two sample and hold (S/H) circuits. The sample control signals (d, e) are time shifted by Δt and are generated by Mono. 1 and 2 (See Fig. 2) using the signals (b, c) that are derived from an oscillator whose frequency is equal to the sampling frequency (f_s). The outputs of these S/H circuits (V_1 and V_2) are applied to special purpose hardware that computes the absolute value of the right-hand side of (4). This is accomplished by modifying the method described in [4] as shown in Fig. 3. In each sampling cycle (Δt, or one cycle of v_s), the two samples are compared with the sampling sinusoidal signal v_s using comparators C_1 and C_2. Hence the average value of the signal at the output of C_1 will be proportional to $((\pi/2) - 2 \sin^{-1} (V_1/V))$ and that for C_2 be proportional to $((\pi/2) - 2 \sin^{-1} (V_2/V))$. The width of each pulse in the EX-OR gate output will be

$$\tau = \frac{\left| \sin^{-1} \dfrac{V_2}{V} - \sin^{-1} \dfrac{V_1}{V} \right|}{2\pi f_s}.$$

By substituting (4) into the above equation one obtains

$$\tau = \frac{\omega_i \Delta_t}{2\pi f_s} = \frac{\omega_i}{2\pi f_s^2} \tag{5}$$

since $f_s = 1/\Delta t$.

At the begining of each sampling cycle, the counter is initiated by the output of Mono. 3, and as shown in Fig. 3, the counter will be enabled during 2τ time in each sampling cycle. Hence the digital number N stored in the latch after each sampling cycle will be

$$N = 2\tau f_c$$

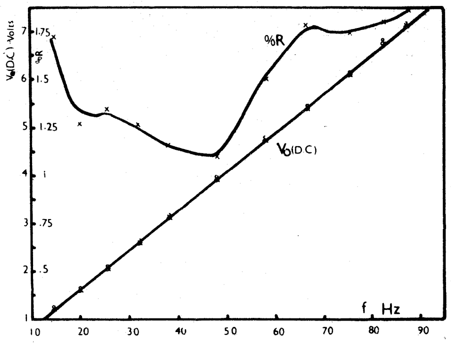

Fig. 4. System linearity and percentage ripple (percent R) versus input frequency f_i.

where f_c is the high-frequency clock of the counter. Using (5), the value of N can be rewritten as

$$N = 2\,\frac{f_c f_i}{f_s^2}. \tag{6}$$

It should be noted that the computation of the inverse sine using this method gives a range of operation of $[0 - (\pi/2)]$ rad. Hence a correct output is obtained only when both samples are taken from a nonchanging sign slope segment of the input signal. Hence an error will occur if V_1 is taken before a peak (or a trough) and sample V_2 after it. However, this erroneous output is loaded to the latch after, at most, $2\Delta t$ time from the peak (or the trough). Hence using C_3, C_4, and the OR-gate, Mono. 4 is triggered at almost the peak (or the trough) and has a time constant of $2\Delta t$. Mono. 4 output g decides whether the content of the counter is loaded to the latch.

IV. EXPERIMENTAL RESULTS

The digital output is converted into analog for test purposes. The system was operated for the decade range 10–100 Hz., with $f_s = 1$ kHz, and $f_c = 4.19$ MHz. This gives $N_{\max} = 838$ (corresponding to 100 Hz.). Hence a 10-bit counter, latch, and DAC were used.

Fig. 4 shows system linearity and ripple content for a decade range of input frequency. System linearity shows the linear relation between DAC output and the input frequency. The ripple content does not exceed 1.8 percent and it was mainly due to the inherent harmonic distortion of the input and sampling signals (about 0.3 percent).

The effect of harmonic distortion can be easily calculated using sets of two successive samples taken from a distorted sinusoid. Then each set is used to compute the frequency using (4). The output for each set will be slightly different from those for other sets. Using these outputs the ripple factor due to harmonic distortion can be calculated. Fig. 5 shows the experimental and calculated results for the harmonic distortion effect.

V. CONCLUSIONS

The frequency of a constant amplitude sinusoid was detected within small fraction of a cycle. This was carried out by a simple computation on two successive samples of the input. The system possesses an erroneous output when computation is made around the peaks (or the troughs). The system compensates for such errors but at the expense of the speed.

The method is very useful for pure and low-distortion sinusoids. However a more complicated equation may be derived to deal with sinusoids with specific harmonics. Implementation of such an equation requires much more hardware than that described here.

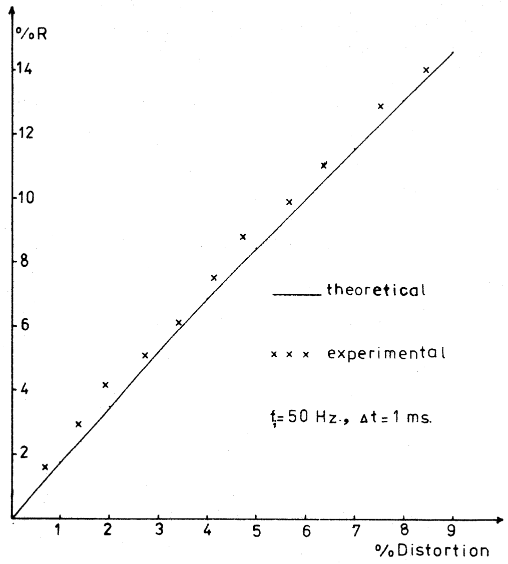

Fig. 5. Percentage ripple (percent R) in the output due to harmonic distortion.

ACKNOWLEDGMENT

Thanks are due to K. M. Ibrahim with whom we had many interesting discussions.

REFERENCES

[1] E. P. McCarthy, "A digital instantaneous frequency meter," *IEEE Trans. Instrum. Meas.*, vol. IM-28, no. 3, pp. 224–226, Sept. 1979.

[2] M. K. Mahmood and J. E. Allos, "Fast peak detection of sinusoidal signals," in *Proc. IEEE Canadian Communications and Energy Conf.* (Montreal, Canada), 1982.

[3] C. A. Karybanas, and G. A. Micholoitsis, "Fast amplitude detection for constant period sinusoidal signals," *Int. J. Electron.*, vol. 49, no. 1, pp. 67–72, 1980.

[4] K. M. Ibrahim and M. A. H. Abdul-Karim," Non-linear ADC using non-linear function of time," *Int. J. Electron.*, accepted for publication.

Digitally Programmable Gain Amplifiers

SUHASH C. DUTTA ROY

***Abstract*—Following a review of the state of the art, some new circuits are presented for designing a set of digitally programmable gain amplifiers. Design features of these circuits are presented, and critical assessments are made of their relative merits and limitations.**

I. INTRODUCTION

Digitally progammable gain amplifiers (PGA's) ease analog-to-digital conversion and multiplexing [1] because they provide an inexpensive method of data acquistion from widely differing sensor levels. They can be realized with an operational amplifier (OA), a switched resistor network, and a switch driving circuit, actuated by a digital word. The basic circuit utilized for this purpose is the inverting or the noninverting finite gain configuration of the OA, as shown in Fig. 1, where the relevant

---

Manuscript received September 20, 1982; revised November 14, 1982.

The author is with the Department of Electrical Engineering, Indian Institute of Technology, New Delhi 110 016, India.

0018-9456/84/0900-0329$01.00 © 1984 IEEE

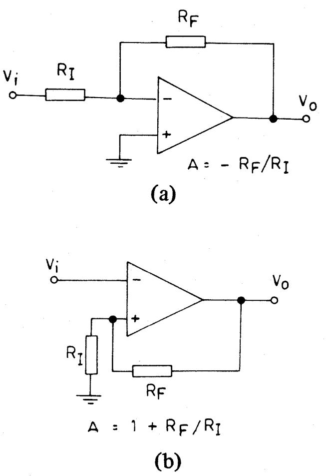

(a)

(b)

Fig. 1. Basic circuit utilized for (a) inverting and (b) noninverting programmable gain amplifier.

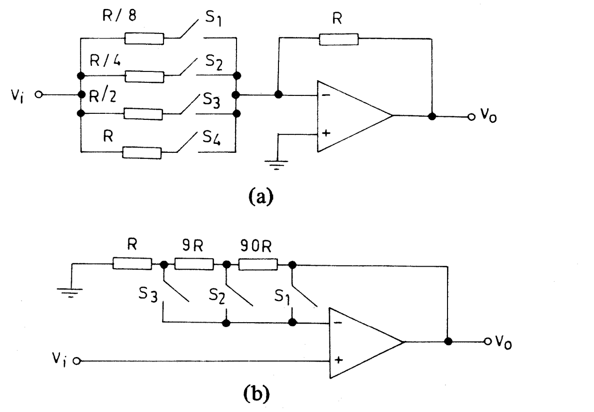

(a)

(b)

Fig. 2. (a) Tobey's inverting PGA for obtaining all integer gains from 1 to 15. (b) Tobey's noninverting PGA for obtaining gains of 1, 10, and 100.

expressions for gain are also included. To achieve programmable gain, we need to vary R_F or R_I or both through appropriate switches, typically realized with FET's.

In this paper, we critically examine the various possible circuits for PGA's so obtained. Some of these circuits are given in the literature, while the others are new. We consider arbitrary as well as integer-valued gains. For the latter case, we investigate the possibility of minimizing the number of switches and resistors, and determine the optimum number of equal-valued resistors required for the fabrication of the resistor network. The error due to the nonzero ON resistance of the switches is examined, along with design modifications required to minimize it.

II. SOME KNOWN CIRCUITS

A. *An Inverting PGA*

An example of inverting PGA using a variable R_I is shown in Fig. 2(a). This circuit, originally presented by Tobey [1], has a gain equal to the decimal value of the binary word $S_1S_2S_3S_4$, where

$$S_i = \begin{cases} 1, & \text{when ON} \\ 0, & \text{when OFF} \end{cases} \qquad i = 1 \text{ to } 4. \tag{1}$$

Clearly, any integer gain from 1 to 15 can be achieved. In general, N binary weighted resistors R, $R/2$, $R/2^2, \cdots, R/2^{N-1}$ and N switches can realize any integer gain from 1 to $2^N - 1$.

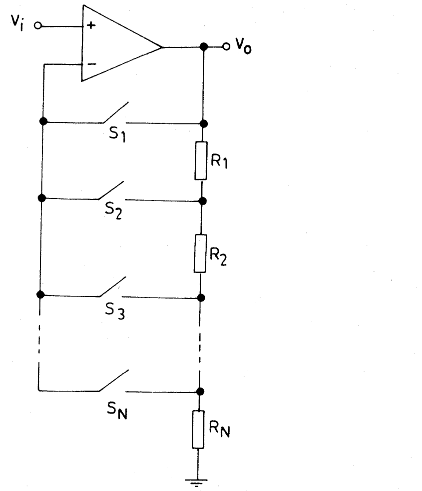

Fig. 3. Woo's generalization of Tobey's noninverting PGA to provide an arbitrary set of N gain values—integer or otherwise.

The circuit provides economy in the number of switches and resistors, but suffers from the drawback that the input impedance varies with the gain. Further, the ON resistance of the switches R_s, typically ranging from 100 to 500 Ω, and their drifts due to temperature and aging, affect the gain accuracy. This error can be made negligible by choosing $R/8 >> R_s$, but this means using high-valued resistors for the R_I network, which are incompatible with low noise, high speed, and low drift performance [1].

The error due to R_s can, however, be minimized by reducing each resistance in the R_I network by R_s.[1] The drift in R_s, δR_s, will typically be a small percentage of R_s, and it is relatively easy to satisfy $R/8 >> \delta R_s$ with moderate valued resistors.

B. *A Noninverting PGA*

The drawbacks of the inverting PGA of Fig. 2(a) can be overcome in the noninverting circuit of Fig. 2(b), where both R_F and R_I are varied by switching. This circuit, also proposed by Tobey [1], has a gain equal to $S_1 \oplus 10\,S_2 \oplus 100\,S_3$, where $\oplus$ denotes the logical EXCLUSIVE OR operation. One can thus obtain decade gain values of 1, 10, and 100. Similarly [2], with four resistors of values $R, R, 2R$, and $4R$, and four switches, one can obtain the binary gain values 1, 2, 4, and 8.

In this circuit, the input impedance is high and independent of switching. Furthermore, since the switches are closed one at a time,[2] and each switch is in series with the inverting terminal of the OA, very little current flows through it. The gain is therefore insensitive to R_s and its drift.

C. *Generalization of the Noninverting PGA*

The noninverting PGA of Fig. 2(b) can be generalized, as shown in Fig. 3, to provide any arbitrary set of gain values—integer or otherwise. This generalized circuit was analyzed by Woo [2] for integer valued gains from 1 to N, and later by Genin [3] for any arbitrary set of increasing gain values $A_1, A_2, \cdots, A_N$ with $A_1 = 1$. Writing the expressions for A_n (with nth switch closed) and A_{n+1} (with $(n+1)$th switch closed), it follows that

$$R_n = \begin{cases} R_T[(1/A_n) - (1/A_{n+1})], & 1 \leqslant n \leqslant N-1 \\ R_T/A_N, & n = N \end{cases} \tag{2}$$

---

[1] If all the switches do not have the same ON resistance, then $R/8$ is to be replaced by $(R/8) - R_{s1}$, $R/4$ by $(R/4) - R_{s2}$, etc.

[2] We assume this to be true for the circuits of Fig. 2(b), and Figs. 3–5.

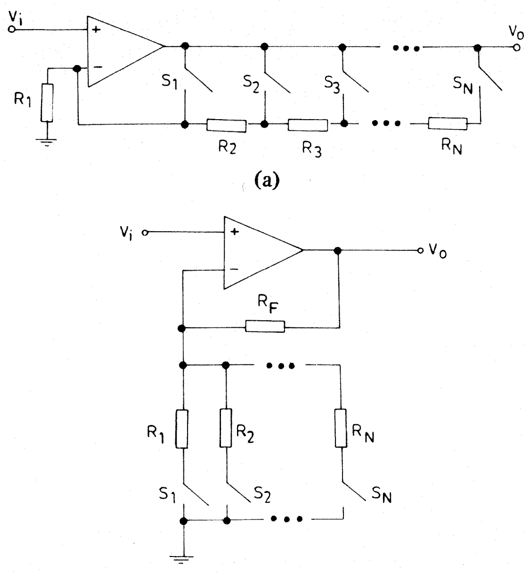

(a)

(b)

Fig. 4. (a) A noninverting PGA which requires equal valued resistors for integer gains. (b) Alternative noninverting PGA which also requires equal valued resistors for integer gains.

where $R_T = R_1 + R_2 + \cdots + R_N$. For integer gains, $A_n = n$ so that (2) simplifies to

$$R_n = \begin{cases} R_T/[n(n+1)], & 1 \leqslant n \leqslant N-1 \\ R_T/N, & n = N \end{cases} \tag{3}$$

III. Some New Circuits

A. A Noninverting PGA

In the PGA circuit of Fig. 3, both R_F and R_I vary with switching. Fig. 4(a) shows an alternative circuit in which R_I is fixed, and R_F is varied by switching. The lowest gain obviously is $A_1 = 1$, achieved when S_1 is closed. In general, when the nth switch is closed, the gain is

$$A_n = 1 + \left(\sum_{i=2}^{n} R_i \right) \Big/ R_1. \tag{4}$$

Similarly, writing the expression for A_{n-1}, it is easy to find the required resistor values as

$$R_n = R_1(A_n - A_{n-1}), \qquad 2 \leqslant n \leqslant N. \tag{5}$$

For integer gains, $A_n = n$ and (5) gives $R_n = R_1$ for all n. This feature of equal-valued resistance is of great advantage in fabrication, trimming, and tracking with temperature and aging. Because of this, the circuit of Fig. 4(a) is superior to that of Fig. 3. High input impedance, independent of switching, is a common feature of both (and of all noninverting PGA's discussed in this paper), but the new circuit has the disadvantage that its gain is sensitive to R_s. If R_s is the same for all the switches and does not drift, then by using a resistance $R_2 - R_s$ in place of R_2, all gains will be exactly realized except for A_1 which will now be $1 + R_s/R_1$ instead of unity. The latter can also be compensated for by using another switch in series with R_1 which opens only when S_1 is closed.

B. Alternative Noninverting PGA

If, in Fig. 1(b), we keep R_F fixed and vary R_I by switching, the circuit of Fig. 4(b) results. When switch S_n is closed, the gain is $A_n = 1 + R_F/R_n$, so that

$$R_n = R_F/(A_n - 1), \qquad 1 \leqslant n \leqslant N. \tag{6}$$

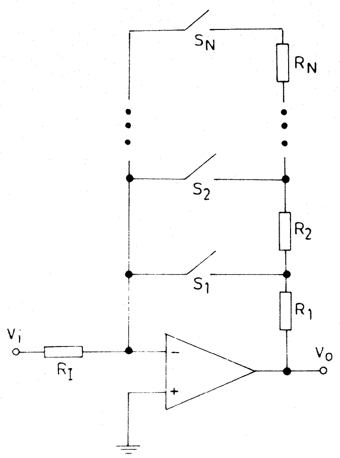

Fig. 5. An inverting PGA whose input impedance is insensitive to switching and whose gain can be compensated for R_s error.

The effect of R_s can be compensated for by reducing each resistance of the R_I network by the amount R_s. For integer gains from 1 to $N + 1$, the resistor values required are

$$R_n = (R_F/n) - R_s. \tag{7}$$

An equal-resistor design for integer gains can be obtained by keeping all switches normally ON, and by opening them one by one. In general, the gain will be

$$A = 1 + R_F \sum_{i=1}^{N} S_i G_i \tag{8}$$

where S_i is given by (1), $G_i = 1/R_i$, and R_i is assumed to include R_s. Let $A_{n+1}(A_n)$ be the gain with S_1 to $S_{n+1}(S_n)$ closed and $S_{n+2}(S_{n+1})$ to S_N open; then from (8), it easily follows that the required resistor values are

$$R_n = R_F/(A_{n+1} - A_n), \qquad 1 \leqslant n \leqslant N. \tag{9}$$

For integer gains, $A_n = n + 1$, so that $R_n = R_F$ for $1 \leqslant n \leqslant N$.

C. Inverting PGA with Constant Input Impedance

The dependence of the input impedance on gain in an inverting PGA can be overcome with a fixed R_I and a variable R_F, as shown in Fig. 5. In this, the effect of R_s can be compensated for by reducing the first resistance R_1 by an amount R_s from the design value. Let $A_{n-1}(A_n)$ be the gain with the $(n-1)$th (nth) switch closed; then it is easy to show that the required resistor values are given by

$$R_n = R_1(|A_n| - |A_{n-1}|), \qquad 1 \leqslant n \leqslant N. \tag{10}$$

If it is desired to have integer gains, then $A_n = n$ so that $R_n = R_1$, $1 \leqslant n \leqslant N$.

IV. Minimizing the Numer of Switches and Resistors

As already pointed out, the circuit of Fig. 2(a) provides economy in the number of switches and resistors because only four switches and four plus one resistors can give $2^4 - 1 = 15$ gain values by operating more than one switch simultaneously. In this sense, the circuits of Fig. 2(b) and Figs. 3-5 are wasteful. The concept of multiple switching can, however, be easily extended to these PGA circuits also. We shall illustrate this with two examples of noninverting PGA's, and in each case, we shall aim at obtaining integer gains from 1 to 16. The first circuit, shown in Fig. 6(a), is of the fixed R_I—variable R_F type. Its gain, assuming $R_s = 0$, is unity plus the decimal value of the binary word $\bar{S}_4\bar{S}_3\bar{S}_2\bar{S}_1$, where S_i is given by (1) and bar de-

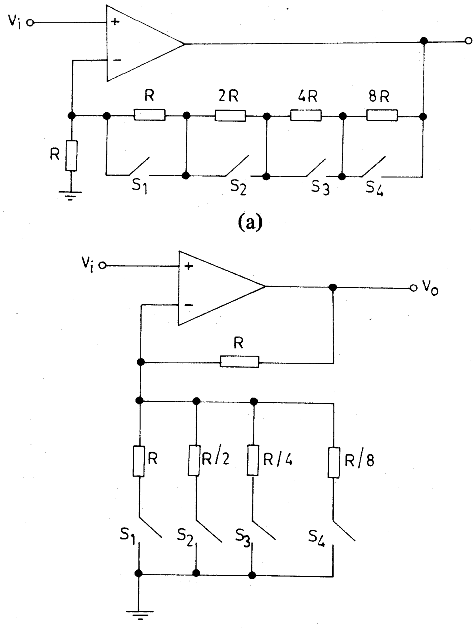

(a)

(b)

Fig. 6. (a) An economic PGA for integer gains from 1 to 16. (b) Alternative economic circuit for integer gains from 1 to 16, in which the effect of R_s can be eliminated.

notes binary complement. The error due to R_s is zero only when all the switches are open i.e., for a gain of 16. For all other gains, the error will be nonzero and cannot be compensated for. The largest error will occur when all the switches are closed i.e., for a nominal gain of unity. Under this condition, the error can be written in the form

$$\text{Error} = (R_s/R) \sum_{i=1}^{4} [1 + R_s/(iR)]^{-1}. \qquad (11)$$

Expanding each term in the summation and neglecting square and higher powers of R_s/R gives

$$\text{Error} \cong (R_s/R)\,[4 - (15/8)\,(R_s/R)] < 4R_s/R. \qquad (12)$$

If it is required to limit the error to a maximum of 1 percent, then (12) shows that R must be no less than 400 R_s.

The situation is vastly improved in the circuit of Fig. 6(b) which is of the fixed R_F—variable R_I type. The gain of this circuit is the same as that of Fig. 6(a), but the effect of R_s, if free from drift, can be completely eliminated by reducing each resistor by the amound R_s.

The circuits of Fig. 6(a) and (b) can be generalized for any integer gains from 1 to 2^N by using N resistors and the same number of switches.

V. EQUAL RESISTOR DESIGN OF ECONOMIC PGA CIRCUITS

In the economical PGA circuits of Figs. 2(a), and 6(a) and (b), R_s can be made negligible compared to the lowest resistance in the switched resistor network. Then it is of advantage to use equal valued resistors r to fabricate the network in IC form. Consider, for example, the circuit of Fig. 6(b), and assume $R_s << R/8$. If we use resistors of value R only, i.e., $r = R$, then we require eight R's (in parallel) for $R/8$, four for $R/4$, and so on. The total number of resistors, therefore, is $N_r = 16$. If we use $r = R/2$, it is easy to see that $N_r = 11$. With $r = R/4$, similarly, we get $N_r = 13$, while for $r = R/8$, the count increases to $N_r = 23$. Thus $r = R/2$ is the optimum choice. As can be easily shown, this conclusion is valid for Fig. 6(a) circuit also.

If the upper gain range is extended to any number between 17 and 32, then it can be shown from similar arguments that $r = R/4$ gives the minimum number of resistors, viz., 17. In general, let the gain range be 1 to 2^N and let $r = R/2^k$ in a circuit of the type of Fig. 6(b).[3] Then resistance values required are $R, R, R/2, R/4, \cdots, R/2^{k-1}, R/2^k, R/2^{k+1}, \cdots, R/2^{N-1}$ The total number of resistors, it can be shown, can be expressed in the following form

$$N_r = (2^N/2^k) + 3 \times 2^k - 3. \qquad (13)$$

Minimizing N_r with respect to k gives

$$k = \text{integer nearest to } [(N/2) - 0.7925]. \qquad (14)$$

For example, $N = 2$ requires $k = 0$, $N = 3$ and 4 both require $k = 1$, while $N = 5$ and 6 both require $k = 2$. These agree with the direct calculations mentioned at the beginning of this section.

VI. CONCLUSIONS

Methods for obtaining an arbitrary set of N digitally programmable gains have been reviewed. Some new circuits have been presented for this purpose, which have the advantage of requiring equal-valued resistors for an arbitrary range of integer gains. For the latter case, methods have been suggested for minimizing the number of switches and resistors. It has been shown to be possible to fabricate the resistor network with an optimum number of equal valued resistors. The error due to nonzero ON resistance of the switches has been carefully examined, and modifications required to minimize it have been discussed.

REFERENCES

[1] G. E. Tobey, "Ease multiplexing and A/D conversion," *Electron Des.*, vol. 8, pp. 84-89, Apr. 12, 1973.
[2] B. B. Woo, "Digitally programmable gain amplifiers with arbitrary range of integer values," *Proc. IEEE*, vol. 68, pp. 934-936, July 1980.
[3] R. Genin, "Comment on 'Digitally programmable gain amplifiers with arbitrary range of integer values'," *Proc. IEEE*, vol. 69, pp. 664-665, May 1981.

---

[3] The calculations are exactly similar for Fig. 6(a) type circuit and the final results are the same in both cases.

Characterization of Frequency Stability: Analysis of the Modified Allan Variance and Properties of Its Estimate

PAUL LESAGE AND THÉOPHANE AYI

***Abstract*—An analytical expression for the modified Allan variance is given for each component of the model usually considered to describe the frequency or phase fluctuations in frequency standards. The relation between the Allan variance and the modified Allan variance is specified and compared with that of a previously published analysis. The uncertainty on the estimate of the modified Allan variance calculated from a finite set of measurement data is discussed.**

Manuscript received December 8, 1983; revised February 17, 1984.

The authors are with the Laboratoire de l'Horloge Atomique, Equipe de Recherche du CNRS, associée à l'Université Paris-Sud, 91405 Orsay, France.

I. INTRODUCTION

Many works [1]-[5] have been devoted to the characterization of the frequency stability of ultrastable frequency sources and have shown that the frequency noise of a generator can be easily characterized by means of the "two-sample variance" [2] of frequency fluctuations, which is also known as the "Allan variance" [2] in the special case where the dead time between samples is zero.

An algorithm for frequency measurements has been developed by J. J. Snyder [6], [7]. It increases the resolution of frequency meters, in the presence of white phase noise. It has been considered in detail by D. W. Allan and J. A. Barnes [8]. They have defined a function called the "modified Allan variance" and they have analyzed its properties for the commonly encountered components of phase or frequency fluctuations [3]. For that purpose, the authors of [8] have expressed the modified Allan variance in terms of the autocorrelation of the phase fluctuations. For each noise component, they have computed the modified Allan variance and deduced an empirical expression for the ratio between the modified Allan variance and the Allan variance.

In this paper, we show that the analytical expression of this ratio can be obtained directly, even for the noise components for which the autocorrelation of phase functions is not defined from the mathematical point of view. We give the theoretical expressions and compare them with those published in [8].

The precision of the estimate of the modified Allan variance is discussed and results related to white phase and white frequency noises are presented.

II. BACKGROUND AND DEFINITIONS

In the time domain, the characterization of frequency stability is currently achieved by means of the two-sample variance [2] $\langle \sigma_y^2(2, T, \tau) \rangle$ of fractional frequency fluctuations. It is defined as

$$\langle \sigma_y^2(2, T, \tau) \rangle = \frac{1}{2} \langle (\bar{y}_{k+1} - \bar{y}_k)^2 \rangle \tag{1}$$

where the quantity $\bar{y}_k$ is the average value of the fractional frequency fluctuations $y(t)$ over the time interval $(t_k, t_k + \tau)$ such that

$$\bar{y}_k = \frac{1}{\tau} \int_{t_k}^{t_k+\tau} y(t)\, dt. \tag{2}$$

In (2), t_k represents the moment at which the kth observation time interval starts. We have

$$t_k = t_0 + kT, \qquad T \geqslant \tau \tag{3}$$

where t_0 is an arbitrary time origin, k is a positive integer, and T is the time interval between the beginning of two successive observations.

In all the following, we assume that the dead time between samples is zero. We then have

$$T = \tau. \tag{4}$$

In this special case, the two-sample variance is well known as the Allan variance $\sigma_y^2(\tau)$

$$\sigma_y^2(\tau) = \langle \sigma_y^2(2, \tau, \tau) \rangle. \tag{5}$$

The relation between the Allan variance and $y(t)$ can be expressed as

$$\sigma_y^2(\tau) = \frac{1}{2\tau^2} \left\langle \left\{ \int_{t_k+\tau}^{t_k+2\tau} y(t)\, dt - \int_{t_k}^{t_k+\tau} y(t)\, dt \right\}^2 \right\rangle. \tag{6}$$

Equation (6) shows that $\sigma_y^2(\tau)$ is proportional to the true variance of the output of a linear filter with input signal $y(t)$ and impulse response $h_1(t)$ in Fig. 1.

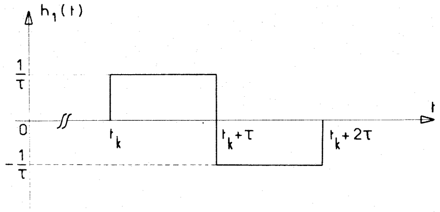

Fig. 1. Variations with time of the linear filter impulse response which represents the signal processing for the Allan variance calculation.

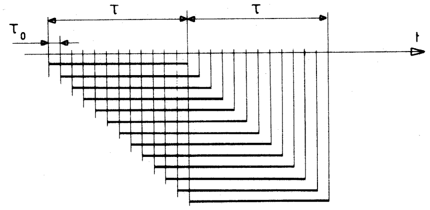

Fig. 2. Illustration of the algorithm considered for the measurement of periodic signal frequency.

The fractional frequency fluctuations $y(t)$ are actually well described by a conventional model which consists of a set of five independent noise processes [2]. Taking into account the finite bandwidth of the processed signal and assuming a single pole filter, the one-sided power spectral density $S_y(f)$ of $y(t)$ can be written as

$$S_y(f) = h_\alpha \frac{f^\alpha}{1 + \left(\frac{f}{f_c}\right)^2} \tag{7}$$

where coefficients h_α do not depend on f. The integer α equals 2, 1, 0, -1, and -2. f_c is the 3-dB bandwidth of the hardware filter.

III. THE MODIFIED ALLAN VARIANCE

The main property of the algorithm developed by J. J. Snyder is to increase the precision on the measure of periodic signal frequency, in presence of white phase noise [7]. It consists in dividing a time interval τ into n cycles of clock period τ_0 such as

$$\tau = n\tau_0. \tag{8}$$

Therefore, from a given observation time interval of duration 2τ, n overlapping time intervals of duration τ can be obtained, as depicted in Fig. 2. Another property of this algorithm is to reduce the total observation time by a factor $n/2$.

Following this way, Allan and Barnes have introduced the "modified Allan variance" [8] such as

$$\text{Mod } \sigma_y^2(\tau) = \frac{1}{2\tau^2} \left\langle \left[\frac{1}{n} \sum_{i=1}^{n} \left\{ \int_{t_0+(i+n)\tau_0}^{t_0+(i+2n)\tau_0} y(t)\, dt - \int_{t_0+i\tau_0}^{t_0+(i+n)\tau_0} y(t)\, dt \right\} \right]^2 \right\rangle. \tag{9}$$

It can be easily seen from (9) that the calculation of each statistical sample involved in the definition of Mod $\sigma_y^2(\tau)$ requires a signal observation of duration 3τ.

The impulse response $h_n(t)$ of the equivalent linear filter consists in finite sum of n shifted impulse responses $h_1(t)$. We have

$$h_n(t) = \frac{1}{n} \sum_{i=1}^{n} h_1(t - i\tau_0). \tag{10}$$

TABLE I
ANALYTICAL EXPRESSION FOR THE MODIFIED ALLAN VARIANCE WITHIN CONDITION $2\pi f_c\tau_0 \gg 1$

NOISE TYPE	α	$\text{Mod}\ \sigma_y^2(\tau)$
WHITE P M	2	$\frac{3\, h_2\, f_c}{8\, n\pi\, \tau^2}$
FLICKER P M	1	$\frac{h_1}{4\,\pi^2 n^2 \tau^2}\left[3n\ln(2\pi f_c\tau) + \sum_{k=1}^{n-1}(n-k)\left\{4\ln\left(\frac{n^2}{k^2}-1\right) - \ln\left(\frac{4n^2}{k^2}-1\right)\right\}\right]$
WHITE F M	0	$\frac{h_0}{2\tau} \times \frac{n^2+1}{2n^2}$
FLICKER F M	- 1	$\frac{2h_{-1}\ln 2}{n^2}\left[\frac{4n^2-3n+1}{2} + \frac{1}{n^2\ln 2} \times \sum_{k=1}^{n-1}(n-k) \times \left\{\frac{n}{2}\left[(k+2n)\ln(k+2n)-(k-2n)\ln(2n-k)\right] + \frac{1}{2}(k+n)(k-2n)\ln(k+n) + \frac{1}{2}(k-n)(k+2n)\ln\lvert k-n\rvert + 3k^2\ln k - k\left[(n+2k)\ln\left(k+\frac{n}{2}\right) - (n-2k)\ln\left\lvert k-\frac{n}{2}\right\rvert\right]\right\}\right]$
RANDOM WALK F M	- 2	$\frac{33}{40} + \frac{1}{8n^2} + \frac{1}{20n^4}$

In order to illustrate (10), variations with time of the shifted functions $h_1(t - i\tau_0)$ and of the impulse response $h_n(t)$ are represented in Fig. 3(a) and (b), respectively, for $n = 10$.

For $n = 1$, the Allan variance and the modified one are equal. We have

$$\text{Mod}\ \sigma_y^2(\tau) = \sigma_y^2(\tau). \tag{11}$$

One can express (9) in terms of the spectral density $S_y(f)$. We have

$$\text{Mod}\ \sigma_y^2(\tau) = \frac{2}{n^2\pi^2\tau^2}\cdot\left\{n\int_0^\infty \frac{1}{f^2} S_y(f)\sin^4(\pi f n\tau_0)\,df + 2\sum_{k=1}^{n-1}(n-k)\int_0^\infty \frac{1}{f^2} S_y(f)\cos(2\pi f k\tau_0)\cdot\sin^4(\pi f n\tau_0)\,df\right\}. \tag{12}$$

It should be noted that the integrals involved in (12) are convergent for each noise component. The analytical expression for the modified Allan variance can therefore be deduced directly from this equation.

In the following, it is assumed that the condition $2\pi f_c\tau_0 \gg 1$ is fulfilled. This means that the hardware bandwidth of the measurement system must be much larger than the reference clock frequency.

We have calculated the modified Allan variance for each noise component. Results are reported in Table I. It appears that the analytical expression for $\text{Mod}\ \sigma_y^2(\tau)$ is relatively simple except for flicker phase and flicker frequency noises where it is given as a finite sum of functions depending on n. In order to compare the Allan variance with the modified one, we

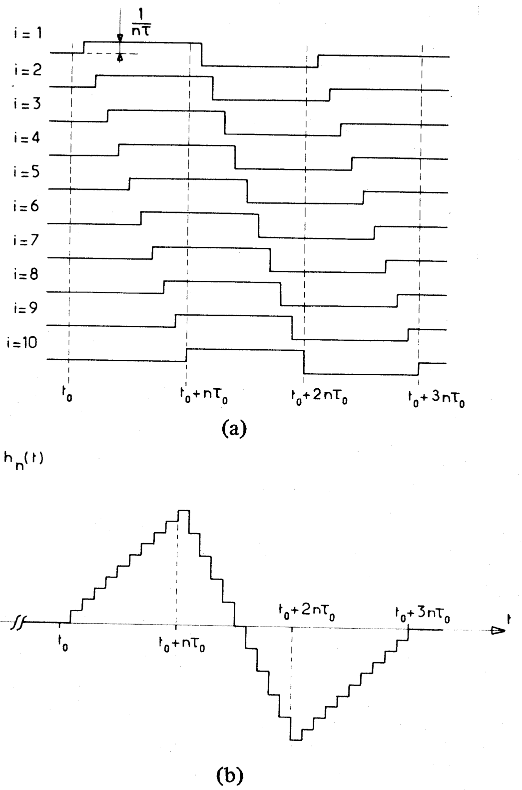

(a)

(b)

Fig. 3. (a) The impulse response $h_n(t)$, associated with the modified Allan variance calculation, represented as a sum of n shifted impulse response $h_1(t)$. It is assumed $n = 10$. (b) Variations with time of the impulse response $h_n(t)$, in the special case where $n = 10$.

TABLE II
ANALYTICAL EXPRESSIONS AND ASYMPTOTICAL VALUS FOR $R(n)$
(Results Are Valid within Condition $2\pi f_c\tau_0 >> 1$)

α	$R(n)$	$\lim_{n\to\infty} R(n)$
2	$\frac{1}{n}$	0
1	$\frac{1}{n^2}\left[n + \frac{1}{3\,\ln(2\pi f_c n\tau_0)} \times \sum_{k=1}^{n-1} (n-k)\left\{4\,\ln\left(\frac{n^2}{k^2}-1\right) - \ln\left(\frac{4n^2}{k^2}-1\right)\right\}\right]$	0
0	$\frac{n^2+1}{2n^2}$	0.5
- 1	$\frac{1}{n^2}\left[\frac{4n^2-3n+1}{2} + \frac{1}{n^2 \ln n^2} \times \sum_{k=1}^{n-1}(n-k) \times \left\{\frac{n}{2}\left[(k+2n)\ln(k+2n)-(k-2n)\ln(2n-k)\right]\right.\right.$ $+ \frac{1}{2}(k+n)(k-2n)\ln(k+n) + \frac{1}{2}(k-n)(k+2n)\ln\lvert k-n\rvert + 3k^2\ln nk - k\left[(n+2k)\ln\left(k+\frac{n}{2}\right)\right.$ $\left.\left.\left.- (n-2k)\ln\left\lvert k-\frac{n}{2}\right\rvert\right]\right\}\right]$	0.787
- 2	$\frac{33}{40} + \frac{1}{8n^2} + \frac{1}{20n^4}$	0.825

consider the ratio $R(n)$ defined in [8] as

$$R(n) = \text{Mod}\,\sigma_y^2(\tau)/\sigma_y^2(\tau). \tag{13}$$

The analytical expressions for $R(n)$, deduced from Table I, are reported in Table II. One can see that $R(n)$ does not depend on the product $f_c\tau_0$, except for flicker phase noise modulation. The asymptotic values of $R(n)$ are also listed in Table II.

Fig. 4 depicts the variations of $R(n)$ with n. It shows that, for large values of n, white phase and flicker phase noise modulations have different dependences. As outlined in [8], this gives a means to easily distinguish these two noise processes, in the time domain. For large n, and for $\alpha = 0, -1, -2$, $R(n)$ remains a constant. Consequently the Allan variance can be deduced from the modified one, for these noise processes.

A comparison with results of [8] shows a good agreement for $\alpha = 2$, 0 and -2. But, for $\alpha = 1$ and -1, our expressions for the modified Allan variance and ratio $R(n)$ disagree, especially for flicker phase noise modulation. This discrepancy might be due to the fact that in [8], Mod $\sigma_y^2(\tau)$ is expressed in terms of the autocorrelation function of phase fluctuations which is not defined for $\alpha = 1$.

IV. UNCERTAINTY ON THE ESTIMATE OF THE MODIFIED ALLAN VARIANCE

Equation (9) shows that the definition of the modified Allan variance theoretically implies an infinite set of time intervals.

Practically, one can only estimate this quantity from a finite set of m successive cycles similar to the one depicted in Fig. 3(b).

Let Mod $\hat{\sigma}_y^2(\tau)$ be the estimated modified Allan variance (EMAV) such as

$$\text{Mod}\,\hat{\sigma}_y^2(\tau) = \frac{1}{2\tau^2 n^2} \times \frac{1}{m}\sum_{k=1}^{m}\left\{\sum_{i=1}^{n} A_{i,k}\right\}^2 \tag{14}$$

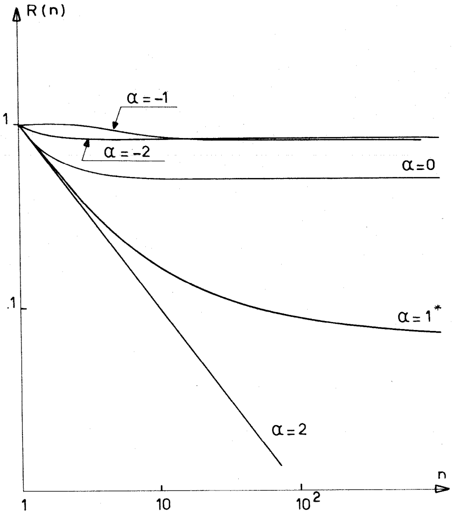

Fig. 4. Variations with n of the ratio $R(n)$, for fractional frequency fluctuations with power law spectrum $S_y(f) = h_\alpha \cdot (1/1 + (f/f_c)^2)f^\alpha$, within condition $2\pi f_c\tau_0 >> 1$. (*For $\alpha = +1$, $R(n)$ is a function of f_c and τ_0. The reported variations are for $2\pi f_c\tau_0 = 10^4$.)

where

$$A_{i,k} = \int_{t_0+(i+n)\tau_0+(k-1)3n\tau_0}^{t_0+(i+2n)\tau_0+(k-1)3n\tau_0} y(t)\,dt - \int_{t_0+i\tau_0+(k-1)3n\tau_0}^{t_0+(i+n)\tau_0+(k-1)3n\tau_0} y(t)\,dt. \tag{15}$$

The EMAV is a random function of m. Its calculation requires an observation time of duration $3m\tau$.

We consider ϵ, the fractional deviation of the EMAV relative to the modified Allan variance defined as follows:

$$\epsilon = \frac{\text{Mod } \hat{\sigma}_y^2(\tau) - \text{Mod } \sigma_y^2(\tau)}{\text{Mod } \sigma_y^2(\tau)}. \qquad (16)$$

The standard deviation $\sigma(\epsilon)$ of ϵ defines the relative uncertainty on the measurement of the modified Allan variance, due to the finite number of averaging cycles. We have

$$\sigma(\epsilon) = \frac{1}{\text{Mod } \sigma_y^2(\tau)} \{\sigma^2 [\text{Mod } \hat{\sigma}_y^2(\tau)]\}^{1/2} \qquad (17)$$

where $\sigma^2 [\text{Mod } \hat{\sigma}_y^2(\tau)]$ denotes the true variance of the EMAV such as

$$\sigma^2 [\text{Mod } \hat{\sigma}_y^2(\tau)] = \langle [\text{Mod } \hat{\sigma}_y^2(\tau)]^2 \rangle - [\text{Mod } \sigma_y^2(\tau)]^2. \qquad (18)$$

We assume that the fluctuations $y(t)$ are normally distributed [10]. One can therefore express $\langle [\text{Mod } \hat{\sigma}_y^2(\tau)]^2 \rangle$ as

$$\begin{aligned} m^2 \langle [\text{Mod } \hat{\sigma}_y^2(\tau)]^2 \rangle &= (m^2 + 2m) [\text{Mod } \sigma_y^2(\tau)]^2 \\ &\quad + 4 \sum_{p=1}^{m-1} (m-p) \left\{ 2 \sum_{i=1}^{n-1} (n-i) I_n + n I_0 \right\}^2 \qquad (19) \end{aligned}$$

where I_n are integrals which depend on n and on the noise process. We have

$$\begin{aligned} 8\pi^2\tau^2 n^2 I_n = \int_0^\infty & \frac{S_y(f)}{f^2} \cos 6\pi n p f \tau_0 \\ & \times \{6 \cos 2\pi f \tau_0 i - 4 \cos 2\pi f \tau_0 (i+n) \\ & - 4 \cos 2\pi f \tau_0 (i-n) + \cos 2\pi f \tau_0 (i+2n) \\ & + \cos 2\pi f \tau_0 (i - 2n)\} \, df. \qquad (20) \end{aligned}$$

For each noise component, the expression for $\sigma(\epsilon)$ can be deduced from the calculation of integrals involved in (20). These expressions are generally lengthy and complicated except for white phase and white frequency noise modulations, where integrals I_n equal zero. We have limited the present analysis to these two noise components. We get for $\sigma(\epsilon)$

$$\sigma(\epsilon) = \frac{2}{m}, \quad \text{for } \alpha = 2 \text{ and } 0. \qquad (21)$$

We now compare (21) with previously published results related to the estimate of the Allan variance [5]. For a given time observation of duration $3m\tau$, it can be easily deduced from [5] that the relative uncertainty on the estimate of the Allan variance varies asymptotically as $1.14\, m^{-1/2}$ and $1.0\, m^{-1/2}$ for $\alpha = 2$ and 0, respectively. For these two noise components, the uncertainty on the EMAV is larger than the uncertainty on the estimated Allan variance, but of the same order of magnitude.

V. CONCLUSION

We have calculated the analytical expression for the modified Allan variance for each component of the model usually considered to characterize random frequency fluctuations in precision oscillators. These expressions have been compared with previously published results and the link between the Allan variance and the modified Allan variance has been specified.

The uncertainty on the estimate of the modified Allan variance has been studied and numerical values have been reported for white phase and white frequency noise modulations.

In conclusion, the modified Allan variance appears to be well suited for removing the ambiguity between white and flicker phase noise modulation. Nevertheless, the calculation of the modified Allan variance requires signal processing which is complicated, compared to the Allan variance. In the presence of white or flicker phase noise, the Allan variance cannot be easily deduced from the modified Allan variance. Furthermore, for a given source exhibiting different noise components, the determination of the Allan variance from the modified one is difficult to perform. For most of time-domain measurements, the use of the Allan variance is preferred.

ACKNOWLEDGMENT

The authors would like to express their thanks to Dr. Claude Audoin for constructive discussions and valuable comments on the manuscript.

REFERENCES

[1] D. W. Allan, "Statistics of atomic frequency standards," *Proc. IEEE*, vol. 54, pp. 221–230, Feb. 1966.

[2] J. A. Barnes *et al.*, "Characterization of frequency stability," *IEEE Trans. Instrum. Meas.*, vol. IM-20, pp. 105–120, May 1971.

[3] L. S. Cutler and C. L. Searle, "Some aspects of the theory and measurement of frequency fluctuations in frequency standards," *Proc. IEEE*, vol. 54, pp. 136–154, Feb. 1966.

[4] J. Rutman, "Characterization of phase and frequency instabilities in precision frequency sources: Fifteen years of progress," *Proc. IEEE*, vol. 66, pp. 1048–1075, Sept. 1978.

[5] P. Lesage and C. Audoin, "Effect of dead-time on the estimation of the two-sample variance," *IEEE Trans. Instrum. Meas.*, vol. IM-28, pp. 6–10, Mar. 1979.

[6] J. J. Snyder, "Algorithm for fast digital analysis of interference fringes," *Appl. Opt.*, vol. 19, pp. 1223–1225, Apr. 1980.

[7] —, "An ultra-high resolution frequency meter," in *Proc. 35th Annu. Symp. Frequency Control* (Fort Monmouth, NJ), 1981, pp. 464–469.

[8] D. W. Allan and J. A. Barnes, "A modified Allan variance with increased oscillator characterization ability," in *Proc. 35th Annu. Symp. Frequency Control* (Fort Monmouth, NJ), 1981, pp. 470–474.

[9] B. Picinbono, "Processus de diffusion et stationnarité," *C.R. Acad. Sci.*, vol. 271, pp. 661–664, Oct. 1970.

[10] P. Lesage and C. Audoin, "Characterization of frequency stability: Uncertainty due to the finite number of measurements," *IEEE Trans. Instrum. Meas.*, vol. IM-22, pp. 157–161, June 1973.

Simultaneous Measurement of Complex Permittivity and Permeability in the Millimeter Region by a Frequency-Domain Technique

PRASAD K. KADABA, SENIOR MEMBER, IEEE

Abstract—**A frequency-domain techique based on the measurement of scattering parameters has been described for the simultaneous measurement of complex permittivity ϵ^* and permeability μ^* in the millimeter region. The technique can be easily adapted for broad-band measurements. Results are given for teflon, plexiglas, fiberglass, and FGM-40,[1] a magnetic absorber in the *X* band. Reflection and transmission error parameters corrections can be implemented to improve the accuracy.**

---

[1] Manufactured by Emerson-Cuming Inc., Canton, MA.

Manuscript received April 14, 1983; revised March 19, 1984. This work was done under Contract IPA-113-81-01114 from AFOSR.

The author is with the Department of Electrical Engineering, University of Kentucky, Lexington, KY 40506.

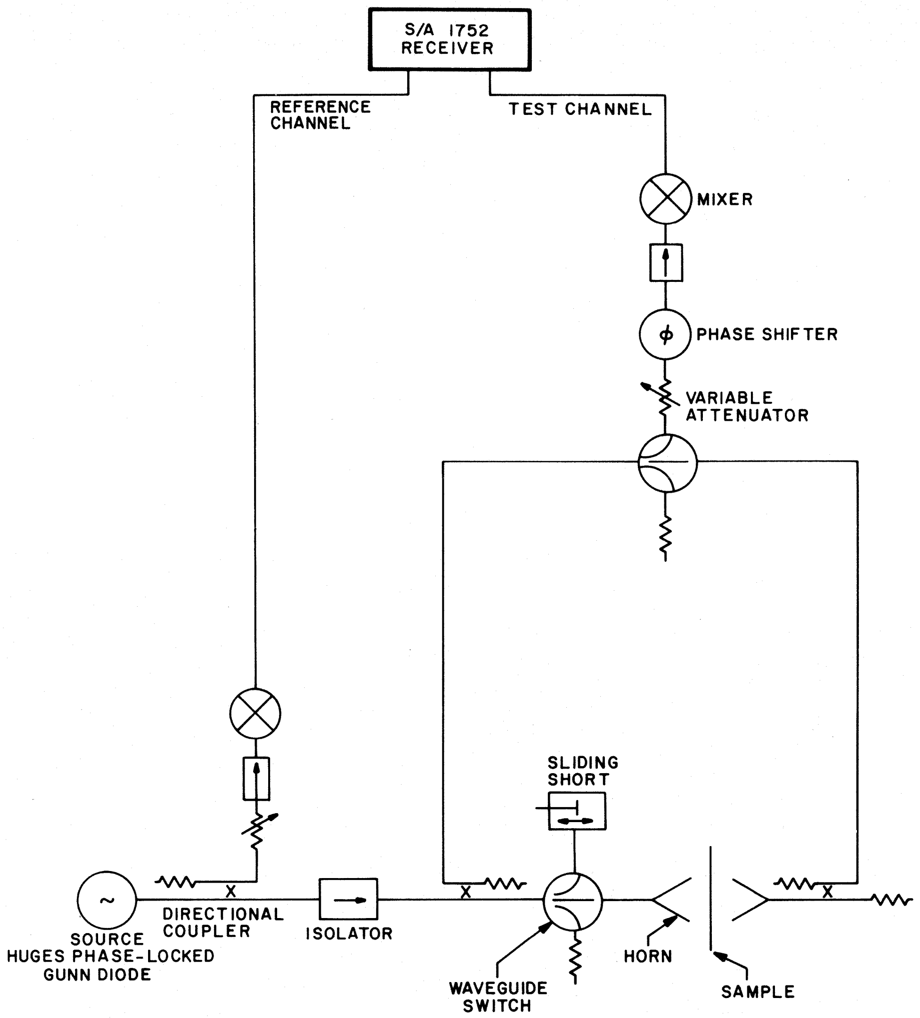

Fig. 1. Schematic of the experimental set-up in the V and W bands to measure reflection and transmission coefficients.

I. INTRODUCTION

The design of radar absorbable materials in defense applications requires accurate data of complex permittivity ϵ^* and of complex permeability μ^*. In the millimeter region of the electromagnetic spectrum, data on both ϵ^* and μ^* are relatively scarce, even on materials readily available through commercial sources. This paper outlines a frequency-domain technique which involves the measurement of reflection and transmission scattering parameters from a sample. Results are reported in the V and W bands for teflon, plexiglas, fiberglass, and FGM-40, a magnetic absorber in the X band. Error corrections are implemented in a few cases to improve the accuracy of the data.

II. DETAILS OF THE EXPERIMENTAL SET-UP

A schematic of the experimental set-up used to measure the reflection coefficient $\overline{\Gamma}$ and the transmission coefficient $\overline{\tau}$ is shown in Fig. 1. The sources that were available are fixed-frequency, phase-locked Gunn diodes—one at 56 GHz in the V-band (Hughes 47744H-1205) and the other at 94 GHz in the W-band (Hughes 47746H-1201). A similar technique has been reported by Redheffer [1]. This earlier work relates to measurements in the K-band using unlocked sources and is concerned with only permittivity measurements. The V-band source has a rated power output of 50 mW and the W-band source is rated at 10 mW. The phaselock-loop system used is described in a paper by Baprawski *et al.* [2]. The transmitting and receiving horns are standard 20-dB-gain horns and the sample was mounted on a 7 × 7-in aluminum frame fixed to a micrometer-driven carriage[2] which can be displaced in three directions. Therefore, it was possible to orient the sample properly with reference to the incident beam. Provision was also made to rotate the sample assembly about a vertical axis at the center of the frame for measurements other than normal incidence. The distance between the transmitting horn and the sample was such that the far-field criterion was satisfied. The sides of the aluminum frame facing the transmitting horn were sloped towards the inner edge to reduce edge effects. The mixers shown in the schematic were single-ended mixers (narrow-band, fixed-tuned) using Shottky barrier diodes with a conversion loss of 7 dB in the V band and 8 dB in the W band. The mixers were preceded by isolators to insure better matching to the incoming signals. The entire experimental set-up was mounted on an optical bench.

The standard-gain horns in the set-up can be replaced by TRG Series 856 collimating, lens-corrected, conical horns. The dielectric lens changes the aperture field from a spherical wave to a plane wave. The sample in this case can be close to the mouth of the horn and is desirable in case of lossy samples when the source power is limited. The experimental set-up shown in Fig. 1 can also be modified for a cost-effective broadband ϵ^* and μ^* measurement capability by replacing the fixed-

---

[2] Newport Research Corporation Model 705 lens positioner assembly.

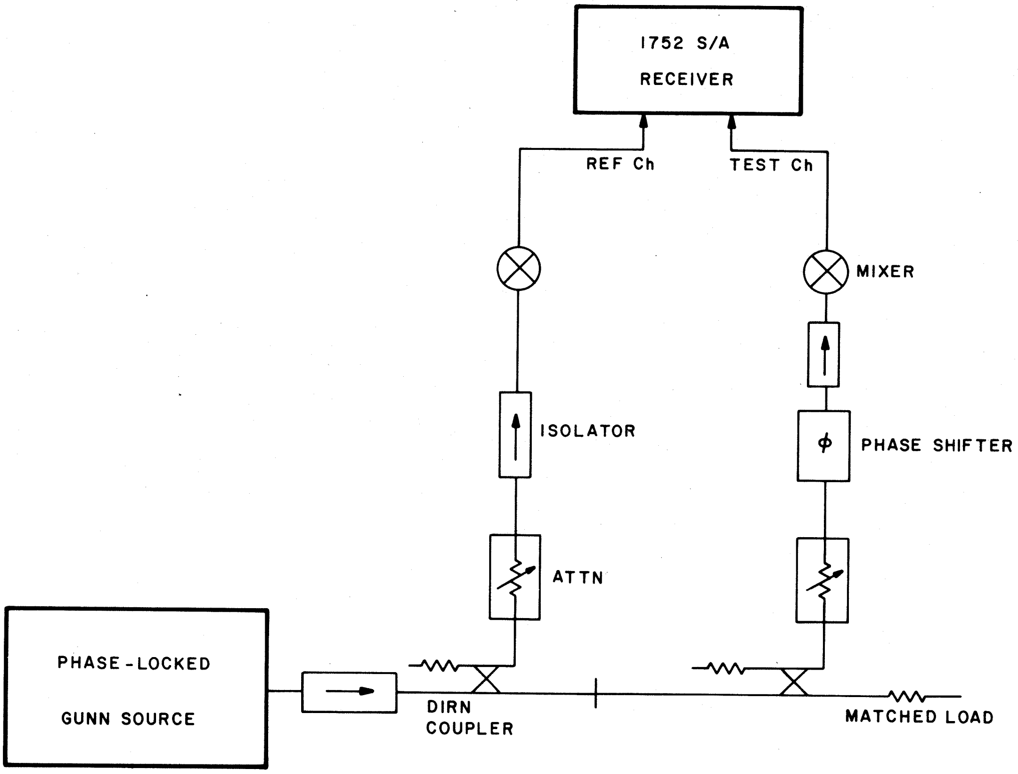

Fig. 2. Schematic of the set-up to calibrate the amplitude and phase angle meters on the SA receiver.

frequency sources with sweepers in conjection with EIP microwave counter (lock box) model 578. With the lock box, commercially available sweepers in the millimeter region can be phase locked to an accuracy and long-term stability equal to that of the internal crystal reference oscillator in the counter unit. In this manner the measurement capability can be extended to 110 GHz.

III. MEASUREMENT PROCEDURE

Initial Adjustments

Using the phase-lock oscillator tune-up procedure instructions supplied by the manufacturer, both the *V*- and *W*-band sources lock and are ready to operate in about 10 min. The Scientific-Atlanta (S/A) receiver needs a warm-up period of about 20 min before data can be taken. The amplitude and phase angle meters on the S/A receiver were calibrated using the set-up shown in Fig. 2. The readings of the calibrated phase shifter and variable attenuator in the test channel arm were compared against the corresponding readings on the amplitude and phase-angle meters in the receiver. The agreement between the phase readings was very good, but the variable attenuator and amplitude meter readings differed by 0.2–0.5 dB. The amplitude meter readings on the receiver were suitably corrected before the reflection and transmission coefficient data of the test sample were analyzed. It was also necessary to modify the S/A 1702 receiver for use in the *V*- and *W*-bands with external mixers. Details are given by the author in a report [3]. The residual drift in the receiver was attributed to the silicon wafers in the mixers. Silicon crystals are rather temperature sensitive. The following improvements were made to overcome the residual drift: i) wrapping the mixers with thermal insulation tape, ii) using cable with low thermal coefficient of drift (0.05 parts/$10^6/^\circ$C),[3] and iii) using cables of same length from the mixers to the reference and test channels.

The orientation of the sample holder with the shorting plate attached (used as a reference in obtaining $\overline{\Gamma}\,(\overline{S}_{11})$ data was first adjusted with respect to the tramsitting horn for maximum amplitude reading at normal incidence. Likewise the receiving horn was aligned with reference to the transmitting horn, with the shorting plate removed (open window) for maximum reading on the amplitude meter. The physical separation between the two antennae was 47 cm, and the sample was placed midway between the two. The above distance from the transmitting antenna to the sample satisfied the far-field criterion both in the *V*- and *W*-bands. After the above initial adjustments the equipment is ready for taking the data.

IV. MEASUREMENT OF $\overline{S}_{11}$ AND $\overline{\tau}$

The samples used in the meaurements were in the form of sheets 7 × 7 in. $\overline{S}_{11}$ data on the samples were normalized with respect to the amplitude and phase readings of the shorting plate. The theoretical treatment of the method [4] demands that the front face of the shorting plate should be in the exact position to be occupied by the test sample. This is necessary in order to get an accurate phase reference. Another assumption made in the theoretical treatment is that the electromagnetic field incident on the sample approximates a plane wave. Both the above conditions seem to be pretty well satisfied in the experimental set-up. The transmission coefficient $\overline{\tau}$ of the samples were obtained using the amplitude and phase readings of the open window as reference. For good phase-measurement accuracy, it is desirable that the inputs to the reference and test channels of the receiver should be of the same level. This condition was maintained during the course of the measurements. Also, the RF inputs to the receiver were below -30 dBm to prevent receiver saturation. With these precautions, $\overline{S}_{11}$ and $\overline{\tau}$ data were accurate to about 2 percent and this leads to good material measurement accuracy. Theoretical details of how to evaluate the ϵ^* and μ^* of the samples from the measured $\overline{S}_{11}$ and $\overline{\tau}$ data are given in the Appendix. The reflection

---

[3] Maunfactured by Flexco Cable, Linden, NJ.

TABLE I
PERMITTIVITY AND PERMEABILITY VALUES IN THE MILLIMETER WAVE REGION

Material	ε'	ε''	μ'	μ''
I. Plexiglas: (Sample thickness: 29.1 mils)				
56 GHz:	2.45	0.05	0.92	-0.05
Error corrected:	2.60	0.06	0.98	0.02
94 GHz:	2.54	0.08	0.91	0.07
II. Fiberglass: (Sample thickness: 19.3 mils)				
56 GHz:	4.46	0.36	1.02	-0.23
94 GHz:	4.42	0.41	0.98	-0.26
III. Teflon: (Sample thickness: 31.2 mils)				
56 GHz:	2.09	0.003	1.01	0.009
94 GHz:	2.07	0.006	0.99	0.011
IV. FGM-40: (Sample thickness: 40 mils)				
56 GHz:	4.2	7.5	1.01	0.02
*18 GHz:	15.	5.2	1.02	0.23

*FGM-40 was measured at 18 GHz for comparison.

TABLE II
PERCENTAGE ERROR RANGES IN THE EVALUATION OF ϵ^* AND μ^* DATA

Frequency (GHz)		Plexiglas	Fiberglass	Teflon	FGM-40
18	ε',μ'				2
	δ				4
56	ε',μ'	2	3	3	6
	δ	4	6	6	9
94	ε',μ'	4	4.5	3	7
	δ	8	9	6	10

and transmission error parameters used to correct the measured $\bar{S}_{11}$ and $\bar{\tau}$ data of the test samples were obtained by a method outlined by Rytting [5]. In this method three known short positions are used to compute the reflection error parameters. The transmission error parameters are obtained by measuring the reflection and transmission scattering parameters with the empty sample holder, using the shorting plate data as reference. The final evaluation of the transmission error parameters involves the reflection error parameters. These error corrections account for imperfections in the line components such as directional couplers, waveguide to coaxial line adapters, etc. Final calculation of ϵ^* and μ^* values of the samples were made by processing the $\bar{S}_{11}$ and $\bar{\tau}$ data on the HP 21MX minicomputer, using the subroutine CDAT of the main EDMSP program developed by Kent [6]. One limitation of this program is that the algorithm does not permit sample thicknesses greater than $\lambda_d/4$, where λ_d is the wavelength in the sample. Efforts are underway to improve the program in this regard. In case of samples whose thicknesses were greater than $\lambda_d/4$ as in the case of FGM-40, ϵ^* and μ^* were calculated using the procedure outlined in the Appendix and using the HP9810A calculator.

V. EXPERIMENTAL RESULTS

$\epsilon^* = \epsilon' - j\epsilon''$ and $\mu^* = \mu' - j\mu''$ values for plexiglas, fiberglass, teflon, and FGM-40 measured at 56 GHz and 94 GHz are shown in Table I. Only the plexiglas data at 56 GHz has been error corrected as an illustration. The error corrections seem to improve the results somewhat. The errors in the final values of permittivity and permeability for the various samples are listed in Table II in terms of ϵ', μ', and loss angle δ defined as $\tan^{-1}$ (ϵ''/ϵ') or $\tan^{-1}$ (μ''/μ'). The ϵ', ϵ'' values for teflon and ϵ' values for plexiglas and fiberglass agree fairly well with what has been reproted in the literature [7]. ϵ'' values for these materials are not readily available in the literature. No data has been reported in the literature in the V-band for FGM-40. From the data shown in Table I, FGM-40 seems to act like a lossy dielectric rather than as a magnetic absorber.

VI. CONCLUSIONS

The frequency-domain technique described in this paper yields good results for ϵ^* and μ^* in the millimeter region for planar samples whose loss parameters are not high. The technique described has the potential for adaptation to broad-band measurements. Improvement in the accuracy of the data is noticeable using reflection and transmission error parameter corrections. ϵ', ϵ'' values for teflon and ϵ' values for plexiglas and fiberglass agree fairly well with literature values. The results for FGM-40 at 56 GHz indicate that this material acts like a lossy dielectric at this frequency rather than as a magnetic absorber.

APPENDIX

The complex permittivity ϵ^* and complex permeability μ^* of a material can be evaluated from the measured reflection coefficient $\bar{\Gamma}$ and transmission coefficient $\bar{\tau}$ as follows.

The reflection scattering coefficient $\bar{S}_{11}$ is identical to $\bar{\Gamma}$ and the transmission scattering coefficient $\bar{S}_{21}$ is related to $\bar{\tau}$ through the relation, $\bar{S}_{21} = \tau e^{-\gamma_0 d}$ where d is the thickness of the sample and $\gamma_0 = j\omega\sqrt{\mu_0 \epsilon_0}$ is the propagation constant for free space. $\omega = 2\pi f$ where f is the frequency of the source and μ_0, ϵ_0 are, respectively, the permeability and permittivity of the free space.

Define new parameters $\bar{V}_1$ and $\bar{V}_2$ and $\bar{X}$ thus:

$$\bar{V}_1 = \bar{S}_{21} + \bar{S}_{11}$$

$$\bar{V}_2 = \bar{S}_{21} - \bar{S}_{11}$$

$$\bar{X} = (1 - \bar{V}_1 \bar{V}_2)/(\bar{V}_1 - \bar{V}_2).$$

The reflection coefficient $\bar{\rho}$ is evaluated from $\bar{X}$ by the equation

$$\bar{\rho} = \bar{X} \pm \sqrt{(\bar{X}^2 - 1)}$$

where the plus or minus sign is chosen such that $|\bar{\rho}| < 1$. The parameter $\bar{Z}$, defined as $\exp\,(-j/\omega d/c)\sqrt{\mu_r^* \epsilon_r^*}$, where c, is the velocity of light and μ_r^*, ϵ_r^* are the values of μ^* and ϵ^* relative to free space, is related to $\bar{V}_1$ and $\bar{\rho}$ by the following equation:

$$\bar{Z} = (\bar{V}_1 - \bar{\rho})/(1 - \bar{V}_1 \bar{\rho}).$$

The magnitude of the incident wave at the far end of the sample is reduced from that of its amplitude at the front end by the attenuation portion of $\bar{Z}$. Two new parameters $\bar{C}_1$ and $\bar{C}_2$ are related to $\bar{\rho}$ and $\bar{Z}$ as follows:

$$\bar{C}_1 = \mu_r^*/\epsilon_r^* = (1 + \bar{\rho}/1 - \bar{\rho})^2$$

$$\bar{C}_2 = \mu_r^* \epsilon_r^* = -\left\{\frac{c}{\omega d} \ln (1/\bar{Z})\right\}^2$$

Finally,

$$\epsilon_r^* = \sqrt{\bar{C}_2/\bar{C}_1}$$

and

$$\mu_r^* = \sqrt{\bar{C}_1 \bar{C}_2}.$$

Further details can be found in a standard text on high-frequency transmission lines or in [3].

ACKNOWLEDGMENT

The author wishes to thank Dr. E. L. Pelton for helpful discussions during the course of this work.

REFERENCES

[1] R. M. Redheffer, "The measurement of dielectric constants," in *Technique of Microwave Measurements*, C. G. Montgomery, Ed. Boston: Technical Lithographers, Lexington, MA, 1963, ch. 10, pp. 591–599.

[2] J. Baprawski, C. Smith, and F. J. Bernues, "Phase-locked solid state mm-wave sources," *Microwave. J.*, pp. 41–44, Oct. 1976.

[3] P. K. Kadaba, "A study of the millimeter wave techniques for measuring complex permittivity and permeability," *AFOSR*, Aug. 1982, final rep. IPA-113-81-01114.

[4] D. G. Aguirre, "Frequency domain measurements of microwave absorber design materials," M.S. thesis, Air Force Institute of Technology, AFIT/GE/EE/80D-8, Wright-Patterson Air Force Base, OH Dec. 1980.

[5] D. Rytting, "Analysis of vector measurement accuracy enhancement techniques," presented at Hewlett-Packard Technical Sem., May 1978, Santa Rosa, CA.

[6] B. M. Kent, tech. memo, AFWAL/TM/81/27/AAWP, August 1981; available at the Technical Library, Wright-Patterson Air Force Base, OH.

[7] See, for example, K. H. Breeden and A. P. Sheppard, *Radio Sci.*, Vol. 3 (New Series), no. 2, p. 205 (1968); J. J. Taub, in *Proc. of Symp. on Submillimeter Waves, Polytechnic Institute of Brooklyn*, pp. 693–708, 1970.

Contributors

Majid A. H. Abdul-Karim, was born in Baghdad, Iraq on June 19, 1947. He received the B.Sc. degree in electrical engineering from the University of Baghdad, 1967. He obtained a scholarship from the Iraqi Government and Gulbenkian Foundation to pursue his graduate studies at the University of Manchester, Institute of Science and Technology, UMIST starting in 1971. He received the M.Sc. degree in digital electronics and the Ph.D. degree in the field of digital techniques applied to the measurement of electrical quantities from U.M.I.S.T., England, in 1972 and 1975, respectively.

He joined military service in 1967 on work in the field of radar. In 1969 he joined the Department of Electrical Engineering, College of Engineering, University of Baghdad as a Demonstrator. Since September 1975 he has been working as a Lecturer at the Department of Electrical Engineering, College of Engineering, University of Baghdad, Iraq. He is currently an Assistant Professor at the University of Baghdad since May 1980.

★

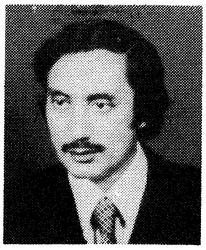

Muslim T. Ahmed (S'72–M'75) was born in Mirzapur, India, on September 14, 1945. He received B.Sc. (Hons.) and Ph.D. degrees in electrical engineering in 1967 and 1974 from the Aligarh Muslim University, Aligarh and the Indian Institute of Technology, Delhi, respectively.

He joined the Department of Electrical Engineering, Aligarh Muslim University in 1967 as a Lecturer and was subsequently appointed Reader in 1975. He became Professor in the same Department in 1982. He teaches, conducts research, and supervises Doctral students in electronics circuits and systems, filter theory and design, microprocessor applications and electronic instrumentation. He has published about 50 technical papers and has written a book.

Dr. Ahmed is a Fellow of the Institution of Electronics and Telecommunication Engineers, India.

Janan E. Allos (M'81) received the B.Sc. degree (with first class honors) in engineering from the Battersea College of Technology, London, England, in 1956. He received the Ph.D. degree from Kings College, London, England, in 1963.

He worked from 1956 to 1960 at Daura Refinery in Baghdad. In 1963 he returned to Baghdad and was appointed Lecturer in the College of Engineering, University of Baghdad. He became Assistant Professor in 1970 and Professor in 1982. Concurrently, between 1964 and 1978, he was Chief Engineer and then Technical Director of Forster and Sabbagh Co., in Baghdad, and until 1982, Research Group Leader at the Department of Electrical Engineering, College of Engineering.

★

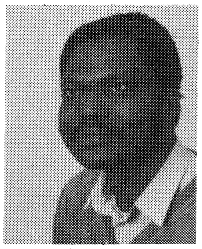

Théophane Ayi was born in Abomey, Benin Republic, on July 28, 1950. He received an engineering degree in system control from the University of Technology of Compiègne, France. He joined the Laboratoire de l'Horloge Atomique in 1981 and is working toward a Ph.D. in electronics at the Paris-Sud University.

He teaches Electronics and is presently Assistant Professor at the Department of Physics of the Paris-Sud University.

★

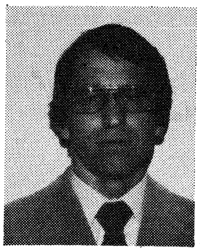

James H. Aylor (S'66–M'68–S'71–M'76–SM'82) received the B.S., M.S., and Ph.D. degrees in electrical engineering from the University of Virginia, Charlottesville, in 1968, 1971, and 1977, respectively.

He is currently an Associate Professor in the Department of Electrical Engineering at the University of Virginia. His research interests are in the areas of digital systems, microcomputer applications and image processing. For the past five years he has been involved in the design of various electronic devices for use by the handicapped, work carried out at the University's Rehabilitation Engineering Center.

Dr. Aylor is a member of Sigma Xi, Tau Beta Pi, and the IEEE Computer Society. He is also founder and chairman of the Technical Committee on Computing and the Handicapped within the Computer Society.

* * *

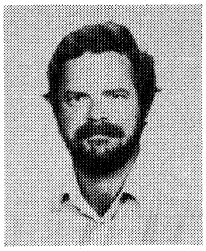

Mallory J. Boyd was born in Monrovia, CA, on July 7, 1953. He received the B.S. degree in electronic and computer engineering at the California Polytechnic University, Pomona, in June 1980.

His experience in military avionics systems began in the U.S. Air Force from 1972 through 1976. During this period, he worked with calibration, repair, and test sequence development for peculiar ground support equipment. He was employed at General Dynamics (Pomona Division), R.F. Guidance Section from 1979 through 1980. His work at General Dynamics was in the area of remotely piloted vehicles (RPV) development for military applications. From June 1980 through the present, he has been working at the Naval Weapons Center (NWC), China Lake, CA. His work at NWC has been primarily in 1) forward-looking infrared (FLIR) imaging systems engineering, and 2) the development of automated FLIR video assessment techniques.

* * *

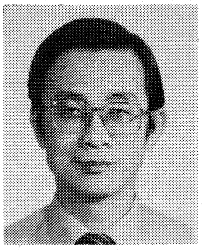

C. Y. Chang (S'69–M'70–SM'81) was born in Kaohsiung, Taiwan, on October 1, 1937. He received the B.S. degree in electrical engineering from National Cheng Kung University, Tainan Taiwan, in 1960, and the M.S. and Ph.D. degrees from National Chiao Tung University in 1962 and 1970, respectively.

From 1962 to 1966 he was a Research Assistant and then Instructor at Chiao Tung University working on setting up a semiconductor research laboratory. From 1966 to 1976, he was a Associate Professor, then Professor in solid-state electronics and semiconductor physics and technologies, and also Chairman of the Department of Electrophysics at Chiao Tung University. In 1981, he became a member of technical staff, Bell Laboratories, Murray Hill, NJ, working in the VLSI Device Group. Since 1977 he has been Professor and Director of the Research Institute of Electronics and Electrical Engineering, National Cheng Kung University Tainan, Taiwan, R.O.C. He is now Professor and Director of Semiconductor and System Laboratories of this university.

Dr. Chang is a member of Phi Tau Phi Honor Society, the Chinese Institute of Electrical Engineers, and the Electrochemical Society.

* * *

Suhash C. Dutta Roy was born in Mymensingh, now in Bangladesh. He received the B.Sc.(Hons.) degree in physics, the M.Sc.(Tech.) degree in radio physics and electronics, and the D.Phil. degree for research on network theory and solid state circuits, all from the University of Calcutta, Calcutta, India in 1956, 1959, and 1965, respectively.

He worked with the Geological Survey of India (1959); the River Research Institute, West Bengal (1960–1961); the University of Kalyani, West Bengal (1961–1965); and the University of Minnesota, USA (1965–1968) before joining the Indian Institute of Technology (IIT), New Delhi, in 1968. He has been a Professor of Electrical Engineering at IIT since January 1970 and was the Chairman of the Department during 1970–1973. During 1973–1974, he was a Visiting Professor at the University of Leeds, England, and during 1978–1979, he was a Visiting Fellow at the Iowa State University, Ames. He teaches circuits, systems, electronics, and signal processing courses, and conducts and supervises research in the same areas.

Dr. Dutta Roy is a Fellow of the Institution of Electronics and Telecommunication Engineers (IETE), India; a member of the Editorial Board of the *International Journal of Circuit Theory and Applications*; and the Honorary Editor for Circuits and Systems, *Journal of the IETE.* He was awarded the 1973 Professor Meghnad Saha Memorial Prize and the 1980 Ram Lal Wadhwa Gold Medal by the IETE, the 1981 Shanti Swarup Bhatnagar Award by the Govt. of India, and the 1981 Vikram Sarabhai Research Award by the Physical Research Laboratory, Ahmedabad.

* * *

Yean-Kuen Fang, was born in Tainan, Taiwan, on October 10, 1944. He received the B.S. degree and M.S. degree in electronics engineering from National Chaio Tung University in 1957 and 1959, respectively. In 1981, he received the Ph.D. degree in semiconductor engineering from the Research Institute of Electrical and Electronics Engineering.

From 1960 to 1978 he was a Senior Design and Research Engineer in private companies. From 1978 to 1980 he was a Instructor in National Cheng Kung University. In 1981 he became an Associate Professor with E. E. Dept. National Cheng Kung University.

Dr. Fang is a member of Phi Tau Phi Honor Society.

* * *

Robert B. Frenkel was born in Hong Kong on September 22, 1939. He has received a B.S. degree in physics from the University of Sydney, and has also received the M.S. degree from the same University and M.Eng. Sci. degree from the University of New South Wales.

He joined the National Measurement Laboratory (then known as the National Standards Laboratory) of the Commonwealth Scientific and Industrial Research Organization in 1963 and has specialized in dc electrical standards.

* * *

Johann H. Hinken (M'79–SM'83) was born in Wagenfeld, Germany, on April 17, 1946. He received the Dipl-Ing. degree in electrical engineering and the Doktor-Ing. degree from the Technische Universität Brauschweig, Braunschweig, Germany, in 1972 and 1978, respectively.

From 1972 to 1978 he was a Teaching and Research Assistant at the Institut für Hochfrequenztechnik of the Technische Universität Braunschweig. There he developed microwave filters and investigated the attenuation of optical film modes. Since 1978, he has been with the Physikalisch-Technische Bundesanstalt, Brauschweig, where he is mainly involved with precision dc measurement applying superconductivity phenomena and microwave means.

* * *

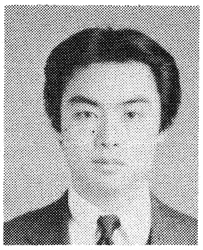

Masahide Hirasawa was born in Tokyo, Japan, on April 8, 1958. He received the B.E. and the M.E. degrees in electrical engineering from Tamagawa University, Tokyo, Japan.

Mr. Hirasawa is a member of the Institute of Electronics and Communication Engineers of Japan, Information Processing Society of Japan and the Japan Society for Simulation Technology.

David L. Hollway (SM'62) was born at Ballarat, Victoria, Australia, on December 5, 1915. He received the B.E.E. and M.Eng.Sc. degrees from Melbourne University, Australia and the D.S.Eng. from Sydney University, Australia, in 1937, 1939, and 1954, respectively.

From 1940 to 1946 he served in the Valve Division of Standard Telephones and Cables Limited, Sydney, handling engineering problems in the production of transmitting, receiving and radar tubes. On joining the Commonwealth Scientific and Industrial Research Organization in 1946 he developed methods of determining electron motion in the presence of space charge and electron beam devices. From 1953 he engaged in research in methods of measurement at microwave and radio frequencies. He retired as Senior Principal Research Scientist in 1980 and is now an Honorary Research Fellow with the CSIRO.

Dr. Hollway is a Fellow of the Institution of Radio and Electronic Engineers, Australia.

★

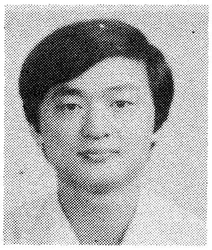

Wei C. Hsu was born in Taichung, Taiwan, in 1957. He received the B.S.E.E. and M.S.E.E. degrees from Cheng-Kung University, Taiwan, in 1979 and 1981, respectively. He is presently a Ph.D. candidate in electrical engineering in Cheng-Kung University.

★

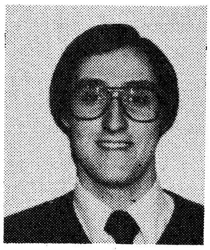

Barry W. Johnson (S'78–M'80–S'80–M'82) received the B.S., M.S., and Ph.D. degrees in electrical engineering from the University of Virginia, Charlottesville, in 1979, 1980, and 1983, respectively.

He was a Graduate Research Assistant at the University's Rehabilitation Engineering Center while working toward his degree. For three years he was involved in the development of electronic aids for the physically handicapped. His major areas of interest include digital control systems and fault tolerant computing. He is currently employed by the Harris Corp, Melbourne, FL.

Dr. Johnson is a member of Eta Kappa Nu and Tau Beta Pi.

★

Prasad K. Kadaba (SM'70) was born in Bangalore, India, on February 14, 1924. He received the M.Sc. degree in physics from the University of Mysore, India, in 1944, the M.S. degree in electrical engineering from the California Institute of Technology, Pasadena, and the Ph.D. degree in physics from the University of California, Los Angeles in 1947 and 1950, respectively.

Since 1964, he has been a Professor in the Electrical Engineering Department, University of Kentucky, Lexington, KY. He has been a Fulbright Scholar at the Institut Jozef Stefan, Ljubljana, Yugoslavia from 1973 to 1974 and Visiting Professor at the Wright-Patterson Air Force Base, Ohio from 1981 to 1982. His research activities are in the areas of dielectric and magnetic relaxation studies, applications of microwave spectroscopy, and nuclear double resonance techniques for pollution studies and currently in millimeterwave measurement techniques.

Dr. Kadaba is a member of Sigma Xi, Eta Kappa Nu, and Tau Beta Pi.

Makoto Kanno (SM'66–F'84), for a photograph and biography please see page 245 of this issue.

★

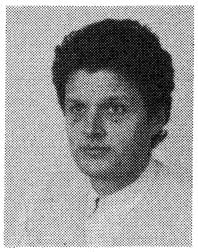

Paul Lesage was born in Boulogne-Billancourt, France on February 11, 1947. He received the M.S. degree and Ph.D. degree in physics from Paris-Sud University, Orsay, France in 1970 and 1980, respectively.

He joined the Laboratoire de l'Horloge Atomique in 1971 and is in charge of problems related to the study and measurement of noise in oscillators and atomic frequency standards. He is currently a Maitre-Assistant at the Physics Department of the University of Paris. He teaches logic, information process and statistical optimization.

★

W. C. Liu was born in Gurkeng, Taiwan, on June 21, 1957. He received the B.S.E.E. and M.S.E.E. degrees from Cheng-Kung University, Taiwan, in 1979 and 1981, respectively. He is presently a Ph.D. candidate in Electrical Engineering Department in Cheng-Kung University.

★

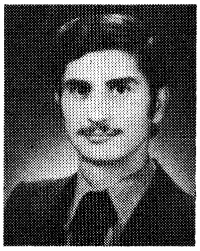

Mahir K. Mahmood (M'83), graduated from the College of Engineering in June 1980 with a B.Sc. degree of the University of Baghdad. In March 1981 he joined the same University and had the Higher Diploma degree in electronics and communication in February 1982, since then he has been working for his M.Sc. degree under a project entitled "Fast detection of the parameters of a pure sinusoidal signals."

From June 1980 to March 1981 he joined a government institute for practical experience.

★

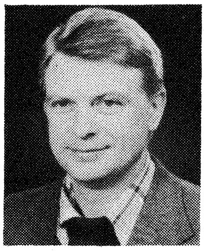

Wolfgang Meier was born in Braunschweig, on April 22, 1937.

He has been a technical engineer since 1960. Prior to 1979 he was employed in the University of Braunschweig and worked in the area of hydrodynamics. In 1979 he joined the Physikalisch-Technische Bundesanstalt in Braunschweig where he is currently involved in the fabrication of Josephson junction devices.

★

Walter Muller (M'79) was born in Mainz, Germany in 1932 and educated in the Netherlands. He received the M.Sc. degree in electrical engineering from Delft University of Technology, the Netherlands in 1957.

From 1957 to 1964 he worked in the Sydney Radio Section of Telecom, Australia, being at various times engaged in radio communications, studios and the radio laboratory. In 1964 he joined the Commonwealth Scientific and Industrial Research Organization (CSIRO) to develop electronics for interferometry. He took two years leave to work with the Department of Civil Aviation, Jakarta, Indonesia and as a lecturer at the Indonesian Academy of Aviation. In 1966 he returned to the CSIRO to join the RF and Microwave Group where he is the project leader for RF voltage.

Mr. Muller is a member of the Royal Institute of Engineers, the Netherlands.

★

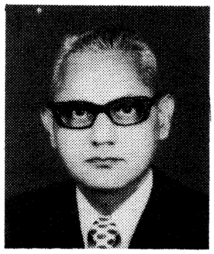

Vempati G. K. Murti (S'59–M'61–SM'69–SM'83) was born at Masulipatnam, India on October 3, 1933. He received the B.E., M.Eng., and Ph.D. degrees, all in electrical engineering from the University of Madras, Yale University, New Haven, CT, and the University of Illinois, Chicago, respectively.

He holds the post of a Professor at the Indian Institute of Technology, Madras and is currently a Visiting Professor with the National University of Singapore, Singapore. His teaching and research interests are in network theory and electrical measurements.

★

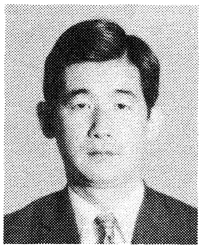

Mitsunobu Nakamura was born in Aichi-ken, Japan, on October 12, 1939. He received the B.E. degree in engineering from University of Tokyo and the Ph.D. degree in science from University of Kyoto, Japan.

He is an Associate Professor of the Department of Electronics, Tanagawa University, Tokyo, Japan, working on percolation problem.

Dr. Nakamura is a member of the Physical Society of Japan and the Japan Society for Simulation Technology.

★

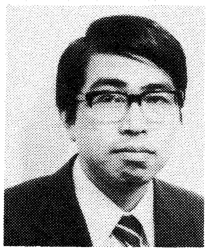

Hiroshi Nakane was born in Hamamatsu, Japan, on September 19, 1944. He received the B.S. and Ph.D. degrees in engineering from Kogakuin University, Tokyo, Japan, in 1967 and 1983, respectively.

In 1969, he joined the Department of Electrical Engineering, Science University of Tokyo, where he has been engaged in high-frequency measurement techniques.

Mr. Nakane is a member of the Institute of Electronics and Communication Engineers of Japan, the Society of Instrument and Control Engineers (Japan), and the Institute of Electrical Engineers of Japan.

★

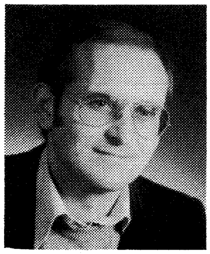

Jürgen Niemeyer was born in Rinteln, Germany, on November 2, 1941. He received the Dipl. Phys. degree in 1970 from the Technische Universität, Braunschweig, Germany, and the Ph.D. degree from the Georg-August-Universität, Göttingen, German, in 1979.

Joing the Physikalisch-Technische Bundesanstalt (PTB) Braunschweig, Germany, in 1971 he was engaged in the development of special Josephson junctions for the voltage standard of the PTB and in research of the influence of magnetic and nonmagnetic impurities on the properties of Josephson junctions.

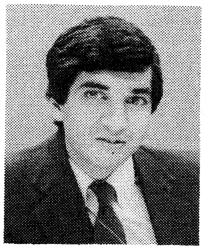

Bidyut Parruck (S'79) was born in India on October 31, 1958. He received the Bachelor of Technology degree in electronics and electrical communication engineering from the Indian Institute of Technology, Kharagpur, India, in June 1981 and the M.S. degree in electrical engineering from Virginia Polytechnic University and State University, Blacksburg in March 1983.

He is currently working as a Member Technical Staff with Advanced Technology Center, ITT, Shelton, CT.

Mr. Parruck is a member of the IEEE Communications Society.

★

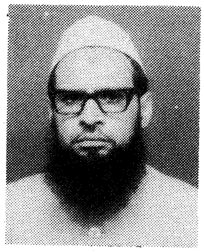

Mahfoozur Rahman was born in India on July 21, 1946. He received the B.Sc. and M.Sc. degrees in electrical engineering from Aligarh Muslim University, Aligarh, India, in 1966 and 1972, respectively, and the Ph.D. degree, also in electrical engineering, from the Indian Institute of Technology, Madras, India, in 1981.

In 1968, he joined the staff of the Z.H. College of Engineering & Technology, Aligarh Muslim University, Aligarh as Lecturer and in 1981 subsequently, he became Reader in the same Department. He has been engaged in the development of Precision Type Transducers and related measurement systems. His current interests are in the application of electronic devices and circuits including microprocessors, in precision measurement and instrumentation systems.

★

Robert L. Ramey (S'47–A'48–M'58–SM'60–SM'71) graduated from Duke University, Durham, NC, and North Carolina State University, Raliegh, and received the Ph.D. degree from North Carolina State University in 1954.

He is currently a Professor of Electrical Engineering at the University of Virginia, Charlottesville. His current research is in the area of microcomputer applications in the control of machine systems. He is the author of three texts: *Matrices and Computers in Electronic Circuit Analysis*, *Physical Electronics*, and *Electronics and Instrumentation.*

Dr. Ramey is a member of Sigma Xi.

★

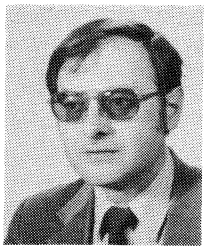

S. I. Reger received the Ph.D. degree in biomedical engineering in 1973.

A year later, he became a Certified Prosthetist and has been working in rehabilitation ever since. His research projects include spinal engineering at the University of Virginia Rehabilitation Engineering Center, Charlottesville, with emphasis on the monitoring of electrical activity from the spinal cord and the stability of spinal reconstructions. Currently, his research involves wheelchair seating and body supports with extensive clinical content. He is also investigating the promotion of bone ingrowth into porous metal prosthesis and the effect of semirigid rods on fracture healing. He is currently an Associate Professor in the Department of Orthopedics and Rehabilitation at the University of Virginia.

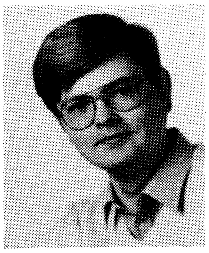

Reinhard Reinschlüssel was born in Duisburg, Germany, on November 5, 1955. He received the Dipl.-Ing. degree in electrical engineering from the Ruhr-Universität, Bochum, Germany, in 1981.

Since 1981 he has been an Assistant at the Institut für Hoch- und Höchstfrequenztechnik of the Ruhr-Universität, Bochum. His present activities are on microwave spectroscopy and the development of a millimeter wave spectrometer.

★

H. Renders was born in Ukkel, Belgium, on March 5, 1955. She received the degree of civil engineer in electrotechnic in 1977 from the University of Brussels (V.U.B.).

Since then she has been a researcher in the field of system identification. She is confronted with measurement problems in electrochemistry and is concerned with the development of special adapted measurement techniques for further use in parameter estimation.

★

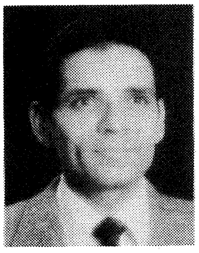

Sedki M. Riad (M'78–SM'83) was born in Egypt on February 19, 1946. He received the B.Sc. and M.Sc. degrees, both in electrical engineering, from Cairo University, Cairo, Egypt in 1966 and 1972, respectively, and the Ph.D. degree in engineering science from the University of Toledo, Toledo, OH in 1976.

From 1966 to 1973, he worked as an Instructor in the Department of Mathematical and Physical Sciences, Faculty of Engineering, Cairo University. From 1975 to 1977, he joined the Electromagnetics Division, National Bureau of Standards, Boulder, CO, as a Guest Worker, where he carried out his Ph.D. dissertation and postdoctoral research. From 1977 to 1979, he worked as an Assistant Professor with the Department of Electrical Engineering and Communication Sciences, University of Central Florida, Orlando. He then joined the Department of Electrical Engineering, Virginia Polytechnic Institute and State University, Blacksburg, as an Assistant Professor (1979–1983), and he is currently an Associate Professor (1983–present).

Dr. Riad is a member of the ISHM and is a registered Professional Engineer in the state of Florida.

★

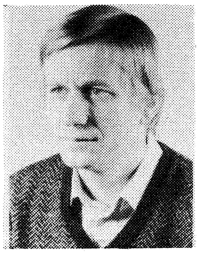

Burkhard Schiek was born in Elbing, Germany, on October 14, 1938. He received the Dipl.-Ing. and the Dr.-Ing. degrees in electrical engineering, both from the Technische Universität Braunschweig, Braunschweig, Germany, in 1964 and 1966, respectively.

From 1964 to 1969 he was an Assistant at the Institut für Hochfrequenztechnik of the Technische Universität Braunschweig, where he worked on frequency multipliers, parametric amplifiers, and varactor phase shifters. From 1966 to 1969, he was involved in MIS interface physics and in the development of MIS varactors. From 1969 to 1978 he was with the Microwave Application Group of the Philips Forschungslaboratorium Hamburg GmbH, Hamburg, Germany, where he was mainly concerned with the stabilization of solid-state oscillators, oscillator noise, microwave integration, and microwave systems. Since 1978 he has been a Professor in the Department of Electrical Engineering, Ruhr-Universität, Bochum, Germany, working on high-frequency measurement techniques and industrial applications of microwaves.

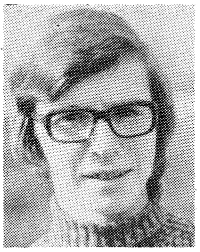

J. Schoukens was born in Lennik, Belgium, on August 18, 1957. He received the degree of civil engineer in electrotechnic in 1980 from the University of Brussels (V.U.B.).

He is presently a Research Assistant of the National Fund for Scientific Research (N.F.W.O.). The prime factors of his research are situated in the field of parameter estimation, especially the estimation of the parameters of continuous time systems.

★

Heinz-Jürgen Siweris was born in Oberhausen, West Germany, on June 26, 1953. He received the Dipl.-Ing. degree in electrical engineering from the Ruhr-University Bochum, West Germany, in 1979.

Since 1979, he has been with the Institut für Hoch- und Höchstfrequenztechnik of the Ruhr-Universität Bochum, where he has been engaged in research on radiometer systems and microwave oscillators.

★

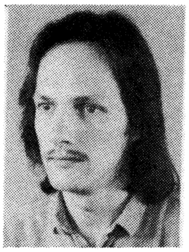

Manfred Spaude was born in Düsseldorf, Germany, on August 18, 1953. He received the Dipl.-Ing. degree in electrical engineering from the Ruhr-Universität, Bochum, Germany, in 1979.

Since 1979 he has been an Assistant at the Institut für Hoch- und Höchstfrequenztechnik of the Ruhr-Universität, Bochum. His present activities are on noise temperature measurements and the development and evaluation of radiometer systems.

★

Alfred G. Sutton received the B.S. degree in chemistry from Huntington College, Huntington, IN, and received the M.S. degree in physics from Purdue University, West Lafayette, IN, in 1974.

He is a systems engineer with experience in computer-controlled automation. He provided computer/software expertise for this project through Comarco, Simutec Division. He has since returned to Oak Ridge National Laboratory, Instrumentation and Controls Division.

★

Saleem M. R. Taha was born in Baghdad, Iraq, in 1956. He received the B.Sc. degree and the M.Sc. degree in electrical engineering from Baghdad University, Baghdad, Iraq, in 1978 and 1982, respectively.

From October 1978 to May 1982, he worked with the State Organization for Technical Industries (SOTI), Baghdad, Iraq. From June 1982 to April 1983, he was with SOTI Computer Center. He is presently an Assistant Lecturer at the Baghdad University. He has contributed to and authored many papers in the areas of digital signal processing, digital measurements instrumentation, computer-aided design, and computer simulation and hybrid circuit design.

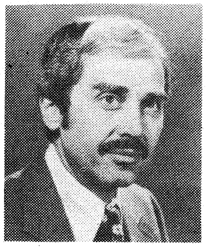

Gabor C. Temes (SM'66–F'73) received his Dipl.Ing. from the Technical University of Budapest, Hugary, in 1952, his Dipl.Phys. from Eotvos University, Budapest, Hugary, in 1954, and the Ph.D. degree in electrical engineering from the University of Ottawa, Ont., Canada, in 1961.

He was a member of the faculty of the Technical University of Budapest from 1952 to 1956. He was employed by Measurement Engineering Ltd., Arnprior, Ont., Canada, from 1957 to 1959. From 1959 to 1964 he was with Northern Electric R and D Laboratories, Ottawa, Ont., Canada. From 1964 to 1966 he was a research group leader at Stanford University, Stanford, CA; from 1966 to 1969, a Corporate Consultant at Ampex Corporation, Redwood City, CA. He is now on the faculty of the University of California, Los Angeles, as a Professor in the Department of Electrical Engineering. Between 1975 and 1979, he was also Chairman of the Department. He is an Associate Editor of the *Journal of the Franklin Institute* and a former Editor of the IEEE Transactions on Circuit Theory. He has published over 100 technical papers. He is coeditor with S. K. Mitra) and co-author of *Modern Filter Theory and Design*, Wiley, 1973, coauthor of *Introduction to Circuit Synthesis and Design*, McGraw-Hill, New York, 1977, and a contributor to several other edited volumes.

Dr. Temes is a former Vice-President of the IEEE Circuits and Systems Society, and a former Chairman of its Best Paper Awards and Nominations Committees. He was a member of the Fellow Award Committee as well as the CANDE Committee of the IEEE Circuits and Systems Society. In 1968 and in 1981, he was a co-winner of the Darlington Award of the IEEE Circuits and Systems Society. In 1981, he received the Outstanding Engineer Merit Award of the Institute for the Advancement of Engineering. In 1982, he won the Western Electric Fund Award of the Amercian Society for Engineering Education.

★

Chii M. Uang was born in Miao-Li, Taiwan, R. O. C., in 1950. He received the B.S.E.E. degree from Cheng-Kung University, Taiwan, in 1978. He is presently a Doctoral candidate in computer science in Cheng-Kung University.

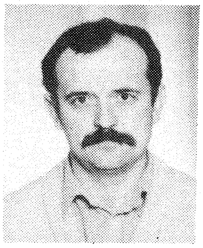

Dragan M. Vasiljević was born in Tabanović, Yugoslavia, on September 10, 1950. He received the B.Eng. degree in electrical engineering from University of Belgrade, Yugoslavia, and the M.S. degree in electronics from the same university in 1974 and 1977, respectively. He is presently completing his doctoral thesis from the quartz oscillator analysis field.

He is currently an Assistant in Electrical Engineering, University of Belgrade. His interest is in the field of oscillators.

★

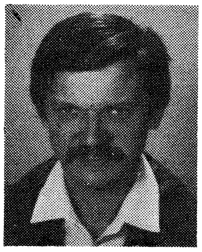

G. Vilain was born in Vilvoorde, Belgium, on August 4, 1954. He received the degree of civil engineer in electrotechnic in 1977 from the University of Brussels (V.U.B.).

Since then he has been attached to the department of General Electricity and Measurement Techniques at the University of Brussels. His research interests include information theory, design of experiment and its applications in measurements.

★

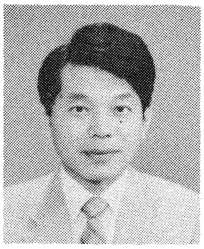

Kenzo Watanabe (M'74) received the B.Eng. and M.Eng. degrees from Shizuoka University, Hamamatsu, Japan, in 1962 and 1966, respectively, and the Dr.Eng. degree from Kyoto University, Kyoto, Japan, in 1976.

From 1966 to 1976, he was a Research Associate at the Research Instiiute of Electronics, and since 1977, he has been an Associate Professor. He is now interested in analog signal processing using active-*RC* and switched-capacitor circuits.

Dr. Watanabe is a member of the Institute of Electronics and Communications Engineers of Japan and the Japan Society of Applied Physics.

1984 Index
IEEE Transactions on Instrumentation and Measurement
Vol. IM-33

This index covers all items—papers, correspondence, reviews, etc.—that appeared in this periodical during 1984, and items from prior years that were commented upon or corrected in 1984. The index is divided into an Author Index and a Subject Index, both arranged alphabetically.

The *Author Index* contains the primary entry for each item; this entry is listed under the name of the first author and includes coauthor names, title, location of the item, and notice of corrections and comments if any. Cross-references are given from each coauthor name to the name of the corresponding first author. The location of the item is specified by the journal name (abbreviated), year, month, and inclusive pages.

The *Subject Index* contains several entries for each item, each consisting of a subject heading, modifying phrase(s), first author's name—followed by + if the paper has coauthors—and enough information to locate the item. For coauthors, title, comments, and corrections if any, etc., it is necessary to refer to the primary entry in the Author Index. Subject cross-references are provided as required by the subject matter. Also provided whenever appropriate are listings under generic headings such as *Bibliographies* (for any paper with at least 50 references, as well as papers that are exclusively bibliographies), *Book reviews*, and *Special issues*.

AUTHOR INDEX

SUBJECT INDEX

+ Check author entry for coauthors

† Check author entry for subsequent corrections/comments

IEEE Instrumentation and Measurement Society

Transactions

Editor

Fred Liguori
38 Clubhouse Rd.
Browns Mills, NJ 08015
(201) 323-2842

Associate Editors

Derek Morris
Division of Physics
National Research Council
Ottawa, Ont. K1A OR6, Canada
(613) 993-2704

Peter Kartaschoff
Post Office Headquarters
Technical Center
CH-3000 Bern 29, Switzerland
+41 (31) 62 43 80

Makoto Kanno, Dean
Faculty of Engineering
Tamagawa University
Machida-shi
Tokyo 194, Japan
0427 32 9111

Editorial Review Committee

Dr. Arthur Ballato
U.S. Army Electronics Technology
And Devices Laboratory
Fort Monmouth, NJ 07703

Dr. Barry Bell
Electrosystems Div.
National Bureau of Standards
Washington, DC 20234

Dr. Harry Cronson
The Mitre Corp. MS J 101
PO Box 208
Bedford, MA 01730

Dr. Leonard S. Cutler
Hewlett-Packard Co.
3500 Deer Creek Rd.
Palo Alto, CA 94304

Dr. John J. Degnan, III
Goddard Space Flight Center
Greenbelt, MD 20771

Dr. Andrew F. Dunn
National Research Council
Ottawa, Ont., Canada K1A OS1

William L. Gans
N.B.S. Div. 723.05
325 Broadway
Boulder, CO 80303

Prof. Paul A. Goud
University of Alberta
Edmonton, Alta., Canada T6G 2E1

Loring Hosley
NAEC 92511
Lakehurst, NJ 08733

A. Ray Howland
The Howland Co. Inc.
Box 1048
Decatur, GA 30031

Prof. Robert G. Irving
California Polytechnic University
3801 W. Temple Ave.
Pomona, CA 91768

Dr. Robert A. Kamper
Electromagnetics Div.
National Bureau of Standards
Boulder, CO 80302

Prof. Reuven Kitai
McMaster University
Hamilton, Ont., Canada L8S 4L7

Dr. Henriecus Koeman
John Fluke Mfg. Co., Inc.
1022 C Ave.
Edmonds, WA 98020

Mr. Frank Koide
Rockwell International
3370 Miraloma Ave.
Anaheim, CA 92803

Dr. Robert A. Lawton 723.05
National Bureau of Standards
Boulder, CO 80303

John Lewis
2710 Shadow Canyon Cr.
Norco, CA 91760

Dr. Michael S. P. Lucas
Kansas State University
Seaton Hall
Manhattan, KS 66506

Dr. T. McComb
National Research Council
DEE, Bldg. M-50
Ottawa, Ont., Canada K1A OR8

Dr. Norris S. Nahman
National Bureau of Standards
Boulder, CO 80303

Dr. Roy H. Nesson
Hughes Aircraft Co.
E 51/A 219 Box 902
El Segundo, CA 90245

Dr. Carlos Urbana Pacheco
Calle 14 No. 1128 Norte Torreon
Coahuila 27000, Mexico

Dr. Gordon R. Partridge
Gen Rad
Bolton, MA 01740

Dr. Oskars Petersons
National Bureau of Standards
Washington, DC 20234

Dr. W. A. Plice
Honeywell Inc.
MN-17-2303 Box 312
Minneapolis, MN 55440

Dr. Morris M. Reichbach
Naval Air Engineering Center
Lakehurst, NJ 08733

Dr. Victor Reinhardt
Bendix Field Eng. Co.
1 Bendix Road
Columbia, MD 21405

Mr. Edwin Richter
RCA Corporation
Burlington, MA 01803

Dr. Lawrence G. Rubin
National Magnet Lab.
MIT Bldg. NW14
Cambridge, MA 02139

Dr. Lauren Rueger 4-326
Applied Physics Lab
Johns Hopkins University
Laurel, MD 20707

Dr. Romanus M. Serbyn
Sound Div.
National Bureau of Standards
Washington, DC 20234

Prof. Willem Steenaart
University of Ottawa
Ottawa, Ont., Canada K1N 6N5

Dr. Harris A. Stover
Defense Communication Engineering
Center
Reston, VA 22090

Prof. Jacques Vanier
Universite Laval
Quebec, Que., Canada G1K 7P4

Dr. Fred L. Walls
National Bureau of Standards
Boulder, CO 80303

William G. Wolber
3151 Sumac Ct.
Columbus, IN 47202

Estimate of Overlength Page Charge

The first five pages (four for Special Issues) are printed free. For every page beyond this limit, there is an overlength page charge of $100 per page. If a manuscript is typed in double space (3 lines per inch) using elite type (12 characters per inch) in an area of 6.5 × 9 inches, a rule of thumb of 3 typewritten pages to 1 printed page is a good estimate. One printed page consists of two columns 3.5 inches wide by 9.5 inches high which is equivalent to 3 double-spaced typewritten pages. To estimate the printed pages for figures or tables from original drawings, first reduce the width to 3.5 inches, then use the same width reduction ratio to calculate the height. Add 0.6 inches for the caption to the calculated height to obtain the column height occupied by each figure or table. Next, add the column heights of all figures or tables, divide the sum by 19 to obtain the estimated printed page length for the figures or tables. Finally, add the estimated pages for text, figures, or tables and 0.17 for title to give you the total estimated printed pages.

INSTITUTIONAL LISTINGS

The IEEE Instrumentation and Measurement Society invites application for Institutional Listings from firms interested in the field of instrumentation and measurement.

An Institutional Listing recognizes contributions to support the publication of the IEEE TRANSACTIONS ON INSTRUMENTATION AND MEASUREMENT. Minimum rates are $100 for listing in one issue, or $300.00 for four issues. Larger contributions will be most welcome. No agency fee is granted for soliciting such contributions. Inquiries, or contributions made payable to the IEEE, plus instructions on how you wish your institutional listing to appear, should be sent to M. Bonaviso, The Institute of Electrical and Electronics Engineers, Inc., 345 East 47 Street, New York, N. Y. 10017.

Invitation for Papers

The objective of the Society is to promote the exchange of technical information among its members. The TRANSACTIONS provides the medium for this communication. The effective use of the medium and the quality of this TRANSACTIONS depend on the membership of the Society who contribute papers reporting new and interesting findings on instrumentation and measurement. Original papers relating to instrumentation and measurement are invited. Tutorial and review papers will be published periodically, unsolicited manuscripts of a tutorial or review nature are welcome, but it would be advisable for prospective authors of such papers to contact the Editor well in advance concerning probable constraints. Short papers (less than three printed pages) giving an interim report of research findings and correspondence (less than two printed pages) disclosing new ideas and preliminary results or commenting on papers published in this TRANSACTIONS are encouraged. Papers that have been published elsewhere in general are not acceptable.

Authors from **Canada** should submit to the Associate Editor **Dr. Derek Morris** in Canada, from **Europe** to the Associate Editor **Prof. Claude Audoin** in France, from **Japan** to the Associate Editor, **Prof. Osamu Nishino,** from the United States and other countries to the Editor one original and three (3) copies of the manuscript or correspondence items for publication in IEEE TRANSACTIONS ON INSTRUMENTATION AND MEASUREMENT, a signed copyright transfer form, and a letter of agreement to pay over length charges for excess over five pages of printed copy. A manuscript should include an abstract (not more than 200 words for a regular paper and not more than 50 words for correspondence), a biographical sketch, and a photograph of the author. For suggestions regarding manuscript preparation, authors should consult "Information for Authors," IEEE TRANSACTIONS ON INSTRUMENTATION AND MEASUREMENT, Vol. IM-30, No. 1, pp. 89–90, March 1981. Particular points are to be observed.

1) Manuscript should be easy to read and should be spaced so that instructions to the typesetter can be added. Double-spaced typing on 8½ × 11-inch (21.5 × 28-cm) pages with 1-inch margins all around is recommended. The manuscript should include:
   a) title—should be short and descriptive of the subject
   b) byline—should give the author's name, affiliation, and complete mailing address without abbreviations
   c) abstract—should state the nature of the investigation and summarize its important conclusions in a single paragraph
   d) text—should be succinct and effective in communication with peers who may not be in the field of speciality
   e) original drawings and photographs of figures and tables
   f) a separate list of captions for the figures and tables
   g) author's brief biography and photograph
   h) a signed copy of the IEEE Copyright Transfer Form
   i) a letter of agreement to pay the overlength page charge or to reduce the text to within the prescribed free publication page limit.

2) Mathematical equations should be typed if possible. Handwritten symbols and acronyms must be clearly identified the first time they are used.

3) Use of the International System (SI) of units is recommended.

4) Drawings for figures should be of high contrast. India ink on 8.5 × 11-inch (21.5 × 28-cm) white tracing paper is recommended. Figures should not contain details so small that a magnifying glass will be needed after they have been reduced in size.

5) The typist should follow the arrangement used in a recent issue of this TRANSACTIONS, especially for format, capitalization, and punctuation of titles and references.

6) Obtain an IEEE Copyright Transfer Form from a recent March issue of this TRANSACTIONS. Complete Part A or Part B, whichever is appropriate.